

Graphitic carbon materials for energy and environment

This thesis is submitted in fulfilment of the requirement for the degree of

Doctor of Philosophy

Engineering (nanotechnology)

By **Ramesh Udayashankar Karunakaran**

February 2018



THE UNIVERSITY
of ADELAIDE

School of Chemical Engineering
Faculty of Engineering, Computer, and Mathematical Science
The University of Adelaide

CONTENTS

ABSTRACT	iii
PREFACE	vi
LIST OF PUBLICATIONS	vii
DECLARATIONS	ix
ACKNOWLEDGEMENTS	x
ABBREVIATIONS	xiii
CHAPTER 1: Introduction	1
1.1 Graphitic carbon materials	3
1.2 Graphitic carbon materials for energy and environmental applications	11
2.0 Addressing significant problems on energy and environmental crisis	24
3.0 Aims and Objective	30
4.0 Thesis structure	31
5.0 References	35
CHAPTER 2: Experimental	53
2.1 Introduction	54
2.2 Materials	54
2.3 Methods	56
2.4 Characterisation	58
2.5 Reference	77
CHAPTER 3: The investigation of the synthesise of ORR catalyts with unique 3D - Hydride structures comprise of N-CNT and N-CMS using both synthetic and natural bio sources	79
CHAPTER 3 (a): A unique 3D nidrogen - doped carbon composite as high performance oxygen reduction catalyts	81
CHAPTER 3 (b): Green Synthesis of three-dimensional hybrid N-doped ORR electro catalyts composed of nitrogen doped micro-spherical and nanotubular structures using Apricot Sap	101

CHAPTER 4: The investigation of four different iron oxide nanoparticle phases dispersed in a 3-D graphene aerogel as ORR electrocatalysts	129
CHAPTER 4 (a): Study of iron oxide nanoparticle phases in graphene aerogels for oxygen reduction reaction	131
CHAPTER 5: Investigation of a synthesis procedure of a unique 3-D macroporous ORR electrocatalyst using sulphonated aniline oligomers and its PF and rGO composites	151
CHAPTER 5 (a): A facile synthesis procedure for sulphonated aniline oligomers with distinct microstructures	154
CHAPTER 5 (b): A unique N-doped macro porous oxygen reduction electro catalysts synthesised using sulphonated aniline oligomers with phenol formaldehyde and reduced graphene oxide composites	174
CHAPTER 6: Investigation of the effect of different functional groups of organic materials on the long-term air stability of ZVI and the effect of air stabilised and less agglomerated ZVI nanoparticles on As adsorption	199
CHAPTER 6 (a): An atmospherically stable and agglomeration-free zero-valent iron reduced graphene oxide (ZVI-rGO) composite for high performing environmental remediation	201
CHAPTER 7: Conclusion and recommendations for future works	241
7.1 Conclusion	242
7.2 Recommendations for future works	249
APPENDIX	251

ABSTRACT

Over the years, carbon has become one of the most intensively investigated topics in both industry and academia and has wide ranging applications in energy conversion, energy storage, adsorption, sensing, photo-electrical water splitting, water purification and gas separation. Recently, carbon materials have been widely used for advancement of energy conversion and water remediation applications due to its unique physicochemical properties, surface chemistry, processability, mechanical stability and chemical resistance. Furthermore, carbon may form porous structures and be assembled in different shapes such as spheres, tubes, fibers, sheets and 3D structures providing a high degree of versatility for multiple applications. The low cost is advantageous in many catalytic applications for the replacement of expensive and less abundant metal catalysts such as platinum, which is heavily relied upon for fuel cells as an oxygen reduction catalyst. In this context, the Ph.D. project focussed on the synthesis of graphitic carbon composite materials with unique morphologies to the benefit of energy and environmental applications. The following four concepts were developed and explored in this thesis and summarised as:

1. Fabrication of a unique 3D- nitrogen doped carbon composite materials of N-doped carbon nanotubes and N-doped carbon spheres from bio source their application as oxygen reduction reaction (ORR) catalysts

The synthesis of nitrogen doped carbon nanotubes (N-CNT) and N-doped carbon micro spheres (N-CMS) composites were demonstrated using low cost and eco-friendly bio source galactose, iron oxide nanoparticles (maghemite) and nitrogen precursor melamine. This unique integrated structure containing N-CNT and N-CMS showed enhanced ORR catalytic activity *via* predominantly four - electron kinetics ($n = 3.55 - 3.64$ in the potential range of 0.10 – 0.70 V (RHE)) with a low HO_2^- yield (22.44 – 16.96 % in the potential range of 0.10 – 0.70 V (RHE)). Furthermore, in the context of eliminating hazardous chemical usage and to utilise more green products as ORR catalysts, galactose containing naturally occurring apricot sap was used to synthesise a similar electro catalyst as described above using maghemite nanoparticles (N-APG-Fe) and a cobalt precursor (N-APG-Co). Both catalysts formed similar integrated structures comprise of N-CNT and N-CMS as mentioned above and showed excellent oxygen reduction properties with an electron transfer number 3.61 for both N-APG-Co and N-APG-Fe catalysts at 0.40 V (RHE) and low HO_2^- yield (> 20.00 %) for both catalysts. The presented

synthetic concept opens doors for new approaches for the development of low cost non-hazardous hybrid catalysts using abundantly available bio sources and green products.

2. Investigation of different phases of low iron oxide catalysts as an alternative for Pt/C catalysts for ORR

To explore the use of cheap, abundant and freely available iron oxide catalyst as a potential substituent for the expensive and scarce Pt catalysts, four different phases of iron oxide nanoparticles (magnetite, maghemite, hematite and goethite) were synthesised and systematically evaluated as oxygen reduction catalysts for ORR. The four different phases were separately synthesised and prudently dispersed in 3D-reduced graphene oxide aerogels without exposing them for any phase changes. These catalysts (rGO/Fe₃O₄, rGO/γ-Fe₂O₃, rGO/α-Fe₂O₃ and rGO/α-FeOOH) investigated as electro catalysts for oxygen reduction did not show significant enhancement for ORR compared to the standard Pt/C catalysts. Comparative study showed that rGO/Fe₃O₄ and rGO/γ-Fe₂O₃ catalysts with inverse spinel structures with magnetic and electron conduction properties showed significantly higher ORR activity compared to rGO/α-Fe₂O₃ and rGO/α-FeOOH with rhombohedral and orthorhombic structures, respectively. The outcome of these investigations revealed the need for the exploration of more spinel structure of different metal oxides to be investigated as low-cost substituent to the expensive Pt/C catalysts for ORR.

3. Synthesis of macro porous N-doped carbon catalysts using sulphonated aniline oligomers (SAO) and SAO/ phenol formaldehyde (PF) and SAO/reduced graphene oxide (rGO) composites for ORR

Sulphonated aniline oligomers (SAO) with distinctive microstructures of flakes and rods were synthesised using aniline and oxidants; and used for the synthesis 3D N-doped composite combining phenol formaldehyde (PF) and reduced graphene oxide (rGO) pyrolysed with a nitrogen precursor (melamine). The electrochemical characterization confirmed that composites with higher concentration of pyridinic nitrogen species (42 At%) showed higher positive onset potential of 0.98 V and performed the ORR with four - electron transfer kinetics ($n = 3.64$) with a low yield of HO₂⁻ (19 %) at 0.50 V (RHE) compared to low concentration of pyridinic nitrogen (37 At%) and higher concentration of graphitic nitrogen (63 At%). Composites prepared with conductive graphene structures displayed higher current density of 7.89 mA/cm², which is more than 60 % of the standard Pt catalysts. This unique procedure

demonstrates a new approach of synthesising macro porous carbon structures with potentially viable composites of carbon materials for many future catalytic applications.

4. Investigation of different organic coating materials to provide long term air stability to Zero-valent iron (ZVI) and evaluation of air stable materials dispersed in rGO as arsenic adsorbents

Zero-valent iron (ZVI) nanoparticles have been extensively investigated for treatment of hazardous and toxic waste from contaminated sites and water remediation both these applications have been hindered due to their low air stability and tendency to agglomerate. To address this problem and stabilize the ZVIs nanoparticles, several coating materials and organic molecules with various functional groups (amine, thiol, hydroxyl and carboxyl) have been demonstrated and evaluated. The results show that the ZVI coated with organic molecules containing carboxyl groups (glycine) has unprecedented stability and shelf life (> 12 months) under atmospheric conditions. To solve the agglomeration problem, the glycine protected ZVI nanoparticles were dispersed in rGO solution to make an atmospherically stable and aggregation-free ZVI-rGO composites. The environmental remediation performance of the prepared composite was evaluated using arsenic (As) solutions and showed an outstanding adsorption efficiency (As(III) (400 mg/g) and As(V) (131 mg/g) over a range of pHs, making ZVI-rGO composites an ideal sorbent for the removal of arsenic in broad remediation applications.

PREFACE

This thesis is submitted as a “thesis by publication” in accordance with “Specifications for Thesis 2013” of The University of Adelaide. The PhD research spanning 4 years generated 10 peer-reviewed journal articles: 6 published (3 as first author), 2 submitted (all first author), and 1 in final preparation (as first author) for submission in 2018. Furthermore, the PhD research was presented at 2 national conferences as first author. The research chapters included in this thesis were published (or submitted or in final preparations for submission) as research articles in highly esteemed journals in the field. The list of publications is provided in the following pages.

LIST OF PUBLICATIONS

Peer-reviewed journal articles

Published / Accepted Articles

1. **R. Karunagaran**, T. T. Tung, C. Shearer, D. Tran, C. Coghlan, C. Doonan, D. Losic “A unique 3D nitrogen - doped carbon composite as high performance oxygen reduction catalysts” *Materials*, 2017, **10**, 921.
2. **R. Karunagaran**, C. Coghlan, T.T. Tung, S. Kabiri, D. Tran, C. Doonan, D. Losic “Study of iron oxide nanoparticle phases in graphene aerogels for oxygen reduction reaction” *New Journal of Chemistry*, 2017, **41**, 15180 - 15186.
3. **R. Karunagaran**, C. Coghlan, C. Shearer, D. Tran, Karan Kulati, T. T. Tung, C. Doonan, D. Losic “Green Synthesis of three-dimensional hybrid N-doped ORR electro catalysts composed of nitrogen doped micro-spherical and nanotubular structures using Apricot Sap” *Materials*, 2018, **11**, 205.
4. T. T. Tung, **R. Karunagaran**, D. Tran, B. Gao, S. N. Chowdhury, I. Pillin, M. Castro, J. Feller, D. Losic “Engineering of graphene/ epoxy nanocomposites with improved distribution of graphene nanosheets for advanced piezo-resistive mechanical sensing” *Journal of Material Chemistry C*, 2016, **4**, 3422 - 3430.
5. K. Gulati, L. Johnson, **R. Karunagaran**, D. Findlay, D. Losic “In situ transformation of chitosan films into microtubular structures on the surface of nanoengineered titanium implants” *Biomacromolecules*, 2016, **17**, 1261 - 1271.
6. T. T. Tung, J. Yoo, F. Alotaibi, J. Nine, **R. Karunagaran**, G. Nguyen, D. Tran, J. Feller, D. Losic “Graphene Oxide – Assisted Liquid Phase Exfoliation of Graphite into Graphene for Highly Conductive Film and Electromechanical Sensors” *ACS Applied materials and Interfaces*, 2016, **8**, 16521 - 16532.

Submitted Articles

1. **R. Karunagaran**, C. Coghlan, D. Tran, T. T. Tung, A. Burgun, C. Doonan, D. Losic
“A facile synthesis procedure for sulphonated aniline oligomers with distinct microstructures” *Journal of Material Science*, 2018.
2. **R. Karunagaran**, S. Kabiri, I. Andelkovic, C. Coghlan, D. Tran, C. Doonan, D. Losic
“An atmospherically stable and agglomeration-free zero-valent iron reduced graphene oxide (ZVI-rGO) composite for high performing environmental remediation” *Journal of Chemical Engineering*, 2017.

Articles in Final Preparation (for submission in 2018)

1. **R. Karunagaran**, C. Coghlan, D. Tran, T. T. Tung, C. Shearer, Alexander Burgun, C. Doonan, D. Losic
“A unique N-doped macro porous oxygen reduction electro catalysts synthesised using sulphonated aniline oligomers with phenol formaldehyde and reduced graphene oxide composites” *Materials*.

Conference Poster Presentations

1. **R. Karunagaran**, T. T. Tung, C. Shearer, D. Tran, C. Coghlan, C. Doonan, D. Losic
“A unique 3D nitrogen - doped carbon composite as high performance oxygen reduction catalysts” Australian Solar Thermal Research Initiative Researcher Development Workshop, Brisbane Australia, February 2015.
2. **R. Karunagaran**, C. Coghlan, T.T. Tung, S. Kabiri, D. Tran, C. Doonan, D. Losic
“Study of iron oxide nanoparticle phases in graphene aerogels for oxygen reduction reaction” Research Day - Centre for Energy Technology, South Australia, Adelaide, November 2016.

DECLARATION

I certify that this work contains no material which has been accepted for the award of any other degree or diploma in my name in any university or other tertiary institution and, to the best of my knowledge and belief, contains no material previously published or written by another person, except where due reference has been made in the text. In addition, I certify that no part of this work will, in the future, be used in a submission in my name for any other degree or diploma in any university or other tertiary institution without the prior approval of the University of Adelaide and where applicable, any partner institution responsible for the joint-award of this degree.

I acknowledge that copyright of published works contained within this thesis resides with the copy right holder(s) of those works.

I also give permission for the digital version of my thesis to be made available on the web, *via* the University's digital research repository, the Library search and also through web search engines, unless permission has been granted by the University to restrict access for a period of time.

I acknowledge the support I have received for my research through the provision of an Australian Government Research Training Program Scholarship.

RAMESH KARUNAGARAN (Signature)

Date:

ACKNOWLEDGEMENT

Four years back in 2013, to accomplish my childhood dream to become a scientist, I approached Prof. Dusan Losic seeking help and guidance. Today, after a challenging 4 years, I stand confident as a young researcher equipped with the necessary skills and abilities to serve the scientific community. This would have never been possible without the help and guidance of Prof. Dusan Losic. The immense confidence he had in me was my driving force to complete my journey. In all my weakness and failures, he trusted and motivated me and converted my weaknesses into my strengths. I sincerely and wholeheartedly thank Prof. Dusan Losic for walking the journey with me and I found myself extremely blessed to have a mentor like him.

I also like to thank Prof Christian Doonan for collaborating with Australian Solar Thermal Research Initiative (ASTRI) and organising the experimental facilities and arranging funding for my studies. I thank him for travelling interstate with me and participating in all scientific discussions and encouraging me to successfully complete my experiments. Dr. Diana Tran and Dr. Campbell Coghlan are the backbones of my research papers. I sincerely thank them for their tireless effort to edit my abstracts and manuscripts and correct appropriately. I am so grateful for their whole-hearted effort for mentoring me to be a good scientist. A special thanks to Dr. Tung Tran, Dr. Ivan Andjelkovic and Shervin Kabiri for sharing their expertise knowledge and motivating me whenever I found myself hopeless.

I am also grateful to Prof. Allan Chaffee for allowing me to use his laboratory at University of Monash, Clayton and for sharing his years of academic and industrial research expertise with me. The effort and support Dr. Christian Vogt extended to design and conduct the experiments at University of Monash is overwhelming. Particularly, for attending the University at midnight to assist me and to shut down the experimental rigs is extremely precious. I thank Dr. Cameron Sherer from the University of Flinders for conducting XPS analysis. I graciously

thank Dr. Campbell Coghlan, Dr. Alexander Burgun and Dr Jessi Teo for the kind cooperation extended to set up the sophisticated experimental procedures in the Chemistry laboratory and assisting me with the experiments.

I like to thank the University of Adelaide and with Australian Solar Thermal Research Initiative (ASTRI) for providing me the scholarship to pursue my study. The support extended by the Adelaide Microscopy team including Ken Neubauer, Animesh Basak, Lyn Waterhouse, Agata Labrinidis, Sarah Gilbert and Ashley Slattery are very much appreciated. The assistance the School of Chemical Engineering and School of Chemistry office staff provided with all my administration related work, chemical ordering and organising travel arrangements can never be forgotten. I also like to extend a special thanks to Jason Peak in the Chemical Engineering workshop for attending all my inquiries without hesitation and helping me with the equipment installations. I am so grateful for the staff of Adelaide Graduate Centre for providing me with appropriate information whenever I approached the.

I would also like to thank the entire students of the Losic group of the Chemical Engineering and the students of Doonan group of Chemistry for providing an enjoyable and more pleasant place to work. I take this opportunity to wish them all success. Every event we celebrated together including visit to Barossa valley, Mouth lofty, Bowling and Laser Tags, BBQs, soccer and cricket matches not only give wonderful memories, but also helped to relieve any stress during the period of my PhD life.

Nothing would have been possible without the support and endless love of my dear wife Subhani. I am so grateful for the sacrifices she made for the last 4 years to help me to accomplish my dream of becoming a scientist. I sincerely thank Subhani and my daughter Nethaya for sacrificing their valuable family time for my PhD. I also thank my sister Shanthi, my brother in law Premananda and their kids Divya and Ashwinth for encouraging me to

complete my studies. Even though my parents are deceased, I thank them for their effort to educate me under much difficult circumstances. There is no doubt their blessing is always there for me. I thank all my teachers who taught me at school and in universities for their wholehearted effort to educate me. Without out their effort, I would have never achieved these milestones. Finally, I thank God for the providing all my needs to pursue and complete my PhD studies.

LIST OF ABBREVIATIONS

3D	3-Dimensional
AO	Aniline Oligomers
ASTRI	Australian Solar Thermal Research Initiative
BET	Brunauer- Emmett-Teller
BTU	British Thermal Units
CB	Carbon Black
C-DOTs	Carbon-Dots
CF	Carbon Fiber
CMS	Carbon Micro Spheres
CNF	Carbon Nanofiber
CNT	Carbon nanotubes
CV	Cyclic Voltammetry
DFT	Density Functional Theory
DI	Deionised
EDX	Energy Dispersive X-ray Spectroscopy
EIA	Energy Information Administration
FTIR	Fourier-Transform Infrared Spectroscopy
GHG	Green House Gases
GO	Graphene Oxide
HIV	Human Immunodeficiency Virus
HSAB	Hard Soft Acid Base Theory
HT	Hydrothermal
IEO	International Energy Outlook

IEP	Iso Electric Point
LSV	Linear Sweep Voltammetry
MNPC	Magnetic Nanoparticle Clusters
MPC	Mesoporous Carbon
MWCNT	Multi-Walled Carbon Nanotube
NMR	Nuclear Magnetic Resonance
NP	Nanoparticle
OMC	Ordered Mesoporous Carbon
ORR	Oxygen Reduction Reaction
PEMFC	Polymer Electrolyte Membrane Fuel cell
PID	Proportional-Integral-Derivative
RDE	Rotating Disc Electrode
RES	Renewable Energy Sources
RGA	Regular Gas Analyser
rGO	Reduced Graphene Oxide
RHE	Reversible Hydrogen Electrode
RO	Reverse Osmosis
RRDE	Rotating Ring Disc Electrode
SAED	Selected Area (Electron) Diffraction
SAO	Sulphonated Aniline Oligomers
SEM	Scanning Electron Microscopy
SWCNT	Single-Walled Carbon Nanotube
TEM	Transition Electron Microscopy
VA	Vertically Aligned

XPS X-ray Photo Electron Spectroscopy

XRD X-ray Diffraction

ZVI Zero Valent Iron

CHAPTER 1

INTRODUCTION

Ramesh Karunagaran

School of Chemical Engineering, University of Adelaide, South Australia 5005, Australia

CHAPTER 1: INTRODUCTION

Graphitic carbon materials for energy and environment

1. Introduction

Carbon is the second most abundant element in the biosphere and the 15th most abundant element in the earth's crust and provides the basis for life on earth.^{1,2} Carbon atoms have four valence electrons which are capable of forming sp^2 , sp^3 and sp – hybridised states that adapt to form single, double, triple and aromatic carbon – carbon bonds.³ This makes carbon capable of forming many allotropes. Natural materials made from elemental carbon may possess different properties arising from their structure. For instance, graphite with sp^2 hybridised carbon atoms is soft, opaque and is electrically conductive, while diamond composed of sp^3 hybridised carbon atoms is hard, transparent and acts as an insulator.⁴⁻⁶ The discovery of fullerenes in 1985 by Kroto *et al.*,⁷ followed by the invention of carbon nanotubes (CNT) in 1991⁸ and recently graphene in 2004⁹ has led to the explosion of newly developed carbon materials for unlimited numbers of applications including electronics, energy storage,¹⁰ sensors,¹¹ catalysis, photo – electrical water splitting,¹² adsorption,¹³ water purification¹⁴ and gas separation.¹⁵ The significant development of carbon materials have been recognized by the scientific community through the awarding of the Nobel Prize in Chemistry in 1996 for fullerenes, the Kavli Prize for carbon nanotubes in 2008 and the Nobel Prize for Physics for graphene in 2010.²

Carbon materials are commonly integrated within polymeric and inorganic materials which serve to increase mechanical strength, toughness and electrical conductivity.¹⁶ Carbon displays a unique surface property with hydrophobic basal planes and hydrophilic surface functional groups such as oxygen, fluorine, nitrogen, carbonyl and carboxyl groups at the edges of the carbon atoms.¹⁷ These sites can act as primary sites for catalytic nanoparticle interaction and

heavy metal adsorption *via* electrostatic, coordination and/or van de Waal type interactions.^{18,}

¹⁹ Furthermore, carbon materials are tuneable and can be tailored to produce different forms such as spheres, tubes, fibres, sheets, and other three-dimensional (3D) architectures. The large surface area of these carbon materials can facilitate rapid diffusion of electrolytes and provide high active sites in electrochemical reactions.^{20, 21} Moreover, they are resistant to acids and bases, remain stable above 1023 K under inert atmosphere, and have the ability to form composites and hybrids with other materials.²²⁻²⁷ Although carbon materials and its composites with other elements have widely been used in research and industrial development, their structural diversity, mechanical properties, physicochemical properties, surface chemistry, processability and chemical resistance still require further exploration.⁵

Herein, the diverse range carbon nanomaterials and their applications are summarised. Firstly, the composite forms of carbon nanomaterials and other elements such as metals and metal oxide nanoparticles, polymers and compounds will be introduced. Secondly, the correlation between these materials' structure and properties related to their applications will also be presented. The selected applications of these materials in area of energy and environmental remediation will be discussed. Finally, research gaps for designing new carbon materials to address discussed limitations for these applications will be identified and used to scope this PhD thesis. These carbon nanoscale materials bring their advantages of low costs, easy-to-synthesis, environmental-friendly and high performance that will be solution for alternation of traditional expensive catalysts for developing sustainable energy and eco-environment.

1.1 Graphitic carbon materials

The degree of the development of the graphitic carbon material technology can be used to classify the different kinds of available carbon materials in three categories; conventional carbon materials, nanotextured carbon and nanosized carbons.²⁸ The conventional carbon

materials include naturally occurring graphite and diamond, the family of carbon blacks and activated carbon. The nanotextured carbon materials comprise of carbon materials such as carbon fibers, pyrolytic carbon and glass-like carbon, while nanosized carbons includes carbon nanotubes, fullerenes, mesoporous carbon materials and graphene (Figure 1).²⁸ In this thesis, the categories of conventional carbons and nanosized carbons are discussed and graphitic carbon composite materials produced with nanosized carbon materials including CNT and graphene are utilised to develop catalysts for energy conversion and adsorbents for heavy metal (arsenic) adsorption.

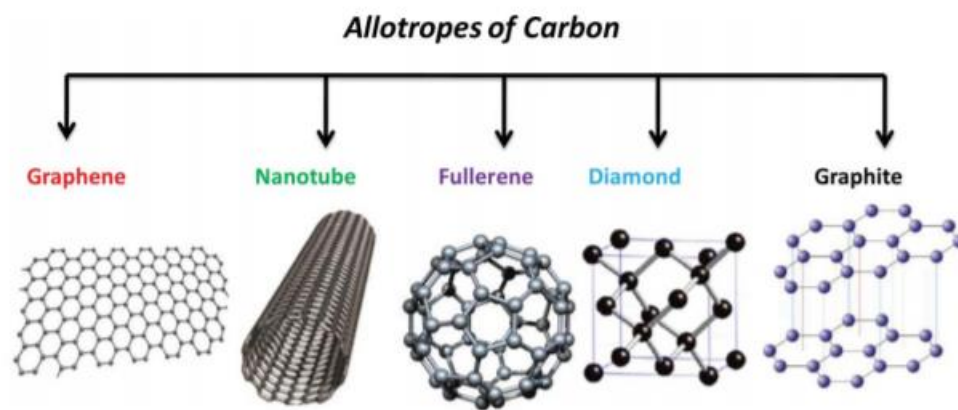


Figure 1. Allotropes of carbon and their crystal structures.²⁹

1.1.1 Conventional graphitic carbon materials

1.1.1.1 Graphite

Naturally occurring mineral graphite is formed from metamorphism in rocks, by the reduction of carbon compounds. Different forms of graphite such as crystalline flake graphite, amorphous graphite or lump graphite are found depending on the ore deposit.²⁸ Graphite is soft, low density, crystalline allotrope of carbon. The crystalline structure of graphite consists of hexagonal rings forming thin parallel plates which are bonded *via* weak Van der Waals forces.³⁰ The layered arrangements of these parallel sheets provide self-lubricating properties to graphite.³¹ Graphite which possess high thermal, mechanical and electrical conductivity,³² high

temperature stability³³ and high refractory³⁴ and chemical inertness³⁵ is extensively utilised for many industries including lubricants, refractory materials, nuclear industry and electrical and mechanical applications.^{31, 34, 36, 37}

1.1.1.2 Diamond

Diamond another naturally occurring allotrope can exist in two forms of polymorphs: cubic closed packed structure and lonsdaleite. The high hardness of diamond is attributed to the four strong covalent bonds formed by each atom utilising sp^3 orbitals in cubic closed packed structure.³⁸ Diamond is an insulator with a band gap of < 5 eV and often not used in electro-chemical applications. However, when the doped with heteroatoms such as Boron, it showed improved electro-chemical stability, higher conductivity and corrosion resistance in both acidic and alkaline media.³⁹⁻⁴¹

1.1.1.3 Activated carbon (AC)

AC belongs to a class of products which is never used by customers as the ultimate product, but rather utilised to manufacture many products across broad sectors including chemical, mineral processing, food, car and household products industries. AC is produced by the carbonization of carbon-based products such as coconut shell, nutshell, animal bones, wood or paper mill waste liquor at high temperature in the exclusion of air. During carbonisation process the organic matters in the carbon materials are broken in to volatile products and evaporated to create a highly porous structure containing pores previously occupied by the volatised matter which accounts to approximately half of the volume of carbon.⁴²

The main purpose of the production of AC carbon is to create maximum adsorption surface and condition these surfaces to have maximum adsorption for unit area. Many techniques have attempted to enhance the active sites including mild oxidation by introducing small amounts of steam or carbon dioxide. Furthermore, to increase the efficiency of the breakdown of

organic matters, strong dehydrators agents such as zinc chloride and phosphoric or sulfuric acid is also used. Large surface area values such as 800 – 1500 m²/g can be achieved for a typical AC. The maximum distribution of the pore volume versus pore diameter was found to in the range of 0.4 – 2.0 nm.⁴³

Various chemical natures of contaminants including high molecular weight, organic, neutral or non-polar are readily adsorbed onto AC. AC primarily remove contaminates from liquid or vapour by means of physical adsorption.⁴⁴ The walls of the AC consist pores (Figure 2) which possess large surface area exerts as attractive forces to seek to adhere other vulnerable surface molecules (contaminants). The contaminants are attracted to ACs because the carbon surface is greater than the forces that keep them dissolved in solution.

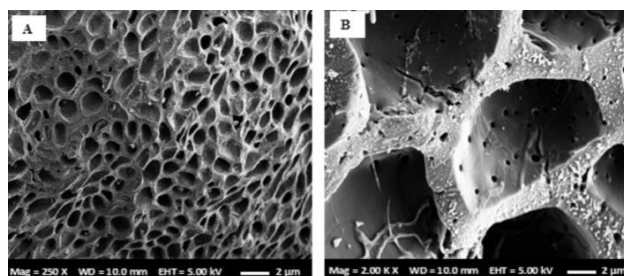


Figure 2. SEM image of activated carbon (A) 250 x, (B) 2000 x.⁴⁵

1.1.1.4 Carbon black

Carbon black possesses a para – crystalline structure of aggregated spherical particles of less than 50 nm (Figure 3). The structure and the particle size diameter determines the specific surface area of the material.⁴⁶ The spherical carbon black particles consist of parallel graphitic layers with interplanar spacing of between 0.35 and 0.38 nm. The sp² hybridised orbitals in the graphitic layer form a triangular in plane formation while the Pz orbitals form weaker delocalised π bonding with the neighbouring carbon facilitating an electron flow.⁵ The specific surface area and structure of carbon black has great influence on the conductivity of the material.⁴⁶ Synthesis of carbon black can be carried out using different processes including

furnace black, thermal black, acetylene black and lampblack.²⁷ The BET surface area differs according to the process and varies from 65 – 80 m²g⁻¹ for acetylene black⁴⁷ to greater than 1000 m²g⁻¹ for thermal blacks.²⁷ Carbon black has been heavily researched for its electrochemical storage, energy conversion and environmental applications and used as an additive for polymers, paints, inks, rubber and construction materials.

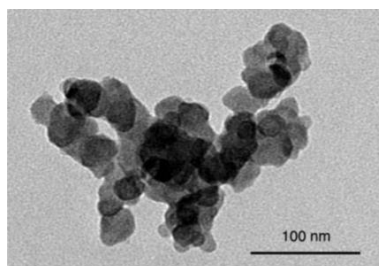


Figure 3. Transition electron micrographs (TEM) image of a N 234 carbon black.⁴⁸

1.1.2. Nanosized graphitic carbon materials

1.1.2.1 Fullerenes

Buckminsterfullerene (C₆₀) was invented in 1985 by Kroto, Curl and Smally and nick named ‘buckyball’ because it resembled the soccer ball.⁷ This unique compound was recognised by the scientific community and the Noble prize for Chemistry was awarded for it in 1996. It consists 60 carbon atoms and 32 faces where 20 of them are hexagons and 12 pentagons.⁴⁹ A carbon atom is placed at a corner where 2 six - member ring and one five-member ring come together.³⁸ In fullerenes all rings are fused, and all the double bonds are conjugated.⁵⁰ Interestingly, in spite of extreme conjugation, fullerene behave as electron deficient alkenes rather than electron rich aromatic system.⁵¹ Buckminsterfullerene are held together and stabilised by weak forces which enables easy solubility of these materials in organic solvents such as benzene.³⁸ The invention of fullerene and revivifying it to graphite science has been a challenge since its invention. However, recent studies have revealed that by the concept of fullerene isomerisation *via* catalysis by trace hydrogen and carbon atoms, fullerenes could be transformed to graphite through CNT and graphene.⁵² C₆₀ and its derivatives have shown strong

antiviral and have demonstrated high potential for treatment of Human Immunodeficiency Virus (HIV)⁵³ and used as photosensitisers.⁵⁴ However, C₆₀ have some major drawbacks such as complicated synthesis procedures, insolubility in aqueous media and aggregation of particles.

1.1.2.2 Mesoporous carbon (MPC)

Mesoporous materials are materials with a pore size between 2 and 50 nm. They can be synthesised through a number of procedures, including carbonisation of aerogels or cryogels,⁵⁵ high degree of activation of carbon materials with physical/chemical methods,^{43, 56} carbonisation of hydrides of carbon materials composed of a thermoset and a thermally unstable compound,⁵⁷ activation of carbon materials with a organometallic compounds or metal oxide precursors,^{58, 59} hard⁶⁰ and soft⁶¹ templating methods. Among them, the templating method (hard and soft) provides well controlled mesoporous, while others only result in a wide range of mesoporous and limited micro pores structures.⁶² MPC are widely used in devices such as ultracapacitors, pseudocapacitors, lithium ion batteries, electro catalytic support and electrochemical hydrogen storage.⁶³

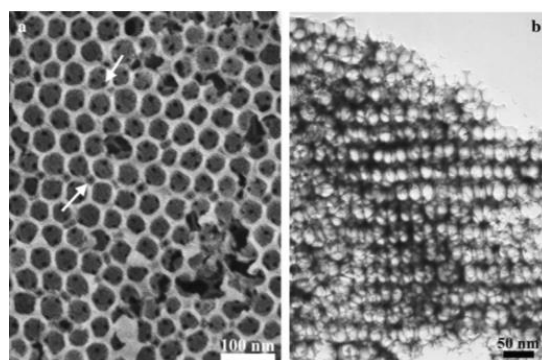


Figure 4. (a) FE-SEM and (b) TEM images of of the ordered mesoporous carbon.⁶⁴

1.1.2.3 Carbon nanotubes (CNTs)

CNTs are carbon in cylinders shape made of graphitic layers which is produced by catalytic decomposition of hydrocarbon vapour.^{65, 66} CNTs can be either single wall (SWCNT) or

multiwall (MWCNT) with a diameter around less than 10 nm for SWCNTs or higher than 10 nm for MWCNTs. The length of CNTs can be many times longer than that of their diameter of up to a few micrometres.²⁷ During synthesis process, single graphene sheets are rolled up to form seamless cylinders and assemble as SWCNT, while multiple graphene layers rolled up to form MWCNTs with an inter-layer distance of 3.6 Å (Figure 5). The statistical probability and restriction of relative dimensions of these individual tubes makes MWCNT a zero-gap semiconductor which allows thermal excitation of electrons to its conduction bands.²⁷ MWCNT is more metallic and conductive than SWCNT, while SWCNT provides greater surface area than MWCNT (5 - 500 m²g⁻¹ for MWCNT and 400 - 900 m²g⁻¹ for SWCNT). Both MWCNT and SWCNT have been investigated separately and used in electrochemical and field emission devices, electronic devices, hydrogen storage, sensors and probes, coating, energy storage and biotechnology.^{67,68} CNTs are also widely used in water purification applications.^{69,70}

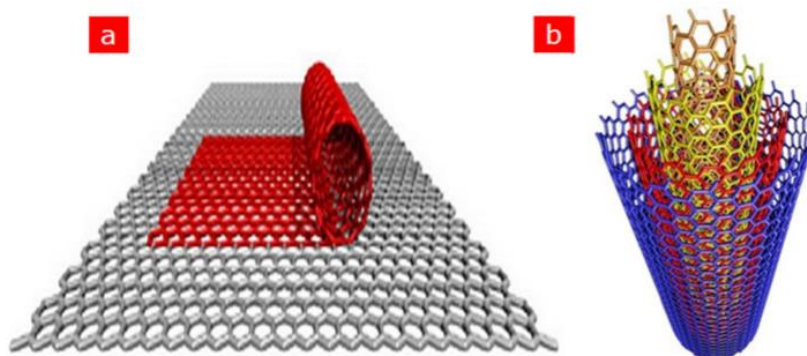


Figure 5. (a) Schematics of SWCNTs which composed of a single layer of curly graphite. (b) Schematics of MWCNTs.⁷¹

1.1.2.4 Graphene

Since the discovery of graphene by Geim and Novoselov in 2004 graphene, a structure of atomically thin carbon atoms arranged in a hexagonal array and defined as a 2D material,⁷² has been a focus on intense research due to its exceptional properties. Graphene possesses a

large specific theoretical surface area ($2630 \text{ m}^2\text{g}^{-1}$),⁷³ high Young's modulus (approx 1.0 TPa),⁷⁴ high intrinsic mobility ($200,000 \text{ cm}^2\text{v}^{-1}\text{s}^{-1}$)⁷⁵ and thermal conductivity (approx. $5000 \text{ Wm}^{-1}\text{K}^{-1}$).⁷⁶ Moreover, flexible graphene membranes can be easily modified and tuned depending on the target application.⁷² Single layer (single hexagonal sheet) to few-layer graphene consisted 3-10 layers can be produced by using exfoliation and cleavage, thermal chemical vapour deposition or plasma chemical vapour deposition methods.⁷⁷ One - atom graphene sheets which are superior to CNT, have all constituent carbon atoms on the surface and 2D planar geometry to facilitate electron transfer and increase electro catalytic activity.⁷⁸

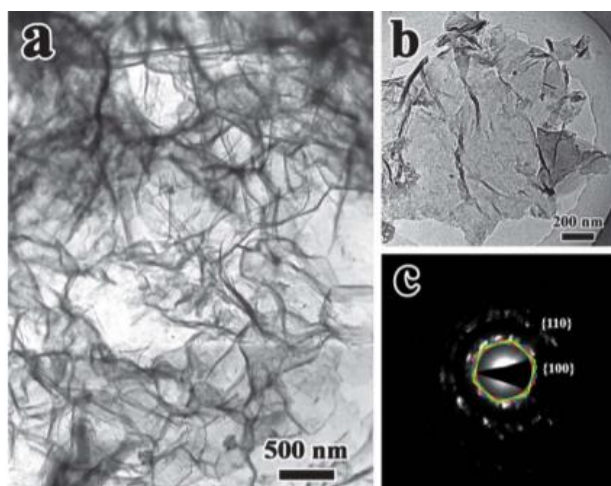


Figure 6. (a) A low – magnification TEM image of many graphene sheets. (b) A high – magnification TEM image of the few - layer graphene sheets. (c) The corresponding SAED pattern in (b).⁷⁹

1.1.2.5 Carbon nanodots

Carbon nanodots are first obtained during purification of single-walled carbon nanotubes through preparative electrophoresis in 2004.^{80, 81} It increasingly became popular due to their easy to handle, abundant and inexpensive nature.⁸⁰ Unlike the conventional carbon blacks which possess weak fluorescence, C-dots due to their low particle sizes (below 10 nm) shows strong fluorescence and commonly referred as fluorescent carbon.⁸⁰ Nuclear magnetic resonance (NMR) investigations on C-dots revealed that C-dots obtained from candle soots are sp^2

hybridised without the presence of any sp^3 carbon atoms indicating presence of conjugated systems.⁸² Due to its unique properties such as high aqueous solubility, easy functionalisation, excellent bio compatibility, high resistance to photo bleaching and low toxicity, C-dots have found important and wide applications in energy⁸³ and catalysis,⁸⁴ biological labelling,⁸⁴ drug delivery⁸⁵, bio imaging,⁸⁶ and sensing.⁸⁷

1.2 Graphitic carbon materials for energy and environmental applications

1.2.1 Graphitic carbon materials as electro catalysts for oxygen reduction catalysts in a Polymer Electrolyte Membrane Fuel Cells (PEMFC).

Fuel cells generate electricity by electrochemically combining a gaseous fuel (hydrogen) and an oxidant gas (oxygen from the air) using electrodes in an ion conducting electrolyte.⁸⁸ A schematic representation of a PEMFC is shown in Figure 7. In a PEMFC, oxygen is reduced at the cathode using oxygen reducing electro catalysts. Carbon materials including carbon black, CNT, mesoporous carbon and graphene are widely employed as ORR catalysts.⁸⁹⁻⁹¹ Among the catalysts, nitrogen doped carbon material such as carbon nanotubes (CNT),⁹² graphene,⁹³ nano tube cups⁹⁴ and mesoporous graphitic arrays⁹⁵ have drawn attention due to their good durability and low cost. Apart from N-doped carbon materials, graphitic carbon materials doped with heteroatoms such as sulphur (S),⁹⁶ boron (B)⁹⁷ and phosphorous (P)⁹⁸ has shown outstanding catalytic activity for ORR.

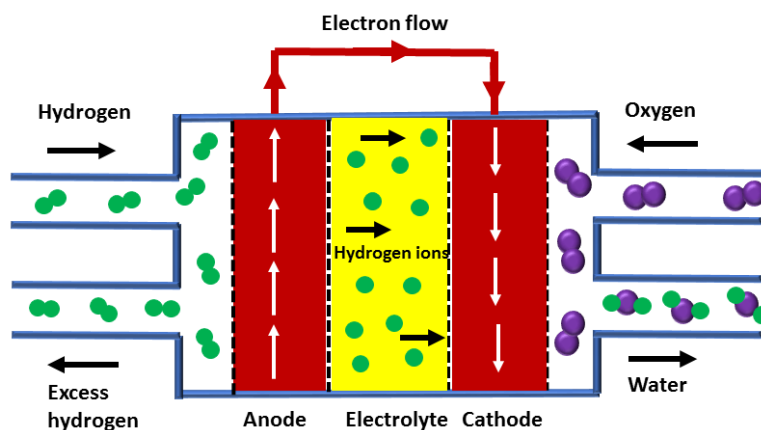


Figure 7: A schematic representation of a PEMFC.⁹⁹

The ORR activity of N-doped carbons starts from the conjugation formed between the nitrogen lone pairs and the π orbitals of graphene. The major breakthrough in metal free N-doped carbon catalysts came in 2009 when Gong *et al.*⁹² developed a vertically aligned N-doped carbon nano tubes (VA-NCNT) using pyrolysis of iron (II) phthalocyanine (a metal heterocyclic molecule containing nitrogen) in the presence of NH_3 vapour. Interestingly, after complete removal of the residual Fe catalyst by electrochemical purification, these metal - free catalysts showed remarkable ORR activity *via* a four – electron transfer and lower over potential and higher stability than Pt/C catalysts.⁹² Gong *et al.*⁹² used quantum mechanics calculations with a B3LPY hybrid density functional theory (Gaussian 03) and reported that to counter balance the strong electronic affinity of nitrogen atom, the carbon atom adjacent to nitrogen shows a substantially high positive charge density. This N - induced charge delocalisation facilitates O-O adsorption on to the positively charged carbon atom adjacent to the N atom, which eventually weaken the O-O bond to facilitate ORR.⁹²

Nitrogen doped carbon materials including N-doped carbon black (N-CB), N-doped graphene (N-GR), N-doped CNT (N-CNT) and N-doped porous carbon, is one of the mostly investigated hetero doped carbons for ORR application.¹⁰⁰ During the heat treatment, nitrogen atoms replace carbon atoms in the basal plane of the graphitic carbon structure in different configurations including pyridinic, pyrrolic or graphitic/quaternary nitrogen⁹³ which contribute differently to the ORR activity (Figure 8). Even though many investigations suggest that these species can contribute to the ORR activity differently, their specific role for ORR activity still remains unclear. However, the many reviews conducted on the activity suggest that the pyridinic nitrogen improve the onset potential, graphitic /quaternary nitrogen influence the limiting current density and the total amount of nitrogen present do not play a vital role in ORR activity.

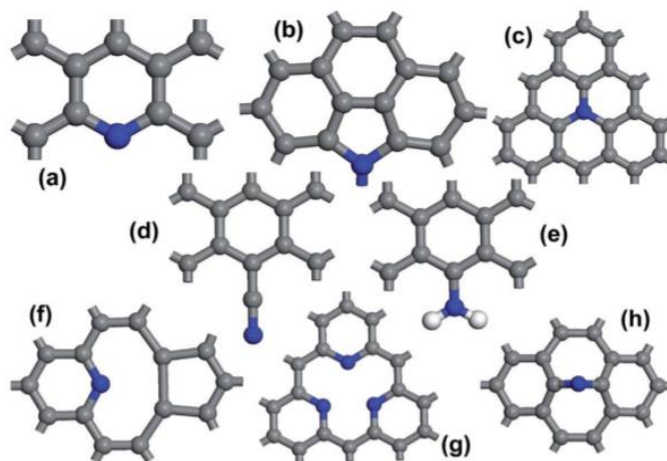


Figure 8. Possible bonding configurations for N in graphitic networks: (a) pyridine – like N, (b) pyrrole-type N (other pyrrolic configurations are possible provided the nitrogen remains sp^3 coordinated), (c) graphite substitutional nitrogen, (d) nitrile $-C\equiv N$, (e) $-NH_2$, (f) pyridinic N – vacancy complex, (g) pyridinic N_3 - vacancy and (h) interstitial nitrogen. Adopted from Ewels *et al.*¹⁰²

Jayabharathi *et al.*⁹⁰ synthesised a N-doped carbon black by coating the carbon black (Vulcan XC 72R) with polyaniline followed by its subsequent annealing at high temperature. Comparing N-doped carbon black with non-doped carbon black showed significant increase in ORR activity on N-doped carbon black and demonstrated the same current density as the Pt/C catalyst. The enhanced activity was ascribed to the pyridinic and pyrrolic nitrogen species introduced on to the graphitic carbon framework. However, carbon black does not provide the necessary catalyst dispersion and prolonged particle attachment for an effective electrochemical activity.¹⁰³⁻¹⁰⁵ Therefore, research to develop a more efficient catalyst support became inevitable. In this context, CNT was used as a catalytic support because the catalyst nanoparticles can be easily dispersed in CNT. Both SWCNT and MWCNT were investigated as ORR catalysts. The comparison ORR activity on Pt catalysts dispersed on SWCNT and MWCNT showed, Pt dispersed in SWCNT outperformed Pt dispersed in MWCNT by providing higher electrochemical active area and catalytic activity.¹⁰⁶ Thus, when compared

with carbon black, the Pt nanoparticles supported on SWCNT showed 75% more power density than carbon black supported Pt nanoparticles.¹⁰⁶ Unlike the deep pores in carbon black which prevents access of catalyst nanoparticles, the CNT surface allows easy access for the deposition of catalyst nanoparticles. However, catalyst nanoparticles with larger diameter suffers easy access of the pores on the catalyst supports.

MPC with precise pore distributions could open the door to processing large molecules that are unable to enter into tiny porous framework (e.g. zeolite). These materials process high surface areas and uniform pore diameters exhibit highly versatile structural and excellent physicochemical properties which promote their application for electrochemical catalysts. Doping MPC materials can significantly alter its electrical, thermal and chemical stability.¹⁰⁷⁻¹⁰⁹ N-doped MPC is commonly synthesised by impregnating nitrogen containing precursors in to the micro channels of the hard templates, followed by polymerising, carbonising and finally removing the hard template.¹⁰⁷⁻¹⁰⁹ The incorporation of the hetero atoms to MPC increases the electron conductivity and narrows the band gap of the MPC.¹¹⁰ Investigation of nitrogen N-MPC on electro chemical activities have indicated that the higher surface area and conductivity of the materials contributed to the enhanced intrinsic activity of these materials.⁹¹

Several groups have conducted studies on metal free N-graphene and reported enhanced catalytic activity towards ORR¹¹¹⁻¹¹⁴ compared to pristine graphene. Qu et al.¹¹² synthesised the first N-graphene using chemical vapour deposition method using methane and ammonia. The reported material displayed ORR activity and was driven by one-step four - electron pathway with an electron transfer number of 3.6 – 4.0 in the potential range 0.4 – 0.8 V. Liao *et al.*¹¹⁵ synthesised N-doped graphene sheets (NG-C) using a two -step calcination strategy using α – hydroxy acid (AHAs) (citric acid) and melamine as carbon and nitrogen precursors, respectively exhibited excellent operational stability than the commercial Pt/C and assisted the ORR *via* a four – electron kinetics. Recently, macroscopic assembled graphene from nanoscale

building blocks has become an interesting research topic. In this context, three dimensionally (3D) self - assembled graphene sheets to disperse nanoparticle has been extensively investigated.¹¹⁶⁻¹¹⁹ Wu *et al.*²² synthesised 3D assembled N- doped graphene sheets (aerogels) with iron nanoparticles *via* chemical or hydrothermal reduction.^{117, 120-122} The synthesised product showed excellent ORR activity in alkaline media *via* four - electron transfer mechanism with high current density and lower H₂O₂ yield.

In recent years the scientific community has shown considerable interest in carbon composite and hybrid materials with different unique morphologies and used them as electro catalysts for ORR.¹⁰⁰ Composite materials made from two different carbon materials have been reported in the literature. For example, Li *et al.*¹²³ used two different carbon materials (rGO and carbon black) and synthesised a Pt nanoparticles supported rGO/carbon black composites to enhance the electro catalytic activity of the Pt catalysts. Here, the carbon black particles were used to intercalate between the rGO sheets to prevent rGO sheets from stacking due to its $\pi - \pi$ interaction. This unique structure facilitated the diffusion of oxygen molecules to the active site to increase ORR activity. Composite materials synthesised using carbon materials and metal nanoparticles with unique morphology e.g. pea-pod like structure, core-shell structure and yolk shell structures have been investigated and reported.²⁴⁻²⁶ A detailed description of the electro chemical properties of the N-doped carbon and hybrid catalysts consisting carbon and Fe is displayed in Table 1.

Table 1. Description of the electrochemical properties of N-doped carbon and hybrid catalysts for ORR. Adopted from Ge *et al.*¹⁰⁰

Catalysts	Electrolyte	Onset potential V (RHE)	Halfwave potential V (RHE)	Number of electrons transferred (n)	Hydrogen peroxide (%)	Current density (mA/cm ²)	BET surface area (m ² /g)	Factors contributed towards increased ORR activity	Reference
N-doped porous carbon	0.10 M KOH	0.86	0.70	3.68 at 0.30 V (RHE)	-	4.59 at 0.00 V (RHE)	783.0	Pyridinic nitrogen species, porous structure and high electrical conductivity.	124
N-doped carbon sheets	0.10 M KOH	0.91	0.73	3.74 at 0.50 V (RHE)	-	-	999.5	Proper combination of graphitic and pyridinic N species with more exposed edge sites.	125
N-doped carbon nanofiber	0.10 M KOH	0.95	0.80	3.96 at 0.80 V (RHE)	Less than 10	5.20 at 0.40 V (RHE)	916.0	Rapid transport of ORR species facilitated by the 3D nanofibrous network.	126
N-doped carbon nanosheets	0.10 M KOH	0.96	0.85	3.67 – 3.94 at 0.05 – 0.75 V (RHE)	4.30 – 16.50 from 0.05 – 0.75 V (RHE)	5.45 at 0.00 V at (RHE)	589.0	Unique planner porous shells comprise of pore size of 22 nm which facilitated electrolyte/ reactant diffusion.	127
N-doped graphene	0.10 M KOH	0.95	0.82	3.80 at 0.65 V (RHE)	-	-	565.1	Low N doping concentrations (3.02 %), high degree of graphitization, enhanced conductivity, high surface area and pore volume.	128
N-doped graphene-CNT	0.10 M KOH	0.91	0.71	≈ 4 at 0.00 - 0.55 V (RHE)	-	-	-	High content of pyridinic N (56 At %) and increased content of quaternary N (15 At%). Quaternary N increased the limiting current.	129
N-doped graphene	0.10 M KOH	-	-	3.60 – 4.00 from 0.40 – 0.80 V (RHE)	-	-	-	Pyridic and pyrrolic N species facilitated oxygen adsorption to the adjacent carbon.	112
N-doped graphene	0.10 M KOH	0.96	-	3.50 (average) from 0.65 – 0.25 V (RHE)	-	-	1167.0	High pyridinic N content	115
3D Fe ₃ O ₄ /NG	0.10 M KOH	-	-	3.72 – 3.95 from 0.75 to -0.20 V (RHE)	11.0 at 0.55 V (RHE)	≈ 8.00 at 0.00 V (RHE)	-	3D macro porous structures facilitated mass transfer	22
Vertically aligned N-doped CNT	0.10 M KOH	-	-	3.90 at 0.65 (RHE)	-	-	-	Pyridic and pyrrolic N species facilitated oxygen adsorption to the adjacent carbon.	92

CHAPTER 1: Introduction

Fe/Fe ₃ C/N/C	0.10 M KOH	0.98	0.87	3.70 – 3.85 from 0.20 – 0.70 V (RHE)	15 at 0.50 V (RHE)	6.03 at 0.50 V RHE	-	Proper combination of pyridic and pyrrolic N species and porous architecture of the composite material which facilitated mass transport	130
Fe/N _x /C	0.10 M KOH	1.05	0.87	≈ 3.90 from 0.20 – 0.80 V (RHE)	≈ 4.5 from 0.2 – 0.80 V (RHE)	≈ 6.30 at 0.10 V (RHE)	1100.0	Fe-N-C active sites. Activity increased according to Fe-N _{4/2} -C > Fe ₄ -N-C > N-C > Fe ₄ -C ≈ C	131
Fe/N/C	0.10 M KOH	1.03	0.82	≈ 3.97 from 0.55 – 0.73 V (RHE)	-	8.31 at 0.30 V (RHE)	326.0	Nature of the porous molecular organic frame work (MOF) nano structure, increased conductivity and Fe and N (pyridic and quaternary) based compounds.	132
Fe/N/C	0.10 M KOH	0.92	0.81	≈ 3.96 from 0.10 – 1.10 V (RHE)	Less than 4.0 from 0.10 – 1.10 V (RHE)	6.06 at 0.20 V (RHE)	56.0	N binding iron species (Fe-N _x) and abundant Fe ²⁺ species.	133
Fe/Fe _{2.5} C/N/C	0.10 M NaOH	0.90	0.72	≈ 3.85 from 0.12 – 0.81 V (RHE)	Less than 6.0 from 0.12 – 0.81 V (RHE)	≈ 4.75 at 0.1 V (RHE)	-	Both pyridinic and graphitic N species and Fe _{2.5} C confined in carbon layers.	25
Fe ₃ C/N/CNT	0.10 M KOH	0.96	0.83	3.99 from 0.30 – 0.90 V (RHE)	Less than 7.7 from 0.30 – 0.90 V (RHE)	≈ 6.00 at 0.00 V (RHE)	151.2	High pyridic N content (33 At %)	134
Fe _x C/NGR	0.10 M KOH	0.92	0.78	3.79 - 3.99 from 0.30 – 0.00 V (RHE)	-	≈ 3.80 at 0.00 V (RHE)	-	Fe-N complexes with high content of pyridinic N, synergetic active site created by both Fe and N species and graphitised carbon nanoshells due to high degree of edge plane exposure.	135
3D Fe _x N/NGA	0.10 M KOH	0.96	-	4.00 at 0.55 V (RHE)	-	6.00 at -0.2 V (RHE)	-	Fe-N-C active sites, dominant FeN phase in the hybrid and small Fe _x V nanoparticles (5 – 20 nm)	136

Based on the literature survey on carbon nanoscale materials, their advantages and catalytic performances, we deduced graphitic carbon composite materials could be further explored to produce a low cost, easily synthesised, environmentally-friendly catalyst for the development of sustainable and eco-friendly fuel cell technology as an alternative to depleting fossil fuels.

In particular, most carbon-based catalysts discussed were synthesised using complicated synthesis procedures using hazardous chemicals making them practically non-feasible industrial catalysts. Here in this thesis, this problem is addressed by the synthesis of catalysts using low cost, scalable and eco-friendly graphitic carbon composites materials using non-hazardous materials for fuel cell technology.

1.2.2 Carbon materials for heavy metal adsorption

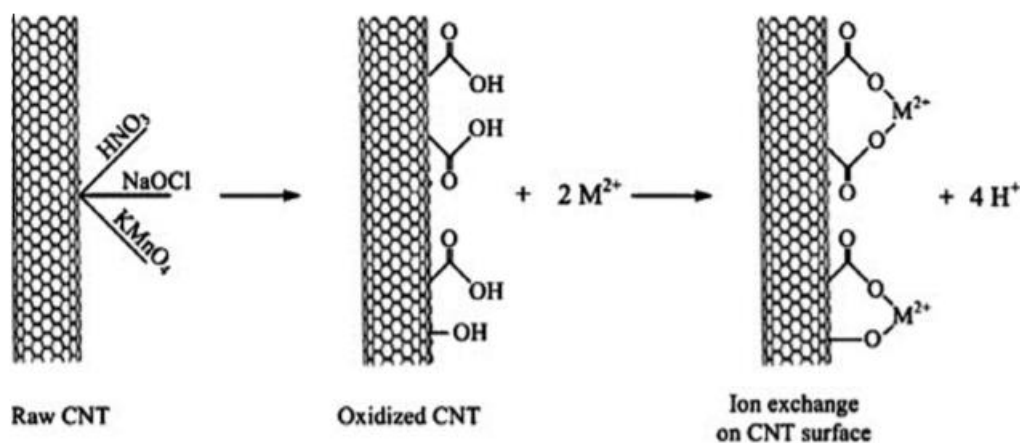
Carbon materials have emerged as an important class of materials due to their exceptional chemical and physical properties.¹³⁷⁻¹³⁹ Their ability to perform under strong acidic, basic environments and at high temperature has made carbon materials ideal for a range of applications.¹³⁷ Furthermore, they are cost effective and environmentally friendly, which make them ideal material to be used as industrial scale adsorbent.^{137, 140, 141}

AC has been used as an adsorbent for removal of organic and inorganic pollutants from liquid and gas phases for many years.¹⁴² AC possesses unique properties including well organised micro porosity, high surface area ($500 - 1500 \text{ m}^2\text{g}^{-1}$) and addition of surface functional groups which make them an ideal material for adsorption of pollutants.¹⁴³ These exceptional properties can be modified to target specific organic, inorganic or metals present in water.¹⁴³ Surface treatments such as oxidation,^{144, 145} ammonification,^{146, 147} sulphuration^{148, 149} and addition of ligands^{150, 151} have been performed on the surface of the AC to increase their surface activity towards adsorption of organic and inorganic contaminants. Activated carbon oxidised by hydrogen peroxide (H_2O_2), nitric acid (HNO_3), ammonium persulphate ($(\text{NH}_4)_2\text{S}_2\text{O}_8$) or ozone (O_3)^{145, 152, 153} can increase the acidic oxygen groups on the activated carbon surface and increase the polarity of the material. At reduced pH, it facilitates the electrostatic attraction between the positively charged metal ions and negatively charged activated carbon surface.¹⁴³ With the discovery of carbon allotropes such as carbon nanotubes and graphene, new generation of carbon materials have emerged as effective adsorbents for water remediation.

Among them, mesoporous carbon, CNT and graphene has been widely employed for heavy metal adsorption.¹⁵⁴⁻¹⁵⁶ Since the unique properties of activated carbon effectively facilitated the adsorption of heavy metals, synthetic approaches such as mesoporous carbon materials were synthesised to obtain similar structure. Considerable efforts have been made to prepare mesoporous adsorbents with large surface area and defined pore structures and the pore shape. However, the MPC synthesised do not possess any surface properties to act as the binding sites for heavy metal adsorption. Therefore, functional groups should be introduced to the MPC to be effective adsorbents. Thiol^{157, 158} and amine functionalised^{155, 159} MPC utilised for heavy metal adsorption has been widely reported. Saha *et al.*¹⁵⁷ synthesised a sulphur functionalised MPC material using soft template method. After functionalisation, the mesoporous carbon behaves as a soft base while mercury, lead and cadmium in solution present as soft acids. According Pearson's hard soft acid base theory (HSAB), soft acids can favour coordination with soft bases to perform adsorption. Li *et al.*¹⁵⁵ prepared nitrogen functionalised mesoporous carbon materials with high nitrogen content using ionic liquid (1-cyanomethyl-3-methylimidazolium bromide) using colloidal silica template. The synthesised material showed high adsorption capacity towards copper ions (Cu^{2+}) *via* electrostatic interaction between pyridinic nitrogen and Cu^{2+} .

Pristine CNT surface lacks enough active site to adsorb heavy metal ions effectively, thus needs surface modifications. Surface modifications of CNT have proven to show enhance adsorption capacity for heavy metals. Abbas *et al.*¹⁵⁶ reviewed nearly 150 published journal articles on adsorption of heavy metal such as Cr (II), Cr (VI), As (III), As (VI), Hg (II), Cu (II), Zn (II), Ni (II), Cd (II), Pb (II) Co (II) using CNT and disclosed that the adsorption capacity of the acid modified carbon is higher than the pristine CNT. Authors further revealed that the adsorption increased due to the electro static interaction between the divalent metal ions and the negatively charged CNT after acid treatment.¹⁵⁶ Acid treatment on CNT can be achieved using oxidising

agents such as KMnO_4 ,¹⁶⁰ H_2O_2 ¹⁶¹ and strong acids including HNO_3 , H_2SO_4 and HCl ¹⁶²⁻¹⁶⁴ which introduces different oxygen containing functional groups on CNT surface and change the surface chemistry of the CNT to facilitate metal ion adsorption (Scheme 1).



Scheme 1. Schematic diagram of the major mechanism for sorption of divalent metal ions onto CNT surface.¹⁶⁵

Even though the CNT has shown promising adsorption efficiencies, the use of CNT for heavy metal adsorption is associated with some drawbacks:

1. Relatively expensive than the traditional adsorbents.¹⁶⁶
2. Regeneration and reuse of these materials remain as a challenge because of its small size.¹⁵⁶
3. Release of these particles as suspended particulate (PM) mater in the work environment caused inhalation hazards.¹⁵⁶
4. Release of chemically modification CNT to the environment can be an issue.¹⁵⁶

Applications of graphene as an adsorbent has been widely reported in the past two decades.^{19, 154, 167-169} Graphene synthesised *via* reduction of graphene oxide is often associated with a residual carboxyl functional groups at the edge of its surface.¹⁵⁴ These surface charges of these functional groups could change according to the pH of the medium. Graphene has an iso electric point (IEP) around 3.8 and at $\text{pH} < 3.8$ graphene has a positive surface charge because

of protonation reaction.¹⁵⁴ At this pH, it can act as an anion exchanger. At $\text{pH} > 3.8$ it possesses a negative charge and can adsorb cations.¹⁵⁴ Huang *et al*¹⁹ investigated the adsorption capacity of thermally modified graphene sheets for Pb^{2+} adsorption and revealed two possible mechanisms; electrostatic interaction or Lewis acid - base interaction. The electrostatic interaction is proceeded *via* positively charged Pb^{2+} and π - electrons in the graphene.¹⁹ Conversely, graphene which can donate electrons and act as a Lewis base¹⁷⁰ and form a Lewis acid - base interaction forming a coordination bond with the electron deficient Pb^{2+} .¹⁹ However, use of graphene as an adsorbent is associated with some drawback such as its small size, collection, reusability and aggregation.¹⁷¹ Furthermore, graphene synthesised by reduction of graphene oxides requires strong acid, oxidising agents and reducing agents and disposal of such materials can be a hazard.¹⁷¹

To prevent aggregation and easy collection of graphene after remediation, metal nanoparticles have been mixed with graphene.^{171, 172} Magnetic nanoparticle embedded graphene can be easily removed by an external magnet after remediation.¹⁷³ Furthermore, these nanoparticle act as mutual spacers between the graphene sheets and prevent them from aggregation.¹⁷⁴ Nanoparticles of metal and metal oxides with high surface area and specific adsorption capability are another group of materials which are extensively used as an adsorbent for heavy metal removal from water. Iron oxide,¹⁷⁵ silver nanoparticle,¹⁷⁶ manganese oxide,¹⁷⁶ aluminium oxide,¹⁷⁷ titanium dioxides,¹⁷⁸ cerium oxide¹⁷⁷ and magnesium oxide¹⁷⁷ have been tested as possible adsorbents for heavy metal removal. These metal nanoparticles provides minimum environmental damage and also does not cause any secondary pollutions.¹⁷⁹ Out of the many nanoparticles tested magnetic nanoparticles were more preferred because they can be easily separated by an external magnet. However, magnetic nanoparticles have the tendency to agglomerated due to their magnetic nature and therefore, should be properly dispersed in a support material to reduce the agglomeration. Magnetic nanoparticles such as iron oxides can

be dispersed in a 2D¹⁸⁰ or 3D reduced graphene oxide architecture¹³ depending on the synthesis conditions. These metal ions apart from preventing reduced graphene oxide sheets being agglomerated, can contribute to the adsorption of heavy metals *via* electrostatic interaction.¹¹³ Andjelkovic *et al.*¹³ synthesised 3D graphene aerogels decorated with goethite nanoparticles and investigated its adsorption capacity towards arsenic species and reported that the arsenic species are adsorbed by ligand interchange between arsenic species and oxyhydroxide nanoparticles.

Agglomeration of ZVI particles due to its magnetic properties and is a major concern because it reduces the effective active sites for the adsorption of arsenic species. To prevent the ZVI particles from aggregating, inert materials has been used as carrier materials for ZVI particles, including readily available materials such as bentonite,¹⁸¹ zeolite¹⁸² and natural clays.¹⁸³ Bio char materials derived from rice hull¹⁸⁴ and pine¹⁸⁵ have also been used as a supporting material for ZVI to reduce agglomeration. Graphene can be as a supporting material for metal nanoparticles for the removal of heavy metals^{13, 186-188} and also can be used by itself to adsorb heavy metals.¹⁹ The adsorption properties of graphene is dependent on the edge oxygen functional groups present in graphene.¹⁸ Oxygen atoms present on these functional groups have much higher affinity towards the metal ions. The oxygen containing functional groups on the graphene have the ability to form interactions such as electrostatic and coordination with the metal ions.¹⁸ Further, the π electrons on the graphene sheets act as a Lewis base and act as an electron donor. The metal ions act as a Lewis acid and accept electron to form a complex through Lewis base interaction.^{18, 19} Alternatively, graphene surface can be used to disperse the metal nanoparticle to avoid agglomeration of nanoparticles.

ZVI stabilised with organic compounds dispersed in different support materials been extensively used for removal of As species as shown in Table 2. However, the efficiency of the As species removal is not very effective because the ZVI particles are not properly air stabilised

or been agglomerated. Therefore, Chapter 6(a) was focussed on enhancing the As species adsorption and discover organic materials that could contribute to enhanced air stability to ZVI and effective supports to prevent them from being agglomerated.

Table 2. Different organic materials and support materials used for the to provide air stability and prevent agglomeration of ZVI and their adsorption capacities towards AS adsorption.

Adsorbent	Coating agent	Support	Agglomeration	Stability (months)	pH	Concentration Range (mg/L)	Adsorbent dosage (g/L)	Adsorption capacity (mg/g)		Reference
								As (III)	As (V)	
ZVI	-	-	Yes	-	7	1	0.1	2	-	189
Chitosan stabilised ZVI	chitosan	-	Yes	-	7	1-20	5.0	94	119	190
Biochar-nZVI	-	Biochar	No	-	4.1	0-400	2.0	-	125	191
nZVI /AC	-	Activated carbon	No	-	6.5	2	1.0	18	12	192
nZVI/ Montmori llonite	-	Montmori llonite	No	-	7	5	1.0	55	46	193
MWCNT-ZVI	EDTA	MWCNT	No	-	7	0.1-1200	2.5	111	166	194
ZVI - rGO	-	rGO	No	-	7	1-10	0.4	35	29	195
Starch stabilised ZVI	starch	-	Yes	-	7	1-10	0.3	12	14	196

2.0 Carbon materials for addressing significant problems in energy and environmental crises

2.1 Depletion of fossil fuels and an alternative suggestion using graphitic carbon composites

The world is progressing towards an energy crisis with the increasing of world population.¹⁹⁷ According to United Nations World Population Prospects (2015 Revision), the world population is growing by 1.18 % and is expected to increase up to 9.7 billion by 2050. The increasing population along with economic development has created a huge increase in energy demand for global production and energy consumption. The International Energy Outlook 2016 (IEO 2016) has projected the energy consumption will rise by 48% form year 2012 - 2040. The energy demand is expected to increase from 549 quadrillion British thermal units (Btu) in 2012 to 815 quadrillion Btu in 2040 (IEO 2016) as can be overviewed from the world energy consumption in the period of 1990 to 2040 in Figure 9.



Figure 9. World energy consumption from 1990 – 2040 obtained from IEO 2016.¹⁹⁸

Energy is supplied by fossil fuels that included petroleum liquids, coal and natural gas and renewable energy sources such as solar, wind, hydropower, biomass, geothermal and fuel cells¹⁹⁹⁻²⁰¹. However, according to Nehring *et al.*,²⁰¹ fossil fuels have supplied approximately

85 – 93% of the world total energy demand for the last five decades. The U.S. Energy Information Administration (EIA) has predicted that this trend will continue for the next few decades and fossil fuels will be used to supply almost 80% percent of the total energy demand in 2040 (EIA 2013).

The dependence on the fossil fuel for the supply of such a large portion of energy demand is associated with two major drawbacks: finite availability of fossil fuel reserves and the environmental pollutions associated with it. Fossil fuel resources are limited and some forecasts project that there may be as little as 150 years of reserves left.²⁰² Furthermore, the combustion of fossil fuels for energy production produces undesirable Green House Gases (GHG) including carbon dioxide (CO₂), nitrogen dioxide (NO₂) and sulphur dioxide (SO₂).²⁰³ Out of all anthropogenic GHG emission derived from the energy sector in 2008, 62% of CO₂ emission was from fossil fuels (EIA, 2010) (Figure 10). It was revealed that the overall CO₂ levels in the environment has increased 31% in the past 200 years.¹⁹⁹ As a consequence, the global mean surface temperature has risen by 0.4 – 0.8 °C above the base line value of 14 °C in the last century which has risen the sea level of average annual rate of 1 – 2 meters.^{199, 204}

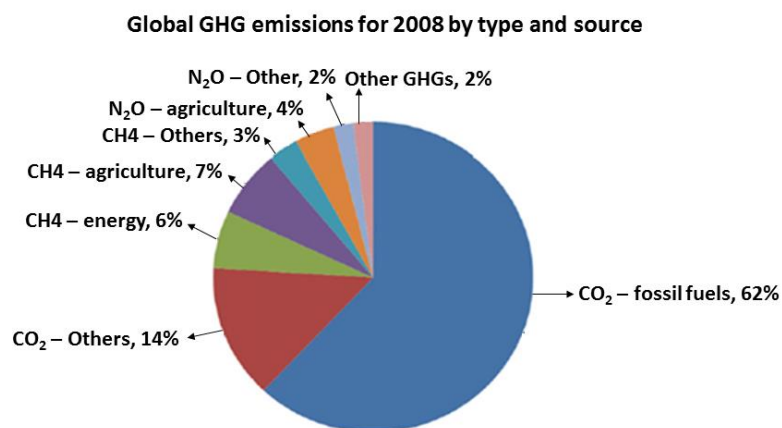


Figure 10. Global anthropogenic GHG emissions by type and process obtained from EIA, 2010.

If these major issues are not addressed, there will be devastating consequences for the world economy, global climate and human well-being. Therefore, rapid and profound measures are needed to minimise these devastating effects from uprising global energy demand and global warming. To reduce conventional fossil fuel usage and CO₂ emissions, alternative energy technologies should be introduced to generate new energies. In this context, two major approaches can be adopted to minimise the conventional fossil fuel usage; the use of Renewable Energy Sources (RES) to generate the alternative energy supply for the world's growing energy demand ^{6, 199, 200} or a synthetic method of producing fuels. In 2001, RES accounts for the supply approximately 14% of the total world energy demand which includes solar, wind, hydropower, biomass, geothermal and fuel cells. The continued rise in global energy demand, the depletion of the world's non-renewable fossil fuel resources and global pollution associated with fossil fuels has initiated a global push towards RES has the potential to produce energy with zero or almost zero emissions of both air pollutants and greenhouse gases.^{199, 200}

Among the RES, fuel cells have captured the interest of the scientific community because its ability to use atmospheric oxygen as fuel and operate with almost zero CO₂ emission. Fuel cells generate electricity by electrochemically combining a gaseous fuel (hydrogen) and an oxidant gas (oxygen from the air) using electrodes in an ion conducting electrolyte.⁸⁸ This electro-chemical process produces water as the by-product. One of the main features of the fuel cell is its ability to convert chemical energy into electrical energy with two or three times higher conversion efficiencies than present electricity generators.⁸⁸ PEMFC which convert the chemical energy stored in hydrogen fuel directly and efficiently to electrical energy by using oxygen in air with no CO₂ emission having demonstrated to dominate the transportation fuel market.⁹⁹ The process offers a pollution-free environment since the generation of electricity which does not produce any environmentally harmful by-products. When hydrogen obtained

from natural gas is used as fuel, a reduction of two million kg of CO₂ emission can be achieved.⁸⁸ Thus, by reducing gases such as CO₂, NO₂ and SO₂, it also eliminates nearly 20,000 kg/year of environmentally disruptive acid rain.⁸⁵ These features of fuel cells stand up to be an efficient and environmentally friendly alternative energy source for the conventional fossil fuel energy.⁸⁸

Although fuel cells are a promising alternative energy source for fossil fuels, the development of this technology suffers from sluggish Kinetics of the ORR at the cathode.²⁰⁵ In a typical PEM system, ORR at cathode contributes to the loss of more than half of the voltage loss because of its slow reaction.²⁰⁶ Thus, to increase reactivity at the cathode, new innovative catalysts which are capable of increasing the reactivity at the cathode are required. Over the decades, high performance of platinum (Pt) based catalysts have dominated the fuel cells industry. However, the limited availability and the high cost of Pt, together with its susceptibility to time-dependant drift and CO deactivation, have restricted their commercialisation.¹⁰¹ Ever since these drawbacks of Pt catalysts were realised, efforts have been made to find a suitable alternative to Pt based catalysts. In this context, carbon materials which are abundantly available, stable under extremely corrosive conditions, provide good electrical conductivity, show high activity and selectivity, have been considered as an alternative to replace the Pt catalysts in the electro chemical reduction of oxygen in fuel cells.^{99, 207, 208} In this thesis, different carbon composite materials (doped and non-doped) with different morphologies have been synthesised and characterised as oxygen reduction catalysts.

2.2 Contamination of drinking water and removal of heavy metal contaminates (arsenic)

All human beings need clean water to survive. Although the earth' atmosphere is almost covered with 70% of water, only a small percentage (0.14%) is available as consumable water which should be purified before consumption.¹³⁷ To increase the available consumable water

for human beings, efforts have been made to convert sea water to drinking water *via* desalination using techniques such as mechanical vapour compression, multiple effect distillation, multi stage distillation, nano filtration, electro dialysis reversal reverse osmosis (RO).²⁰⁹ However, these bear high processing costs and currently only wealthy countries utilise these technologies.²¹⁰ Where water desalination is not practical the scarcity of clean water has become a major concern which can hinder economic developments, degrade environment, devastate human health and form political instability.^{137, 210} With only small amount of water is fresh and consumable, the world will encounter a major crisis in 2030, when one third of its population will not have access to clean water.¹³⁷ The increasing economic and industrial development further contribute to the contamination of water systems by the increase of uncontrolled release of industrial, domestic and agricultural effluents to the environment. Furthermore, when water flows through the rocks, additional pollution of water systems may be introduced by dissolutions of heavy metals.^{211, 212} Heavy metals such as lead (Pb), mercury (Hg), cadmium (Cd) and arsenic (As) can be released to the water. These toxic heavy metals can enter human body when consumed without purification. Long term exposure of heavy metals causes adverse health effects to human systems such as cardiovascular, neurological, urinary and blood systems and effect body parts such as kidney, brain, lungs, heart and skin and trigger cancer formation to these organs.²¹³ Therefore, to address this crisis, reduce further pollution and provide clean drinking water, we need technology which will cheaply and efficiently remove toxic heavy metals from water.

Several purification methods have been tested for water remediation in the past including oxidation and precipitation processes,²¹⁴ coagulation²¹⁵ and electro-coagulation,²¹⁶ co-precipitation,²¹⁷ ion exchange,²¹⁸ adsorption,²¹⁹ filtration,²²⁰ reverse osmosis,²²¹ biological treatment²²² and solvent extraction.²²³ Among these methods, adsorption is widely favoured because it is economical, eco-friendly and rapid.¹³⁷ In the last few decades several materials

have been dedicated to effectively adsorb and pollutants and contaminants from water, such as bark,²²⁴ peanut skins,²²⁵ cotton,²²⁶ chitin,²²⁷ biomass,²²⁸ chitosan,²²⁹ fly ash,²³⁰ bentonite,²³¹ peat,²³² polymers,²³³ alumina,^{234, 235} metal organic frameworks,²³⁶ and iron oxides coated sand²³⁷ and zero valent irons (ZVI).^{238, 239} However, many of these materials have a high capacity but suffer from other setbacks such as stability, cost and lack of scalability. Among these catalysts, ZVI is favoured because its low cost, low toxicity, availability, environmental compatibility and high reactivity.²⁴⁰ However, its application as a potential heavy metal adsorbent is hindered because it undergoes rapid oxidation if not stored in an inert environment after preparation as after preparation the samples will aggregate due to their magnetic property, which can subsequently change their chemistry and impede their usage for the removal of pollutants.^{241, 242} Therefore, for ZVI to be used in the industrial scale, its surface should be protected from atmospheric air oxidation and prevented from agglomeration.

To overcome these challenges and to provide stability to the ZVI, the surface charge of the nanoparticle should be altered. Impartation of electro - static repulsion forces and steric stabilization of the ZVI surfaces can alter the surface chemistry of the ZVI and provide stability to the ZVI.²⁴³⁻²⁴⁵ The materials used to coat the ZVI should provide strong long range repulsive forces preventing the attraction due to magnetic forces between them.^{243, 246} Steric stabilisation can be achieved by coating the nanoparticles with long chain hydrophilic polymers which interact with the nanoparticles prevent agglomeration. The long hydrophilic chains of these polymers extend in to the solution to provide stability.²⁴⁶

In this context, several materials with different functional groups have been employed to stabilise ZVI in the past. Feng and Zhao²⁴⁷ applied a simple and green approach using starch to form a cluster structure with mono and bimetallic Fe⁰ nanoparticles for degradation of organics under inert atmosphere. Wijesekara *et al.*²⁴⁸ further compared the stability of nano-ZVI that had been exposed to starch and different mercapto acids. Using mercaptoacetic acid

(MA), mercaptopropionic acid (MP) and mercaptosuccinic acid (MS) they found that, MA and MS coated nano ZVI were stable for 3 weeks, resulting in rapid oxidation when exposed to air after this period. Other organic compounds, such as carboxymethyl cellulose,²⁴⁹ polyacrylic acid,²⁵⁰ and cellulose acetate²⁵¹ have also been used to coat ZVI particles. However, long term particle stability of ZVI is rarely achieved. Moreover, the functional groups responsible to provide long - term stability has not been properly investigated. Therefore, to address this gap, five different organic chemicals were evaluated with four different functional groups (-SH, -OH, -NH₂ and -COOH) for the air stabilising capabilities on ZVI. The synthesised materials were exposed to air and the stability in atmospheric air is also evaluated. To reduce particle agglomeration, the ZVI provided the long-term stability was entrapped on rGO and investigated for adsorption of As species.

3.0 Aims and objectives

The broad aim of the work described in this thesis was to develop graphitic carbon based composite materials with specific morphologies using low cost materials, less complicated and environmentally friendly processes for applications in energy and environmental protection.

In this context, four different approaches (objective 1-3) were dedicated to synthesising graphitic carbon composite materials for the benefit of the energy sector and one approach (objective 4) was devoted to synthesising graphitic carbon composite materials for the environmental sector. The first three approaches (objective 1-3) were to synthesise oxygen reduction catalysts using graphitic carbon composite materials which can be used in the automotive industry to provide a sustainable technology with clean and efficient energy production at low cost and potentially replace the high cost Pt catalyst. The final approach (objective 4) was to synthesise graphitic carbon composite material to adsorb As species from drinking water to benefit water remediation and to prevent possible life-threatening illnesses.

3.1 Objective 1

To investigate the unique synthesis procedure and electro-catalytic properties for ORR of a unique hybrid structure consist of iron oxide embedded carbon nano spheres and N-doped CNT using low cost bio sources (Chapter 3 (a) and naturally occurring apricot sap containing galactose (Chapter 3 (b)).

3.2 Objective 2

To determine the effect of different nanoparticle phases of iron oxides dispersed in a 3D- rGO synthesised at low temperature without using any nitrogen precursors and evaluate their activity as electro catalyst for ORR (Chapter 4(a)).

3.3 Objective 3

To explore a synthesis procedure to synthesise non-conducting and scientifically under explored sulphonated poly aniline with defined nano/micro structures using excess aniline monomer (Chapter 5 (a)), investigate their ability to make composite materials with other potential materials and convert the products into a value-added product for electro chemical reaction including ORR (Chapter 5 (b)).

3.4 Objective 4

To determine efficiencies of different organic functional groups towards providing long term air stability to ZVI and reduce particle agglomeration by dispersing them in rGO. Determine the efficiency of air stable and less aggregated material for arsenic species adsorption (Chapter 6(a)).

4.0 Thesis structure

This thesis demonstrates three different approaches to synthesise carbon composite materials and evaluated for their activities for; electro chemical activity as electro catalysts for ORR reactions and adsorption for heavy metals (arsenic species).

To synthesise electro catalysts using carbon material for ORR, we adopted three different approaches. Firstly, we synthesised a unique catalyst with a hybrid structure containing both N-doped carbon spheres and CNTs using poly saccharides (galactose) and naturally occurring tree sap (apricot sap). These materials were investigated as potential ORR electro catalysts in basic media. Secondly, we described a unique synthesis procedure to synthesise SAO with unique micro structures and produced macro porous graphitic carbon structures using decomposed SO₂ produced by the decomposition of sulphonated groups in SAO in the gas at high temperature. Using this concept, we fabricated a unique N-doped macro porous graphitic carbon material by pyrolysis of SAO at high temperature. The produced carbon composite materials were tested as electro catalysts for ORR in alkaline media. Finally, we synthesised a graphitic carbon composite material using different phases of iron oxides and dispersed in a 3 dimensionally aligned rGO aerogels at low temperature without the use of any N-dopants. The 3D rGO aerogels with different phases of iron oxide phases were explored for their electro catalytic activity for oxygen reduction. The ultimate objective of this research is to make a suitable carbon catalyst for the cathode of the fuel cell for use in vehicles as an alternative energy source for fossil fuels with almost zero CO₂ emission.

Finally, in the context of synthesising a suitable carbon composite to adsorb heavy metals, we addressed the issues regarding air stability and aggregation of the ZVI, which over the years has been prevented being utilised as a potential adsorbent. Here, we explored different organic coating materials to coat ZVI and dispersed them on a rGO support. The organic materials provided best air stability was evaluated as an adsorbent for adsorption of arsenic species as a case study.

Chapter 1 covers three different subchapters: (a) a detailed literature survey on graphitic carbon materials including graphite, diamond, AC, CB, Fullerenes, MPC, CNT, graphene, C-dots and graphitic carbon composites (b) their applications as ORR catalysts and adsorbent for

heavy metals and (c) discussion regarding the research problem and research gap with proposal. The understanding of the graphitic carbon materials described in the literature provided the necessary background information towards targeting and synthesising the materials used for this work. The literature reviewed on the research problem provided the information about the necessary gaps in energy and environmental sector where graphitic carbon materials can be efficiently used.

Chapter 2 demonstrates the detailed discussion on the concepts, experimental procedures and the equations used to analyse the catalysts performance for ORR using RRDE techniques.

Chapter 3 consists of two sub Chapter 3(a) and Chapter 3(b). Firstly, a synthesis procedure to produce a unique hybrid structure containing N-CMS spheres and CNTs using bio source galactose was demonstrated Chapter 3(a). This work was published in Materials. Secondly, to address the global need of green materials to replace hazardous materials for electro – chemical applications, a galactose containing naturally occurring tree sap (Apricot sap) was also used to synthesise a similar hydride structure containing both N-CMS and N-CNT. Both catalysts were tested for oxygen reduction for PEMFC fuel cell in the alkaline medium (Chapter 3(b)). This work was accepted to be published in Materials.

Chapter 4 explores the use of four different iron phases dispersed in a 3D rGO aerogels as potential catalysts for ORR. Four different phases of iron oxides were synthesised and explored separately, their capability to reduce oxygen in an electro chemical system, in the absence of any nitrogen doping. The different phases of iron oxide synthesised were hydro thermally deposited on the 3D rGO aerogels at low temperatures (80 °C) to eliminate any possibility of phases during the reduction process. The influence of ORR, the electrochemical properties and ability to reduce oxygen of the spinal structure, on magnetic nature and electrical conductivity

of magnetite, maghemite, hematite and goethite were evaluated. This work was published in the New Journal of Chemistry.

Chapter 5 contains two sub chapters Chapter 5(a) and Chapter 5(b). In the first sub chapter (Chapter 5(a)), a unique synthesis procedure to synthesise SAO with defined micro structures was demonstrated. The ideal aniline to APS ratio, pH and the solvent responsible to synthesise sulphonated aniline with well-defined micro structures was established. This work was submitted to the Journal of Material Science. The second sub chapter (Chapter 5(b)) explains the synthesis procedure to convert SAO to macro porous structures using the SO₂ produced during the pyrolysis process of SAO. In order to make the synthesised macro porous material catalytically active for ORR, SAO was pyrolysed with nitrogen precursors. The synthesis procedures of N-doped composites materials of SAO with PF and rGO also examined. The synthesised N-SAO, N-SAOPF and N-SAO_rGO composite materials were evaluated as ORR catalysts in alkaline medium. The second sub chapter is under preparation for submission.

Chapter 6 demonstrate the two major issues associated which hinders the efficiency of ZVI performing as excellent adsorbents: air stability and agglomeration. To address this, four different functional groups such as hydroxyl, thiol, carboxyl and amine groups were investigated as potential functional groups responsible to provide air stability to ZVI. To reduce agglomeration of the ZVI particles, the ZVI particles were modified with rGO and finally the glycine coated ZVI-rGO composite was explored for As removal. This work was submitted to the Chemical Engineering Journal.

Chapter 7 summarises the results of investigation carried out to advance the use of graphitic carbon materials to benefit energy and environmental sectors to provide alternative energy sources with low environmental impact and clean drinking water.

5. References

1. A. E. Hartemink and K. McSweeney, *Soil Carbon*, Springer, 2014.
2. M.-M. Titirici, R. J. White, N. Brun, V. L. Budarin, D. S. Su, F. del Monte, J. H. Clark and M. J. MacLachlan, *Chemical Society Reviews*, 2015, **44**, 250-290.
3. J.-T. Wang, C. Chen and Y. Kawazoe, *Scientific Reports*, 2013, **3**, 3077.
4. W. Saslow, T. Bergstresser and M. L. Cohen, *Physical Review Letters*, 1966, **16**, 354.
5. P. Trogadas, T. F. Fuller and P. Strasser, *Carbon*, 2014, **75**, 5-42.
6. D. D. L. Chung, *Acta Crystallographica Section A*, 1983, **39**, 192-192.
7. H. W. Kroto, J. R. Heath, S. C. O'Brien, R. F. Curl and R. E. Smalley, *Nature*, 1985, **318**, 162-163.
8. S. Iijima, *Nature*, 1991, **354**, 56.
9. K. S. Novoselov, A. K. Geim, S. V. Morozov, D. Jiang, Y. Zhang, S. V. Dubonos, I. V. Grigorieva and A. A. Firsov, *Science*, 2004, **306**, 666-669.
10. Y. Li, X. Li, D. Geng, Y. Tang, R. Li, J. P. Dodelet, M. Lefevre and X. Sun, *Carbon*, 2013, **64**, 170-177.
11. L. Dai, P. Soundarrajan and T. Kim, *Pure and Applied Chemistry*, 2002, **74**, 1753-1772.
12. C. M. Willemse, K. Tlhomelang, N. Jahed, P. G. Baker and E. I. Iwuoha, *Sensors*, 2011, **11**, 3970.
13. I. Andjelkovic, D. N. H. Tran, S. Kabiri, S. Azari, M. Markovic and D. Losic, *ACS Applied Materials & Interfaces*, 2015, **7**, 9758-9766.
14. Y. Han, Z. Xu and C. Gao, *Advanced Functional Materials*, 2013, **23**, 3693-3700.
15. V. Chandra, S. U. Yu, S. H. Kim, Y. S. Yoon, D. Y. Kim, A. H. Kwon, M. Meyyappan and K. S. Kim, *Chemical Communications*, 2012, **48**, 735-737.
16. L. Golovko, A. Shumsky, V. Povazhny and A. Larina, *Advanced Multilayered and Fibre-Reinforced Composites*, Springer, 1998.

17. J. A. Menéndez, *Thermochimica Acta*, 1998, **312**, 79-86.
18. Y. Cao and X. Li, *Adsorption*, 2014, **20**, 713-727.
19. Z.-H. Huang, X. Zheng, W. Lv, M. Wang, Q. H. Yang and F. Kang, *Langmuir*, 2011, **27**, 7558-7562.
20. X. Yang, C. Li and Y. Chen, *Journal of Physics D: Applied Physics*, 2017, **50**, 055501.
21. S. Y. Sawant, T. H. Han and M. H. Cho, *International Journal of Molecular Sciences*, 2016, **18**, 25.
22. Z.-S. Wu, S. Yang, Y. Sun, K. Parvez, X. Feng and K. Müllen, *Journal of the American Chemical Society*, 2012, **134**, 9082-9085.
23. H. T. Chung, J. H. Won and P. Zelenay, *Nature Communications*, 2013, **4**, 1922.
24. Z. Wen, S. Ci, F. Zhang, X. Feng, S. Cui, S. Mao, S. Luo, Z. He and J. Chen, *Advanced Materials*, 2012, **24**, 1399-1404.
25. L. Gu, L. Jiang, J. Jin, J. Liu and G. Sun, *Carbon*, 2015, **82**, 572-578.
26. D. Deng, L. Yu, X. Chen, G. Wang, L. Jin, X. Pan, J. Deng, G. Sun and X. Bao, *Angewandte Chemie International Edition*, 2013, **52**, 371-375.
27. P. Serp and B. Machado, *Nanostructured Carbon Materials for Catalysis*, *Royal Society of Chemistry*, 2015.
28. G. Rius, *Carbon for Sensing Devices*, *Springer*, 2015.
29. S. K. Tiwari, V. Kumar, A. Huczko, R. Oraon, A. D. Adhikari and G. Nayak, *Critical Reviews in Solid State and Materials Sciences*, 2016, **41**, 257-317.
30. C. Cousins and M. Heggie, *Physical Review B*, 2003, **67**, 024109.
31. K. Feneberger, *Industrial Lubrication and Tribology*, 1973, **25**, 176-178.
32. R. Sengupta, M. Bhattacharya, S. Bandyopadhyay and A. K. Bhowmick, *Progress in Polymer Science*, 2011, **36**, 638-670.

33. M. Okada, N. Ohta, O. Yoshimoto, M. Tatsumi and M. Inagaki, *Carbon*, 2017, **116**, 737-743.
34. W. Tu-Lung, *AIAA Journal*, 1969, **7**, 851-858.
35. C. Ford, *Corrosion*, 1946, **2**, 219-233.
36. R. Nightingale, *Graphite in Nuclear Industry*, New York and London Academic Press, 1962.
37. W. Rasnick, T. Arehart, D. Littleton and P. Steger, *Porous graphite air-bearing components as applied to machine tools*, Oak Ridge Y-12 Plant, 1974.
38. A. L. Dicks, *Journal of Power Sources*, 2006, **156**, 128-141.
39. G. M. Swain, *Advanced Materials*, 1994, **6**, 388-392.
40. J. Xu, M. C. Granger, Q. Chen, J. W. Strojek, T. E. Lister and G. M. Swain, *Analytical Chemistry*, 1997, **69**, 591A-597A.
41. Q. Chen, M. C. Granger, T. E. Lister and G. M. Swain, *Journal of The Electrochemical Society*, 1997, **144**, 3806-3812.
42. W. A. Helbig, *Journal of Chemical Education*, 1946, **23**, 98.
43. Z. Hu, M. P. Srinivasan and Y. Ni, *Advanced Materials*, 2000, **12**, 62-65.
44. L. Li, P. A. Quinlivan and D. R. Knappe, *Carbon*, 2002, **40**, 2085-2100.
45. K. N. Aboua, Y. A. Yobout, K. B. Yao, D. L. Gone and A. Trokourey, *Journal of Environmental Management*, 2015, **156**, 10-14.
46. D. Pantea, H. Darmstadt, S. Kaliaguine and C. Roy, *Applied Surface Science*, 2003, **217**, 181-193.
47. G. Hoogers, *Fuel cell technology handbook*, CRC press, 2002.
48. R. Chakrabarti, J. Delannoy, M. Couty and K. S. Schweizer, *Soft Matter*, 2011, **7**, 5397-5407.
49. S. Iijima, T. Ichihashi and Y. Ando, *Nature*, 1992, **356**, 776.

50. R. Bakry, R. M. Vallant, M. Najam-ul-Haq, M. Rainer, Z. Szabo, C. W. Huck and G. K. Bonn, *International Journal of Nanomedicine*, 2007, **2**, 639.
51. P. Fowler and A. Ceulemans, *The Journal of Physical Chemistry*, 1995, **99**, 508-510.
52. M. I. Heggie, G. L. Haffenden, C. D. Latham and T. Trevethan, *The Journal of Philosophical Transactions A*, 2016, **374**, 20150317.
53. S. H. Friedman, D. L. DeCamp, R. P. Sijbesma, G. Srdanov, F. Wudl and G. L. Kenyon, *Journal of the American Chemical Society*, 1993, **115**, 6506-6509.
54. Y. Yamakoshi, N. Umezawa, A. Ryu, K. Arakane, N. Miyata, Y. Goda, T. Masumizu and T. Nagano, *Journal of the American Chemical Society*, 2003, **125**, 12803-12809.
55. H. Tamon, H. Ishizaka, T. Yamamoto and T. Suzuki, *Carbon*, 1999, **37**, 2049-2055.
56. J. J. Freeman, *Journal of Chemical Technology and Bio Technology*, 1988, **48**, 240-241.
57. J. Ozaki, N. Endo, W. Ohizumi, K. Igarashi, M. Nakahara, A. Oya, S. Yoshida and T. Iizuka, *Carbon*, 1997, **35**, 1031-1033.
58. H. Tamai, T. Kakii, Y. Hirota, T. Kumamoto and H. Yasuda, *Chemistry of Materials*, 1996, **8**, 454-462.
59. A. Oya, S. Yoshida, J. Alcaniz-Monge and A. Linares-Solano, *Carbon*, 1995, **33**, 1085-1090.
60. J. H. Knox, B. Kaur and G. Millward, *Journal of Chromatography A*, 1986, **352**, 3-25.
61. J. Jin, S. Tanaka, Y. Egashira and N. Nishiyama, *Carbon*, 2010, **48**, 1985-1989.
62. T. Kyotani, *Carbon*, 2000, **38**, 269-286.
63. A. Eftekhari and Z. Fan, *Materials Chemistry Frontiers*, 2017.
64. L. Kao and T. Hsu, *Materials Letters*, 2008, **62**, 695-698.
65. K. P. De Jong and J. W. Geus, *Catalysis Reviews*, 2000, **42**, 481-510.

66. M. Kumar and Y. Ando, *Journal of Nanoscience and Nanotechnology*, 2010, **10**, 3739-3758.
67. M. F. De Volder, S. H. Tawfick, R. H. Baughman and A. J. Hart, *Science*, 2013, **339**, 535-539.
68. R. H. Baughman, A. A. Zakhidov and W. A. De Heer, *Science*, 2002, **297**, 787-792.
69. R. Das, M. Ali, S. Hamid, S. Ramakrishna and Z. Chowdhury, *Desalination*, 2014, **336**, 97-109.
70. M. Mujumder, N. Chopra and B. J. Hinds, *ACS Nano*, 2011, **5**, 3867-3877.
71. N. Yang, Y. Chen, T. Ren, P. Zhang and D. Yang, *Sensors and Actuators: B Chemical*, 2015, **207**, 690-715.
72. D. Boukhvalov and M. Katsnelson, *Journal of Physics: Condensed Matter*, 2009, **21**, 344205.
73. A. K. Geim and K. S. Novoselov, *Nature Materials*, 2007, **6**, 183-191.
74. C. Lee, X. Wei, J. W. Kysar and J. Hone, *Science*, 2008, **321**, 385-388.
75. K. I. Bolotin, K. Sikes, Z. Jiang, M. Klima, G. Fudenberg, J. Hone, P. Kim and H. Stormer, *Solid State Communications*, 2008, **146**, 351-355.
76. A. A. Balandin, S. Ghosh, W. Bao, I. Calizo, D. Teweldebrhan, F. Miao and C. N. Lau, *Nano Letters*, 2008, **8**, 902-907.
77. W. Choi, I. Lahiri, R. Seelaboyina and Y. S. Kang, *Critical Reviews in Solid State and Materials Sciences*, 2010, **35**, 52-71.
78. J. Shui, M. Wang, F. Du and L. Dai, *Science Advances*, 2015, **1**, e1400129.
79. H. Huang, Y. Xia, X. Tao, J. Du, J. Fang, Y. Gan and W. Zhang, *Journal of Materials Chemistry*, 2012, **22**, 10452-10456.
80. H. Li, Z. Kang, Y. Liu and S. T. Lee, *Journal of Materials Chemistry*, 2012, **22**, 24230-24253.

81. X. Xu, R. Ray, Y. Gu, H. J. Ploehn, L. Gearheart, K. Raker and W. A. Scrivens, *Journal of the American Chemical Society*, 2004, **126**, 12736-12737.
82. H. Liu, T. Ye and C. Mao, *Angewandte Chemie International Edition*, 2007, **46**, 6473-6475.
83. K. S. Fernando, S. Sahu, Y. Liu, W. K. Lewis, E. A. Guliyants, A. Jafariyan, P. Wang, C. E. Bunker and Y. P. Sun, *ACS Applied Materials & Interfaces*, 2015, **7**, 8363-8376.
84. J. Shen, Y. Zhu, X. Yang and C. Li, *Chemical Communications*, 2012, **48**, 3686-3699.
85. Q. Wang, X. Huang, Y. Long, X. Wang, H. Zhang, R. Zhu, L. Liang, P. Teng and H. Zheng, *Carbon*, 2013, **59**, 192-199.
86. C. Ding, A. Zhu and Y. Tian, *Accounts of Chemical Research*, 2013, **47**, 20-30.
87. J. Zong, X. Yang, A. Trinchì, S. Hardin, I. Cole, Y. Zhu, C. Li, T. Muster and G. Wei, *Biosensors and Bioelectronics*, 2014, **51**, 330-335.
88. A. B. Stambouli, *Renewable and Sustainable Energy Reviews*, 2011, **15**, 4507-4520.
89. A. Kongkanand and S. Kuwabata, *The Journal of Physical Chemistry B*, 2005, **109**, 23190-23195.
90. C. Jeyabharathi, P. Venkateshkumar, M. S. Rao, J. Mathiyarasu and K. L. N. Phani, *Electrochimica Acta*, 2012, **74**, 171-175.
91. H. W. Liang, X. Zhuang, S. Brüller, X. Feng and K. Müllen, *Nature Communications*, 2014, **5**, 4973.
92. K. Gong, F. Du, Z. Xia, M. Durstock and L. Dai, *Science*, 2009, **323**, 760-764.
93. L. Lai, J. R. Potts, D. Zhan, L. Wang, C. K. Poh, C. Tang, H. Gong, Z. Shen, J. Lin and R. S. Ruoff, *Energy & Environmental Science*, 2012, **5**, 7936-7942.
94. Y. Tang, B. L. Allen, D. R. Kauffman and A. Star, *Journal of the American Chemical Society*, 2009, **131**, 13200-13201.
95. R. Liu, D. Wu, X. Feng and K. Müllen, *Angewandte Chemie*, 2010, **122**, 2619-2623.

96. Z. Yang, Z. Yao, G. Li, G. Fang, H. Nie, Z. Liu, X. Zhou, X. a. Chen and S. Huang, *ACS Nano*, 2011, **6**, 205-211.
97. L. Yang, S. Jiang, Y. Zhao, L. Zhu, S. Chen, X. Wang, Q. Wu, J. Ma, Y. Ma and Z. Hu, *Angewandte Chemie*, 2011, **123**, 7270-7273.
98. D.-S. Yang, D. Bhattacharjya, S. Inamdar, J. Park and J.-S. Yu, *Journal of the American Chemical Society*, 2012, **134**, 16127-16130.
99. O. T. Holton and J. W. Stevenson, *Platinum Metals Review*, 2013, **57**, 259-271.
100. X. Ge, A. Sumboja, D. Wu, T. An, B. Li, F. T. Goh, T. A. Hor, Y. Zong and Z. Liu, *ACS Catalysis*, 2015, **5**, 4643-4667.
101. L. Dai, Y. Xue, L. Qu, H. J. Choi and J.-B. Baek, *Chemical Reviews*, 2015, **115**, 4823-4892.
102. C. P. Ewels, D. Erbahar, P. Wagner, X. Rocquefelte, R. Arenal and P. Pochel, *Paraday Discussions*, 2014, **173**, 215-232.
103. K. Kinoshita, *Journal of The Electrochemical Society*, 1990, **137**, 845-848.
104. A. Gomez-Caminero, P. Howe, M. Hughes, E. Kenyon, D. Lewis, M. Moore, J. Ng, A. Aitio and G. Becking, Environmental health criteria 224 arsenic and arsenic compounds, *World Health Organization*, 2001.
105. J. Liu, Z. Zhou, X. Zhao, Q. Xin, G. Sun and B. Yi, *Physical Chemistry Chemical Physics*, 2004, **6**, 134-137.
106. W. Zhang, P. Sherrell, A. I. Minett, J. M. Razal and J. Chen, *Energy & Environmental Science*, 2010, **3**, 1286-1293.
107. A. Lu, A. Kiefer, W. Schmidt and F. Schüth, *Chemistry of Materials*, 2004, **16**, 100-103.
108. Y. Xia and R. Mokaya, *Chemistry of Materials*, 2005, **17**, 1553-1560.
109. Y. Xia and R. Mokaya, *Advanced Materials*, 2004, **16**, 1553-1558.

110. P. Zhang, J. Zhang and S. Dai, *Chemistry-A European Journal*, 2017, **23**, 1986-1998.
111. Z. Luo, S. Lim, Z. Tian, J. Shang, L. Lai, B. MacDonald, C. Fu, Z. Shen, T. Yu and J. Lin, *Journal of Materials Chemistry*, 2011, **21**, 8038-8044.
112. L. Qu, Y. Liu, J. B. Baek and L. Dai, *ACS Nano*, 2010, **4**, 1321-1326.
113. D. Deng, X. Pan, L. Yu, Y. Cui, Y. Jiang, J. Qi, W.-X. Li, Q. Fu, X. Ma and Q. Xue, *Chemistry of Materials*, 2011, **23**, 1188-1193.
114. D. Geng, Y. Chen, Y. Chen, Y. Li, R. Li, X. Sun, S. Ye and S. Knights, *Energy & Environmental Science*, 2011, **4**, 760-764.
115. Y. Liao, Y. Gao, S. Zhu, J. Zheng, Z. Chen, C. Yin, X. Lou and D. Zhang, *ACS Applied Materials & Interfaces*, 2015, **7**, 19619-19625.
116. H. P. Cong, X.-C. Ren, P. Wang and S.-H. Yu, *ACS Nano*, 2012, **6**, 2693-2703.
117. Z. S. Wu, S. Yang, Y. Sun, K. Parvez, X. Feng and K. Müllen, *Journal of the American Chemical Society*, 2012, **134**, 9082-9085.
118. L. Xie, F. Su, L. Xie, X. Li, Z. Liu, Q. Kong, X. Guo, Y. Zhang, L. Wan, K. Li, C. Lv and C. Chen, *ChemSusChem*, 2015, **8**, 2917-2926.
119. C. Zhu, H. Li, S. Fu, D. Du and Y. Lin, *Chemical Society Reviews*, 2016, **45**, 517-531.
120. Z. Han, Z. Tang, S. Shen, B. Zhao, G. Zheng and J. Yang, *Scientific Reports*, 2014, **4**, 5025.
121. K. Hu, X. Xie, T. Szkopek and M. Cerruti, *Chemistry of Materials*, 2016, **28**, 1756-1768.
122. W. Chen and L. Yan, *Nanoscale*, 2011, **3**, 3132-3137.
123. Y. Li, Y. Li, E. Zhu, T. McLouth, C.-Y. Chiu, X. Huang and Y. Huang, *Journal of the American Chemical Society*, 2012, **134**, 12326-12329.
124. P. Zhang, F. Sun, Z. Xiang, Z. Shen, J. Yun and D. Cao, *Energy & Environmental Science*, 2014, **7**, 442-450.

125. G. Nam, J. Park, S. T. Kim, D.-b. Shin, N. Park, Y. Kim, J.-S. Lee and J. Cho, *Nano Letters*, 2014, **14**, 1870-1876.
126. H.-W. Liang, Z.-Y. Wu, L.-F. Chen, C. Li and S.-H. Yu, *Nano Energy*, 2015, **11**, 366-376.
127. W. Wei, H. Liang, K. Parvez, X. Zhuang, X. Feng and K. Müllen, *Angewandte Chemie International Edition*, 2014, **53**, 1570-1574.
128. F. Pan, J. Jin, X. Fu, Q. Liu and J. Zhang, *ACS Applied Materials & Interfaces*, 2013, **5**, 11108-11114.
129. S. Ratso, I. Kruusenberg, M. Vikkisk, U. Joost, E. Shulga, I. Kink, T. Kallio and K. Tammeveski, *Carbon*, 2014, **73**, 361-370.
130. J. S. Lee, G. S. Park, S. T. Kim, M. Liu and J. Cho, *Angewandte Chemie*, 2013, **125**, 1060-1064.
131. P. Song, Y. Zhang, J. Pan, L. Zhuang and W. Xu, *Chemical Communications*, 2015, **51**, 1972-1975.
132. S. Zhao, H. Yin, L. Du, L. He, K. Zhao, L. Chang, G. Yin, H. Zhao, S. Liu and Z. Tang, *ACS Nano*, 2014, **8**, 12660-12668.
133. L. Lin, Q. Zhu and A.-W. Xu, *Journal of the American Chemical Society*, 2014, **136**, 11027-11033.
134. W. Yang, X. Liu, X. Yue, J. Jia and S. Guo, *Journal of the American Chemical Society*, 2015, **137**, 1436-1439.
135. B. J. Kim, D. U. Lee, J. Wu, D. Higgins, A. Yu and Z. Chen, *The Journal of Physical Chemistry C*, 2013, **117**, 26501-26508.
136. H. Yin, C. Zhang, F. Liu and Y. Hou, *Advanced Functional Materials*, 2014, **24**, 2930-2937.

137. B. Chen, Q. Ma, C. Tan, T. T. Lim, L. Huang and H. Zhang, *Small*, 2015, **11**, 3319-3336.
138. A. Aygün, S. Yenisoy-Karakaş and I. Duman, *Microporous and mesoporous materials*, 2003, **66**, 189-195.
139. R. Saito, G. Dresselhaus and M. S. Dresselhaus, *Physical Properties of Carbon Nanotubes*, *World Scientific*, 1998.
140. S. Cetin and E. Pehlivan, *Colloids and Surfaces A: Physicochemical and Engineering Aspects*, 2007, **298**, 83-87.
141. C. X. Guo, H. B. Yang, Z. M. Sheng, Z. S. Lu, Q. L. Song and C. M. Li, *Angewandte Chemie International Edition*, 2010, **49**, 3014-3017.
142. J. A. Menéndez-Díaz and I. Martín-Gullón, *Interface Science and Technology*, 2006, **7**, 1-47.
143. J. Rivera-Utrilla, M. Sánchez-Polo, V. Gómez-Serrano, P. Alvarez, M. Alvim-Ferraz and J. Dias, *Journal of Hazardous Materials*, 2011, **187**, 1-23.
144. J. Jaramillo, P. M. Álvarez and V. Gómez-Serrano, *Fuel Processing Technology*, 2010, **91**, 1768-1775.
145. V. Gómez-Serrano, M. Acedo-Ramos, A. J. López-Peinado and C. Valenzuela-Calahorro, *Fuel*, 1994, **73**, 387-395.
146. R. Pietrzak, H. Wachowska and P. Nowicki, *Energy & Fuels*, 2006, **20**, 1275-1280.
147. P. Nowicki, R. Pietrzak and H. Wachowska, *Energy & Fuels*, 2009, **23**, 2205-2212.
148. B. R. Puri and R. S. Hazra, *Carbon*, 1971, **9**, 123-134.
149. H.-C. Hsi, M. J. Rood, M. Rostam-Abadi, S. Chen and R. Chang, *Journal of Environmental Engineering*, 2002, **128**, 1080-1089.

150. M. D. Gutiérrez-Valero, P. Arranz-Mascarós, M. L. Godino-Salido, M. D. López-León, R. López-Garzón and R. Cuesta, *Microporous and Mesoporous Materials*, 2008, **116**, 445-451.
151. Q. He, Z. Hu, Y. Jiang, X. Chang, Z. Tu and L. Zhang, *Journal of Hazardous Materials*, 2010, **175**, 710-714.
152. C. Moreno-Castilla, M. Ferro-Garcia, J. Joly, I. Bautista-Toledo, F. Carrasco-Marin and J. Rivera-Utrilla, *Langmuir*, 1995, **11**, 4386-4392.
153. H. Valdés, M. Sánchez-Polo, J. Rivera-Utrilla and C. Zaror, *Langmuir*, 2002, **18**, 2111-2116.
154. Y. Leng, W. Guo, S. Su, C. Yi and L. Xing, *Chemical Engineering Journal*, 2012, **211**, 406-411.
155. Z. Li and S. Ren, *Journal of Materials Science*, 2015, **50**, 4600-4609.
156. A. Abbas, A. M. Al-Amer, T. Laoui, M. J. Al-Marri, M. S. Nasser, M. Khraisheh and M. A. Atieh, *Separation and Purification Technology*, 2016, **157**, 141-161.
157. D. Saha, S. Barakat, S. E. Van Bramer, K. A. Nelson, D. K. Hensley and J. Chen, *ACS Applied Materials & Interfaces*, 2016, **8**, 34132-34142.
158. Y. Shin, G. E. Fryxell, W. Um, K. Parker, S. V. Mattigod and R. Skaggs, *Advanced Functional Materials*, 2007, **17**, 2897-2901.
159. Y. Gao, X. Chen, J. Zhang and N. Yan, *ChemPlusChem*, 2015, **80**, 1556-1564.
160. N. Zhang, J. Xie and V. K. Varadan, *Smart Materials and Structures*, 2002, **11**, 962.
161. Y. Peng and H. Liu, *Industrial & Engineering Chemistry Research*, 2006, **45**, 6483-6488.
162. W. Xia, C. Jin, S. Kundu and M. Muhler, *Carbon*, 2009, **47**, 919-922.
163. D. V. Kosynkin, A. L. Higginbotham, A. Sinitskii, J. R. Lomeda, A. Dimiev, B. K. Price and J. M. Tour, *Nature*, 2009, **458**, 872.

164. D. Bikiaris, A. Vassiliou, K. Chrissafis, K. Paraskevopoulos, A. Jannakoudakis and A. Docoslis, *Polymer Degradation and Stability*, 2008, **93**, 952-967.
165. G. P. Rao, C. Lu and F. Su, *Separation and Purification Technology*, 2007, **58**, 224-231.
166. Y. T. Ong, A. L. Ahmad, S. H. S. Zein and S. H. Tan, *Brazilian Journal of Chemical Engineering*, 2010, **27**, 227-242.
167. Y. Wu, H. Luo, H. Wang, C. Wang, J. Zhang and Z. Zhang, *Journal of Colloid and Interface Science*, 2013, **394**, 183-191.
168. L. Hao, H. Song, L. Zhang, X. Wan, Y. Tang and Y. Lv, *Journal of Colloid and Interface Science*, 2012, **369**, 381-387.
169. X. Deng, L. Lü, H. Li and F. Luo, *Journal of Hazardous Materials*, 2010, **183**, 923-930.
170. H. Shinohara and A. Tiwari, *Graphene: An Introduction to the Fundamentals and Industrial Applications*, John Wiley & Sons, 2015.
171. M. Yusuf, F. Elfghi, S. A. Zaidi, E. Abdullah and M. A. Khan, *RSC Advances*, 2015, **5**, 50392-50420.
172. H. Guoxin and Z. Xu, *Fullerenes, Nanotubes and Carbon Nanostructures*, 2015, **23**, 283-289.
173. V. Chandra, J. Park, Y. Chun, J. W. Lee, I.-C. Hwang and K. S. Kim, *ACS Nano*, 2010, **4**, 3979-3986.
174. B. Jang, O. B. Chae, S.-K. Park, J. Ha, S. M. Oh, H. B. Na and Y. Piao, *Journal of Materials Chemistry A*, 2013, **1**, 15442-15446.
175. J.-f. Liu, Z.-s. Zhao and G.-b. Jiang, *Environmental Science & Technology*, 2008, **42**, 6949-6954.

176. T. Sreeprasad, S. M. Maliyekkal, K. Lisha and T. Pradeep, *Journal of Hazardous Materials*, 2011, **186**, 921-931.
177. M. Hua, S. Zhang, B. Pan, W. Zhang, L. Lv and Q. Zhang, *Journal of Hazardous Materials*, 2012, **211**, 317-331.
178. Y. Ku and I. L. Jung, *Water Research*, 2001, **35**, 135-142.
179. X. Wang, Y. Guo, L. Yang, M. Han, J. Zhao and X. Cheng, *J. Environ. Anal. Toxicol.*, 2012, **2**, 1000154.
180. N. T. Vuong Hoan, N. T. Anh Thu, H. V. Duc, N. D. Cuong, D. Quang Khieu and V. Vo, *Journal of Chemistry*, 2016, **2016**.
181. G. Sheng, X. Shao, Y. Li, J. Li, H. Dong, W. Cheng, X. Gao and Y. Huang, *The Journal of Physical Chemistry A*, 2014, **118**, 2952-2958.
182. S. A. Kim, S. Kamala-Kannan, K.-J. Lee, Y.-J. Park, P. J. Shea, W. H. Lee, H. M. Kim and B. T. Oh, *Chemical Engineering Journal*, 2013, **217**, 54-60.
183. X. Li, Y. Zhao, B. Xi, X. Mao, B. Gong, R. Li, X. Peng and H. Liu, *Applied Surface Science*, 2016, **370**, 260-269.
184. J. Yan, L. Han, W. Gao, S. Xue and M. Chen, *Bioresource Technology*, 2015, **175**, 269-274.
185. S. Wang, B. Gao, Y. Li, A. E. Creamer and F. He, *Journal of Hazardous Materials*, 2017, **322**, 172-181.
186. S. Thakur, G. Das, P. K. Raul and N. Karak, *The Journal of Physical Chemistry C*, 2013, **117**, 7636-7642.
187. Y. Wei, C. Gao, F. L. Meng, H.-H. Li, L. Wang, J. H. Liu and X. J. Huang, *The Journal of Physical Chemistry C*, 2011, **116**, 1034-1041.
188. L. Fan, C. Luo, M. Sun, X. Li and H. Qiu, *Colloids and Surfaces B: Biointerfaces*, 2013, **103**, 523-529.

189. S. R. Kanel, J. M. Greneche and H. Choi, *Environmental Science & Technology*, 2006, **40**, 2045-2050.
190. A. Gupta, M. Yunus and N. Sankararamakrishnan, *Chemosphere*, 2012, **86**, 150-155.
191. S. Wang, B. Gao, Y. Li, A. E. Creamer and F. He, *Journal of Hazardous Materials*, 2017, **322, Part A**, 172-181.
192. H. Zhu, Y. Jia, X. Wu and H. Wang, *Journal of Hazardous Materials*, 2009, **172**, 1591-1596.
193. S. Bhowmick, S. Chakraborty, P. Mondal, W. Van Renterghem, S. Van den Berghe, G. Roman-Ross, D. Chatterjee and M. Iglesias, *Chemical Engineering Journal*, 2014, **243**, 14-23.
194. N. Sankararamakrishnan, A. Gupta and S. R. Vidyarthi, *Journal of Environmental Chemical Engineering*, 2014, **2**, 802-810.
195. C. Wang, H. Luo, Z. Zhang, Y. Wu, J. Zhang and S. Chen, *Journal of Hazardous Materials*, 2014, **268**, 124-131.
196. M. Mosafieri, S. Nemati, A. Khataee, S. Nasserri and A. A. Hashemi, *Journal of Environmental Health Science and Engineering*, 2014, **12**, 74.
197. E. D. Coyle and R. A. Simmons, *Understanding the Global Energy Crisis*, *Purdue University Press*, 2014.
198. J. Conti, P. Holtberg, J. Diefenderfer, A. LaRose, J. Turnure and L. Westfall, *US Energy Information Administration (EIA)*, 2014, doi: DOE/EIA-0484.
199. N. L. Panwar, S. C. Kaushik and S. Kothari, *Renewable and Sustainable Energy Reviews*, 2011, **15**, 1513-1524.
200. I. Kralova and J. Sjöblom, *Journal of Dispersion Science and Technology*, 2010, **31**, 409-425.
201. R. Nehring, *Philosophical Transactions: Biological Sciences*, 2009, **364**, 3067-3079.

202. S. Shafiee and E. Topal, *Energy Policy*, 2009, **37**, 181-189.
203. M. Höök and X. Tang, *Energy Policy*, 2013, **52**, 797-809.
204. R. Sims, *Solar Energy*, 2004, **76**, 9-17.
205. J. Wang, N. Markovic and R. Adzic, *The Journal of Physical Chemistry B*, 2004, **108**, 4127-4133.
206. W. Sheng, H. A. Gasteiger and Y. Shao-Horn, *Journal of The Electrochemical Society*, 2010, **157**, B1529-B1536.
207. Y. J. Wang, D. P. Wilkinson and J. Zhang, *Dalton Transactions*, 2012, **41**, 1187-1194.
208. V. A. Sethuraman, J. W. Weidner, A. T. Haug, M. Pemberton and L. V. Protsailo, *Electrochimica Acta*, 2009, **54**, 5571-5582.
209. T. Younos, *Journal of Contemporary Water Research & Education*, 2005, **132**, 39-45.
210. J. E. Miller, Sandia national labs unlimited release report, *SAND-2003-0800*, 2003.
211. J. Matschullat, *Science of the Total Environment*, 2000, **249**, 297-312.
212. G. E. Brown, A. L. Foster and J. D. Ostergren, *Proceedings of the National Academy of Sciences*, 1999, **96**, 3388-3395.
213. L. Järup, *British Medical Bulletin*, 2003, **68**, 167-182.
214. M. Bissen and F. H. Frimmel, *Acta Hydrochimica Et Hydrobiologica*, 2003, **31**, 97-107.
215. D. Lakshmanan, D. Clifford and G. Samanta, *Journal of American Water Works Association*, 2008, **100**, 76.
216. H. K. Hansen, P. Núñez and R. Grandon, *Minerals Engineering*, 2006, **19**, 521-524.
217. X. Meng, G. P. Korfiatis, C. Christodoulatos and S. Bang, *Water Research*, 2001, **35**, 2805-2810.
218. J. Kim and M. M. Benjamin, *Water Research*, 2004, **38**, 2053-2062.

219. Y. H. Xu, T. Nakajima and A. Ohki, *Journal of Hazardous Materials*, 2002, **92**, 275-287.
220. O. X. Leupin and S. J. Hug, *Water Research*, 2005, **39**, 1729-1740.
221. M. Kang, M. Kawasaki, S. Tamada, T. Kamei and Y. Magara, *Desalination*, 2000, **131**, 293-298.
222. I. A. Katsoyiannis and A. I. Zouboulis, *Water Research*, 2004, **38**, 17-26.
223. M. G. M. Alam, S. Tokunaga and T. Maekawa, *Chemosphere*, 2001, **43**, 1035-1041.
224. J. Randall, V. Garrett, R. Bermann and A. Waiss Jr, *Forest Products Journal*, 1974.
225. J. M. Randall, E. Hautala and G. McDonald, *Journal of Applied Polymer Science*, 1978, **22**, 379-387.
226. E. J. Roberts and S. P. Rowland, *Environmental Science & Technology*, 1973, **7**, 552-555.
227. K. Kurita, Y. Koyama and A. Taniguchi, *Journal of Applied Polymer Science*, 1986, **31**, 1169-1176.
228. Z. Holan, B. Volesky and I. Prasetyo, *Biotechnology and Bioengineering*, 1993, **41**, 819-825.
229. P. Tong, Y. Baba, Y. Adachi and K. Kawazu, *Chemistry Letters*, 1991, **20**, 1529-1532.
230. C. Weng and C. Huang, *Journal of Environmental Engineering*, 1994, **120**, 1470-1487.
231. S. A. Khan and M. A. Khan, *Waste Management*, 1995, **15**, 271-282.
232. T. Viraraghavan and G. A. Rao, *International Journal of Environmental Studies*, 1993, **44**, 9-27.
233. M. J. DeMarco, A. K. SenGupta and J. E. Greenleaf, *Water Research*, 2003, **37**, 164-176.
234. Y. Kim, C. Kim, I. Choi, S. Rengaraj and J. Yi, *Environmental Science & Technology*, 2004, **38**, 924-931.

235. T.-F. Lin and J. K. Wu, *Water Research*, 2001, **35**, 2049-2057.
236. M. Z. Yi-nan Wu , Bingru Zhang , Baozhen Wu , Jie Li , Junlian Qiao , Xiaohong Guan and Fengting Li, *Nanoscale*, 2014, **6**, 1105-1112.
237. V. K. Gupta, V. K. Saini and N. Jain, *Journal of Colloid and Interface Science*, 2005, **288**, 55-60.
238. S. Bang, G. P. Korfiatis and X. Meng, *Journal of Hazardous Materials*, 2005, **121**, 61-67.
239. J. Farrell, J. Wang, P. O'Day and M. Conklin, *Environmental Science & Technology*, 2001, **35**, 2026-2032.
240. R. Crane and T. Scott, *Journal of Hazardous Materials*, 2012, **211**, 112-125.
241. H.-S. Kim, J.-Y. Ahn, K.-Y. Hwang, I.-K. Kim and I. Hwang, *Environmental Science & Technology*, 2010, **44**, 1760-1766.
242. Z. J. Li, L. Wang, L. Y. Yuan, C. L. Xiao, L. Mei, L. R. Zheng, J. Zhang, J. H. Yang, Y. L. Zhao and Z. T. Zhu, *Journal of Hazardous Materials*, 2015, **290**, 26-33.
243. J. Adusei-Gyamfi and V. Acha, *RSC Advances*, 2016, **6**, 91025-91044.
244. B. Bardos, B. Bone, P. Daly, D. Elliott, S. Jones, G. Lowry and C. Merly, *NanoRem Project. DOI*, 2014, **10**, 5036.7367.
245. Y.-P. Sun, X. Q. Li, W.-X. Zhang and H. P. Wang, *Colloids and Surfaces A: Physicochemical and Engineering Aspects*, 2007, **308**, 60-66.
246. A. Tiraferri, K. L. Chen, R. Sethi and M. Elimelech, *Journal of Colloid and Interface Science*, 2008, **324**, 71-79.
247. F. He and D. Zhao, *Environmental Science & Technology*, 2005, **39**, 3314-3320.
248. S. Wijesekara, B. Basnayake and M. Vithanage, *Environmental Science and Pollution Research*, 2014, **21**, 7075-7087.

249. F. He, D. Zhao, J. Liu and C. B. Roberts, *Industrial & Engineering Chemistry Research*, 2007, **46**, 29-34.
250. B. Schrick, B. W. Hydutsky, J. L. Blough and T. E. Mallouk, *Chemistry of Materials*, 2004, **16**, 2187-2193.
251. L. Wu, M. Shamsuzzoha and S. Ritchie, *Journal of Nanoparticle Research*, 2005, **7**, 469-476.

CHAPTER 2

EXPERIMENTAL SECTION

Ramesh Karunakaran

School of Chemical Engineering, University of Adelaide, South Australia 5005, Australia

2.0 EXPERIMENTAL

2.1 INTRODUCTION

The experimental details are given in each thesis chapter in the style of journal publications. The aim of this chapter is to provide a detailed description of the experimental techniques used for this study.

2.2 MATERIALS

Table 2.2.1 provided a list of chemicals and their purity used in this thesis.

Table 2.2.1: Specifications of chemicals used in this thesis.

Chemical name	Formula	Purity, Supplier
3-mercapto propionic acid	HSCH ₂ CH ₂ COOH	≥ 99%, Sigma Aldrich
Ammonia	NH ₃	30%, analytical reagent grade, Chem-Supply
Ammonium persulphate	(NH ₄) ₂ S ₂ O ₈	98%, Sigma Aldrich
Aniline	C ₆ H ₅ NH ₂	99%, Sigma Aldrich
Carbon monoxide	CO	Industrial, BOC
Cobalt (II) acetate	(CH ₃ COO) ₂ Co	≥ 99%, Sigma Aldrich
Cobalt sulphate heptahydrate	CoSO ₄ .7H ₂ O	≥ 99%, Sigma Aldrich
Copper (II) sulphate pentahydrate	CuSO ₄ .5H ₂ O	≥ 98%, Sigma Aldrich
D-(+)- Galactose	C ₆ H ₁₂ O ₆	≥ 98.5%, Sigma Aldrich
Dopamine hydrochloride	(OH) ₂ C ₆ H ₃ CH ₂ CH ₂ NH ₂ .HCl	98%, Sigma Aldrich
Ethanol	C ₂ H ₅ OH	100%, undenatured, Chem- Supply
Ethylene diamine	NH ₂ CH ₂ CH ₂ NH ₂	≥ 99%, Sigma Aldrich
Glycerol	HOCH ₂ CH(OH)CH ₂ OH	≥ 99%, Sigma Aldrich
Glycine	NH ₂ CH ₂ COOH	≥ 98.5. Signa Aldrich

CHAPTER 2: Experimental

Hydrochloric acid	HCl	32%, analytical reagent grade, Chem-Supply
Hydrogen peroxide	H ₂ O ₂	30%, analytical reagent grade, Chem-Supply
Iron (II) chloride tetra hydrate	FeCl ₂ .4H ₂ O	≥ 99%, Sigma Aldrich
Iron (III) chloride hexahydrate	FeCl ₃ .6H ₂ O	98%, Chem-Supply
Iron sulphate heptahydrate	FeSO ₄ .7H ₂ O	≥ 98.5%, Sigma Aldrich
Melamine	C ₃ H ₆ N ₆	99%, Sigma Aldrich
Mercapto propyl tri methoxy silane	HS(CH ₂) ₃ Si(OCH ₃) ₃	95%, Sigma Aldrich
Nafion dispersion	C ₇ HF ₁₃ O ₅ S.C ₂ F ₄	10%, Fuel Cell Stores, USA
Nitrogen	N ₂	Gas - 99.999%, BOC
Para formaldehyde	HO(CH ₂ O) _n H	95%, Sigma Aldrich
Phenol	C ₆ H ₅ OH	≥ 99%, Sigma Aldrich
Phosphoric acid	H ₃ PO ₄	85%, analytical reagent grade, Chem-Supply
Poly ethylene glycol	H(OCH ₂ CH ₂) _n OH	Average M _w 1500, Sigma Aldrich
Polyvinyl pyrolidone	(C ₆ H ₉ NO) _n	M _w 40,000, Sigma Aldrich
Potassium permanganate	KMnO ₄	≥ 98.5%, Sigma Aldrich
Sodium acetate	CH ₃ COONa	99%, Sigma Aldrich
Sodium arsenate dibasic	Na ₂ HAsO ₄ .7H ₂ O	≥ 98%, Sigma Aldrich
Sodium arsenite	Na ₂ AsO ₃	≥ 98%, Sigma Aldrich
Sodium borohydride	NaBH ₄	≥ 98%, Sigma Aldrich
Sodium hydroxide	NaOH	> 97%, Sigma Aldrich
Sulphuric acid	H ₂ SO ₄	98%, analytical reagent grade Chem-Supply
Thiourea	NH ₂ CSNH ₂	99%, Sigma Aldrich

2.3 METHODS

The materials used in this this thesis were synthesised using mainly two methods: hydrothermal treatment and pyrolysis.

2.3.1 Hydro thermal treatment

Hydro thermal treatment is used for crystallisation of suspensions (materials dispersed in water) of materials at high temperature and pressure conditions. Hydro thermal treatment is conducted using an autoclave. The autoclave consists of a Teflon liner and a stainless-steel vessel (Fig. 1). The hydro thermal process is conducted by filling the suspension of the material to 1/3 of the volume of the Teflon liner and aligning it within a stainless-steel vessel. The stainless vessel is properly tightened to avoid any damages caused by the internal pressure built within the autoclave. The autoclave filled with the suspension is heated in an oven at required temperature for the required time and cooled to room temperature. The hydrothermally treated sample is collected, centrifuged and washed to obtain the final product.



Figure 1. Images of a teflon liner and the stainless-steel cover of the autoclave.

2.3.2 Pyrolysis

Pyrolysis is the thermochemical decomposition of organic materials exposed to high temperature in the absence of any oxygen or in the presence of an inner gas environment.¹ In our experiments, a tubular furnace was used to pyrolyse the hydro thermally treated carbon

materials to synthesise graphitic carbon materials for oxygen reduction. A schematic diagram of a tubular furnace used in this thesis is shown in Fig. 2. Initially, the quartz tube was cleaned with ethanol and placed between the heating elements. Then the sample was weighed and placed in a ceramic boat and carefully placed inside the glass tube and the two ends of the glass tube were closed with stainless steel and rubber seals prevent any gas leakages. The stainless-steel seals are made with small holes to enable Ar gas circulation. Ar gas inlet is connected to one side of the stainless-steel seal and the other end is connected *via* a tube to the container with water to monitor the gas flow. The gas pressure in the cylinder is regulated to 100kPa and the inner gas flow to the tube was maintained below 200 sccm. Prior to the experiment, the tube was saturated with argon gas for 15 min. Once the tube is saturated by Ar, the temperature of the furnace was gradually increased at the rate of 10 °C/min up to 900 or 950 °C and maintained at that temperature for the required time. The samples were collected once the sample temperature approaches room temperature under Ar environment.

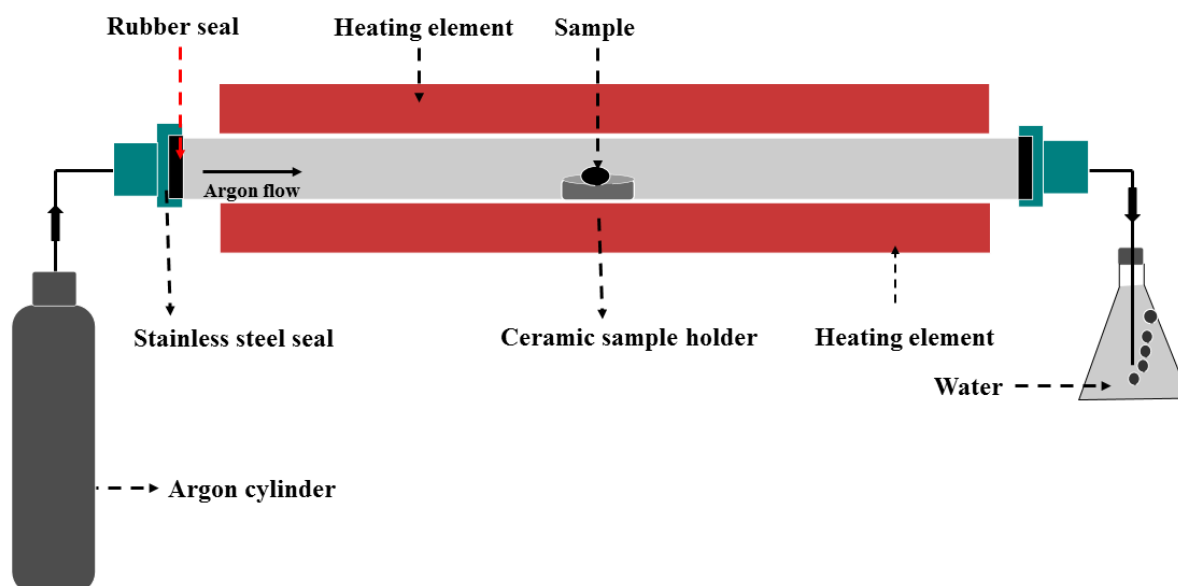


Figure 2. A schematic diagram of a tubular furnace.

2.4 CHARACTERISATION

2.4.1 CHARACTERISATION OF MATERIALS

2.4.1.1 Electron microscopy

Transition electron microscopy (TEM) was used to determine the particle sizes of metal nanoparticles and the morphology of the graphitic carbon materials. Scanning electron microscopy (SEM) was used to analyse the morphology of the graphitic carbon composites and the energy – dispersion X-ray spectroscopy (EDX) was used to investigate the distribution elemental compositions throughout the samples. The details of these techniques are given in the following sub sections.

2.4.1.1.1 Transition electron microscopy

Transition electron microscope operates using the same principles as of an optical microscope. A filament (cathode) is used as a source to irradiate electron beam with uniform current density. Commonly a hairpin shaped tungsten wire is used as the filament. The acceleration voltage of 100 – 250 kV is used to irradiate electrons. A series of condenser - lens system permits variations to the illumination aperture and the illuminated area of the specimen. The electron intensity is distributed on to a florescence screen behind the specimen and imaged with a lens system. The image can be either recorded digitally *via* a florescence screen coupled by a fibre – optics plate to a CCD camera.

In this thesis, a FEI Tecnai G2 spirit transition electron microscope equipped with a FEG LaB6 emitter and Bio Twin lens design located at Adelaide microscopy was used (Fig.3). The imaging was obtained *via* an in- column Olympus – SIS veleta CCD camera. The acceleration voltage of 120 kV is used to irradiate the electrons. The samples were ultrasonicated with ethanol and drop casted on to a copper or holey grid. Copper grids were used to analyse samples

containing metal nanoparticles while holey carbon grids were used to image samples containing graphitic carbon materials.

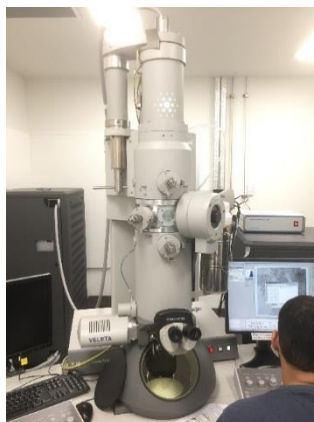


Figure 3. FEI Tecnai G2 spirit transition electron microscope equipped with a FEG LaB6 emitter and Bio Twin lens.

2.4.1.1.2 Scanning electron microscope (SEM)

In SEM, the sample is scanned using an electron beam and the intensity of the lines scanned are measured by an electron detector located above the sample. A tiny amount (few micro grams) of samples was sprinkled on to the sample holder attached with a conductive double sided adhesive carbon tape. The samples used in our studies were coated with a conductive material platinum to prevent any charge build-up during irradiation with electron beam. In our studies, SEM images were collected by using Quanta 450, FEI (USA) (Fig.4) at an accelerating voltage of 10 keV.

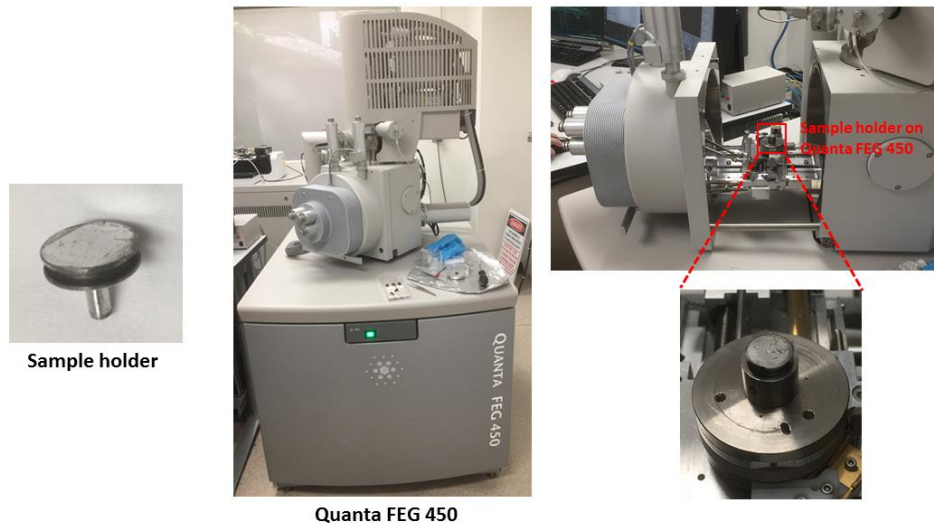


Figure 4. Image of a sample holder and Quanta 450, FEI (USA).

2.4.1.2 Powder X-ray Diffraction

Powder X-ray Diffraction (XRD) is commonly used technique to characterise crystalline solids and determine their crystal phases using a database. In this technique, a high energy radiation source (X- rays) are reflected by atoms in the crystal lattice. The X-rays interacted by the atoms are reflected by the electron shell and exit the sample in the same angle as they entered the sample (Fig. 5). Since X-rays can penetrate several layers of atoms the distance travelled by X-ray photons are different from one atom to the other. For example, the wave interact with N must travel an additional distance of PN and NQ than the wave hitting M. The reflected beams can be out of phase and extinguish each other (destructive interference) or in-phase which their intensities can be add up (constructive interference). For instance, the distance of PN + NQ is equal to a multiple of wave length, the waves are assumed to be in plane and high intensity reflection is observed.² The intensity of the reflection is dependent on the incident angle θ . By geometry, $[PN] = [NQ] = d.\sin\theta$. This is summarised by the Bragg equation in equation 1, where λ is the wave length and n is an integer.³

$$2d.\sin\theta = n\lambda \quad (1)$$

In a typical power X-ray diffractometer, the sample is irradiated with X-ray while the sample is tilted over angle θ . A detector measures the reflected intensity over an angle of 2θ . If constructive interference occurs, a high intensity over 2θ will be observed. The positions of the constructive interference can be compared with the similar patterns of the known samples in the data base. In our studies, XRD was performed by using a Miniflex 600, Rigaku apparatus manufactured in Japan. The powder samples were compressed manually on to a 15 x 15 x 1 mm plastic sample holder and the XRD was analysed at 40 KV and 15 mA in the range of $2\theta = 10 - 80^\circ$ at a scan rate of $10^\circ/\text{min}$.

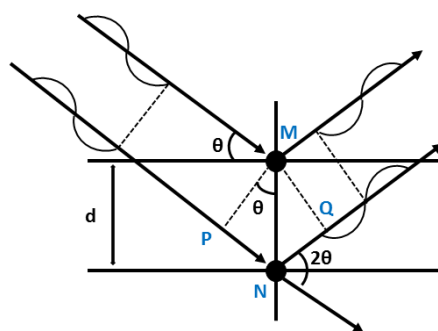


Figure 5. Illustration of a X-ray beam being reflected by two atom layers in a crystal lattice. Adopted from Vogt *et al.*²

2.4.1.3 N₂ adsorption

Nitrogen adsorption at low temperature is a common method used to determine the pore size and surface area of samples in powder form. In a nitrogen adsorption experiment the samples are weighed and loaded on to a glass sample holder which is connected to a gas sorption analyser. The samples are initially degassed in a vacuum at elevated temperature to remove any bound gases or moisture on the sample surface. The gas sorption analyser is equipped with a manifold which can be either loaded with gases or evacuate gas. The degasses samples are cooled in a liquid nitrogen bath at 77K. The N₂ gas is introduced to the manifold and the pressure is recorded when the sample holder is closed with a closed – valve. When the valve is

opened the gas is expanded into the manifold lowering the pressure. When the sample start to adsorb the gasses, it further reduces the pressure. The difference of this pressure is the base for the calculation of the amount of gas adsorbed by the sample at specific pressure.

In our experiments, gas adsorption isotherms were measured using a Micrometric 3-Flex analyser or ASAP 2020 analyser (Micromeritics Instrument Corporation, Norcross, GA, USA) (Fig.6) at 77K utilising liquid nitrogen. Brunauer-Emmett-Teller (BET) surface area was calculated using experimental points at a relative pressure of $P/P_0 = 0.05 - 0.25$. Pore size distribution was analysed using N_2 isotherms utilising DFT modelling software on a Micromeritics 3-Flex analyser. For all analysis UHP grade (99.999%) N_2 was used.



Figure 6. Image of a Micrometric 3-Flex analyser.

2.4.1.4 Raman spectroscopy

Raman spectroscopy is spectroscopic technique commonly used to identify vibrational, rotational and other frequency modes in a system. A laser beam in the visible, near infrared or near ultra violet range is used to excite and initiate these modes. The laser beam interacts with the sample and the molecular vibrations, phonons or other excitations modes alters the energy of the laser photons up and down. These specific shifts provide information regarding

vibrational modes of the samples. Raman spectroscopy (LabRAM Evolution, Horiba Jvon Yvon, Japan) was used to characterise the synthesised materials in our experiments.

2.4.1.5 X-ray Photo Electron Spectroscopy (XPS)

The electron characteristics of atoms of different chemical compounds differs according to the binding energies of electrons in the core shells.² In XPS, a soft X-radiation higher than that of the binding energy of the core electrons is given to remove the core electron out of the atoms. The binding energy of the shell electron is calculated using the following equation.⁴

$$h\gamma = E_B + E_K + W \quad (2)$$

Where,

The incident energy = $h\gamma$ (plank constant times frequency)

E_B = Binding energy of core shell electrons

E_K = Kinetic energy of the electrons ejected

W = instrument specific work function

By measuring the E_K value using a detector the binding energy of the shell electrons can be calculated. In our experiments X-ray photo electron spectroscopy (XPS) was conducted on a SPECS instrument (Berlin Germany). All XPS measurements were performed using a non-monochromatic Mg source operated at 200 W. High resolution XP spectra were collected using a pass energy of 10 eV for C 1s and 20 eV for N1s.

2.4.1.6 Fourier – Transform Infrared Spectroscopy

In Fourier – Transform Infrared (FTIR) spectroscopy, the sample is irradiated with an infrared radiation. When the radiation passes through the samples, some radiation is adsorbed by the sample and the rest is transmitted through the sample. The transmission intensity at different

wavelengths is detected representing a molecular ‘fingerprint’ of the sample. Different chemical structures produce different spectral fingerprints. The principle of FTIR spectroscopy is based on the vibration modes (stretching and bending) of molecules which are excited at different wavelengths of IR radiations causing absorption of IR beam.⁵ For our analysis, FTIR analysis was conducted by using a spectrum 100, Perkin Elmer, (USA) in the wavelength of 400 – 4000 cm^{-1} .

2.4.1.7 Solid state ^{13}C Nuclear Magnetic Resonance (NMR) Spectroscopy

The solid state cross-polarisation ^{13}C NMR spectrums were obtained on a Bruker 200 Avance spectrometer equipped with a 4.7 T wide-bore superconducting magnet operating at a resonance frequency of 50.33 MHz. The sample was packed into a 7 mm diameter zirconia rotor with Kel-F end caps and spun at 5 kHz. Chemical shift values were calibrated to the methyl resonance of hexamethylbenzene at 17.36 ppm and a 50 Hz Lorentzian line broadening was applied to the acquired spectrum. The cross-polarisation pulse sequence used a 3.2 μs , 195 w, 90° pulse, a contact time of 1 ms and a recycle delay of 1s and 50,000 scans were collected. The absolute signal intensity obtained for the sample was corrected for that derived from an empty rotor.

2.4.1.8 Thermometric -Mass Spectrometer Analysis

The thermometric-MS experiment was carried out using a custom-build high temperature pulsed-gas sampling equipment coupled with a mass spectrometer (Fig.7) for real-time analysis of the gaseous mixture.⁶ A schematic overview of the system is displayed in Scheme 1. The reaction cell is in direct contact with a copper block containing a 100 W heater cartridge controlled by a proportional-integral-derivative (PID) temperature controller (CAL Controls, Cal 3300) and K-type thermocouple attached to the side of the cell. The pressure in the reaction cell is monitored by a piezo-resistive manometer (Keller, Leo Record series, 30 bar range). The

cell is connected to a pulsed nozzle (Parker, Series 9 Pulse Valve) which is used to pulse controlled amounts of gas from the reaction cell *via* a 1/16" stainless steel tube into the vacuum system, comprised of a residual gas analyser (RGA) for sampling of the gas mixture (*vide infra*). For our analysis, we loaded 10 mg of samples into the reaction cell for thermometric – mass spectrometer analysis.

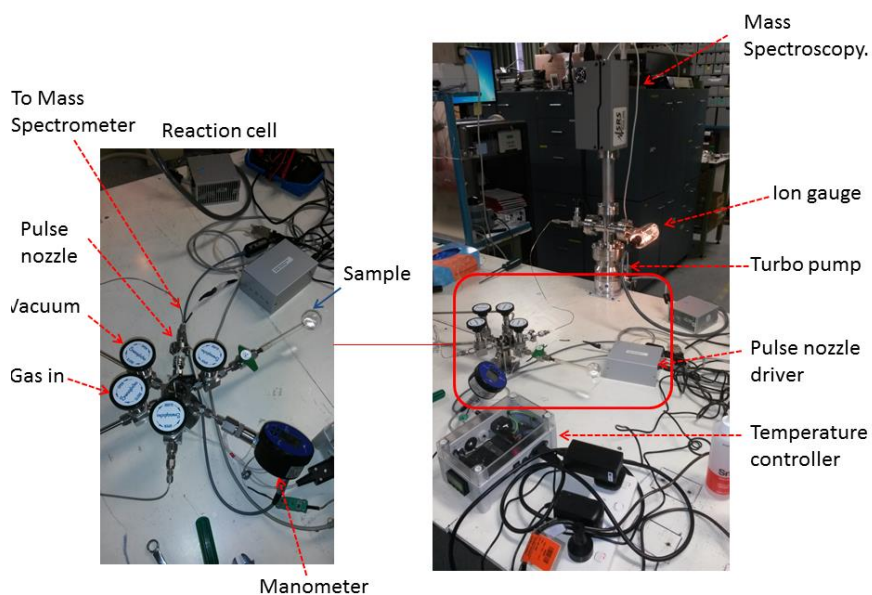
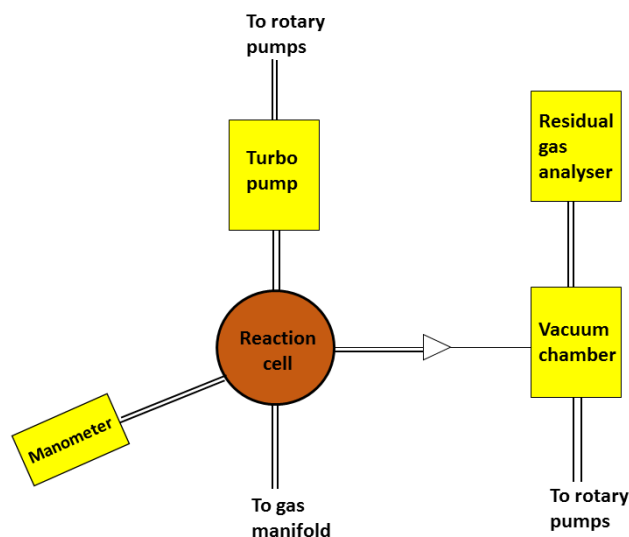


Figure 7. The setup of a custom-build high temperature pulsed-gas sampling equipment coupled with a mass spectrometer.



Scheme 1. Schematic representation of custom-build high temperature pulsed-gas sampling equipment.⁶

2.4.2 ADSORPTION CHARACTERISATION OF ARSENIC SPECIES

2.4.2.1 Sample preparation

Batch adsorption tests were carried out, individually for As(III) and As(V), to examine the effect of contact time, pH and to determine the adsorption capacity of the adsorbent. Experiments were performed in 200 mL plastic tubes with 5 mg of adsorbent and 100 mL of arsenic solution in DI water at room temperature ($22\text{ }^{\circ}\text{C} \pm 1$) at 600 rpm on a magnetic stirrer.

For kinetic experiments, 5 mg/L arsenic solutions at pH 7 were mixed for 5, 10, 15, 20, 30, 45, 60, 120 and 180 min. After the specified contact times the suspensions were immediately filtered through a 0.22 μm Teflon filter.

The effect of pH on arsenic adsorption was examined between pH 3 and 10. Initial pH of 5 mg/L arsenic solution was adjusted using diluted HCl or NaOH solution. After the addition of sorbent, the solutions were mixed for 120 min then immediately filtered through a 0.22 μm Teflon filter and analysed.

Isotherm studies were carried out at pH 8 for As(V) and As(III). Experiments were performed by mixing concentrations of As(V) or As(III) solutions with a constant dose of adsorbent (0.05 g/L) for 120 min. The concentrations of arsenic were in the range of 3 to 150 mg/L.

The arsenic concentrations were measured with Inductively Coupled Plasma-Mass spectroscopy.

2.4.2.2 Inductively Coupled Plasma – Mass Spectroscopy

Inductively coupled plasma – mass spectroscopy (ICP – MS) involves ionisation of liquid using hot argon plasma and subsequent detection by mass spectrum. The liquid samples to be analysed are broken up into atoms and ionised by hot plasma produced by a plasma torch. The sample is injected on to the plasma torch using a peristaltic pump and a nebuliser. The elemental compositions are determined by mass spectrometer.

In our experiments, ICP-MS analysis was conducted to analyse the arsenic concentration on the samples. The samples containing arsenic was diluted with nitric acid (2% v/v) to measurable parts per billion (ppb) range. The elemental compositions of the samples were determined after a calibration using a known concentration of standard liquids. To conduct adsorption studies reported in this thesis, an Inductively Coupled Plasma-Mass spectroscopy. (ICP-MS 7500cs Agilent Technologies, USA) was used.

2.4.3 ELECTRO CHEMICAL CHARACTERISATION

2.4.3.1 Rotating Disc Electrode Theory

Rotating disk electrode technique is a popular method used to determine the reactant transportation and the electron transfer kinetics at the catalytic surface of the electrode. At excess electrolyte environments, material transports occur *via* diffusion or convection. In the absence of solution convections, the diffusion layer at the electrode becomes thicker and

thicker with prolonged reaction time until non - steady state current density is achieved. In the presence of a dynamic solution convection such as stirring and electrode rotating, a constant diffusion layer can be achieved which leads to state of steady state current density. Here, the diffusion controls the rate of transportation of reactants through the diffusion layer while convection controls the thickness of the diffusion layer. RDE with a rotating electrode can quantitatively control the diffusion layer thickness and very often used to analyse the electro catalysts.⁷

2.4.3.2 Rotating Ring – Disc Electrode (RRDE) Technique

RRDE consist of a central disc electrode and a ring electrode separated by an insulated barrier. When the working electrode rotates, it drags the electrolyte solution onto its surface and on the same time flings the solution outwards in a radial direction because of the centrifugal force. Because of this counter interacting forces the solution flows in a laminar manner across the electrode surface. Therefore, with the electrode rotation speed the convection velocity increases and as a result the diffusion layer near the disc / ring surface become thinner with the increasing diffusion / convection rate due to electro – chemical reaction. Thus, the diffusion – convection rate can be controlled by the rotation rate. The diffusion – convection process near the disc / electrode surface can be calculated based on experimental conditions. The calculations can reveal information on electrode potential against applied potential.

2.4.3.3 Rotating Disc Electrode apparatus

The working electrode of the RDE includes a conductive disc is placed within an insulating material as shown in Fig.8. The conductive is made of glassy carbon. The shaft and the insulating material (Teflon) should be properly sealed to prevent any electrolyte leakages. The shaft is the directly connected to a motor by a chuck which can be rotated at a required rpm. The rate of rotation can be controlled by a rate control box. The rate of rotation can be adjusted

from 100 to 3000 rpm. During the rotation of the working electrode, the electrolyte solution will be moved towards the electrode surface and thrown away. The disc and the ring tips connects with the ring electrode. During the experiment, the disc and the ring current flows through the middle of the shaft to the external circuit. In order to maintain a laminar flow condition near the RRDE surface, the electrode rotation is controlled below 5000 rpm. A higher rotation speed will cause turbulence flow which will lead to errors in measurements. A bi - potentiostat is connected to four electrodes disc, ring, reference and counter electrode. It can control and adjust the disc and ring potential with reference and counter electrodes. The disc potential can be scanned linearly at a fixed ring electrode potential.

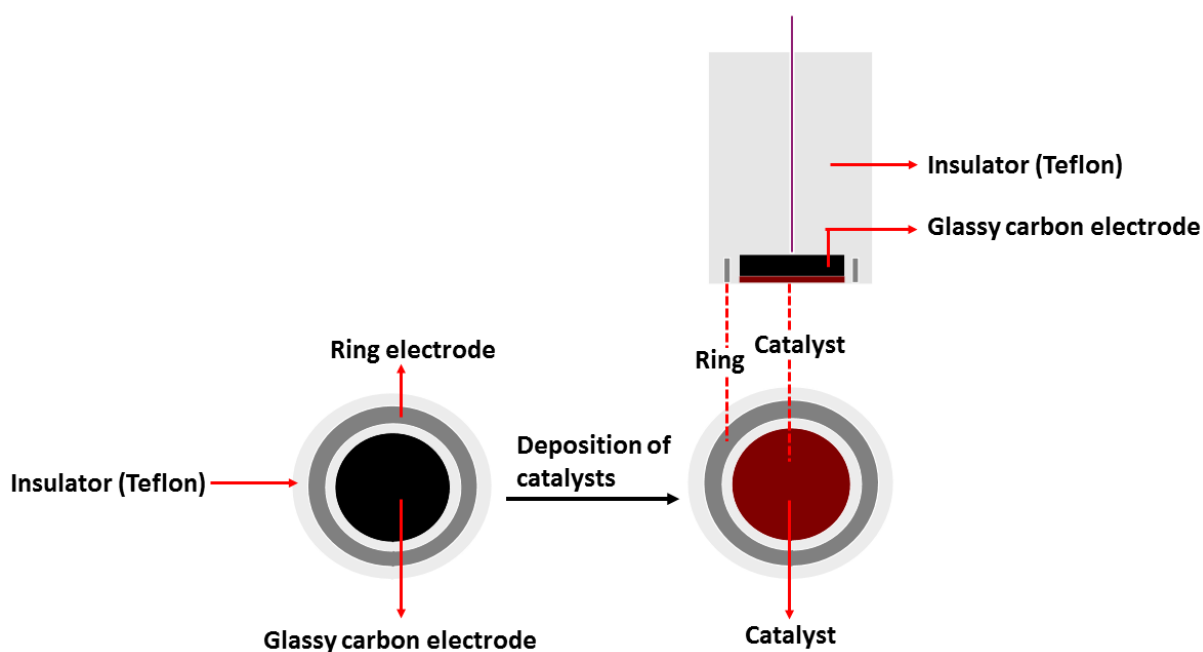


Figure 8. Schematic diagram of a rotating – ring disc electrode.

A three – electrode cell RRDE – 3A apparatus used to determine the ORR activity is shown in Fig. 9a. The working electrode is the electrode which is attached to the motor. This can rotate at a given rpm. The working electrode is place in the middle of a cylinder type container to avoid any interference form turbulent flow within the electrolyte solution. The working

electrode should be immersed in to the electrolyte and should be free of air bubbles. The cell consists of three electrodes the working, counter and reference electrodes. The working electrode is glassy carbon, the counter electrode is the Pt foil and reference electrode is Reversible Hydrogen Electrode (RHE). The electrolyte used is diluted KOH (0.1 M). The gas inlet is connected with pure O₂ (4.2 grade 99.98%) according to the requirement. When conducting ORR, the electrolyte solution is purged with oxygen for 30 – 60 min prior to the experiment and continue air flow during the measurement. A schematic representation of the experimental process is shown in Fig. 9b.

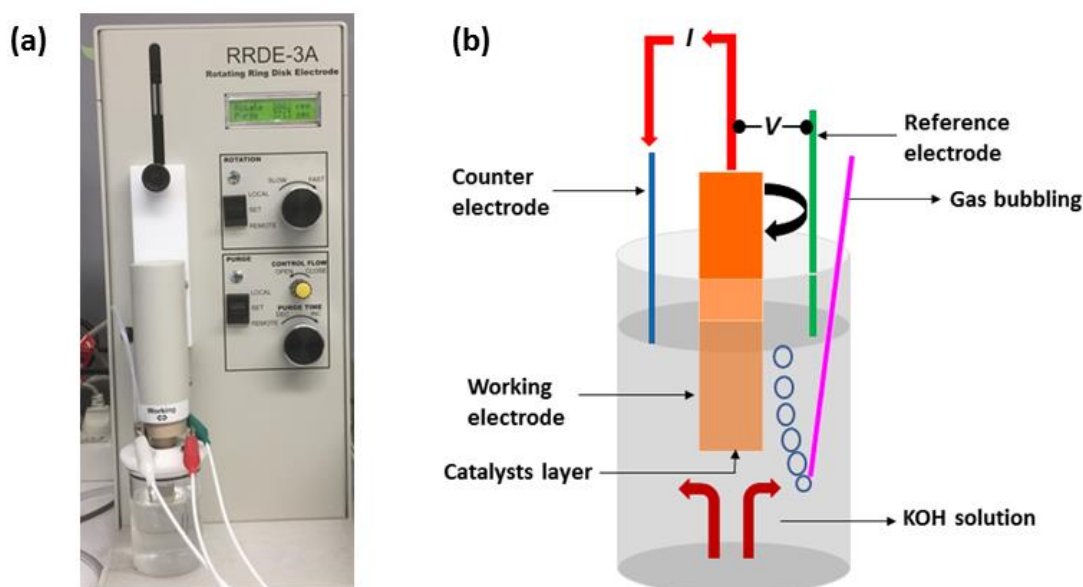


Figure 9. (a) RRDE – 3A apparatus used conduct ORR analysis and (b) Schematic representation of a process of ORR analysis.

2.4.3.4 Preparation of catalyst layer

The working electrode surface is polished with 1 μm , 0.3 μm and 0.05 μm γ -Al₂O₃ to form a mirror surface. The polished surface is then cleaned with acetone followed by deionised water and ultrasonicated for 3 times and dried overnight. The catalyst is mixed with 1% (w/w) Nafion

(1-2 mg catalysts in 2 mL of 1% w/w nafion solution) and ultrasonicated until uniformly dispersed. Then a measured amount of catalysts suspension (10 μ L) is drop casted on to the catalyst surface and dried overnight.

2.4.3.5 Experimental procedure of RDE

The working electrode with the catalyst layer was immersed into the electrolyte (0.1 M KOH) bubbling with oxygen for 30 min prior to the commencement of the experiment. Platinum coil and RHE was used as the counter and reference electrode. Prior to collecting data, the electrode is repeatedly cycled for 20 time between 0 and 1.2V at the scan rate of 100 mV/s to remove any possible surface contamination. After completion of these repeated cycles and stable cyclic voltammograms (CVs) are obtained, measurements are obtained.

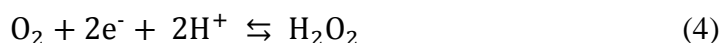
2.4.3.6 Proposed ORR Mechanisms and their investigations based on the RRDE data

ORR is a complex mechanism and in general, it is proposed the oxygen is reduced through two parallel pathways either by a direct four - electron pathway or a two - electron pathway. In the four-electron pathway, the O_2 is directly reduced to either H_2O (in acidic solution) or OH^- (in basic solution). When the ORR is driven through a two - electron pathway, the O_2 is initially reduced to H_2O_2 (acidic solution) or to HO_2^- (basic solution) *via* a two - electrons pathway and further reduced to H_2O_2 (in acidic medium) or OH^- (in basic medium) through another two – electron pathway.⁸⁻¹⁰

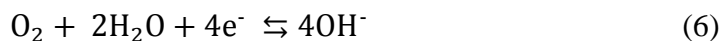
ORR through a four – electron pathway in acidic medium



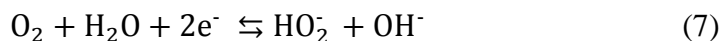
ORR through a two – electron pathway in acidic medium



ORR *via* a four – electron pathway in basic medium

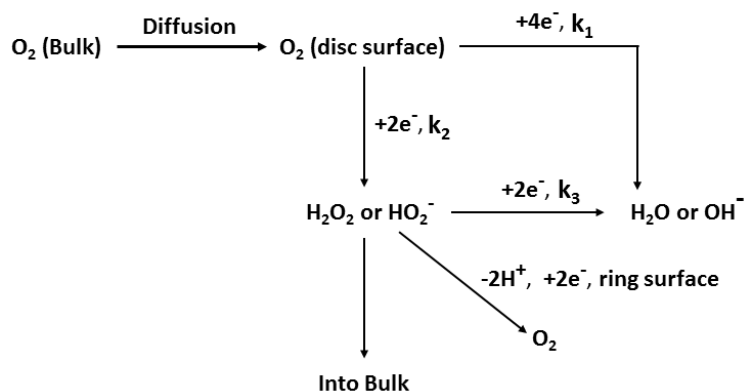


ORR *via* a two – electron pathway in basic medium



Since H_2O_2 formation in ORR determines the electron transfer pathway, detection of H_2O_2 produced during the ORR is important for the fundamental understandings of electro - chemical mechanism. Rotating Disc Electrode Theory (RDE) analysis is considered as a well-known technique to analyse the H_2O_2 yield produced during ORR reaction.

During RRDE analysis, H_2O_2 produced will be transported to the ring electrode by means of forced convection. If the H_2O_2 produced at the electrode surface is chemically stable, the ORR at the RRDE surface can be schematically represented as in Scheme 2.¹¹



Scheme 2. Schematic of the process of oxygen reduction reaction on RRDE.¹¹

The k_1 , k_2 and k_3 are the rate constants.

For convenience we express O_2 as A and H_2O_2 or HO_2^- as B.¹¹

The diffusion - convection constants of O_2 can be expressed as

$$B_A = 0.201D_A^{2/3}\nu^{-1/6} \quad (9)$$

D_A is the diffusion coefficient of oxygen and ν is the kinetic viscosity.

The diffusion - convection constants of H_2O_2 or HO_2^- can be expressed as

$$B_B = 0.201D_B^{2/3}\nu^{-1/6} \quad (10)$$

D_B is the diffusion coefficient of H_2O_2 or HO_2^-

Assuming all reactions are steady state on the disc electrodes, O_2 mass balance can be expressed as

$$B_A\omega^{1/2}(C_A^0 - C_A^s) = (k_1 + k_2)C_A^s \quad (11)$$

C_A^0 is the bulk concentration and C_A^s is the surface concentration of oxygen.

The mass balance of H_2O_2 is expressed as

$$k_2C_A^s = B_B\omega^{1/2}C_B^s + k_3C_B^s \quad (12)$$

Where C_B^s is the surface concentration of H_2O_2 or HO_2^-

Or

$$\frac{C_A^s}{C_B^s} = \frac{B_B\omega^{1/2} + k_3}{k_2} \quad (13)$$

The total current of the disc electrode can be expressed as

$$I_d = 4F\pi r_1^2 k_1 C_A^s + 2F\pi r_1^2 k_2 C_A^s + 2F\pi r_1^2 k_3 C_B^s \quad (14)$$

Since there is no H_2O_2 formation in solution at the beginning the concentration of H_2O_2 can be assumed as zero.

Therefore, the diffusion current for H_2O_2 removal from the disc electrode can be expressed as

$$I_{d,B} = 2F\pi r_1^2 B_B \omega^{1/2} C_B^S \quad (15)$$

The current at the ring electrode can be expressed as

$$I_r = I_{d,B} N = 2F\pi r_1^2 B_B \omega^{1/2} C_B^S N \quad (16)$$

Where N is the collection efficiency.

The following equation can be derived combining the equations (11), (14) and (16)

$$\frac{I_d}{I_r} = \frac{1}{N} \left(1 + \frac{2k_1}{k_2} \right) + \frac{2k_3}{B_B N} \left(1 + \frac{k_1}{k_2} \right) \omega^{-1/2} \quad (17)$$

The equation (17) can be utilised to express different situations

1. According to Scheme 2, k_3 needs to have a higher value to reduce H_2O_2 or HO_2^- to H_2O or OH^- . If k_3 is too small the produced H_2O_2 or HO_2^- cannot be further reduced to H_2O or OH^- . If we apply the very small value of k_3 to equation (11) the slope will approach zero revealing that the rotating rate (ω) is independent to the $\frac{I_d}{I_r}$. Therefore, the plot $\frac{I_d}{I_r}$ vs $\omega^{-1/2}$ will give a parreral line to the $\omega^{-1/2}$ axis. However, the intercept is dependent on the applied potential and different intercepts can be obtained for different potentials.^{7,11}
2. If the plot $\frac{I_d}{I_r}$ vs $\omega^{-1/2}$ gives a straight line using the slope $\frac{2k_3}{B_B N} \left(1 + \frac{k_1}{k_2} \right)$ and the intercept $\frac{1}{N} \left(1 + \frac{2k_1}{k_2} \right)$, k_1 , k_2 and k_3 can be calculated.^{7,11}
3. If the reaction is dominated *via* a two – electron transfer pathway where $k_2 \gg k_1$ then the obtained intercept using $\frac{I_d}{I_r}$ vs $\omega^{-1/2}$ plot will be close to a single value of $\frac{1}{N}$.
4. In the case of the reaction is carried out *via* a direct four - electron transfer pathway to produce H_2O or OH^- from O_2 , where should be $k_1 \gg k_2$. In this case equation (17)

became non – applicable because I_r approaches zero. In this case the disc current can be expressed as

$$I_{d,A} = 4F\pi r_1^2 B_A \omega^{1/2} C_A^0 \quad (18)$$

It is assumed that all O_2 transported from the bulk to the electrode surface is consumed for both four – electron and two – electron transfer reduction.⁷

$$B_A \omega^{1/2} (C_A^0 - C_A^S) = (k_1 + k_2) C_A^S \quad (11)$$

Combining equation (18) and (11)

$$I_{d,A} = 4F\pi r_1^2 (k_1 + k_2 + B_A \omega^{1/2}) C_A^S \quad (19)$$

Combining equations (12), (16), (17) and (19) equation 20 can be obtained

$$\frac{I_{d,A} - I_d}{I_r} = \frac{1}{N} \left(1 + \frac{2k_3}{k_2} \frac{B_A}{B_B} \right) + \frac{2B_A}{k_2 N} \omega^{1/2} \quad (20)$$

The rate constant k_2 can be determined from the slope of $\frac{2B_A}{k_2 N}$ of plot $\frac{I_{d,A} - I_d}{I_r}$ vs $\omega^{1/2}$ using equation (20). The values of I_d and I_r can be determined using equation (18) at different electrode rotating rates. Substituting the obtained k_2 into the intercept $\frac{1}{N} \left(1 + \frac{2k_1}{k_2} \right)$ obtained from equation (17), k_1 can be calculated. k_3 can be obtained from the slope of $\frac{2k_3}{B_B N} \left(1 + \frac{k_1}{k_2} \right)$ of equation (17) if k_1 and k_2 are known.⁷

2.4.3.7 Measurement of formed percentage of peroxide and the apparent electron – transfer number by RRDE

The overall electron – transfer number for ORR is always less than four because it is carried out with the production of intermediate H_2O_2 the electro – transfer of the ORR process is always less than four. This electron – transfer number is commonly referred as apparent electron

transfer number. RRDE is used to determine the apparent electron – transfer number along with the percentage of H₂O₂ produced during ORR. The values are expressed as a function of both ring and disc current. Using the Scheme 2 and equation (11) disc current can be expressed as equation (21).⁷

$$I_d = nF\pi r_1^2 B_A \omega^{1/2} (C_A^0 - C_A^S) = nF\pi r_1^2 (k_1 + k_2) C_A^S \quad (21)$$

$$\frac{4}{n} I_d = 4FAk_1 C_A^S + 4FAk_2 C_A^S \quad (22)$$

According Scheme 2, the disc current can be also expressed as

$$I_d = 4F\pi r_1^2 k_1 C_A^S + 2F\pi r_1^2 k_2 C_A^S + 2F\pi r_1^2 k_3 C_B^S \quad (23)$$

The limiting current at the ring electrode I_r can be expressed as

$$I_r = 2F\pi r_1^2 B_B \omega^{1/2} C_B^S N \quad (24)$$

C_B^S can be expressed as

$$C_B^S = \frac{I_r}{N} \frac{1}{2F\pi r_1^2 B_B \omega^{1/2}} \quad (25)$$

Combining (11) and (25) equation (26) can be obtained

$$\frac{4I_d}{N} = I_d - \frac{I_r k_3}{B_B \omega^{1/2} N} + 2FAk_2 C_A^S \quad (26)$$

According to equations (13) and (25) C_A^S can be expressed as

$$C_A^S = C_B^S \frac{k_3 + B_B \omega^{1/2}}{k_2} = \frac{I_r}{N} \frac{1}{2F\pi r_1^2 B_B \omega^{1/2}} \frac{k_3 + B_B \omega^{1/2}}{k_2} \quad (27)$$

Substituting equation (27) in to (26) expression for apparent electron – transfer number of ORR can be obtained.

$$n = \frac{4I_d N}{I_d N + I_r} \quad (28)$$

When I_r is equal to zero, according to equation (28) the apparent number of electron is four.

In the case of ORR is a complete two – electron transfer process the $I_r = I_d N$ and the equation (28) will give a value of two.⁷

Mass flow is used to calculate the H_2O_2 or HO_2^- produced at the electrode.

$$\% H_2O_2 = 100 \frac{\text{total mole of peroxide produced}}{\text{total mole of oxygen reacted}}$$

$$\% H_2O_2 = 100 \frac{2F\pi r_1^2 k_2 C_A^S - 2F\pi r_1^2 k_3 C_B^S}{\frac{2}{n}(nF\pi r_1^2 k_1 C_A^S + nF\pi r_1^2 k_2 C_A^S)} \quad (29)$$

Substituting (27), (28) and (29) equation (30) can be obtained.

$$\% H_2O_2 = 100 \frac{nI_r}{2I_d N} = 100 \frac{2I_r}{I_d N + I_r} = 100 \frac{4 - n}{2} \quad (30)$$

Using equation (30) with the known N , disc current and ring current the apparent electron transfer number and the % H_2O_2 produced at the disc can be calculated.⁷

2.5 Reference

1. D. Czajczynska, L. Anguilano, H. Ghazal, R. Kryzyska, A. J. Reynolds, N. Spencer and H. Jouhara, *Thermal Science and Engineering Progress*, 2017, **3**, 171-197.
2. C. Vogt, *Monash University*, 2013.
3. A. Sironi, *Angewandte Chemie International Edition*, 2008, **47**, 8558-8558.
4. J. F. Watts and J. Wolstenholme, *An Introduction to Surface Analysis by XPS and AES*, 2005, 1-15.
5. D. A. Skoog, F. J. Holler and S. R. Crouch, *Cengage Learning*, 2017.
6. A. Burgun, C. J. Coghlan, D. M. Huang, W. Chen, S. Horike, S. Kitagawa, J. F. Alvino, G. F. Metha, C. J. Sumby and C. J. Doonan, *Angewandte Chemie International Edition*, 2017, **56**, 8412-8416.
7. W. Xing, G. Yin and J. Zhang, *Elsevier*, 2014.

8. O. T. Holton and J. W. Stevenson, *Platinum Metals Review*, 2013, **57**, 259-271.
9. J. Zhang, *Springer Science & Business Media*, 2008.
10. X. Ge, A. Sumboja, D. Wu, T. An, B. Li, F. W. T. Goh, T. S. A. Hor, Y. Zong and Z. Liu, *ACS Catalysis*, 2015, **5**, 4643-4667.
11. A. Damjanovic, M. A. Genshaw and J. O. Bockris, *The Journal of Chemical Physics*, 1966, **45**, 4057-4059.

CHAPTER 3

The investigation of the synthesise of ORR catalysts with unique 3D - Hydride structures comprise of N-CNT and N-CMS using both synthetic and natural bio sources.

Ramesh Karunagaran

School of Chemical Engineering, University of Adelaide, South Australia 5005, Australia

3.1 Chapter overview

This chapter describes the synthesis procedure of a unique 3-D hybrid structure composed of both N-CNT and N-CMS using bio source galactose and naturally occurring apricot sap and the analysis of their electrocatalytic performance for ORR in an alkaline electrolyte.

The experimental investigation of this chapter has been discussed in two peer-reviewed articles (Chapter (a) and Chapter (b)), which are enclosed in this chapter.

The first paper (Chapter 3(a)) investigated the synthesis procedure to produce a unique hybrid structure containing N-CMS spheres and CNTs from galactose, as the bio source, using a two-step process hydrothermal and pyrolysis. The formation of hybrid structures of N-CNT and N-CMS was confirmed using TEM and SEM analysis. The performance of this unique catalyst was tested as an ORR electrocatalyst in an alkaline medium and has revealed to drive the reaction predominantly *via* a four-electron pathway.

The second paper (Chapter 3(b)) details the synthesis of similar hybrid catalysts using a freely available natural source; apricot sap. This paper describes the synthesise of similar 3-D hybrid structures comprised of both N-CNT and N-CMS using a three-step process: apricot resin preparation, hydrothermal treatment and pyrolysis. The performance of this catalysis was investigated for ORR in an alkaline medium and it was shown that this catalyst performs the ORR with a predominant four-electron pathway. The stability of these catalysts was also investigated.

In the following pages, the two articles together with the supporting information is detailed.

CHAPTER 3(a)

A Unique 3D Nitrogen-Doped Carbon Composite as High-Performance Oxygen Reduction Catalyst

Ramesh Karunakaran

School of Chemical Engineering, University of Adelaide, South Australia 5005, Australia

The chapter is based on the following peer-reviewed article:

R. Karunakaran, T. T. Tung, C. Shearer, D. Tran, C. Coghlan, C. Doonan, D. Losic “A unique 3D nitrogen - doped carbon composite as high performance oxygen reduction catalysts” *Materials*, 2017, **10, 921. (Published)**

Statement of Authorship

Title of Paper	A unique 3D nitrogen-doped carbon composite as high performance oxygen reduction catalysts
Publication Status	<input checked="" type="checkbox"/> Published <input type="checkbox"/> Accepted for Publication <input type="checkbox"/> Submitted for Publication <input type="checkbox"/> Unpublished and Unsubmitted work written in manuscript style
Publication Details	<i>Materials</i> , 2017, 10 , 921

Principal Author

Name of Principal Author (Candidate)	Ramesh Karunakaran		
Contribution to the Paper	Under the supervision of D. Losic and Christian Doonan, I developed, designed and conducted the experiments, interpreted, processed the data and wrote the manuscript for submission.		
Overall percentage (%)	80%		
Certification:	This paper reports on the original research I conducted during the period of my Higher Degree by Research candidature and is not subjected to any obligations or contractual agreements with third party that would constrain its inclusion in this thesis. I am the primary author of this paper.		
Signature		Date	15 February 2018

Co-Author Contributions

By signing the Statement of Authorship, each author certifies that:

- i. the candidate's stated contribution to the publication is accurate (as detailed above);
- ii. permission is granted for the candidate to include the publication in the thesis; and
- iii. the sum of all co-author contributions is equal to 100% less the candidate's stated contribution.

Name of Co-Author	Tran Thanh Tung		
Contribution to the Paper	I helped Ramesh Karunakaran (candidate) with interpreting experimental results and improving the manuscript for submission. I give consent for Ramesh Karunakaran to present this paper for examination towards the Doctorate of Philosophy.		
Signature		Date	15 February 2018

Name of Co-Author	Cameron Shearer		
Contribution to the Paper	I conducted the XPS analysis and interpreted the results for Ramesh Karunakaran. I give consent for Ramesh Karunakaran to present this paper for examination towards the Doctorate of Philosophy.		
Signature		Date	15 February 2018

Name of Co-Author	Diana Tran		
Contribution to the Paper	I helped Ramesh Karunakaran with designing experiments and improving the manuscript for submission. I give consent for Ramesh Karunakaran to present this paper for examination towards the Doctorate of Philosophy.		
Signature		Date	15 February 2018

Name of Co-Author	Campbell Coghlan		
Contribution to the Paper	I acted as the secondary supervisor for Ramesh Karunakaran and helped him to design the experiments and improve the final draft of the manuscript for submission. I give consent for Ramesh Karunakaran to present this paper for examination towards the Doctorate of Philosophy.		
Signature		Date	15 February 2018

Name of Co-Author	Christian Doonan		
Contribution to the Paper	I acted as the secondary supervisor for Ramesh Karunakaran and aided in design and development of experiment and evaluation of manuscript for submission. I give consent for Ramesh Karunakaran to present this paper for examination towards the Doctorate of Philosophy.		
Signature		Date	15 February 2018



CHAPTER 3(a): R. Karunakaran, T. T. Tung, C. Shearer, D. Tran, C. Coghlan, C. Doonan, D. Losic "A unique 3D nitrogen - doped carbon composite as high performance oxygen reduction catalysts" *Materials*, 2017, **10**, 921.(Published)

Name of Co-Author	Dusan Losic		
Contribution to the Paper	I acted as the Primary supervisor for Ramesh Karunakaran and aided in design and development of experiment and evaluation of manuscript for submission. I give consent for Ramesh Karunakaran to present this paper for examination towards the Doctorate of Philosophy.		
Signature		Date	15 February 2018



Article

A Unique 3D Nitrogen-Doped Carbon Composite as High-Performance Oxygen Reduction Catalyst

Ramesh Karunakaran ¹, Tran Thanh Tung ¹, Cameron Shearer ³ , Diana Tran ¹, Campbell Coghlan ², Christian Doonan ^{2,*} and Dusan Losic ^{1,*} 

¹ School of Chemical Engineering, University of Adelaide, SA 5005, Australia; ramesh.karunakaran@adelaide.edu.au (R.K.); tran.tung@adelaide.edu.au (T.T.T.); diana.tran@adelaide.edu.au (D.T.)

² School of Chemistry, University of Adelaide, SA 5005, Australia; cam.coghlan@adelaide.edu.au

³ School of Chemical and Physical Sciences, Flinders University, SA 5005, Australia; Cameron.Shearer@flinders.edu.au

* Correspondence: Christian.doonan@adelaide.edu.au (C.D.); Dusan.losic@adelaide.edu.au (D.L.); Tel.: +61-8-8313-5770 (C.D.); +61-8-8013-4648 (D.L.)

Received: 8 July 2017; Accepted: 4 August 2017; Published: 9 August 2017

Abstract: The synthesis and properties of an oxygen reduction catalyst based on a unique 3-dimensional (3D) nitrogen doped (N-doped) carbon composite are described. The composite material is synthesised via a two-step hydrothermal and pyrolysis method using bio-source low-cost materials of galactose and melamine. Firstly, the use of iron salts and galactose to hydrothermally produce iron oxide (Fe₂O₃) magnetic nanoparticle clusters embedded carbon spheres. Secondly, magnetic nanoparticles diffused out of the carbon sphere when pyrolysed in the presence of melamine as nitrogen precursor. Interestingly, many of these nanoparticles, as catalyst-grown carbon nanotubes (CNTs), resulted in the formation of N-doped CNTs and N-doped carbon spheres under the decomposition of carbon and a nitrogen environment. The composite material consists of integrated N-doped carbon microspheres and CNTs show high ORR activity through a predominantly four-electron pathway.

Keywords: N-doped carbon spheres; N-doped carbon nanotubes; ORR; hybrid; catalysts

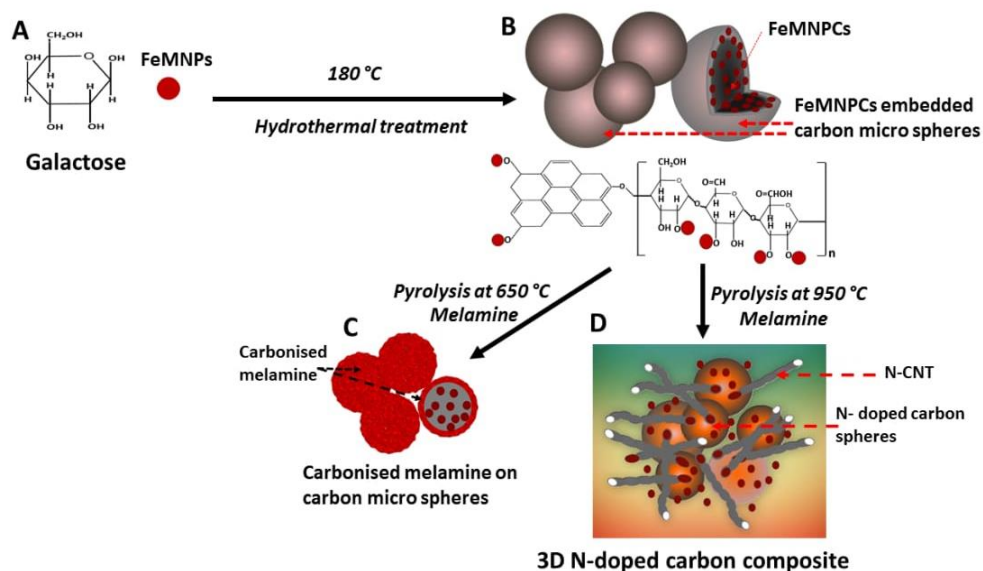
1. Introduction

Rising energy demands and the depletion of non-renewable fossil fuels have generated significant interest in renewable energy sources such as solar, wind, and geothermal [1]. Among alternate energy devices currently being considered, particularly for mobile applications, fuel cells have been widely investigated due to their theoretically high efficiencies and low carbon footprint [2]. In a hydrogen fuel cell O₂ and H₂ are converted into electricity and water. This process involves reducing O₂ at the cathode, a reaction typically carried out by expensive platinum-based catalysts. Thus, the commercial viability of hydrogen fuel cells requires the development of low-cost and efficient oxygen reduction reaction (ORR) catalysts [3].

Recent research efforts have focused on the development of alternative catalysts that can be synthesised from readily available starting materials while also overcoming the drawbacks of the Pt catalysts [4]. Several materials, such as transition metals, spinel catalysts, perovskite catalysts, metal carbon hybrid catalysts and non-metal doped catalysts, have been used as an alternative for Pt catalysts [5]. Among the possible alternatives, doped carbon nanomaterials (i.e., graphitic carbons) have been recognised as promising materials due to their high catalytic activity and low production cost [6]. Gong et al. [7] first reported that non-metal N-doped carbon materials can show outstanding ORR performance. Since then, doping graphitic carbons with heteroatoms (e.g., nitrogen, boron,

sulphur, phosphorous) has been used to increase ORR catalytic activity [8]. Transition metals such as iron and cobalt can facilitate both the incorporation of the heteroatoms and the formation of active sites within the graphitic carbon structure [9]. The primary approach to synthesizing nitrogen-doped (N-doped) mesoporous carbon materials with high ORR activity is via direct gas sources or pyrolysis of nitrogen-containing compounds [10–13]. Among these N-doped mesoporous materials, carbon nanospheres have shown high activity for ORR catalysis [14,15]. The reason has been attributed to the increased surface area and hierarchical complexity of nanosphere morphologies [16]. However, multiple processing steps and the requirement of hazardous chemicals for synthesis have hindered the practical applications of these materials.

To address these synthetic issues, unique 3D N-doped carbon composites that combine both spherical and nanotubular structures were synthesised in this work. These materials were produced using a cost-effective, environmentally-friendly and scalable method from a readily available biosource of monosaccharide (galactose) and melamine by using a two-step hydrothermal and pyrolysis method (Scheme 1). Iron oxide (Fe_2O_3) magnetic nanoparticle clusters (FeMNPCs) were introduced to initiate the N-doping of the material [17]. In fact, transition metals such as Fe serve to facilitate N incorporation into graphitic structures under pyrolysis [17]. The FeMNPCs (with sizes of 40–80 nm) are encapsulated within carbon microspheres formed from the carbonisation of galactose-based polysaccharide. The purified samples were subsequently introduced to the pyrolysis of melamine at 650 °C as an N precursor, forming a carbonised layer around the microspheres, in which ratios of melamine to carbon were chosen based on previous research [18,19]. Finally, heating at 950 °C causes decomposition of the microsphere, followed by diffusion of FeMNPCs out of the carbon spheres to catalyse N-CNTs formation. Baker et al. [20] and Ozkan and co-workers [21] previously reported that metal particles can catalyse the growth of carbon fibres. The ORR catalytic properties of the as-prepared composite materials were evaluated by electrochemical characterisation, and their structural and chemical composition, as well as on the basis of their reproducibility.



Scheme 1. Schematic for the synthesis of the 3D N-doped carbon composites with combined N-doped microspheres and N-CNT. (A) Galactose and FeMNPs dispersed in water; (B) carbon microsphere formation with FeMNPC embedded (GAL-Fe-HT); (C) carbonised melamine associated with microspheres at 650 °C; (D) carbon nanotubes are formed from the diffused FeMNPC catalysts, forming the composite material (GAL-Fe-N).

2. Materials and Methods

2.1. Materials

D-(+)-Galactose (Sigma Aldrich, purity > 98.5%), iron (II) chloride tetra hydrate ($\text{FeCl}_2 \cdot 4\text{H}_2\text{O}$) (Sigma Aldrich, St. Louis, MO, USA), iron (III) chloride hexahydrate ($\text{FeCl}_3 \cdot 6\text{H}_2\text{O}$) (Chem Supply, Gillman, SA, Australia), hydrochloric acid (HCl) (Chem Supply, Gillman, SA, Australia), ammonia (Chem Supply, Gillman, SA, Australia), melamine (Sigma Aldrich, St. Louis, MO, USA), and platinum standard catalyst (20 wt.% Vulcan XC-72) were used as purchased.

2.2. Methods

2.2.1. Synthesis of Maghemite Nanoparticles

Maghemite nanoparticles were synthesised according to a previously reported method [22]. Briefly, $\text{FeCl}_2 \cdot 4\text{H}_2\text{O}$ (39.76 g) and $\text{FeCl}_3 \cdot 6\text{H}_2\text{O}$ (16.29 g) were mixed with 100 mL of HCl (1 M) under stirring until all solids were dissolved. The pH of the mixture was adjusted to 9.8 using 2M ammonia solution. Then the solution was further stirred for another 2 h, followed by washing several times with DI water and ethanol with a centrifuge. Finally, the purified product was dried at 60 °C in a vacuum oven until its weight was constant.

2.2.2. Synthesis of Iron Oxide Embedded Carbonaceous Spheres from Galactose

Maghemite nanoparticles (200 mg) were added to a suspension of 0.02 mole galactose in 40 mL water and mixed stirring for 30 min. The mixture was transferred to a Teflon autoclave and heated to 180 °C for 18 h. Then the product was collected, centrifuged repeatedly washed, six times with deionised water and 4 times with 0.5 M H_2SO_4 . The product was collected and freeze dried for 24 h (referred to as GAL-Fe-HT). GAL-Fe-HT was then annealed at 950 °C under argon (Ar) for 3 h and denoted as GAL-Fe-A.

2.2.3. Synthesis of N-doped Carbon Spheres with Iron Oxide Nanoparticles

GAL-Fe-HT was mixed with melamine (1:10 *w/w*) and ground using a mortar and pestle, followed by annealing under the same conditions (950 °C for 3 h under Ar) and denoted as GAL-Fe-N.

2.2.4. Synthesis of Carbon Spheres Without Iron Oxide Nanoparticles

A suspension of 0.02 mole galactose in 40 mL water was mixed and stirred for 30 min. The mixture was transferred to a Teflon autoclave and heated to 180 °C for 18 h. Then the product was collected, centrifuged, and washed six times with deionised water and 4 times with 0.5 M H_2SO_4 . To dope the product with nitrogen, GAL-HT was mixed with melamine (1:10 *w/w*) and ground using a mortar and pestle, followed by annealing under the same conditions (950 °C for 3 h under Ar) and denoted as GAL-N.

2.3. Preparation of Catalytic Inks

The catalytic ink was prepared by dispersing 2 mg of catalyst in a 1 mL of 10 *v/v*% nafion in water. Then, 10 μL of the prepared ink was carefully deposited onto the 3 mm glassy carbon rotating disc electrode (RDE) and dried in the air. For the rotating ring disc analysis, the ink was deposited on a 4 mm glassy carbon rotating ring disc (RRDE) electrode. A similar procedure was followed for Pt/C (20 wt.% Vulcan XC-72) catalyst as the standard catalyst.

2.4. Characterisation

Several analytical techniques were used to characterise the synthesised products. The morphology and the structure of these samples were investigated by scanning electron microscopy (SEM) and

transition electron microscopy (TEM). SEM images were collected using Quanta 450, FEI (USA) at an accelerating voltage of 10 keV. TEM measurement was carried out by using a Technai G2 Spirit, FEI (Hillsboro, OR, USA), operated at 120 keV. X-ray diffraction (XRD) was performed using a Miniflex 600, Rigaco (Tokyo, Japan) operated at 40 KV and 15 mA in the range of $2\theta = 10\text{--}70^\circ$ at a scan rate of $10^\circ/\text{min}$. Fourier transform infrared (FTIR) spectroscopy was conducted using a spectrum 100, Perkin Elmer, (Shelton, CT, USA). Raman analysis was done using a LabRAM Evolution, Horiba Jvon (Japan) with a laser excitation wavelength of 532 nm. Gas adsorption isotherms were conducted using a Micromeritics 3-Flex or ASAP2020 analyser (Micro metrics Instruments Corporation, Norcross, GA, USA). BrunauerEmmett—Teller (BET) surface area and pore size distribution were calculated using software on the Micromeritics 3-Flex or ASAP 2020 analyser. X-ray photo electron spectroscopy (XPS) was conducted on a SPECS instrument (Berlin, Germany). All XPS measurements were performed using a non-monochromatic Mg source operated at 200 W. High resolution XP spectra were collected using a pass energy of 10 eV for C 1s and 20 eV for N1s.

Electrochemical Characterisation

The ORR reactions were conducted using a rotating disc (RDE) and rotating ring disc electrode (RRDE) apparatus connected to a bi potentiostat (CH 1760 C, CH Instruments Inc., (Bee Cave, TX, USA) in a standard three-electrode cell with oxygen-saturated KOH (0.1 mol L^{-1}) solution. The reaction was scanned at a scan rate of 0.01 Vs^{-1} between 0 and 1.1 V. The glassy carbon electrode was used as the working electrode, while platinum and reversible hydrogen electrodes (RHE) were used as the counter and reference electrodes, respectively. RRDE voltammograms were obtained after several repeated cycles were run between 0 and 1.1 V until stable voltammograms were obtained.

3. Discussion

The morphology of the prepared composite materials was investigated using SEM. Figure 1A shows smooth carbon microspheres of hydrothermally reduced galactose with FeMNPCs (GAL-Fe-HT) with sizes ranging from 1 to 6 μm . The presence of FeMNPs encapsulated within the sphere was confirmed by TEM (Figure 1B). The FeMNPCs are encapsulated within the carbon sphere through coulombic interactions formed between surface functional groups (i.e., OH, C=O) of galactose and Fe_2O_3 [23]. N-doping was introduced by pyrolysing the GAL-Fe-HT with melamine at 950°C . SEM images were analysed at the intermediate stages of pyrolysis at 650 and 950°C . At the intermediate stage, the microspheres undergo a significant shift in surface chemistry as the melamine becomes carbonised and attaches to the spheres (Figure 1C). Close inspection of the TEM image (Figure 1D) shows that subsequent heating from 650 to 950°C causes the carbonised melamine surrounding the spheres to decompose causing surface damage to the carbon sphere allowing the FeMNPCs contained within the spheres to be released. Energy dispersive X-ray (EDX) analysis conducted on these particles (Figure 1D) revealed an iron content of 7.52 wt.%, confirming the presence of the iron oxide particles (Supplementary Information (SI)). We note that a novel morphological change occurred as the FeMNPs were released. Figure 1E shows that the C and N precursors from pyrolysed melamine formed N-CNT along with N-doped carbon spheres, giving rise to a unique 3D architecture. EDX analysis conducted on the carbon microspheres and CNT showed 2.55 and 2.77 At.% (atomic percentage) of N, confirming diffusion of N precursors into both carbon spheres and CNT. To verify this hypothesis, GAL-Fe-HT was pyrolysed without melamine at 950°C (GAL-Fe-A). Separately, galactose carbon spheres (GAL) were synthesised without iron oxide nanoparticles and pyrolysed at 950°C with melamine (GAL-N). The SEM of the GAL-Fe-A or GAL-N (SI) displayed only carbon spheres. This confirms that the formation of the N-CNT resulted from the iron oxide particles.

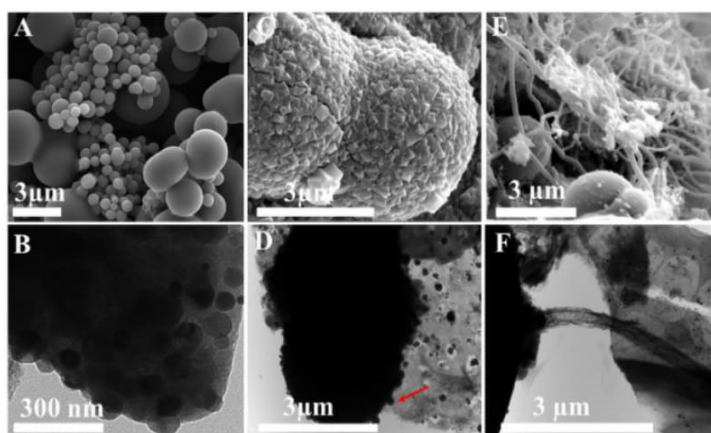


Figure 1. (A) SEM image of GAL-Fe-HT prepared using the hydrothermal process combining galactose and FeMNPCs; (B) TEM image confirming interior spheres were embedded with FeMNPs; (C) SEM image of GAL-Fe-HT pyrolysed at 650 °C with melamine; (D) TEM image of diffusion of FeMNPs from the sphere pyrolysed at 950 °C with melamine (red arrow FeMNPC); (E) SEM image of final composite material (GAL-Fe-N) with integrated N-doped carbon microspheres and N-CNT; and (F) TEM image of CNT forming from the FeMNPC within the sphere.

The CNT structure was analysed further using SEM and TEM. SEM of the CNTs (Figure 2A) shows both capped and uncapped CNTs. Interestingly, EDX analysis of the capped CNT reveals a high percentage (31.86 At.%) of Fe at the tip, indicating the presence of FeMNPCs. Furthermore, the TEM images (Figure 2B,C) confirm that the FeMNPCs are located at the tips of the CNTs and possess a hollow corrugated structure containing an irregular compartmentalised morphology. When melamine is pyrolysed, the decomposition product carbon is exposed on the surface of the reduced metallic Fe particle [24]. Then, the carbon diffuses through the Fe particles and precipitates on the other side, which is relatively cooler than the exposed surface [25]. The resultant products form a thin-walled, hollow and aligned CNT with a corrugated morphology [25]. Terrones et al. [26] synthesised similar carbon nano fibers (CNF) and reported that the nitrogen precursor from the decomposed melamine is bonded to C in sp^2 pyridine like and sp^3 bridge-head nitrogen type in CNF. Authors postulated that the formation of a rough corrugated morphology occurs when the nitrogen content of the material is increased as a replacement of C with N during doping. Also, the curvature of CNF occurs due to the carbon vacancies formed within the predominantly hexagonal graphene network of CNF [26]. A detailed analysis of the Raman spectrum, XRD diffraction peaks, BET surface area analysis and FTIR spectrum of GAL-Fe-N are presented in the SI. XRD analysis conducted on the maghemite nanoparticles is also presented in SI.

The surface of the GAL-N and GAL-Fe-N composite materials was probed by XPS and the data presented in Figure 3. Figure 3A,B shows that the carbon spectra include peaks at C-C (284.79 eV), C-N (285.75 eV) and C-O (287.76 eV) for GAL-N and GAL-Fe-N, respectively [27]. While the N1s XPS spectra shows three distinct peaks attributed to: pyridine-N (398.8 eV), graphitic-N (401.09 eV) and quaternary amine-N (402.42 eV) (Figure 3C,D) for both catalysts [28], pyrrolic nitrogen was not detected on these samples because at high pyrolysis temperatures (e.g., 800 °C), the pyrrolic nitrogen atom in the five-sided ring is thermally unstable and is converted into a graphitic nitrogen atom in the graphitic carbon frame-work [29]. The pyridinic N (27.80 At.%) present in GAL-N and (37.37 At.%) in GAL-Fe-N provides essential Lewis basicity to the adjacent carbon atoms, which is vital to initial oxygen uptake and for ORR catalysis [30]. However, the presence of Fe was not detected by XPS. This confirms Fe-N_x species are not present in the catalyst, which could also act as an active site [31].

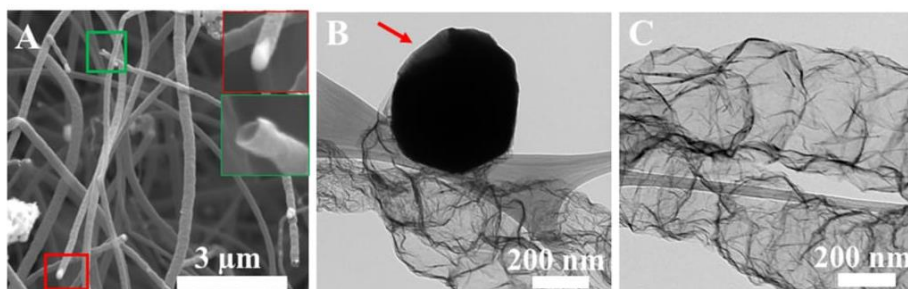


Figure 2. SEM image of (A) carbon nanofibers; the inset red and green outlines are the FeMNPCs attached to the tip of the tube and the cross section of a hollow nanotube, respectively; TEM image of (B) formation of a CNT from a FeMNPC, red arrow shows the utilised area of carbon precursors and (C) hollow corrugated CNT.

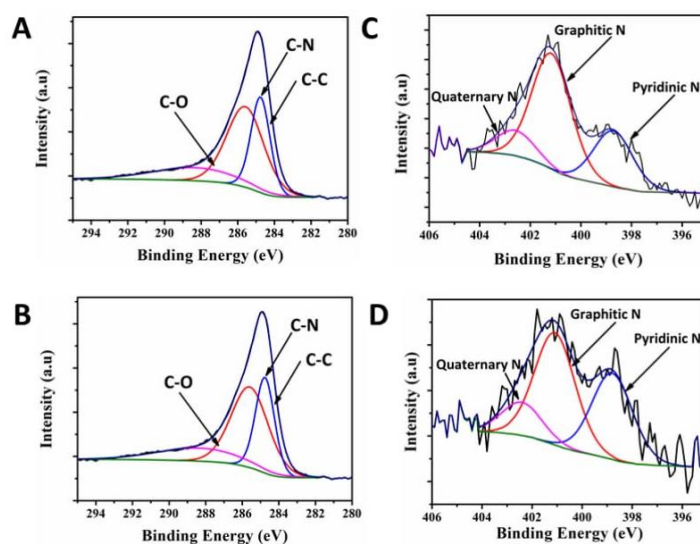


Figure 3. (A,B) are the XPS spectra of the deconvoluted C1s region; and (C,D) are the deconvoluted N1s region of GAL-N and GAL-Fe-N, respectively.

Figure 4A,B shows the ring and the disc current of the GAL-N, GAL-Fe-A, GAL-Fe-N and Pt/C catalysts with 2000 rpm recorded at scan rate of 10 mVs^{-1} , respectively Table 1 shows that the onset overpotential for GAL-Fe-N (0.29 V) is less by 160 mV and 40 mV than those of GAL-Fe-A (0.45 V) and GAL-N (0.33 V), respectively. The greater onset overpotential of GAL-Fe-A reveals that the magnetic nanoparticles present in the micro spheres did not provide enough active sites to efficiently initiate the ORR reaction. Conversely, both N-doped catalysts (GAL-N and GAL-Fe-N) provided greater catalytic activity than GAL-Fe-A catalysts and showed a lower onset overpotential when compared with GAL-Fe-A. The 40 mV lower overpotential for GAL-Fe-N when compared to GAL-N indicates that GAL-Fe-N provided more active sites for oxygen reduction than the N-doped carbon spheres in GAL-N. The half wave potential of GAL-Fe-N shifted negatively when compared to Pt/C, indicating that the reaction is carried out by mixed kinetic and diffusion mechanisms where the current is controlled by both mass transport and kinetics electron transfer [32].

The % HO_2^- yield and the overall electron transfer number for the ORR reaction was calculated using RRDE values and is shown in Figure 4C,D, respectively. The results presented in Table 1 reveal that amongst all the catalysts, GAL-Fe-N performed effectively by driving the reaction via a predominantly four-electron pathway in the potential range of 0.10–0.70 V. Within this potential range, the electron transfer number changed from 3.55 to 3.64, with a HO_2^- yield of 22.44–16.96%, showing

excellent ORR performance. Previous work suggests two different active sites for ORR reaction for M-N/C catalysts; M-N_x species, and N-atom-doped carbon materials [33]. Catalysts comprised of M-N_x species as active sites showed enhanced catalytic activity with lower HO₂⁻ yield (less than 4) and a higher electron transfer number of 3.96 [33]. Furthermore, previous reports suggest that the ORR catalytic activity of the N-C catalysts is lower than that of Fe-N-C catalysts [31]. Since no Fe was detected by the XPS in GAL-Fe-N, the activity of GAL-Fe-N can be ascribed to the nitrogen species doped in the carbon matrix (N-C). Liu et al. [31] reported that the halfwave potential of the catalysts with N-C active sites shifts more negatively than that of Fe-N-C catalysts. The negative shift of the half wave potential and relatively high HO₂⁻ yield confirms the active site of GAL-Fe-N is N-C. However, when compared to GAL-Fe-N, GAL-N showed lower electron transfer numbers of 2.97 to 3.33, and a significantly higher HO₂⁻ (52.11–42.09%). The high electron transfer number and low HO₂⁻ yield clearly demonstrated that the hybrid materials present in GAL-Fe-N (N-CNT and N-carbon spheres) provided more active sites for oxygen reduction than the N-carbon spheres present in GAL-N. Furthermore, the non-doped catalyst (GAL-Fe-A) provided different electron transfer activity from the N-doped GAL-Fe-N and GAL-N, showing a decrease in electron transfer number.

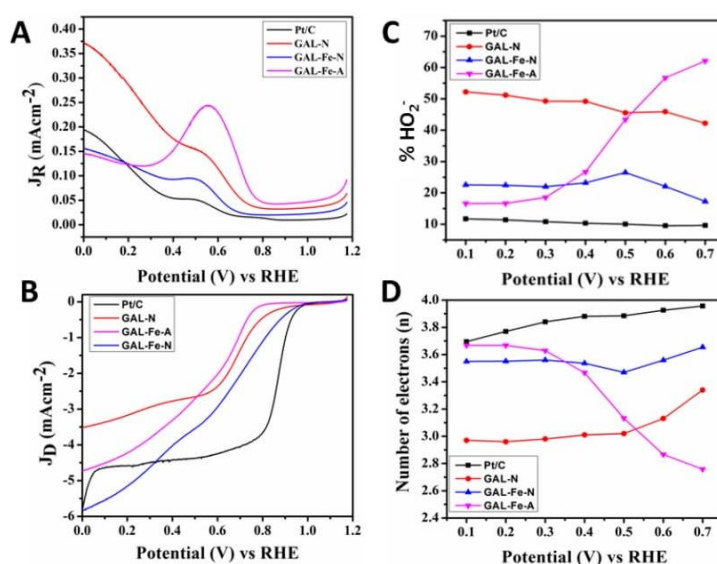


Figure 4. Rotating ring disc voltammograms recorded with GAL-N, GALFe-A, GALFe-N and Pt/C electrodes. (A) Ring current; (B) disc current; (C) HO₂⁻ peroxide produced (%) against applied potential; and (D) number of total electrons transfers against applied potential.

Table 1. Electrochemical properties of catalysts.

Catalyst	Onset Overpotential (V) RHE	Number of Electrons (n) (0.1–0.7 V) RHE	% HO ₂ ⁻ (0.1–0.7 V) RHE
GAL-N	0.33	2.97–3.33	52.11–42.09
GAL-Fe-A	0.45	3.66–2.75	16.39–62.31
GAL-Fe-N	0.29	3.55–3.64	22.44–16.96
Pt/C	0.26	3.71–3.97	11.67–9.59

The enhanced catalytic activity on GAL-Fe-N can be attributed to the doped nitrogen in the graphitic framework, which altered the electro-neutrality of nanocarbons in both N-CNT and N-carbon spheres [34]. This significantly improved the catalytic activity for the ORR reaction by creating favourable charged sites for oxygen adsorption [8]. The pyridinic nitrogen structures (N is bound to the 2 nearest carbon atoms) with their strong Lewis basicity and electronic affinity in the N-CNT

and N-carbon microspheres, induced a high positive charge density on the adjacent carbon atoms. As a result, the electron donor properties of nitrogen-doped (N-doped) GAL-Fe-N, triggered a favourable diatomic O–O adsorption weakening the O–O bond strength to facilitate ORR activity [35]. The recyclability of GAL-Fe-N was assessed by cycling the catalysts between 0.00 V and 1.15 V at 100 mV S⁻¹ in an O₂ saturated 0.1M KOH solution (SI). The result shows that after 6000 cycles the onset overpotential had increased 30 mV, showing only a slight deterioration of the catalysts.

The electron transfer kinetics of ORR using RRDE were evaluated using the model proposed by Damjanovic et al. (SI.4) [36]. The materials' rate constants were assessed within a range of 0.10–0.60 V and the results are displayed in Figure 5. For GAL-Fe-A, the k_1/k_2 ratio declined from 6.20 to 0.78, suggesting a two-electron transfer kinetic pathway as the potential increases. In contrast, the N-doped GAL-Fe-N (Figure 5D) is predominantly driven through four-electron kinetics, as the dissociation barrier of O₂ on the carbon atoms adjacent to the N-doped material is reduced [37]. Although GAL-N showed $k_1/k_2 > 1$, the reaction produced a higher yield of H₂O₂. A comparison of the performance with the state-of-the-art catalysts (Table S1 in Supplementary Materials) shows that GAL-Fe-N is similar in activity. N-doped CNTs were not compared, as they could not be isolated from the hybridised material or synthesised independently using this method.

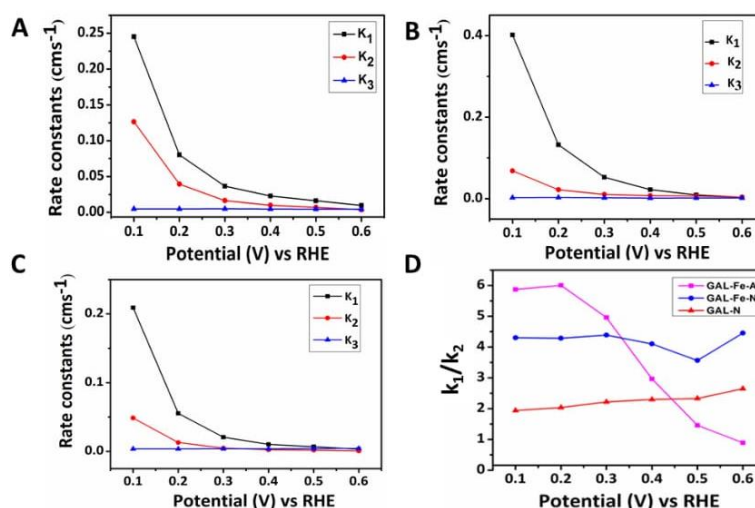


Figure 5. The rate constants for (A) GAL-N; (B) GAL-Fe-A; (C) GAL-Fe-N in the potential range of 0.1 V to 0.6 V; and (D) Comparison of k_1/k_2 ratio for GAL-N, GAL-Fe-A and GAL-Fe-N.

4. Conclusions

In summary, we have reported a new two-step process for the preparation of low-cost and environmentally friendly 3D N-doped carbon composite materials with integrated microsphere and nanotube morphologies. The use of melamine as a source of nitrogen and carbon for the formation of N-doped CNTs through the disruption of the surface on the carbon microspheres results from the release of FeMNPCs. The unique N-doped 3D composite prepared contains both N-doped microspheres and nanotubular structures, and functions as an ORR catalyst through a predominant four-electron transfer pathway.

Supplementary Materials: The following are available online at www.mdpi.com/1996-1944/10/8/921/s1, Figure S1: EDX analysis on FeNP diffused out of sphere on GAL-Fe-N, Figure S2: SEM image of carbon sphere (A) GAL-Fe-A and (B) GAL-N, Figure S3: (A) Raman and (B) XRD spectra of GAL-Fe-A and GAL-Fe-N, Figure S4: (A) N₂ adsorption/ desorption isotherm curve of (A) GAL-Fe-A and GAL-Fe-N and (B) pore size distribution of (B) GAL-Fe-A and (C) GAL-Fe-N, Figure S5: FTIR spectrum of (a) GAL-Fe-HT and (b) GAL-Fe-N, Figure S6: RDE polarisation curves GAL-Fe-N with a scan rate of 10 mV s⁻¹ before and after 6000 potential cycles in 0.1 M Oxygen saturated KOH, Figure S7: (A) XRD pattern of maghemite nanoparticles, Table S1: Comparison of the performance of GAL-Fe-N towards ORR with other similar carbon-based electro catalysts.

Acknowledgments: The authors thank the support of Australian Research Council (IH 150100003), Australian Research Council Research Hub for Graphene Enabled Industry Transformation, The Australian Solar Thermal Research Initiative (ASTRI), and The University of Adelaide, School of Chemical Engineering and, School of Chemistry. The technical support provided by Adelaide Microscopy and the Micro Analysis Research Facility at Flinders Microscopy (Flinders University) was great appreciated.

Author Contributions: Ramesh Karunakaran prepared the catalysts, analysed sample characterisation and wrote the manuscript. Cameron Shearer conducted the XPS analysis. Tran Thanh Tung, Diana Tran, Campbell Coghlan, Christian Doonan and Dusan Losic assisted in manuscript preparation.

Conflicts of Interest: The authors declare no conflict of interest

References

1. Balat, M. Global Bio-Fuel Processing and Production Trends. *Energy Explor. Exploit.* **2007**, *25*, 1–25. [[CrossRef](#)]
2. Dodds, P.E.; Staffell, I.; Hawkes, A.D.; Li, F.; Grünewald, P.; McDowall, W.; Ekins, P. Hydrogen and fuel cell technologies for heating: A review. *Int. J. Hydrogen Energy* **2015**, *40*, 2065–2083. [[CrossRef](#)]
3. Nie, Y.; Li, L.; Wei, Z. Recent advancements in Pt and Pt-free catalysts for oxygen reduction reaction. *Chem. Soc. Rev.* **2015**, *44*, 2168–2201. [[CrossRef](#)] [[PubMed](#)]
4. Liu, J.; Li, E.; Ruan, M.; Song, P.; Xu, W. Recent progress on Fe/N/C electrocatalysts for the oxygen reduction reaction in fuel cells. *Catalysts* **2015**, *5*, 1167–1192. [[CrossRef](#)]
5. Ge, X.; Sumboja, A.; Wu, D.; An, T.; Li, B.; Goh, F.T.; Hor, T.A.; Zong, Y.; Liu, Z. Oxygen reduction in alkaline media: From mechanics to recent advances of catalysts. *ACS Catal.* **2015**, *5*, 4643–4667. [[CrossRef](#)]
6. Byon, H.R.; Suntivich, J.; Shao-Horn, Y. Graphene-based non-noble-metal catalysts for oxygen reduction reaction in acid. *Chem. Mater.* **2011**, *23*, 3421–3428. [[CrossRef](#)]
7. Gong, K.; Du, F.; Xia, Z.; Durstock, M.; Dai, L. Nitrogen-doped carbon nanotube arrays with high electrocatalytic activity for oxygen reduction. *Science* **2009**, *323*, 760–764. [[CrossRef](#)] [[PubMed](#)]
8. Wang, D.W.; Su, D. Heterogeneous nanocarbon materials for oxygen reduction reaction. *Energy Environ. Sci.* **2014**, *7*, 576–591. [[CrossRef](#)]
9. Liu, G.; Li, X.; Ganesan, P.; Popov, B.N. Development of non-precious metal oxygen-reduction catalysts for PEM fuel cells based on N-doped ordered porous carbon. *Appl. Catal. B* **2009**, *93*, 156–165. [[CrossRef](#)]
10. Li, Y.; Li, T.; Yao, M.; Liu, S. Metal-free nitrogen-doped hollow carbon spheres synthesized by thermal treatment of poly (O-phenylenediamine) for oxygen reduction reaction in direct methanol fuel cell applications. *J. Mater. Chem.* **2012**, *22*, 10911–10917. [[CrossRef](#)]
11. Zhou, X.; Yang, Z.; Nie, H.; Yao, Z.; Zhang, L. Catalyst-free growth of large scale nitrogen-doped carbon spheres as efficient electrocatalysts for oxygen reduction in alkaline medium. *J. Power Sources* **2011**, *196*, 9970–9974. [[CrossRef](#)]
12. Rybarczyk, M.K.; Lieder, M.; Jablonska, M. N-doped mesoporous carbon nanosheets obtained by pyrolysis of a chitosan–melamine mixture for the oxygen reduction reaction in alkaline media. *RSC Adv.* **2015**, *5*, 44969–44977. [[CrossRef](#)]
13. Feng, L.; Yang, L.; Huang, Z.; Luo, J.; Li, M.; Wang, D.; Chen, Y. Enhancing electrocatalytic oxygen reduction on nitrogen-doped graphene by active sites implantation. *Sci. Rep.* **2013**, *3*, 3306. [[CrossRef](#)] [[PubMed](#)]
14. Liu, Y.L.; Shi, C.X.; Xu, X.Y.; Sun, P.C.; Chen, T.H. Nitrogen-doped hierarchically porous carbon spheres as efficient metal-free electrocatalysts for an oxygen reduction reaction. *J. Power Sources* **2015**, *283*, 389–396. [[CrossRef](#)]
15. Yang, T.; Liu, J.; Zhou, R.; Chen, Z.; Xu, H.; Qiao, S.Z.; Monteiro, M.J. N-doped mesoporous carbon spheres as the oxygen reduction reaction catalysts. *J. Mater. Chem. A* **2014**, *2*, 18139–18146. [[CrossRef](#)]
16. He, Y.; Han, X.; Du, Y.; Song, B.; Xu, P.; Zhang, B. Bifunctional Nitrogen-Doped Microporous Carbon Microspheres Derived from Poly(O-methylaniline) for Oxygen Reduction and Supercapacitors. *ACS Appl. Mater. Interfaces.* **2016**, *6*, 3601–3608. [[CrossRef](#)] [[PubMed](#)]
17. Nallathambi, V.; Lee, J.W.; Kumaraguru, S.P.; Wu, G.; Popov, B.N. Development of high performance carbon composites catalyst for oxygen reduction reaction in PEM Proton Exchange Membrane Fuel Cell. *J. Power Sources.* **2008**, *183*, 34–42. [[CrossRef](#)]
18. Sheng, Z.H.; Shao, L.; Chen, J.J.; Bao, W.-J.; Wang, F.B.; Xia, X.H. Catalyst-free synthesis of nitrogen-doped graphene via thermal annealing graphite oxide with melamine and its excellent electrocatalysis. *ACS Nano* **2011**, *5*, 4350–4358. [[CrossRef](#)] [[PubMed](#)]

19. Xing, T.; Zheng, Y.; Li, L.H.; Cowie, B.C.; Gunzelmann, D.; Qiao, S.Z.; Huang, S.; Chen, Y. Observation of Active Sites for Oxygen Reduction Reaction on Nitrogen-Doped Multilayer Graphene. *ACS Nano* **2014**, *8*, 6856–6862. [[CrossRef](#)] [[PubMed](#)]
20. Baker, R.T.K.; Harris, P.S.; Terry, S. Unique form of filamentous carbon. *Nature* **1975**, *253*, 37–39. [[CrossRef](#)]
21. Matter, P.H.; Ozkan, U.S. Non-metal catalysts for dioxygen reduction in an acidic electrolyte. *Catal. Lett.* **2006**, *109*, 15–123. [[CrossRef](#)]
22. Darezereshki, E. Synthesis of maghemite ($\gamma\text{-Fe}_2\text{O}_3$) nanoparticles by wet chemical method at room temperature. *Mater. Lett.* **2010**, *64*, 1471–1472. [[CrossRef](#)]
23. Yu, G.; Sun, B.; Pei, Y.; Xie, S.; Yan, S.; Qiao, M.; Fan, K.; Zhang, X.; Zong, B. $\text{Fe}_x\text{O}_y\text{/C}$ spheres as an excellent catalyst for Fischer–Tropsch synthesis. *J. Am. Chem. Soc.* **2009**, *3*, 935–937. [[CrossRef](#)] [[PubMed](#)]
24. Wirth, C.T.; Bayer, B.C.; Gamalski, A.D.; Esconjauregui, S.; Weatherup, R.S.; Ducati, C.; Baehtz, C.; Robertson, J.; Hofmann, S. The phase of iron catalyst nanoparticles during carbon nanotube growth. *Chem. Mater.* **2012**, *24*, 4633–4640. [[CrossRef](#)]
25. Terrones, M.; Hsu, W.K.; Kroto, H.W.; Walton, D.R. Nanotubes: A revolution in materials science and electronics. In *Fullerenes and Related Structures*; Springer: Berlin, Germany, 1999; Volume 199, pp. 189–234.
26. Terrones, M.; Terrones, H.; Grobert, N.; Hsu, W.; Zhu, Y.; Hare, J.; Kroto, H.; Walton, D.; Kohler-Redlich, P.; Rühle, M. Efficient route to large arrays of CN_x nanofibers by pyrolysis of ferrocene/melamine mixtures. *Appl. Phys. Lett.* **1999**, *75*, 3932–3934. [[CrossRef](#)]
27. Cheng, J.; Li, Y.; Huang, X.; Wang, Q.; Mei, A.; Shen, P.K. Highly stable electrocatalysts supported on nitrogen-self-doped three-dimensional graphene-like networks with hierarchical porous structures. *J. Mater. Chem. A* **2015**, *3*, 1492–1497. [[CrossRef](#)]
28. Wu, Z.S.; Yang, S.; Sun, Y.; Parvez, K.; Feng, X.; Müllen, K. 3D Nitrogen-Doped Graphene Aerogel-Supported Fe_3O_4 Nanoparticles as Efficient Electrocatalysts for the Oxygen Reduction Reaction. *J. Am. Chem. Soc.* **2012**, *134*, 9082–9085. [[CrossRef](#)] [[PubMed](#)]
29. Wu, G.; Santandreu, A.; Kellogg, W.; Gupta, S.; Ogoke, O.; Zhang, H.; Wang, H.-L.; Dai, L. Carbon nanocomposite catalysts for oxygen reduction and evolution reactions: From nitrogen doping to transition-metal addition. *Nano Energy* **2016**, *29*, 83–110. [[CrossRef](#)]
30. Peng, H.; Mo, Z.; Liao, S.; Liang, H.; Yang, L.; Luo, F.; Song, H.; Zhong, Y.; Zhang, B. High Performance Fe- and N- Doped Carbon Catalyst with Graphene Structure for Oxygen Reduction. *Sci. Rep.* **2013**, *3*, 1765. [[CrossRef](#)]
31. Liu, Y.L.; Xu, X.Y.; Shi, C.X.; Ye, X.W.; Sun, P.C.; Chen, T.H. Iron- nitrogen co doped hierarchically mesoporous carbon spheres as highly efficient electrocatalysts for oxygen reduction reaction. *RSC Adv.* **2017**, *7*, 8879–8885. [[CrossRef](#)]
32. Narayanamoorthy, B.; Datta, K.; Balaji, S. Kinetics and mechanism of electrochemical oxygen reduction using Platinum/clay/Nafion catalyst layer for polymer electrolyte membrane fuel cells. *J. Colloid Interface Sci.* **2012**, *387*, 213–220. [[CrossRef](#)] [[PubMed](#)]
33. Lin, L.; Zhu, Q.; Xu, A.W. Noble-metal-free Fe-N/C catalysts for Highly Efficient Oxygen Reduction Reaction under both Alkaline and Acidic Conditions. *J. Am. Chem. Soc.* **2014**, *136*, 11027–11033. [[CrossRef](#)] [[PubMed](#)]
34. Liang, Y.; Li, Y.; Wang, H.; Zhou, J.; Wang, J.; Regier, T.; Dai, H. Co_3O_4 nanocrystals on graphene as a synergistic catalyst for oxygen reduction reaction. *Nat. Mater.* **2011**, *10*, 780–786. [[CrossRef](#)] [[PubMed](#)]
35. Subramanian, N.P.; Li, X.; Nallathambi, V.; Kumaraguru, S.P.; Colon-Mercado, H.; Wu, G.; Lee, J.W.; Popov, B.N. Nitrogen-modified carbon-based catalysts for oxygen reduction reaction in polymer electrolyte membrane fuel cells. *J. Power Sources* **2009**, *188*, 38–44. [[CrossRef](#)]
36. Damjanovic, A.; Genshaw, M.A.; Bockris, J.O. Distinction between Intermediates Produced in Main and Side Electrode Reactions. *J. Chem. Phys.* **1966**, *45*, 4057–4059. [[CrossRef](#)]
37. Su, D.S.; Perathoner, S.; Centi, G. Nanocarbons for the development of advanced catalysts. *Chem. Rev.* **2013**, *113*, 5782–5816. [[CrossRef](#)] [[PubMed](#)]



Supplementary Materials: A Unique 3D Nitrogen-Doped Carbon Composite as High-performance Oxygen Reduction Catalyst

Ramesh Karunagaran, Tran Thanh Tung, Cameron Shearer, Diana Tran, Campbell Coghlan, Christian Doonan², Dusan Losic

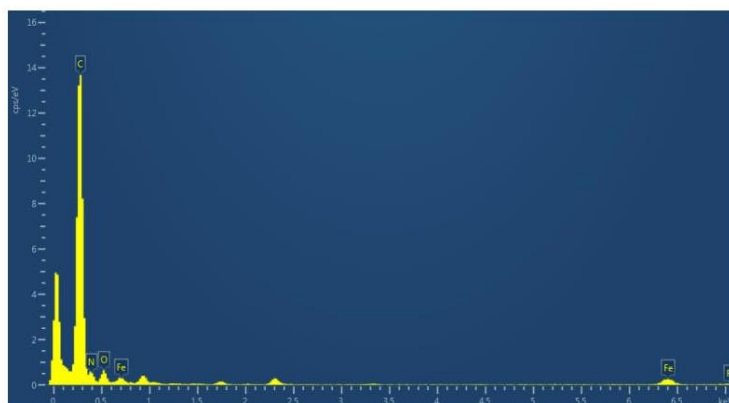


Figure S1 : EDX analysis on FeNP diffused out of sphere on GAL-Fe-N.

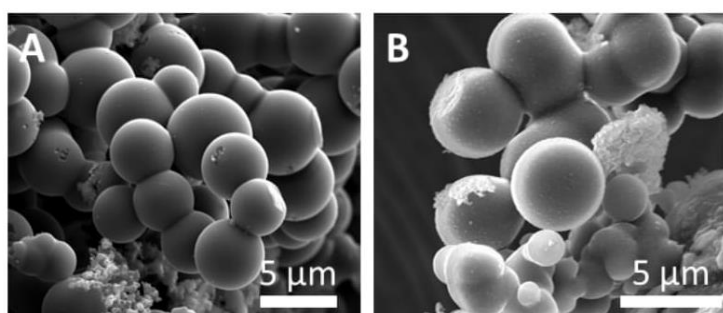


Figure S2 : SEM image of carbon sphere (A) GAL-Fe-A and (B) GAL-N

1. Raman and XRD characterisation

Raman spectroscopy performed on GAL-Fe-A and GAL-Fe-N (Figure S3A) showed characteristic peaks at 1338 cm^{-1} (D band) and 1585 cm^{-1} (G band) corresponds to the amorphous disordered carbon associated with the defects in the edges and vibrational bands of the highly ordered graphitic carbon domains, respectively [1,2]. The broad peak at 2684 cm^{-1} corresponding to the 2D peak indicates a few layers of the graphitic carbon structure [3-4]. The I_D/I_G ratio calculated to find the disorder associated with these samples showed 1.05 and 1.27 for GAL-Fe-A and GAL-Fe-N, respectively. Most notably the intensity ratio of the N-doped samples in the presence of iron (GAL-Fe-N), was higher than GAL-Fe-A. This can be ascribed to the incorporation of N and Fe in the graphene lattice which are distorting the hexagonally bonded carbon atoms in the graphitic framework and creating defects [5-6]. To determine the crystal structure of the prepared composites, XRD was performed on GAL-Fe-A and GAL-Fe-N and is shown in Figure S3B. The graph showed three characteristic peaks at 25.85 , 42.21 , 44.36 °C corresponding to (002), (110), and (101) facets, respectively for the amorphous graphitic carbon [7-8].

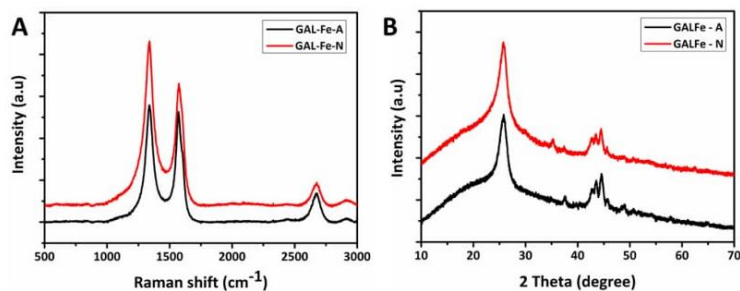


Figure S3: (A) Raman and (B) XRD spectra of GAL-Fe-A and GAL-Fe-N.

2. Surface area analysis of GAL-Fe-A and GAL-Fe-N

The nitrogen sorption isotherm and pore size distribution of GAL-Fe-A and GAL-Fe-N is shown in Fig. S4. The characteristic type IV isotherm and H4 hysteresis loop shows the presence of mesoporous slip-like pores [9]. The Barret-Joyner-Halenda (BJH) analysis measured a surface area of 311.03 and 101.76 m²/g for GAL-Fe-A and GAL-Fe-N, respectively. Pore size distribution curves for GAL-Fe-A (Figure S4B) were calculated from the adsorption branch of the isotherm shows three different pores with mean pore sizes of 5.36 Å, 8.04 Å and 12.68 Å. The results show that the pores associated on the surface of the carbon microspheres contributed to the high surface area in GAL-Fe-A. However, the N-doping process disrupted the surface and interfered with the pores responsible for the higher adsorption and exposed the larger pores, therefore reducing the adsorption in GAL-Fe-N.

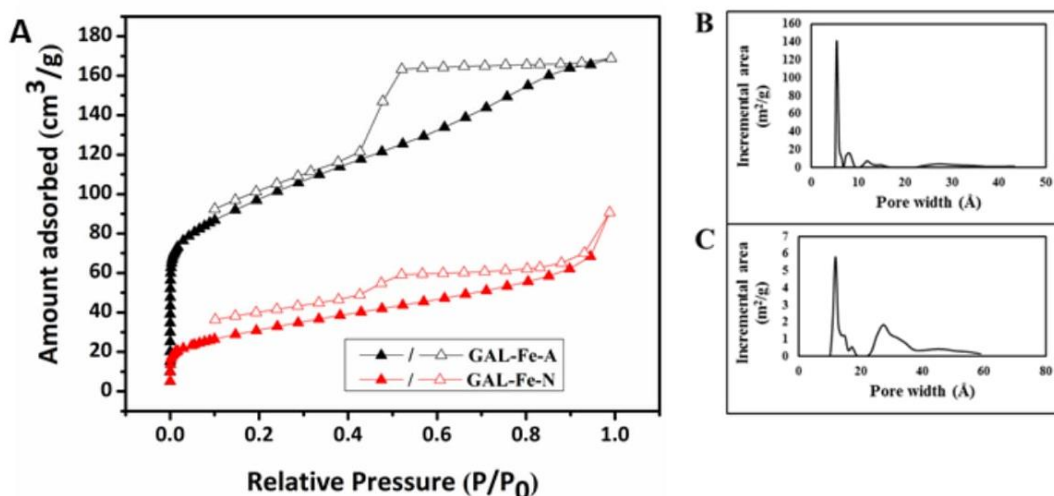


Figure S4: (A) N₂ adsorption/ desorption isotherm curve of (A) GAL-Fe-A and GAL-Fe-N and (B) pore size distribution of (B) GAL-Fe-A and (C) GAL-Fe-N.

3. FTIR analysis of GAL-Fe-HT and GAL-Fe-A.

FTIR analysis was conducted to analyse the functional groups present in the hydrothermally treated GAL-Fe-HT and N-doped GAL-Fe-N as presented in Fig. S5. The results show that GAL-Fe-HT had characteristic peaks at 1213, 1590, 1706 and 3390 cm⁻¹ [10-12] which can be attributed to C-O and C-H stretching, stretching vibration of C=O, carbonyl vibrations and stretching vibration of O-H, respectively. The reduction of the intensities of these peaks in GAL-Fe-N (Figure S5b) can be attributed to the reduction of oxygen functional groups due to dehydration during the annealing process.

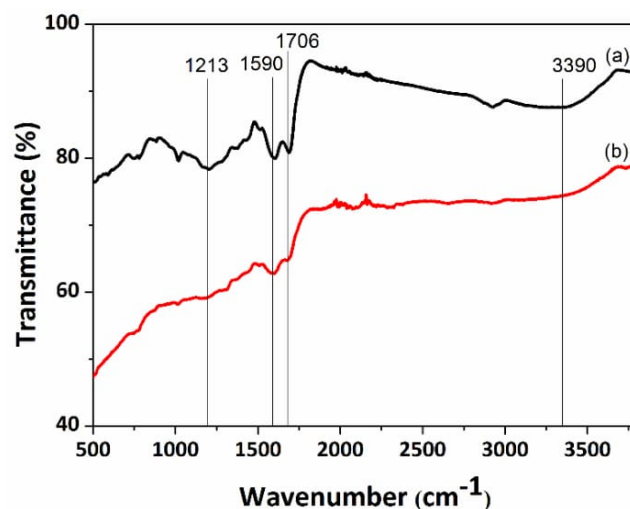


Figure S5 : FTIR spectrum of (a) GAL-Fe-HT and (b) GAL-Fe-N.

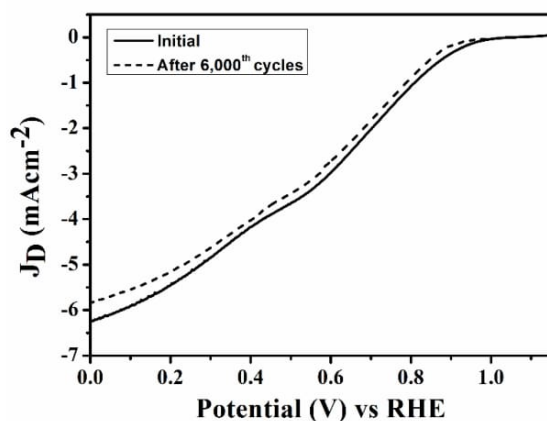


Figure S6: RDE polarisation curves GAL-Fe-N with a scan rate of 10 mVs⁻¹ before and after 6000 potential cycles in 0.1 M Oxygen saturated KOH.

4. Kinetics of electron transfer reaction of ORR.

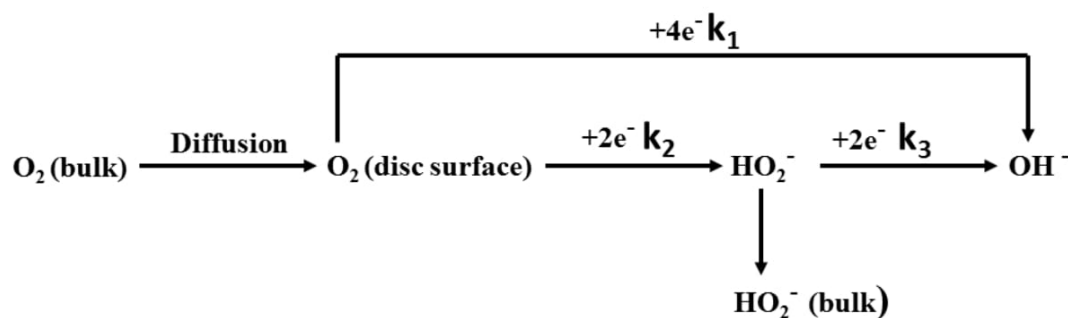
Equation 1 and 2 were employed to further elaborate the dependance of number of electrons (n) and percentage of H₂O₂ with the applied potential.

$$n = \frac{4I_D}{I_D + \frac{I_R}{N}} \quad (1)$$

$$\%H_2O_2 = 100 \frac{2I_R}{I_D N + I_R} \quad (2)$$

where I_D and I_R are the disc and ring currents, respectively and N is the collection efficiency [13].

To further study the kinetics of the ORR using RRDE voltammetry, Scheme 2 developed by Damjanovic et al. and Hsueh et al. was used for this study [14-15]. Damjanovic et al. [14] suggested that the mechanism of ORR should follow one of the two different pathways or a combination of both of them [14]. In other words, the reduction mechanism could follow a direct four electron pathway via k_1 kinetics and directly reduce oxygen to water or it could be driven through a two-electron pathway via k_2 kinetics producing peroxide intermediates and then be further reduced to water through another two-electron pathway through k_3 kinetics.



Scheme 2: Proposed model for electrochemical reduction of oxygen proposed by Damjanovic et al. and Hsueh et al.

A series of Equations (3, 4 and 5) suggested by Hsueh et al. [15] was used to calculate the rate constants k_1 , k_2 and k_3 . where I_d , I_r , I_{dL} and ω are the disc current, ring current, limiting disc current and the rotation speed, respectively. D_{O_2} , $D_{H_2O_2}$ and ν are the diffusion coefficient of oxygen, diffusion coefficient of H_2O_2 and kinematic viscosity, respectively. N is the collection efficiency.

$$k_1 = S_1 Z_1 \frac{I_1^{N-1}}{I_1^{N+1}} \quad (3)$$

$$k_2 = \frac{2 S_2 Z_1}{I_1^{N+1}} \quad (4)$$

$$k_3 = \frac{N S_1 Z_2}{I_1^{N+1}} \quad (5)$$

Where S_1 and I_1 are the slope and intercept corresponding to I_d / I_r vs $\omega^{-1/2}$ plots and S_2 is the slope of $I_{dL} / I_{dL} - I_d$ vs $\omega^{-1/2}$ plot. $Z_1 = 0.62 D_{O_2}^{2/3} \nu^{-1/6}$, $Z_2 = 0.62 D_{H_2O_2}^{2/3} \nu^{-1/6}$, D_{O_2} is $1.4 \times 10^{-5} \text{ cm}^2 \text{ s}^{-1}$, $D_{H_2O_2}$ is $6.8 \times 10^{-6} \text{ cm}^2 \text{ s}^{-1}$ and ν is $0.01 \text{ cm}^2 \text{ s}^{-1}$ [16].

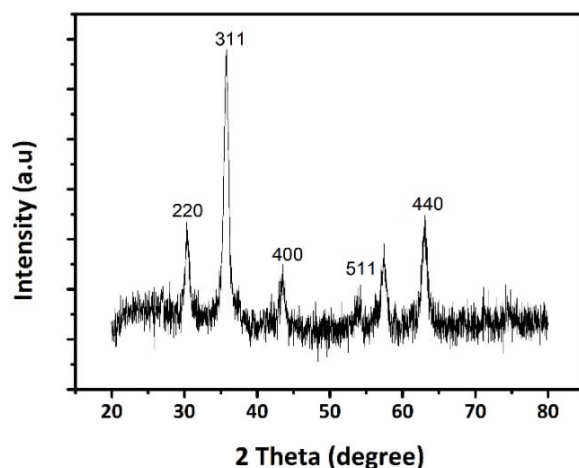


Figure S7: (A) XRD pattern of maghemite nanoparticles.

5. Mechanism of carbon sphere formation.

The water-soluble galactose can be attributed to the hydrophilicity of the resin solution due to the presence of oxygen containing functional groups formed from the sugars present in apricot sap. FeMNPs has the affinity to electrostatically bind to the negatively charged oxygen functional groups carbonaceous colloids [17]. During the polymerisation and carbonisation process of galactose, metal oxide nanoparticles can electrostatically attach to the oxygen functional groups and scattered as metal nanoparticles or metal clusters within the spheres. By collectively analysing the FTIR and Raman results of the annealed products, we can conclude the presence of hydrophilic oxygen groups and hydrophobic graphitic carbons present in the same product. It can be assumed that the mechanism

follows a similar pattern suggested by Sun *et.al* [18] using LaMer model [19] where the spheres were constructed with a hydrophilic shell and a hydrophobic core as shown in Scheme1.

Table S1: Comparison of the performance of GAL-Fe-N towards ORR with other similar carbon-based electro catalysts.

Material	Process	Sphere dimension	Onset over potential (V)	(n)/ Potential (V) RHE	Reference
N-doped mesoporous carbon spheres	Self-polymerisation	200 nm	0.37	3.40 / 0.575	(20)
N-doped hollow carbon spheres	Pyrolysis	400-700 nm	0.43	3.82 / 0.575	(21)
N-doped carbon spheres	Spray pyrolysis	130 – 500 nm	-	3.86/ 0.625	(22)
N-CNT	Pyrolysis	-	0.35	3.70 – 3.90/	(23)
Integrated 3-d N-doped carbon sphere with CNT (GAL-Fe-N)	pyrolysis	1-6 μ m	0.31	0.600 - 0.700 3.55 / 0.600	This study

6. References

1. V. Datsyuk, V.; Kalyva, M.; Papagelis, K.; Parthenios, J.; Tasis, D.; Siokou, A.; Kallitsis, I.; Galiotis, C. Chemical oxidation of multiwalled carbon nanotubes. *Carbon*. **2008**, *46*, 833.
2. S. R. Ahmad, S. R.; Young, R. J.; Kinloch, I. A. Raman spectra and mechanical properties of graphene/polypropylene nanocomposites. *Int. J. Chem. Eng. and Appl.* **2015**, *6*, 1.
3. Graf, D.; Molitor, F.; Ensslin, K.; Stampfer, C.; Jungen, A.; Hierold, C.; Wirtz, L. Spatially Resolved Raman Spectroscopy of Single- and Few-Layer Graphene. *Nano Lett.* **2007**, *7*, 238.
4. Yoon, D.; Moon, H.; Cheong, H.; Choi, J. S.; Choi, J. A.; Park, B. H. J. Variations in the Raman Spectrum as a Function of the Number of Graphene Layers. *Korean Phys. Soc.* **2009**, *55*, 1299.
5. Pimenta, M.; Dresselhaus, G.; Dresselhaus, M.S.; Cancado, L.; Jorio, A.; Saito, R. Studying disorder in graphite-based systems by Raman spectroscopy. *Phys. Chem. Chem. Phys.* **2007**, *9*, 1276.
6. Schwan, J.; Ulrich, S.; Batori, V.; Ehrhardt, H.; Silva, S. Raman spectroscopy on amorphous carbon films. *J. Appl. Phys.* **1996**, *80*, 440.
7. Suryawanshi, A.; Mhamane, D.; Nagane, S.; Patil, S.; Aravindan, V.; Ogale, S.; Srinivasan, M. Indanthrone derived disordered graphitic carbon as promising insertion anode for sodium ion battery with long cycle life. *Electrochim. Acta.* **2014**, *146*, 218.
8. Ma, X.; Yuan, C.; Liu, X. Mechanical, microstructure and surface characterizations of carbon fibers prepared from cellulose after liquefying and curing. *Materials.* **2013**, *7*, 75.
9. Khalfaoi, M.; Knani, S.; Hachicha, M.; Lamine, A. B. New theoretical expressions for the five adsorption type isotherms classified by BET based on statistical physics treatment. *J. Colloid Interface Sci.* **2003**, *263*, 350.
10. Elumalai, E. K.; Kayalvizhi, K.; Silvan, S. Coconut water assisted green synthesis of silver nanoparticles. *J. Pharm. Bioallied Sci.* **2014**, *6*, 241.
11. Chen, J.; Xia, N.; Zhou, T.; Tan, S.; Jiang, F.; Yuan, D. Mesoporous carbon spheres: Synthesis, characterization and supercapacitance. *Int. J. Electrochem. Sci.* **2009**, *4*, 1063.
12. Wang, H.; Hao, Q.; Yang, X.; Lu, L.; Wang, X. Graphene oxide doped polyaniline for supercapacitors. *Electrochem. Commun.* **2009**, *11*, 1158.

13. Liang, Y.; Li, Y.; Wang, H.; Zhou, J.; Wang, J.; Regier, T.; Dai, H. Co₃O₄ nanocrystals on graphene as a synergistic catalyst for oxygen reduction reaction. *Nat.Mater.* **2011**, 10, 780.
14. Damjanovic, A.; Genshaw, M. A.; Bockris, J. O. Distinction between Intermediates Produced in Main and Side Electrode Reactions. *J. Chem. Phys.* **1966**, 45, 4057.
15. Hsueh, K. L.; Chin, D. T.; Srinivasan, S. Electrode kinetics of oxygen reduction: A theoretical and experimental analysis of the rotating ring-disc electrode method. *J. Electroanal. Chem. Interfacial Electrochem.* **1983**, 153, 79.
16. Muthukrishnan, A.; Nabae, Y.; Chang, C. W.; Okajima, T.; Ohsaka, T. A high-performance Fe and nitrogen doped catalyst derived from diazoniapentaphene salt and phenolic resin mixture for oxygen reduction reaction. *Catal. Sci. Tech.* **2015**, 5, 1764.
17. Yu, G.; Sun, B.; Pei, Y.; Xie, S.; Yan, S.; Qiao, M.; Fan, K.; Zhang, X.; Zong, B. Fe x O y@ C spheres as an excellent catalyst for Fischer– Tropsch synthesis. *J. Am. Chem. Soc.* **2009**, 132, 935.
18. Sun, X.; Li, Y. Colloidal carbon spheres and their core/shell structures with noble-metal nanoparticles. *Angew. Chem. Int. Ed.* **2004**, 43, 597.
19. Mer, V. K. L. Nucleation in Phase Transitions. *Ind. Eng. Chem.* **1952**, 44, 1270.
20. J.Tang, J. Liu, C. Li, Y. Li, M.O. Tade, S. Dai and Y. Yamauchi, Synthesis of Nitrogen-Doped Mesoporous Carbon Spheres with Extra-Large Pores through Assembly of Diblock Copolymer Micelles. *Angew. Chem. Int. Ed.* **2015**, 54, 588.
21. Y.Li, T. Li, M.Yao and S. Liu, Metal-free nitrogen-doped hollow carbon spheres synthesized by thermal treatment of poly (o-phenylenediamine) for oxygen reduction reaction in direct methanol fuel cell applications. *J. Mater. Chem.* **2012**, 22 , 10911.
22. X. Zhou, Z. Yang, H. Nie, Z. Yao, L. Zhang and S. Huang, Catalyst-free growth of large scale nitrogen-doped carbon spheres as efficient electrocatalysts for oxygen reduction in alkaline medium. *J. Power Sources.* **2011**, 196 , 9970.
23. C. Xiong, Z. Wei, B. Hu, S. Chen, L. Li, L. Guo, W. Ding, X. Liu, W. Ji and X. Wang, Nitrogen-doped carbon nanotubes as catalysts for oxygen reduction reaction *J. PowerSources.* **2012**, 215, 216.

CHAPTER 3(b)

Green Synthesis of three-dimensional hybrid N-doped ORR electro catalysts composed of nitrogen doped micro-spherical and nanotubular structures using Apricot Sap

Ramesh Karunakaran

School of Chemical Engineering, University of Adelaide, South Australia 5005, Australia

The chapter is based on the following peer-reviewed article:

R. Karunakaran, C. Coghlan, C. Shearer, D. Tran, Karan Kulati, T. T. Tung, C. Doonan, D. Lolic “Green Synthesis of three-dimensional hybrid N-doped ORR electro catalysts composed of nitrogen doped micro-spherical and nanotubular structures using Apricot Sap” *Materials*, 2018, **11**, 205. (Published)

Statement of Authorship

Title of Paper	Green Synthesis of three-dimensional hybrid N-doped ORR electro catalysts composed of nitrogen doped micro-spherical and nanotubular structures using Apricot Sap
Publication Status	<input checked="" type="checkbox"/> Published <input type="checkbox"/> Accepted for Publication <input type="checkbox"/> Submitted for Publication <input type="checkbox"/> Unpublished and Unsubmitted work written in manuscript style
Publication Details	<i>Materials</i> , 2018, 11 , 205.

Principal Author

Name of Principal Author (Candidate)	Ramesh Karunakaran	
Contribution to the Paper	Under the supervision of D. Losic and Christian Doonan, I developed, designed and conducted the experiments, interpreted, processed the data and wrote the manuscript for submission.	
Overall percentage (%)	80%	
Certification:	This paper reports on the original research I conducted during the period of my Higher Degree by Research candidature and is not subjected to any obligations or contractual agreements with third party that would constrain its inclusion in this thesis. I am the primary author of this paper.	
Signature	Date	15 February 2018

Co-Author Contributions

By signing the Statement of Authorship, each author certifies that:

- the candidate's stated contribution to the publication is accurate (as detailed above);
- permission is granted for the candidate to include the publication in the thesis; and
- the sum of all co-author contributions is equal to 100% less the candidate's stated contribution.

Name of Co-Author	Tran Thanh Tung	
Contribution to the Paper	I helped Ramesh Karunakaran (candidate) with interpreting experimental results and improving the manuscript for submission. I give consent for Ramesh Karunakaran to present this paper for examination towards the Doctorate of Philosophy.	
Signature	Date	15 February 2018

Name of Co-Author	Cameron Sherear		
Contribution to the Paper	I conducted the XPS analysis and interpreted the results for Ramesh Karunakaran. I give consent for Ramesh Karunakaran to present this paper for examination towards the Doctorate of Philosophy.		
Signature		Date	15 February 2018

Name of Co-Author	Diana Tran		
Contribution to the Paper	I helped Ramesh Karunakaran with designing experiments and improving the manuscript for submission. I give consent for Ramesh Karunakaran to present this paper for examination towards the Doctorate of Philosophy.		
Signature		Date	15 February 2018

Name of Co-Author	Karan Gulati		
Contribution to the Paper	I aided Ramesh Karunakaran to conduct SEM analysis and interpret SEM the images. I give consent for Ramesh Karunakaran to present this paper for examination towards the Doctorate of Philosophy.		
Signature		Date	15 February 2018

Name of Co-Author	Campbell Coghlan		
Contribution to the Paper	I acted as the secondary supervisor for Ramesh Karunakaran and helped him to design the experiments and improve the final draft of the manuscript for submission. I give consent for Ramesh Karunakaran to present this paper for examination towards the Doctorate of Philosophy.		
Signature		Date	15 February 2018

CHAPTER 3(b): R. Karunakaran, C. Coghlan, C. Shearer, D. Tran, Karan Kulati, T. T. Tung, C. Doonan, D. Losic "Green Synthesis of three-dimensional hybrid N-doped ORR electro catalysts composed of nitrogen doped micro-spherical and nanotubular structures using Apricot Sap" *Materials*, 2018, **11**, 205. **(Published)**

Name of Co-Author	Christian Doonan		
Contribution to the Paper	I acted as the secondary supervisor for Ramesh Karunakaran and aided in design and development of experiment and evaluation of manuscript for submission. I give consent for Ramesh Karunakaran to present this paper for examination towards the Doctorate of Philosophy.		
Signature		Date	15 February 2018

Name of Co-Author	Dusan Losic		
Contribution to the Paper	I acted as the Primary supervisor for Ramesh Karunakaran and aided in design and development of experiment and evaluation of manuscript for submission. I give consent for Ramesh Karunakaran to present this paper for examination towards the Doctorate of Philosophy.		
Signature		Date	15 February 2018



Article

Green Synthesis of Three-Dimensional Hybrid N-Doped ORR Electro-Catalysts Derived from Apricot Sap

Ramesh Karunakaran ¹, Campbell Coghlan ², Cameron Shearer ³ , Diana Tran ¹ , Karan Gulati ¹, Tran Thanh Tung ¹, Christian Doonan ² and Dusan Losic ^{1,*}

¹ School of Chemical Engineering, University of Adelaide, Adelaide, SA 5005, Australia; ramesh.karunakaran@adelaide.edu.au (R.K.); diana.tran@adelaide.edu.au (D.T.); k.gulati@griffith.edu.au (K.G.); tran.tung@adelaide.edu.au (T.T.T.)

² School of Chemistry, University of Adelaide, Adelaide, SA 5005, Australia; cam.coghlan@adelaide.edu.au (C.C.); christian.doonan@adelaide.edu.au (C.D.)

³ School of Chemical and Physical Sciences, Flinders University, Adelaide, SA 5042, Australia; cameron.shearer@flinders.edu.au

* Correspondence: dusan.losic@adelaide.edu.au; Tel.: +61-8-8013-4648

Received: 10 January 2018; Accepted: 26 January 2018; Published: 28 January 2018

Abstract: Rapid depletion of fossil fuel and increased energy demand has initiated a need for an alternative energy source to cater for the growing energy demand. Fuel cells are an enabling technology for the conversion of sustainable energy carriers (e.g., renewable hydrogen or bio-gas) into electrical power and heat. However, the hazardous raw materials and complicated experimental procedures used to produce electro-catalysts for the oxygen reduction reaction (ORR) in fuel cells has been a concern for the effective implementation of these catalysts. Therefore, environmentally friendly and low-cost oxygen reduction electro-catalysts synthesised from natural products are considered as an attractive alternative to currently used synthetic materials involving hazardous chemicals and waste. Herein, we describe a unique integrated oxygen reduction three-dimensional composite catalyst containing both nitrogen-doped carbon fibers (N-CF) and carbon microspheres (N-CMS) synthesised from apricot sap from an apricot tree. The synthesis was carried out via three-step process, including apricot sap resin preparation, hydrothermal treatment, and pyrolysis with a nitrogen precursor. The nitrogen-doped electro-catalysts synthesised were characterised by SEM, TEM, XRD, Raman, and BET techniques followed by electro-chemical testing for ORR catalysis activity. The obtained catalyst material shows high catalytic activity for ORR in the basic medium by facilitating the reaction via a four-electron transfer mechanism.

Keywords: oxygen reduction reaction (ORR); catalysis; carbon nanotubes; carbo microsphere; N-doped carbon

1. Introduction

The continued rise in global energy demand and the depletion of the world's non-renewable resources has initiated a global push towards renewable energy sources. Among the most promising methods for producing renewable energy are fuel cells, which have emerged as a promising avenue of research due to their ability to generate high power density [1]. Fuel cells are devices that electrochemically combine gaseous fuel (e.g., hydrogen) and an oxidant gas (e.g., oxygen) to produce electricity and heat by an oxygen reduction reaction (ORR) [1]. The efficiency of fuel cells and their practical applicability is dependent on the ORR catalyst present in the cell [2]. However, slow kinetics have hindered fuel cells from being utilised outside of a laboratory environment [3]. Currently,

platinum (Pt) catalysts have outperformed all other catalysts in areas such as activity, stability, and selectivity [4] and have dominated the fuel cell industry as the preferred ORR catalysts [5–7]. However, these catalysts have been overlooked for industrial scale-up due to their high cost and low availability [8]. To overcome this problem, non-precious transition metals (Fe, Co, Ni) in addition to hetero atoms have been trialed to enhance the ORR activity [9–13]. The transition metals have the ability to significantly increase ORR catalytic activity by facilitating the incorporation of hetero atoms, such as nitrogen, in the carbon matrix during pyrolysis [14–17]. The incorporation of electro-negative nitrogen into a graphitic carbon framework has shown to induce high positive charge density on adjacent carbon atoms [18]. The electron donor properties of nitrogen-doped adjacent carbon atoms trigger a favourable diatomic O₂ adsorption and ultimately weaken the O₂ bond strength to facilitate ORR activity [15,18–21].

The high electrical conductivity of the mesoporous carbon materials [22] and their metal oxide hybrids has been utilised in applications such as lithium-ion batteries [23,24], super capacitors [25,26], and catalysts [27–29] in recent years. Various chemical approaches have been developed to synthesise nitrogen-doped carbon materials for ORR catalysis utilising materials such as graphene [30] and carbon nanotubes (CNTs) [31]. Carbon materials doped with nitrogen precursors, such as melamine (C₃H₆N₆) [32,33], ethylene diamine (C₂H₄(NH₂)₂) [34], o-phenylenediamine (C₆H₈N₂) [11], and ammonia (NH₃) [35], have shown high ORR activity. Mesoporous N-doped carbon spheres synthesised using multiple different methods, such as the one-pot soft template method [22], spray pyrolysis [36,37], and self-polymerisation [38], each show outstanding catalytic potential for ORR catalysis. However, high cost, hazardous chemical usage and waste has limited their translation into scale-up industrial applications [22,36–38].

To address this problem, green chemistry approaches using low-cost natural materials to synthesise mesoporous carbon (e.g., plant *Typha orientalis* [39], catkin [40], lignin [41], and soya chunks [42]) have been successfully demonstrated as efficient ORR catalysts. Apricot trees (*Prunus armeniaca* L.) are widely cultivated in areas where a scarcity of water remains the main obstacle for cultivation [43]. In many regions, apricot trees suffer from gummosis, a bark disease [44] resulting in the formation of sap which oozes out from the wounds caused from factors including weather, infection, insects, or mechanical damage. The sap commonly appears as an amber-coloured material, which contains various sugar components, such as xylose, arabinose, rhamnose, glucose, mannose, and galactose [45]. Analysis performed by Lluveras et al. [45] revealed that apricot sap consists of polysaccharides, primarily arabinose and galactose. Polysaccharides, such as galactose, glucose, sucrose, and starch, have been shown to undergo dehydration and subsequent aromatisation when hydrothermally treated at 160–200 °C, resulting in their conversion to char material with nano- or micrometer-size smooth carbon spheres [27,46].

Carbon microspheres (CMS) have recently attracted attention due to their unique applications, high density, and high strength in carbon product fabrication [47]. Carbon-spheres synthesised using polysaccharides have successfully been implemented in the application of catalysis for synthetic fuel [27], Li-ion batteries [48], and electrochemical capacitors [49]. Previously, hybrid CMS containing transition metals have been synthesised using polysaccharides [27,46]. The ability of the iron oxides to bind with the oxygen functional groups in the sugar molecules through coulombic and/or electrostatic interactions has resulted in the formation of iron oxide encapsulated carbon spheres [27]. Similar hybrid materials can be synthesised using the polysaccharides present in apricot sap, which have not been used for any catalytic application in the past.

This work explores the use of apricot sap containing sugar molecules as a natural source and method for the generation of a new type of three-dimensional (3D) hybrid N-doped ORR electro-catalysts composed of microspherical and nanotubular structures. These catalysts were synthesised through a three-step process as shown in Scheme 1. Firstly, an apricot sap resin suspension containing polysaccharides of arabinose and galactose was prepared. Secondly, the apricot resin solution was hydrothermally treated with iron oxide nanoparticle or cobalt precursors to obtain a char

material with carbon microspheres embedded with magnetic nanoparticles. Finally, the char material was pyrolysed (950 °C) with a nitrogen precursor of melamine to dope the graphitic carbons with nitrogen. The pyrolysed composite material forms an integrated composite material with both carbon fibers (CFs) and CMS. A similar integrated structure was reported in our previous paper, where we hypothesised that the decomposition of melamine during pyrolysis causes disruption to the iron oxide magnetic nanoparticle clusters' (FeMNP) surface that is embedded in the carbon sphere to diffuse FeMNP particles out of the sphere to catalyse the formation of N-doped carbon fibers (N-CFs) [50]. This hybrid carbon catalyst contains N-CFs and N-doped carbon microspheres (N-CMS) with magnetic nanoparticles, forming a unique 3D intergrated morphology.



Scheme 1. Schematic procedure of three-dimensional (3D)-integrated N-doped carbon microspheres (CMS) and N-doped carbon fibers N-CFs catalysts from apricot sap. (A) Apricot sap collected from the apricot tree; (B) apricot sap dissolved in water (apricot resin suspension); (C) apricot resin suspension containing FeMNP, hydrothermally treated to produce magnetic insoluble char material (carbonised resin) with FeMNP embedded CMS structures (HT-APG-Fe); and (D) HT-APG-Fe pyrolysed with melamine to form N-doped integrated structures containing N-CFs and N-CMS (N-APG-Fe). FeMNP: iron oxide magnetic nanoparticle.

The structural and chemical composition of the prepared N-doped 3D integrated catalyst with FeMNPs (N-APG-Fe) and cobalt nanoparticle clusters (CoMNPs) (N-APG-Co) were characterized with SEM, TEM, XRD, Raman, and BET followed by testing their electrochemical catalytic properties and ORR activity. The conversion process of the naturally occurring waste and apricot sap material into an effective electro-catalyst for ORR reaction is also described.

2. Results and Discussion

2.1. Formation of Integrated Morphology of N-CFs and N-CMS

The steps involved in the synthesis of N-APG-Fe are shown in Scheme 1. In the first step, apricot sap (Scheme 1A) was dissolved in water (70 °C) to make a translucent light-orange colour resin suspension (Scheme 1B). In the second step, the resin suspension was hydrothermally treated in the presence of FeMNPs. During this process, the oxygen functional groups (i.e., OH and C=O) bind to the iron oxide particles through Coulombic interactions to form a hybrid material [27]. During the hydrothermal process (Scheme 1(Ca)), sugar molecules polymerise (Scheme 1(Cb)) to

form intermolecular crosslinks between linear or branched oligosaccharides due to dehydration [46]. As a result of dehydration and polymerisation, oxygen functional groups associated with the sugar molecules were reduced along with their negative charges to make the polymerised material more water-insoluble. Subsequently, the insoluble material (char) settles as FeMNPs-embedded spheres with a hydrophobic core and hydrophilic shell [46,51,52] (Scheme 1(Cc)). In the final process, the hydrothermally obtained char is pyrolysed in the presence of melamine at 950 °C to introduce N atoms into the carbon framework. The pyrolysed composite material forms an integrated composite material with both N-CF and N-microspheres (Scheme 1D). During pyrolysis, the decomposition of melamine caused disruption to the spheres' surface and caused the FeMNPs embedded within the sphere to diffuse out [50], which catalysed the formation of N-CF [53]. The synthesised hybrid material, which consists of both N-CF and N-CMS, formed a unique 3D integrated morphology.

2.2. Structural and Chemical Characterisation of Prepared 3D N-Doped Carbon Composites

The morphology of the hydrothermally induced char material (HT-APG-Fe) was determined using SEM (Figure 1), which shows the formation of carbon microspheres (1–6 μm). The image of a broken sphere (Figure 1A, inset) shows FeMNPs embedded within the microspheres. EDX analysis conducted on the particles (Figure S1 in supporting information (SI)) indicated that an average of 57% (wt %) of the material consisted of Fe, confirming the presence of FeMNPs in the carbon sphere. The magnetic property of the material was confirmed by applying an external magnet to the sample.

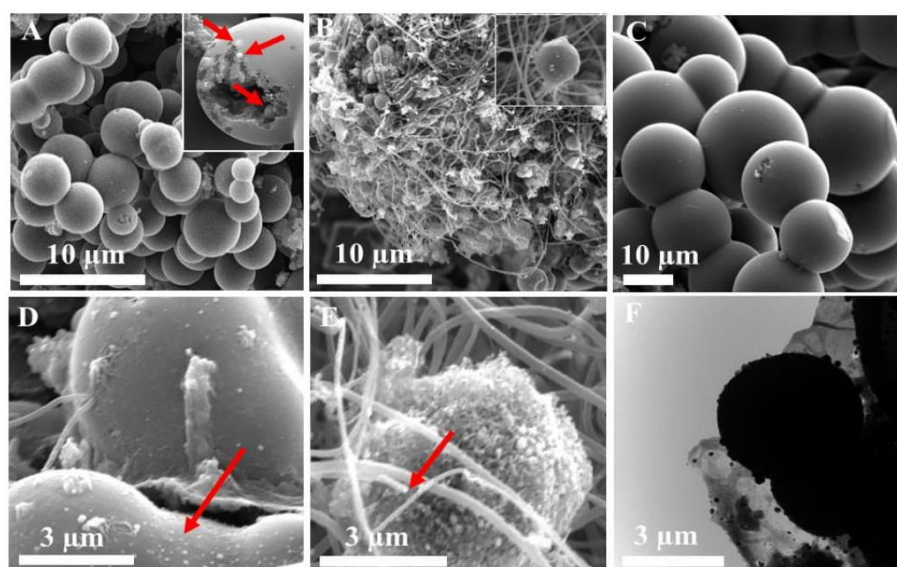


Figure 1. SEM images of (A) carbon microspheres formed from char material of hydrothermally treated apricot resin (HT-APG-Fe), (B) integrated structure composed of CMS and CFs of HT-APG-Fe pyrolysed with melamine at 950 °C (N-APG-Fe) (inset shows the presence of micro spheres and CFs), (C) carbon micro spheres of HT-APG-Fe pyrolysed without melamine at 950 °C (APG-Fe), (D) formation of CFs from FeMNP from the sphere interior of N-APG-Fe (red arrow shows FeMNP diffused out of the sphere after pyrolysis with melamine), (E) formation of CF from FeMNP diffused out of the sphere in N-APG-Fe (red arrow shows the CF forming from the tip of FeMNP), and (F) TEM image of FeMNP diffused out of the sphere in N-APG-Fe.

In order to make HT-APG-Fe catalytically active, it was pyrolysed with a N precursor (melamine) (N-APG-Fe) at 950 °C to introduce N atoms into the carbon framework and improve catalytic properties (Figure 1B). The nitrogen doping eliminates the electro-neutrality of the carbon framework and

generates favourable charged sites for oxygen adsorption [19,54]. Similarly, to compare the catalytic activity of the N-doped and non N-doped catalysts, HT-APG-Fe was pyrolysed without melamine (APG-Fe) at 950 °C and the SEM image is presented in Figure 1C. The SEM revealed that APG-Fe formed interconnected smooth microspheres in the range of 1–6 μm. Interestingly, in contrast to the smooth CMS formed in APG-Fe (Figure 1C), the catalysts pyrolysed with melamine (N-APG-Fe) (Figure 1B) formed an integrated composite material with both CF and CMSs. EDX analysis was performed to determine the N-doping on CMS and CF and revealed an average of 2.55 and 2.04 (At %) of N presented in the CMS and the CF, respectively. During pyrolysis, the decomposition of melamine causes disruption to the FeMNPC's surface that is embedded in the carbon sphere for the FeMNPC particles to diffuse out of the sphere and form N-CFs (Figure 1D,F).

To demonstrate if this synthetic procedure is generic for the formation of 3D integrated N-CMS and N-CF structures, we repeated the procedure using cobalt precursors, which is commonly used as an alternate transition metal to fabricate ORR catalysts. The SEM images of the hydrothermally produced structures (Figure S2A), pyrolysed with and without melamine (Figure S2B,C), respectively, revealed that integrated structures with carbon spheres and CFs, similar to N-APG-Fe, were produced when the hydrothermally reduced char materials containing cobalt oxide nanoparticles were pyrolyzed with melamine. The hydrothermally produced char material without any nanoparticles (HT-APG, Figure S3A), when pyrolysed with melamine (Figure S3B), did not produce any integrated products of CMS and CFs. As the integrated structures were only seen on the catalysts with transition metals (Figures 1B and S2B in SI), we deduce that both a transition metal oxide and a nitrogen precursor are needed for the synthesis of the integrated structure comprised of both N-CMS and N-CFs. Previously, we reported a 3D integrated structure of N-CMS and N-CFs using sugar galactose (N-GAL-Fe) [50]. A similar morphology was observed in N-APG-Fe, which demonstrates that the presence of galactose in the apricot sap also contributes significantly to the formation of the integrated structure.

The morphologies of N-CF in N-APG-Fe and N-APG-Co (Figure 2A,B) were further investigated with TEM. The images clearly illustrate that the N-CFs originate from the tip of the MNPC. An EDX analysis was conducted on the particles at the tip of the CF (Figure 2A,B) and revealed 59.20% and 18.50% (wt.%) of Fe and Co, respectively, suggesting that the CFs are formed by a metal-induced mechanism [53]. The TEM images of CF from N-APG-Fe (Figure 2C) and N-APG-Co (Figure 2D) show that the CFs possess an irregular corrugated morphology with a width of approximately 150–500 nm, similar to those reported by M. Terrones et al. [55]. To investigate the presence of N-doping on these CFs (which facilitate ORR) [31], an EDX elemental analysis was performed on CFs grown from Fe (Fe-CF) and Co (Co-CF). The N-content was found to be 2.04 and 6.32 At. % for Fe-CF and Co-CF, respectively, compared to 0% in the non-doped sample, confirming nitrogen doping on CF. This reveals that C and N precursors from pyrolysed melamine had diffused into the metal clusters to form the CF [53,56].

The XRD analysis conducted on N-APG, APGFe-N, and APGCo-N is shown in Figure 3A. The diffraction peaks seen at 25.78°, 42.66°, and 44.83° for APGFe-N and APGCo-N correspond to diffraction facets (002), (110), and (101), respectively, assigned to the presence of graphitic carbon [57–59]. Similarly, N-APG showed peaks at 23.96°, 42.53°, and 44.67° for diffraction facets (002), (110), and (101), respectively. The positive shift of the (002) peak of N-APG from 23.96° to 25.78° in N-APG-Fe and N-APG-Co can be assigned to the formation of the graphitic crystalline structure induced by the reduction of the oxygen functional group containing sugar molecules with a metal MNPC [60].

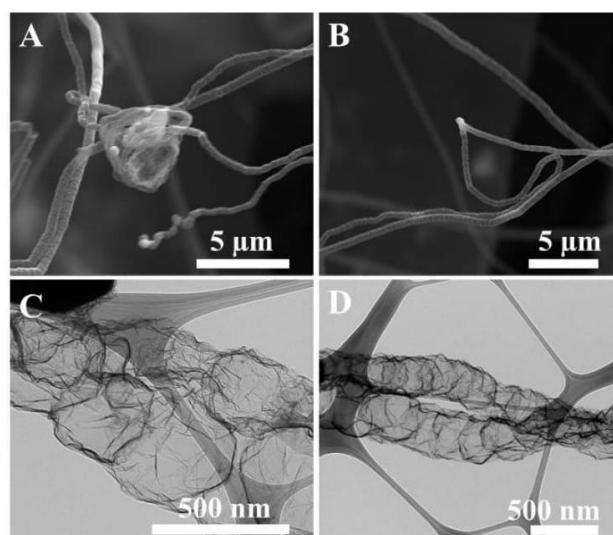


Figure 2. SEM images of N-CF obtained from (A) N-APG-Fe and (B) N-APG-Co. TEM image of (C) N-APG-Fe and (D) N-APG-Co.

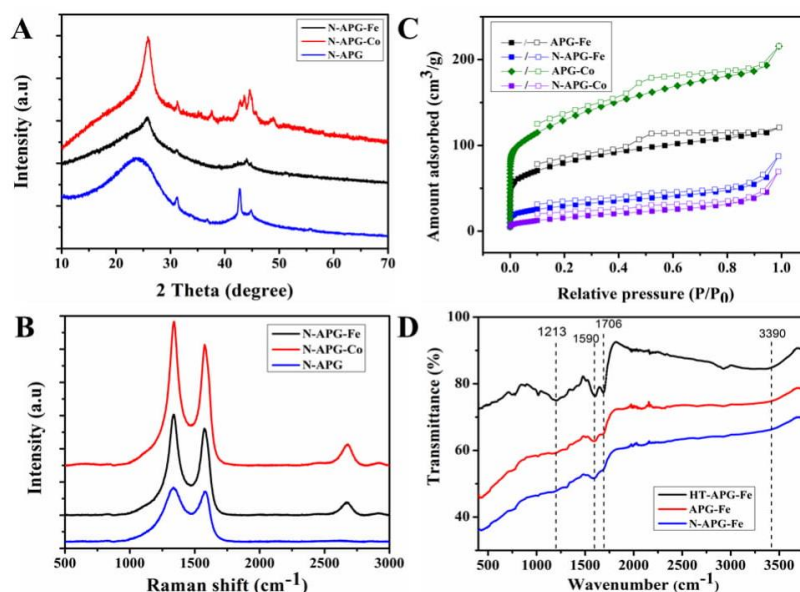


Figure 3. (A) XRD spectrum of N-APG, N-APG-Fe, and N-APG-Co, (B) Raman spectrum of N-APG, N-APG-Fe, and N-APG-Co, (C) N₂ adsorption/desorption isotherm of APG-Fe, N-APG-Fe, N-APG-Co, and N-APG-Co, (D) FTIR spectrum of HT-APG-Fe, APG-Fe, and N-APG-Fe.

The Raman spectrum performed on N-APG, N-APG-Fe, and N-APG-Co is shown in Figure 3B. N-APG-Fe and N-APG-Co show three characteristic peaks at 1342, 1581, and 2684 cm^{-1} for the D, G, and 2D bands, respectively, while N-APG showed only the D and the G band at 1338 and 1583 cm^{-1} , respectively. The additional 2D band indicates the presence of crystalline graphitic carbon material formed during the annealing process. This was facilitated by the reduction of oxygen groups in the sugar molecules by the addition of FeMNPC [61,62]. The I_D/I_G of N-APG (1.07), N-APG-Fe (1.16),

and N-APG-Co (1.13) shows the disruption of sp^2 bonds and the formation of sp^3 defect sites [63,64], which are associated with the N-doping on the carbon framework. The higher I_D/I_G for N-APG-Fe and N-APG-Co compared to N-APG revealed that the transition metal particles have facilitated the incorporation of N atoms to the carbon framework to distort the graphitic framework [15,65]. This shows that the addition of transition metals formed greater positive sites on the adjacent carbon atoms to adsorb oxygen, thus enhancing the ORR activity.

The N_2 sorption isotherms of non-doped APG-Fe and APG-Co differ from the doped N-APG-Fe and N-APG-Co (Figure 3C). The characteristic type IV isotherm and H4 hysteresis loop for APG-Fe and APG-Co shows the presence of mesoporous slip-like pores [62,66,67] with mean pore size distributions of 4.64, 5.62, 7.68, and 13.84 Å (Figure S4). The surface area of the prepared catalysts was measured using Brunauer-Emmett-Teller (BET) and is shown in Table 1. The surface area measured for the doped catalysts was much lower than that of the non-doped catalysts. We hypothesise that the mesopores on the surface of the carbon microspheres on the non-doped catalysts contributed to the higher surface area. The significant reduction in the surface area of the doped sample can be assigned to the disruption of these mesopores or blocked pores due to the decomposition of melamine during pyrolysis.

Table 1. Surface area of doped and non-doped apricot catalysts with Fe and Co.

Catalyst	Surface Area (m^2/g)
APG-Fe	235.38
N-APG-Fe	73.15
APG-Co	375.62
N-APG-Co	39.86

The presence of any carbonyl groups was analysed by FTIR, which can form condensation products with melamine. The FTIR spectra of hydrothermally treated (HT-APG-Fe), pyrolysed without melamine (APG-Fe), and N-doped (N-APG-Fe) materials are presented in Figure 3D. HT-APG-Fe showed characteristic peaks at 1213, 1590, 1706, and 3390 cm^{-1} [68–70], which can be attributed to C-O and C-H stretching, the stretching vibration of C=O, carbonyl vibrations, and the stretching vibration of O-H, respectively. The presence of oxygen functional groups suggests that the carbon spheres were formed with a hydrophilic shell containing oxygen groups as suggested by Sun et al. [46] and Mer et al. [54]. When the peaks corresponding to the carbonyl groups of doped N-APG-Fe and non-doped APG-Fe were compared, a reduction of the intensity of the N-APG-Fe was observed. Since carbonyl groups can interact with the amine group of melamine [71], we hypothesised that the melamine was attached to the carbon spheres before undergoing complete decomposition. It is likely that these condensation products caused surface disruption of the microspheres and studies need to be undertaken to confirm this hypothesis.

XPS measurements were performed to determine the nitrogen species present in the N-APG-Fe catalyst. The high-resolution XPS C 1s spectrum (Figure S5) showed a variety of carbon bonds, including C-C (285.04 eV), C-N (286.03 eV), and O-C=O (290.03 eV) [72–74]. The high-resolution N 1s XPS spectra displayed in Figure S5B showed three distinct peaks, including pyridine-N (398.38 eV), graphitic-N (401.35 eV), and nitrogen oxide-N (403.12 eV) [75,76]. The high percentage (45.57 At. %) of pyridinic N (in the N1s analysis) along with 63.03 At. % of C-N (in the C1s analysis) in N-APG-Fe clearly demonstrates efficient N-doping on the carbon framework to facilitate O_2 adsorption. Similar peaks for C 1s and N 1s were observed for N-APG-Co (Figure S6). The N-doping on the graphitic carbon framework altered the electro-neutrality of the nano-carbon material. The pyridinic nitrogen with its strong electronic affinity induced high positive charge density on the adjacent carbon atoms. Thus, the electron donor properties of the N-doped adjacent carbon atoms are favourable for weakening the strength of the O-O bond to facilitate ORR activity [2,19,77]. However, the XPS analysis did not show any presence of Fe or Co. This showed that Fe-N-C sites were not formed and only N-C carbon has been formed.

2.3. Electrochemical Characterisation of Catalytic Performance

The electrochemical activity of N-doped (N-APG, N-APG-Fe, and N-APG-Co) catalysts were examined by cyclic voltammetry (CV) (Figure S7). The voltammograms between 0 and 1.2 V show well-defined cathodic peaks centered at 0.55, 0.67, and 0.74 V, respectively. The voltammograms of N-APG-Fe and N-APG-Co showed a higher positive overpotential shift, 120 and 190 mV, respectively, compared N-APG. These results indicate that the hybrid structures of N-CF and N-CMS formed by the introduction of Fe and Co have aided to increase ORR activity and O₂ uptake. Since the XPS did not detect any Fe-N-C active sites, these enhancements of ORR activity can be attributed to N-C catalytic sites merely in both the N-CF and N-CMS in the hybrid structure in N-APG-Fe and N-APG-Co.

To understand the reaction kinetics of N-APG, N-APGFe and N-APGCo, Rotating Ring Disc Electrode(RRDE) was employed to quantify the overall electron transfer number (n) and percentage of hydrogen peroxide (% HO₂⁻). To explore the dependence on galactose sugar in the electron transfer kinetics, N-GAL-Fe was contrasted against these catalysts in the potential range between 0.10–1.15 V and the ring (Figure 4A) and disc (Figure 4B) currents. The onset potential measured for these catalysts (Table 2) showed a positive shift for N-APG-Fe (0.88 V) and N-APG-Co (0.86 V) compared to N-APG (0.84 V), revealing that the hybrid structures have initiated the ORR faster. However, the half-wave potential (E_{1/2}) of all of these catalysts shifted negatively compared to the standard Pt/C. The negative shift in the E_{1/2} is due to the absence of any M-N-C catalytic active sites present in the catalysts. Liu et al. [78] described that M-N-C active sites perform the ORR reaction with a more positive E_{1/2} compared to N-C active sites in the catalysts.

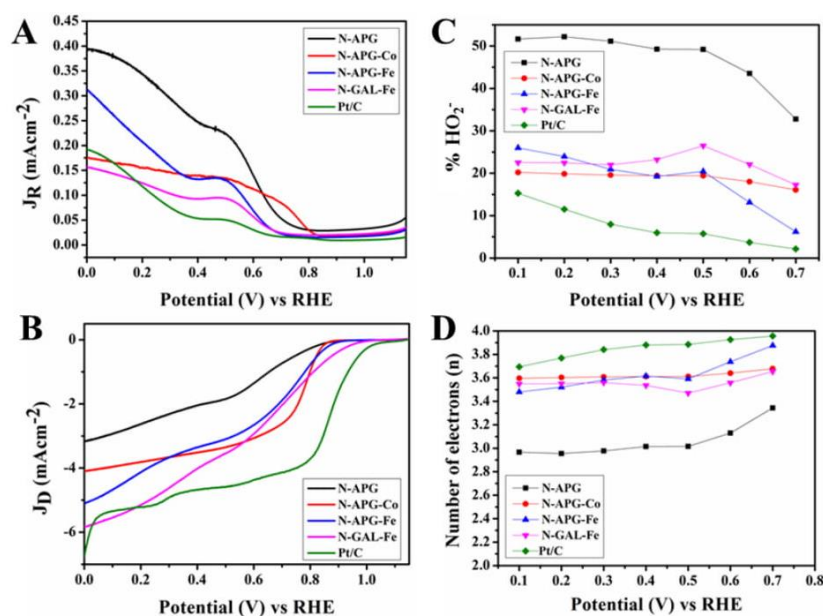


Figure 4. Rotating ring disc voltammograms of (A) ring current, (B) disc current of N-APG, N-APG-Co, N-APG-Fe, N-GAL-Fe, and Pt/C electrodes in oxygen-saturated 0.10 M KOH at 2000 rpm at a scan rate of 10 mV/s. (C) Percentage HO₂⁻ and (D) number of electrons of N-APG, N-APG-Fe, N-APG-Co, and Pt/C electrodes at various potential calculated according to RRDE data. RHE: reversible hydrogen electrode

Table 2. Surface area of doped and non-doped apricot catalysts with Fe and Co.

Product	Current density (mA/cm ²) at 0 V (RHE)	Onset Potential (RHE) (V)	Number of Electrons (n) (0.10–0.70 V) (RHE)	% HO ₂ ⁻ (0.10–0.70 V) (RHE)
N-APG	3.05	0.84	2.96–3.34	51.64–32.77
N-APG-Co	4.03	0.86	3.59–3.67	20.16–16.08
N-APG-Fe	4.91	0.88	3.48–3.87	25.99–6.19
N-GAL-Fe	5.81	0.96	3.54–3.65	22.54–17.25
Pt/C	6.70	1.04	3.69–3.95	15.20–2.15

The number of electrons transferred using N-APG, N-APG-Co, N-APG-Fe, and N-GAL-Fe catalyst electrodes within the potential region 0.10–0.70 V is shown in Table 2. The electron transfer number towards four of these catalysts reveals that the ORR reaction is carried out predominantly via a four-electron transfer mechanism. The catalytically analysed values and comparison chart of n and % HO₂⁻ at 0.40 V (Figure S8) shows that both of the N-doped apricot and galactose catalysts follow a similar trend, showing the significance of galactose in the electron transfer mechanism. Unlike the doped catalysts, the non-doped catalysts did not perform effectively (Figure S9). The electro-chemical properties summarised in Table S1 in the SI of these catalysts showed a negative onset potential and lower electron transfer numbers than the doped catalysts. This shows that the doping of nitrogen has created more catalytically active sites for ORR. The stability of the N-APG-Co and N-APG-Fe was determined by cycling the catalysts between 0.00 V and 1.15 V at 100 mV s⁻¹ in an oxygen-saturated 0.1 M KOH solution (Figure S10 in the SI). The results show that after 6000 cycles the onset overpotential had increased by 30 mV and 40 mV for N-APG-Co and N-APG-Fe, respectively, indicating only a slight deterioration of the catalysts.

The kinetics of electron transfer using the details obtained from RRDE and the scheme suggested by Damjanovic et al. [79] are described in the SI. The rate constants were calculated based on these equations for the N-APG, N-APG-Co, N-APG-Fe, and N-GAL-Fe in the potential region of 0.10–0.65 V (Figure S11 in SI). The calculated rate constants showed that N-APG-Co, N-APG-Fe, and N-GAL-Fe were predominantly driven by a four-electron k₁ kinetics, while in N-APG, the ORR was carried out via both the k₁ and k₂ pathways. The calculated value of the ratio of k₁/k₂ presented in Table S2 in the SI and Figure 5 showed k₁/k₂ > 1 for all catalysts. The higher values of k₁/k₂ for N-APG-Co, N-APG-Fe, and N-GAL-Fe compared to N-APG showed a dominant four-electron k₁ electron transfer pathway for these catalysts that demonstrates that the presence of the hybrid structure of N-CF and N-CMS significantly contributes to the generation of the active sites for oxygen adsorption.

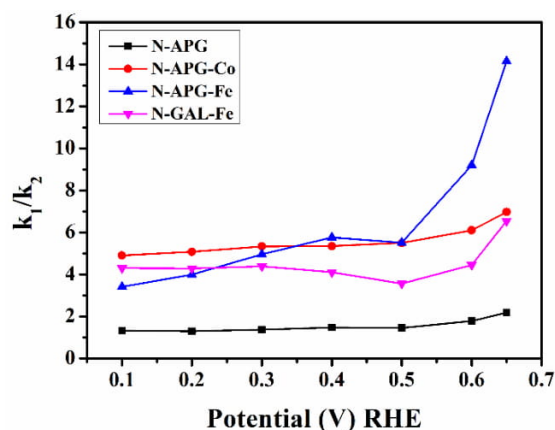


Figure 5. The ratio of rate constant k₁/k₂ for, N-APG, N-APG-Fe, N-APG-CO and N-GAL-Fe in the potential range of 0.10–0.65V.

In order to compare the efficiency of the N-doped apricot catalysts and galactose catalysts, the materials were contrasted against similar catalysts, and the comparison is presented in Table S3 in the SI. The comparison revealed that these catalysts had similar levels of activity compared with other synthetic material presented in the literature. While the performance of these materials is lower than the highest-performing Pt catalysts, the advantages of this approach are the scalable, stable, low-cost, and natural non-hazardous starting materials and the ease of their synthesis. However, the use of apricot sap in industrial large-scale production may be limited by its low yield. Our previous paper demonstrated the synthesis of a similar hydride structure comprising N-CF and N-CMS to fabricate C-N electrodes for ORR using galactose as the source. This approach has the potential to be implemented to synthesise C-N electrodes with similar integrated hybrid structures using natural and synthetic feedstocks containing polysaccharides. Furthermore, the production of efficient ORR catalysts at a lower cost to current catalysts, using natural resources and environment-friendly processes, may provide a step forward for natural products.

3. Materials and Methods

3.1. Materials

Apricot sap from an Apricot Moorpark tree (*Prunus armeniaca*) (South Australia) was collected from a local garden. Iron (II) chloride tetra hydrate ($\text{FeCl}_2 \cdot 4\text{H}_2\text{O}$) (Sigma Aldrich, St Louis, MO, USA), iron (III) chloride hexa hydrate ($\text{FeCl}_3 \cdot 6\text{H}_2\text{O}$) (Chem Supply, Gillman, Australia), hydrochloric acid (HCl) (Chem Supply, Gillman, Australia), ammonia (Chem Supply, Gillman, Australia), cobalt (II) acetate (Sigma Aldrich, St Louis, MO, USA), melamine (Sigma Aldrich, St Louis, MO, USA), and platinum standard catalyst (20 w% Vulcan XC-72) were used as purchased.

3.2. Methods

3.2.1. Synthesis of Carbonaceous Spheres from Apricot Sap (HT-APG)

The apricot sap (cca 100 g) was cut by a knife from a tree. The sap was washed with fresh water and dried in open air for 12 h. The sap (25 g) was dissolved in water (100 mL) and heated to 70 °C with manual stirring. The resin suspension was sealed and left for 24 h in an open environment. The obtained transparent light orange suspension was then filtered to obtain a contaminant-free resin suspension. The resin suspension (50 mL) was transferred in to an autoclave and heated at 180 °C for 18 h. The char was centrifuged and washed with distilled water (6×35 mL). The washed char was then freeze dried for 24 h. The final product weighed 1.62 g.

3.2.2. Synthesis of Cobalt Embedded Carbonaceous Spheres (HT-APG-Co)

Cobalt (II) acetate (150 mg) was dissolved with 50 mL of filtered resin suspension and stirred for 30 min. The product was then transferred to an autoclave and heated for 18 h at 180 °C. The product was cooled to room temperature and transferred in to a centrifuge tube and centrifuged with repeated washing with distilled water for six times (6×35 mL) and four times with 0.5 M H_2SO_4 . The washed char was then freeze-dried for 24 h.

3.2.3. Synthesis of Maghemite Nanoparticles

Maghemite nanoparticles were synthesised according to the previously established method [80]. Briefly, $\text{FeCl}_2 \cdot 4\text{H}_2\text{O}$ (39.76 g) and $\text{FeCl}_3 \cdot 6\text{H}_2\text{O}$ (16.29 g) were dissolved in 1 M HCl (100 mL). The solution was stirred for 2 h and the pH adjusted to 9.8 using 2 M ammonia solution. Finally, the product was centrifuged and washed three times with distilled water (35 mL) and once with ethanol (35 mL) and dried for 6 h at 60–70 °C.

3.2.4. Synthesis of Fe-Embedded Carbonaceous Spheres (HT-APG-Fe)

Maghemite nanoparticles (200 mg) were suspended in the filtered resin suspension (50 mL) and stirred for 30 min, transferred to an autoclave, and heated for 18 h at 180 °C. The product was collected and centrifuged by washing with distilled water (6×35 mL) and four times with 0.5 M H₂SO₄. The product was then freeze-dried for 24 h and denoted as HT-APG-Fe.

3.2.5. Synthesis of Fe-Embedded Carbonaceous Spheres with Galactose (HT-GAL-Fe)

Maghemite nanoparticles (200 mg) were added into a suspension of 0.02 mole galactose in 40 mL water and mixed with stirring for 30 min. The mixture was transferred in to a Teflon autoclave and heated up to 180 °C for 18 h. Then, the product was collected, centrifuged, and repeatedly washed, six times with deionised water and four times with 0.5 M H₂SO₄. The product was collected and freeze-dried for 24 h (referred to as HT-GAL-Fe).

3.2.6. Pyrolysis of Carbonaceous Spheres with N-Precursor (N-Doped Carbon Spheres)

Each of the hydrothermally treated samples HT-APG, HT-APG-Fe, HT-APG-Co, and HT-GAL-Fe were ground together with melamine (1:10 *w/w*) using a mortar and a pestle. The mixture was placed in a tubular furnace and pyrolysed at 950 °C for 3 h under Ar at the rate of 10 °C/min. The N-doped products are referred to as N-APG, N-APG-Fe, N-APG-Co, and N-GAL-Fe, respectively.

3.2.7. Pyrolysis of Carbonaceous Spheres without N-Precursor

Hydrothermally synthesised HT-APG, HT-APG-Fe, HT-APG-Co, and HT-GAL-Fe were individually pyrolysed at 950 °C for 3 h under Ar at the rate of 10 °C/min in the tubular furnace. The pyrolysed products are referred to as APG, APG-Fe, APG-Co, and GAL-Fe, respectively.

3.2.8. Preparation of Catalytic Inks

Catalytic ink was prepared by ultra-sonication of each catalyst (2 mg) and suspended in Nafion suspension (1 mL of 1%). The prepared ink (10 µL) was carefully deposited on a glassy carbon rotating disc electrode (3 mm) and a rotating ring disc electrode (4 mm). The sample was then allowed to dry in air for 12 h.

3.3. Characterization

Scanning electron microscopy (SEM) images and energy-dispersive X-ray spectroscopy (EDX) were obtained using a Quanta 450 (FEI, Hillsboro, OR, USA) at an accelerating voltage of 10 kV. For EDX, three readings were obtained and the average was recorded. Transition electron microscopy (TEM) investigation was carried out using a Tecnai G2 Spirit (FEI, Hillsboro, OR, USA) operated at 120 kV. X-ray diffraction (XRD) was performed at 40 kV and 15 mA in the range of $2\theta = 10\text{--}70^\circ$ at a speed of $10^\circ/\text{min}$ using a Miniflex 600 (Rigaku, Akishima, Tokyo, Japan). Gas adsorption isotherms were conducted using a Micromeritics 3-Flex or ASAP2020 analyser (Micro metrics Instruments Corporation, Norcross, GA, USA). The Brunauer–Emment–Teller (BET) surface area and pore size distribution were calculated using software on the Micromeritics 3-Flex or ASAP 2020 analyser (Beckman Coulter, Indianapolis, IN, USA). Fourier transform infrared (FTIR) spectroscopy was conducted using Spectrum 100 (Perkin Elmer, Waltham, MA, USA). Raman analysis was conducted using a LabRAM Evolution (Horiba Yvon, Kyoto, Japan) using a 532 nm wavelength. XPS was conducted on a custom-built SPECS instrument (Berlin, Germany). All XPS (X-ray photo electron spectroscopy) measurements were performed on sample prepared by drop-casting onto Si using a non-monochromatic Mg source operating at 120 kV and 200 W. High resolution XPS spectra were collected using a pass energy of 10 eV with an energy step of 0.1 eV.

Electrochemical Characterization

The ORR reactions were conducted utilising a Rotating Ring Disc Electrode (RRDE) apparatus connected to a bi potentiostat (CH 1760 C, CH Instruments Inc., Austin, TX, USA) in a standard three-electrode cell with an oxygen-saturated KOH (0.1 mol/L) solution. The glassy carbon electrode, platinum, and reversible hydrogen electrode (RHE) were used as the working, counter, and reference electrodes, respectively. The scan rate of the reaction was 0.01 Vs^{-1} in the range of 0 and 1.1 V. The cycle was repeated until stable voltammograms were obtained before the RRDE readings were derived at different speeds from 400 to 2400 rpm.

The reaction kinetics of the catalysts were examined by employing RRDE to quantify the overall electron transfer number (n) and percentage of hydrogen peroxide ($\% \text{HO}_2^-$) at rotation speeds from 400 to 2400 rpm in an oxygen-saturated 0.1 M KOH solution. To elucidate the overall number of electrons (n) and $\% \text{HO}_2^-$ produced in the ring against the applied potential, Equations (1) and (2) were employed [10,81].

$$n = \frac{4I_D}{I_D + \frac{I_R}{N}} \quad (1)$$

$$\% \text{H}_2\text{O}_2 = 100 \frac{2I_R}{I_D N + I_R} \quad (2)$$

where I_D and I_R are the disc and ring currents, respectively, and N is the collection efficiency.

4. Conclusions

The phenomenon of converting a naturally occurring apricot sap from an apricot tree into a 3D hybrid ORR electro-catalyst composed of N-CF and N-CMS is reported and verified by SEM and TEM. The MNPs initially embedded within the CMS diffused out of the CMS to catalyse for the formation of corrugated hollow N-CF due to the surface destruction caused by the decomposition of melamine during pyrolysis. The 3D integrated N-CMSs and N-CF ORR electro-catalysts prepared using FeNP (N-APG-Fe) or CoNP (N-APG-Co) showed a predominant four-electron transfer pathway for the ORR within the potential region of 0.10–0.70 V. The spherical morphology obtained from non-hazardous apricot sap can be employed in a wide range of areas, such as catalysis applications, absorption studies, and drug delivery.

Supplementary Materials: The following are available online at www.mdpi.com/xxx/s1, Figure S1: EDX analysis of FeMNPC, Figure S2: SEM images of (A) hydrothermally treated apricot sap resin and cobalt acetate (HT-APG-Co), (B) pyrolysed HT-APG-Co at 950 °C with the presence of nitrogen precursor melamine (N-APG-Co), and (C) pyrolysed HT-APG-Co at 950 °C without melamine (APG-Co), Figure S3: SEM images of (A) hydrothermally treated apricot sap resin (HT-APG), (B) pyrolysed HT-APG at 950 °C with the presence of nitrogen precursor melamine (N-APG), and (C) pyrolysed HT-APG at 950 °C without melamine (APG), Figure S4: Pore size distribution of (A) APG-Fe and (B) APG-Co, Figure S5: XPS core level spectra of N-APG-Fe for (A) C1s and (B) N1s, Figure S6: XPS core level spectra of N-APG-Co for (A) C1s and (B) N1s, Figure S7: Cyclic Voltammetry of (A) N-APG, (B) N-APG-Fe, and (C) N-APG-Co at a scan rate of 10 mV/s in oxygen-saturated 0.1M KOH solution, Figure S8: (A) Comparison of number of electrons and (B) $\% \text{HO}_2^-$ of N-APG, N-APG-Co, N-APG-Fe, N-GAL-Fe, and Pt/C catalysts electrodes at 0.4 V applied potential in oxygen-saturated 0.10 M KOH electrolyte at 2000 rpm at a scan rate of 10 mV/s, Figure S9: Rotating ring disc voltammograms of (A) ring current and (B) disc current of catalysts electrodes APG, APG-Co, APG-Fe, GAL-Fe, and Pt/C, pyrolysed without the presence of melamine in oxygen saturated 0.1 M KOH at 2000 rpm at a scan rate of 10 mV/s. (C) Percentage peroxide, and (D) number of electrons of APG, APG-Fe, APG-Co, and Pt/C electrodes at various potential calculated according to RRDE data, Figure S10: RDE polarisation curves of (A) N-APG-Co and (B) N-APG-Fe with a scan rate of 100 mVs^{-1} before and after 6000 potential cycles in an oxygen saturated KOH solution, Figure S11: Rate constants of (A) N-APG, (B) N-APG-Co, (C) N-APG-Fe, and (D) N-GAL-Fe, Table S1: Electro chemical properties of non-doped apricot sap and galactose catalysts, Table S2: Comparison of performance of N-APG-Fe, N-APG-Co, and N-GAL-Fe with other similar carbon-based catalysts.

Acknowledgments: The authors are thankful for the support of the Australian Solar Thermal Research Initiative (ASTRI), ARC Hub for Graphene Enabled Industry Transformation (IH 150100003), the University of Adelaide, School of Chemical Engineering and School of Chemistry. The technical support provided by Adelaide Microscopy and the Micro Analysis Research Facility at Flinders Microscopy (Flinders University) was greatly appreciated.

Author Contributions: Ramesh Karunakaran performed the experiments and analyzed the data, Cameron Shearer conducted the XPS analysis, Campbell Coghlan and Dusan Losic conceived and designed the experiments, and all other authors assisted in writing the manuscript.

Conflicts of Interest: The authors declare no conflict of interest.

References

1. Boudghene, S.A.; Traversa, E. Fuel cells, an alternative to standard sources of energy. *Renew. Sustain. Energy Rev.* **2002**, *6*, 295–304. [[CrossRef](#)]
2. Xing, T.; Zheng, Y.; Li, L.H.; Cowie, B.C.; Gunzelmann, D.; Qiao, S.Z.; Huang, S.; Chen, Y. Observation of active sites for oxygen reduction reaction on nitrogen-doped multilayer graphene. *ACS Nano* **2014**, *8*, 6856–6862. [[CrossRef](#)] [[PubMed](#)]
3. Song, C.; Zhang, J. Electrocatalytic oxygen reduction reaction. In *PEM Fuel Cell Electrocatalysts and Catalyst Layers*; Springer: Berlin, Germany, 2008; pp. 89–134.
4. Holton, O.T.; Stevenson, J.W. The role of platinum in proton exchange membrane fuel cells. *Platin. Met. Rev.* **2013**, *57*, 259–271. [[CrossRef](#)]
5. Zhang, S.; Yuan, X.Z.; Hin, J.N.C.; Wang, H.; Friedrich, K.A.; Schulze, M. A review of platinum-based catalyst layer degradation in proton exchange membrane fuel cells. *J. Power Sources* **2009**, *194*, 588–600. [[CrossRef](#)]
6. Markovic, N.; Schmidt, T.; Stamenkovic, V.; Ross, P. Oxygen reduction reaction on Pt and Pt bimetallic surfaces: A selective review. *Fuel Cells* **2001**, *1*, 105–116. [[CrossRef](#)]
7. Markovic, N.M.; Gasteiger, H.A.; Ross, P.N. Oxygen reduction on platinum low-index single-crystal surfaces in sulfuric acid solution: Rotating ring-Pt(hkl) disk studies. *J. Phys. Chem.* **1995**, *99*, 3411–3415. [[CrossRef](#)]
8. Qu, L.; Liu, Y.; Baek, J.B.; Dai, L. Nitrogen-doped graphene as efficient metal-free electrocatalyst for oxygen reduction in fuel cells. *ACS Nano* **2010**, *4*, 1321–1326. [[CrossRef](#)] [[PubMed](#)]
9. Liang, J.; Zhou, R.F.; Chen, X.M.; Tang, Y.H.; Qiao, S.Z. Fe–N decorated hybrids of CNTs grown on hierarchically porous carbon for high-performance oxygen reduction. *Adv. Mater.* **2014**, *26*, 6074–6079. [[CrossRef](#)] [[PubMed](#)]
10. Liang, Y.; Li, Y.; Wang, H.; Zhou, J.; Wang, J.; Regier, T.; Dai, H. Co₃O₄ nanocrystals on graphene as a synergistic catalyst for oxygen reduction reaction. *Nat. Mater.* **2011**, *10*, 780–786. [[CrossRef](#)] [[PubMed](#)]
11. Wu, Z.S.; Yang, S.; Sun, Y.; Parvez, K.; Feng, X.; Müllen, K. 3D Nitrogen-doped graphene aerogel-supported Fe₃O₄ nanoparticles as efficient electrocatalysts for the oxygen reduction reaction. *J. Am. Chem. Soc.* **2012**, *134*, 9082–9085. [[CrossRef](#)] [[PubMed](#)]
12. Xiang, Z.; Xue, Y.; Cao, D.; Huang, L.; Chen, J.F.; Dai, L. Highly efficient electrocatalysts for oxygen reduction based on 2D covalent organic polymers complexed with non-precious metals. *Angew. Chem. Int. Ed.* **2014**, *53*, 2433–2437. [[CrossRef](#)] [[PubMed](#)]
13. Bezerra, C.W.; Zhang, L.; Lee, K.; Liu, H.; Marques, A.L.; Marques, E.P.; Wang, H.; Zhang, J. A review of Fe–N/C and Co–N/C catalysts for the oxygen reduction reaction. *Electrochim. Acta* **2008**, *53*, 4937–4951. [[CrossRef](#)]
14. Liu, G.; Li, X.; Ganesan, P.; Popov, B.N. Development of non-precious metal oxygen-reduction catalysts for PEM fuel cells based on N-doped ordered porous carbon. *Appl. Catal. B* **2009**, *93*, 156–165. [[CrossRef](#)]
15. Nallathambi, V.; Lee, J.W.; Kumaraguru, S.P.; Wu, G.; Popov, B.N. Development of high performance carbon composite catalyst for oxygen reduction reaction in PEM proton exchange membrane fuel cells. *J. Power Sources* **2008**, *183*, 34–42. [[CrossRef](#)]
16. Yang, D.S.; Song, M.Y.; Singh, K.P.; Yu, J.S. The role of iron in the preparation and oxygen reduction reaction activity of nitrogen-doped carbon. *Chem. Commun.* **2015**, *51*, 2450–2453. [[CrossRef](#)] [[PubMed](#)]
17. Wiesener, K. N₄-chelates as electrocatalyst for cathodic oxygen reduction. *Electrochim. Acta* **1986**, *31*, 1073–1078. [[CrossRef](#)]
18. Tang, Y.; Allen, B.L.; Kauffman, D.R.; Star, A. Electrocatalytic activity of nitrogen-doped carbon nanotube cups. *J. Am. Chem. Soc.* **2009**, *131*, 13200–13201. [[CrossRef](#)] [[PubMed](#)]
19. Wang, D.W.; Su, D. Heterogeneous nanocarbon materials for oxygen reduction reaction. *Energy Environ. Sci.* **2014**, *7*, 576–591. [[CrossRef](#)]
20. Yang, Z.; Nie, H.; Chen, X.; Xiaohua, C.; Huang, S. Recent progress in doped carbon nanomaterials as effective cathode catalysts for fuel cell oxygen reduction reaction. *J. Power Sources* **2013**, *236*, 238–249. [[CrossRef](#)]

21. Vaughan, O. Carbon catalysts: Active sites revealed. *Nat. Nanotechnol.* **2016**, *1*, 361–365. [[CrossRef](#)]
22. Yang, T.; Liu, J.; Zhou, R.; Chen, Z.; Xu, H.; Qiao, S.Z.; Monteiro, M.J. N-doped mesoporous carbon spheres as the oxygen reduction reaction catalysts. *J. Mater. Chem. A* **2014**, *2*, 18139–18146. [[CrossRef](#)]
23. Liu, H.J.; Bo, S.; Cui, W.; Li, F.; Wang, C.; Xia, Y. Nano-sized cobalt oxide/mesoporous carbon sphere composites as negative electrode material for lithium-ion batteries. *Electrochim. Acta* **2008**, *53*, 6497–6503. [[CrossRef](#)]
24. Zhang, W.M.; Hu, J.S.; Guo, Y.G.; Zheng, S.F.; Zhong, L.S.; Song, W.G.; Wan, L.J. Tin-nanoparticles encapsulated in elastic hollow carbon spheres for high-performance anode material in lithium-ion batteries. *Adv. Mater.* **2008**, *20*, 1160–1165. [[CrossRef](#)]
25. Du, H.; Jiao, L.; Wang, Q.; Yang, J.; Guo, L.; Si, Y.; Wang, Y.; Yuan, H. Facile carbonaceous microsphere templated synthesis of Co₃O₄ hollow spheres and their electrochemical performance in supercapacitors. *Nano Res.* **2013**, *6*, 87–98. [[CrossRef](#)]
26. Zhou, J.; He, J.; Zhang, C.; Wang, T.; Sun, D.; Di, Z.; Wang, D. Mesoporous carbon spheres with uniformly penetrating channels and their use as a supercapacitor electrode material. *Mater. Charact.* **2010**, *61*, 31–38. [[CrossRef](#)]
27. Yu, G.; Sun, B.; Pei, Y.; Xie, S.; Yan, S.; Qiao, M.; Fan, K.; Zhang, X.; Zong, B. Fe_xO_y@C spheres as an excellent catalyst for Fischer–Tropsch synthesis. *J. Am. Chem. Soc.* **2009**, *132*, 935–937. [[CrossRef](#)] [[PubMed](#)]
28. Wen, Z.; Wang, Q.; Zhang, Q.; Li, J. Hollow carbon spheres with wide size distribution as anode catalyst support for direct methanol fuel cells. *Electrochem. Commun.* **2007**, *9*, 1867–1872. [[CrossRef](#)]
29. Xiong, K.; Li, J.; Liew, K.; Zhan, X. Preparation and characterization of stable Ru nanoparticles embedded on the ordered mesoporous carbon material for applications in Fischer–Tropsch synthesis. *Appl. Catal. A* **2010**, *389*, 173–178. [[CrossRef](#)]
30. Jafri, R.I.; Rajalakshmi, N.; Ramaprabhu, S. Nitrogen doped graphene nanoplatelets as catalyst support for oxygen reduction reaction in proton exchange membrane fuel cell. *J. Mater. Chem.* **2010**, *20*, 7114–7117. [[CrossRef](#)]
31. Gong, K.; Du, F.; Xia, Z.; Durstock, M.; Dai, L. Nitrogen-doped carbon nanotube arrays with high electrocatalytic activity for oxygen reduction. *Science* **2009**, *323*, 760–764. [[CrossRef](#)] [[PubMed](#)]
32. Friedel, B.; Greulich-Weber, S. Preparation of monodisperse, submicrometer carbon spheres by pyrolysis of melamine–formaldehyde resin. *Small* **2006**, *2*, 859–863. [[CrossRef](#)] [[PubMed](#)]
33. Rybarczyk, M.K.; Lieder, M.; Jablonska, M. N-doped mesoporous carbon nanosheets obtained by pyrolysis of a chitosan–melamine mixture for the oxygen reduction reaction in alkaline media. *RSC Adv.* **2015**, *5*, 44969–44977. [[CrossRef](#)]
34. Zhou, X.; Yang, Z.; Nie, H.; Yao, Z.; Zhang, L.; Huang, S. Catalyst-free growth of large scale nitrogen-doped carbon spheres as efficient electrocatalysts for oxygen reduction in alkaline medium. *J. Power Sources* **2011**, *196*, 9970–9974. [[CrossRef](#)]
35. Feng, L.; Yang, L.; Huang, Z.; Luo, J.; Li, M.; Wang, D.; Chen, Y. Enhancing electrocatalytic oxygen reduction on nitrogen-doped graphene by active sites implantation. *Sci. Rep.* **2013**, *3*, 3306. [[CrossRef](#)] [[PubMed](#)]
36. Zhang, L.; Kim, J.; Dy, E.; Ban, S.; Tsay, K.; Kawai, H.; Shi, Z.; Zhang, J. Synthesis of novel mesoporous carbon spheres and their supported Fe-based electrocatalysts for PEM fuel cell oxygen reduction reaction. *Electrochim. Acta* **2013**, *108*, 480–485. [[CrossRef](#)]
37. Peng, H.; Mo, Z.; Liao, S.; Liang, H.; Yang, L.; Luo, F.; Song, H.; Zhong, Y.; Zhang, B. High performance Fe- and N-doped carbon catalyst with graphene structure for oxygen reduction. *Sci. Rep.* **2013**, *3*, 1765. [[CrossRef](#)]
38. Tang, J.; Liu, J.; Li, C.; Li, Y.; Tade, M.O.; Dai, S.; Yamauchi, Y. Synthesis of nitrogen-doped mesoporous carbon spheres with extra-large pores through assembly of diblock copolymer micelles. *Angew. Chem. Int. Ed.* **2015**, *54*, 588–593. [[CrossRef](#)]
39. Chen, P.; Wang, L.K.; Wang, G.; Gao, M.R.; Ge, J.; Yuan, W.J.; Shen, Y.H.; Xie, A.J.; Yu, S.H. Nitrogen-doped nanoporous carbon nanosheets derived from plant biomass: An efficient catalyst for oxygen reduction reaction. *Energy Environ. Sci.* **2014**, *7*, 4095–4103. [[CrossRef](#)]
40. Ma, Y.; Zhao, J.; Zhang, L.; Zhao, Y.; Fan, Q.; Hu, Z.; Huang, W. The production of carbon microtubes by the carbonization of catkins and their use in the oxygen reduction reaction. *Carbon* **2011**, *49*, 5292–5297. [[CrossRef](#)]

41. Lai, C.; Kolla, P.; Zhao, Y.; Fong, H.; Smirnova, A.L. Lignin-derived electrospun carbon nanofiber mats with supercritically deposited Ag nanoparticles for oxygen reduction reaction in alkaline fuel cells. *Electrochim. Acta* **2014**, *130*, 431–438. [[CrossRef](#)]
42. Rana, M.; Arora, G.; Gautam, U.K. N- and S-doped high surface area carbon derived from soya chunks as scalable and efficient electrocatalysts for oxygen reduction. *Sci. Technol. Adv. Mater.* **2015**, *16*, 014803. [[CrossRef](#)] [[PubMed](#)]
43. Nicolás, E.; Torrecillas, A.; Dell’Amico, J.; Alarcón, J.J. The effect of short-term flooding on the sap flow, gas exchange and hydraulic conductivity of young apricot trees. *Trees* **2005**, *19*, 51–57. [[CrossRef](#)]
44. Weaver, D. A gummosis disease of peach trees caused by *Botryosphaeria dothidea*. *Phytopathol* **1974**, *64*, 1429–1432. [[CrossRef](#)]
45. Lluveras-Tenorio, A.; Mazurek, J.; Restivo, A.; Colombini, M.P.; Bonaduce, I. Analysis of plant gums and saccharide materials in paint samples: Comparison of GC-MS analytical procedures and databases. *Chem. Cent. J.* **2012**, *6*, 115. [[CrossRef](#)] [[PubMed](#)]
46. Sun, X.; Li, Y. Colloidal carbon spheres and their core/shell structures with noble-metal nanoparticles. *Angew. Chem. Int. Ed.* **2004**, *43*, 597–601. [[CrossRef](#)] [[PubMed](#)]
47. Mi, Y.; Hu, W.; Dan, Y.; Liu, Y. Synthesis of carbon micro-spheres by a glucose hydrothermal method. *Mater. Lett.* **2008**, *62*, 1194–1196. [[CrossRef](#)]
48. Roberts, A.D.; Li, X.; Zhang, H. Porous carbon spheres and monoliths: Morphology controlling, pore size tuning and their applications as Li-ion battery anode materials. *Chem. Soc. Rev.* **2014**, *43*, 4341–4356. [[CrossRef](#)] [[PubMed](#)]
49. Wang, J.; Shen, L.; Ding, B.; Nie, P.; Deng, H.; Dou, H.; Zhang, X. Fabrication of porous carbon spheres for high-performance electrochemical capacitors. *RSC Adv.* **2014**, *4*, 7538–7544. [[CrossRef](#)]
50. Karunagaran, R.; Tung, T.T.; Shearer, C.; Tran, D.; Coghlan, C.; Doonan, C.; Losic, D. A unique 3D nitrogen-doped carbon composite as high performance oxygen reduction catalysts. *Materials* **2017**, *10*, 921. [[CrossRef](#)] [[PubMed](#)]
51. Sakaki, T.; Shibata, M.; Miki, T.; Hirosue, H.; Hayashi, N. Reaction model of cellulose decomposition in near-critical water and fermentation of products. *Bioresour. Technol.* **1996**, *58*, 197–202. [[CrossRef](#)]
52. Mer, V.K.L. Nucleation in phase transitions. *Ind. Eng. Chem.* **1952**, *44*, 1270–1277. [[CrossRef](#)]
53. Terrones, M.; Hsu, W.K.; Kroto, H.W.; Walton, D.R. Nanotubes: A revolution in materials science and electronics. In *Fullerenes and Related Structures*; Springer: Berlin, Germany, 1999; pp. 189–234.
54. Sun, Q.T.M.; Zhang, T.; Wang, G. Rational synthesis of novel π -conjugated poly(1,5-diaminoanthraquinone) for high-performance supercapacitors. *RSC Adv.* **2014**, *4*, 7774–7779. [[CrossRef](#)]
55. Terrones, M.; Terrones, H.; Grobert, N.; Hsu, W.; Zhu, Y.; Hare, J.; Kroto, H.; Walton, D.; Kohler-Redlich, P.; Rühle, M. Efficient route to large arrays of CN_x nanofibers by pyrolysis of ferrocene/melamine mixtures. *Appl. Phys. Lett.* **1999**, *75*, 3932–3934. [[CrossRef](#)]
56. Terrones, M.; Redlich, P.; Grobert, N.; Trasobares, S.; Hsu, W.K.; Terrones, H.; Zhu, Y.Q.; Hare, J.P.; Reeves, C.L.; Cheetham, A.K. Carbon nitride nanocomposites: Formation of aligned C_xN_y nanofibers. *Adv. Mater.* **1999**, *11*, 655–658. [[CrossRef](#)]
57. Lee, K.H.; Han, S.W.; Kwon, K.Y.; Park, J.B. Systematic analysis of palladium–graphene nanocomposites and their catalytic applications in Sonogashira reaction. *J. Colloid Interface Sci.* **2013**, *403*, 127–133. [[CrossRef](#)] [[PubMed](#)]
58. Gupta, V.; Saleh, T.A. Syntheses of carbon nanotube-metal oxides composites; adsorption and photo-degradation. In *Carbon Nanotubes—From Research to Applications*; InTech: San Francisco, CA, USA, 2011. [[CrossRef](#)]
59. Manoj, B.; Kunjomana, A. Study of stacking structure of amorphous carbon by X-ray diffraction technique. *Int. J. Electrochem. Sci.* **2012**, *7*, 3127–3134.
60. Wu, G.; Dai, C.; Wang, D.; Li, D.; Li, N. Nitrogen-doped magnetic onion-like carbon as support for Pt particles in a hybrid cathode catalyst for fuel cells. *J. Mater. Chem.* **2010**, *20*, 3059–3068. [[CrossRef](#)]
61. Ferrari, A.C. Raman spectroscopy of graphene and graphite: Disorder, electron-phonon coupling, doping and nonadiabatic effects. *Solid State Commun.* **2007**, *143*, 47–57. [[CrossRef](#)]
62. Xie, Z.L.; Huang, X.; Titirici, M.M.; Taubert, A. Mesoporous graphite nanoflakes via ionothermal carbonization of fructose and their use in dye removal. *RSC Adv.* **2014**, *4*, 37423–37430. [[CrossRef](#)]

63. Pimenta, M.; Dresselhaus, G.; Dresselhaus, M.S.; Cancado, L.; Jorio, A.; Saito, R. Studying disorder in graphite-based systems by Raman spectroscopy. *Phys. Chem. Chem. Phys.* **2007**, *9*, 1276–1290. [[CrossRef](#)] [[PubMed](#)]
64. Schwan, J.; Ulrich, S.; Batori, V.; Ehrhardt, H.; Silva, S. Raman spectroscopy on amorphous carbon films. *J. Appl. Phys.* **1996**, *80*, 440–447. [[CrossRef](#)]
65. Ghanbarlou, H.; Rowshanzamir, S.; Kazeminasab, B.; Parnian, M.J. Non-precious metal nanoparticles supported on nitrogen-doped graphene as a promising catalyst for oxygen reduction reaction: Synthesis, characterization and electrocatalytic performance. *J. Power Sources* **2015**, *273*, 981–989. [[CrossRef](#)]
66. Sing, K.S. Reporting physisorption data for gas/solid systems with special reference to the determination of surface area and porosity (Recommendations 1984). *Pure Appl. Chem.* **1985**, *57*, 603–619. [[CrossRef](#)]
67. Khalfaoui, M.; Knani, S.; Hachicha, M.; Lamine, A.B. New theoretical expressions for the five adsorption type isotherms classified by BET based on statistical physics treatment. *J. Colloid Interface Sci.* **2003**, *263*, 350–356. [[CrossRef](#)]
68. Chen, J.; Xia, N.; Zhou, T.; Tan, S.; Jiang, F.; Yuan, D. Mesoporous carbon spheres: Synthesis, characterization and supercapacitance. *Int. J. Electrochem. Sci.* **2009**, *4*, 1063–1073.
69. Wang, H.; Hao, Q.; Yang, X.; Lu, L.; Wang, X. Graphene oxide doped polyaniline for supercapacitors. *Electrochem. Commun.* **2009**, *11*, 1158–1161. [[CrossRef](#)]
70. Elumalai, E.K.; Kayalvizhi, K.; Silvan, S. Coconut water assisted green synthesis of silver nanoparticles. *J. Pharm. Bioallied Sci.* **2014**, *6*, 241. [[CrossRef](#)] [[PubMed](#)]
71. Talbot, W.F. Manufacture of Melamine-Aldehyde Condensation Products. U.S. Patent Application No. 2260239 A, 21 October 1941.
72. Permatasari, F.A.; Aimon, A.H.; Iskandar, F.; Ogi, T.; Okuyama, K. Role of C–N Configurations in the photoluminescence of graphene quantum dots synthesized by a hydrothermal route. *Sci. Rep.* **2016**, *6*, 21042. [[CrossRef](#)] [[PubMed](#)]
73. Lu, M.; Cheng, H.; Yang, Y. A comparison of solid electrolyte interphase (SEI) on the artificial graphite anode of the aged and cycled commercial lithium ion cells. *Electrochim. Acta* **2008**, *53*, 3539–3546. [[CrossRef](#)]
74. Martínez, L.; Román, E.; Nevshupa, R. X-Ray Photoelectron spectroscopy for characterization of engineered elastomer surfaces. In *Advanced Aspects of Spectroscopy*; InTech: San Francisco, CA, USA, 2012. [[CrossRef](#)]
75. Kelemen, S.R.; Gorbaty, M.L.; Kwiatek, P.J. Quantification of nitrogen forms in coals. *Energeia* **1995**, *6*, 1–3.
76. Zhang, L.S.; Liang, X.Q.; Song, W.G.; Wu, Z.Y. Identification of the nitrogen species on N-doped graphene layers and Pt/NG composite catalyst for direct methanol fuel cell. *Phys. Chem. Chem. Phys.* **2010**, *12*, 12055–12059. [[CrossRef](#)] [[PubMed](#)]
77. Subramanian, N.P.; Li, X.; Nallathambi, V.; Kumaraguru, S.P.; Colon-Mercado, H.; Wu, G.; Lee, J.W.; Popov, B.N. Nitrogen-modified carbon-based catalysts for oxygen reduction reaction in polymer electrolyte membrane fuel cells. *J. Power Sources* **2009**, *188*, 38–44. [[CrossRef](#)]
78. Liu, Y.L.; Xu, X.Y.; Shi, C.X.; Ye, X.W.; Sun, P.C.; Chen, T.H. Iron-nitrogen Co-doped hierarchically mesoporous carbon spheres as highly efficient electrocatalysts for oxygen reduction reaction. *RSC Adv.* **2017**, *7*, 8879–8885. [[CrossRef](#)]
79. Damjanovic, A.; Genshaw, M.A.; Bockris, J.O. Distinction between intermediates produced in main and side electrodic reactions. *J. Chem. Phys.* **1966**, *45*, 4057–4059. [[CrossRef](#)]
80. Darezereshki, E. Synthesis of maghemite (γ -Fe₂O₃) nanoparticles by wet chemical method at room temperature. *Mater. Lett.* **2010**, *64*, 1471–1472. [[CrossRef](#)]
81. Wang, S.; Dou, S.; Tao, L.; Huo, J.; Dai, L. Etched and doped Co₉S₈/graphene hybrid for oxygen electrocatalysis. *Energy Environ. Sci.* **2016**, *9*, 1320–1326.



Supplementary Information

Green Synthesis of Three-Dimensional Hybrid N-Doped ORR Electro-Catalysts Derived from Apricot Sap

Ramesh Karunagaran ¹, Campbell Coghlan ², Cameron Shearer ³, Diana Tran ¹, Karan Gulati ¹, Tran Thanh Tung ¹, Christian Doonan ² and Dusan Losic ^{1,*}

¹ School of Chemical Engineering, University of Adelaide, SA 5005, Australia; ramesh.karunagaran@adelaide.edu.au (R.K.); diana.tran@adelaide.edu.au (D.T.); k.gulati@griffith.edu.au (K.G.); tran.tung@adelaide.edu.au (T.T.T.)

² School of Chemistry, University of Adelaide, SA 5005, Australia; cam.coghlan@adelaide.edu.au (C.C.); christian.doonan@adelaide.edu.au (C.D.)

³ School of Chemical and Physical Sciences, Flinders University, SA 5042, Australia; cameron.shearer@flinders.edu.au

* Correspondence: dusan.losic@adelaide.edu.au; Tel.: +61-8-8013-4648

Received: 10 January 2018; Accepted: 26 January 2018; Published: 28 January 2018

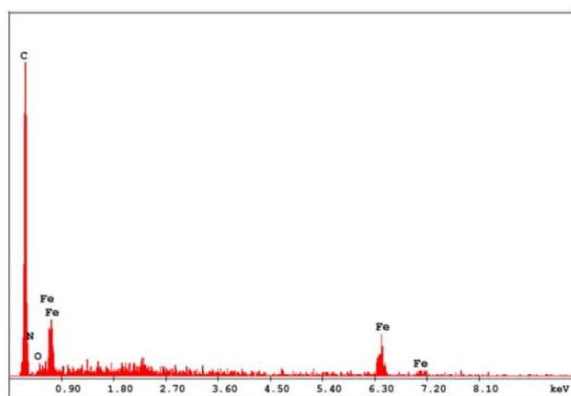


Figure S1. EDX analysis of FeMNPC embedded in the CMS.

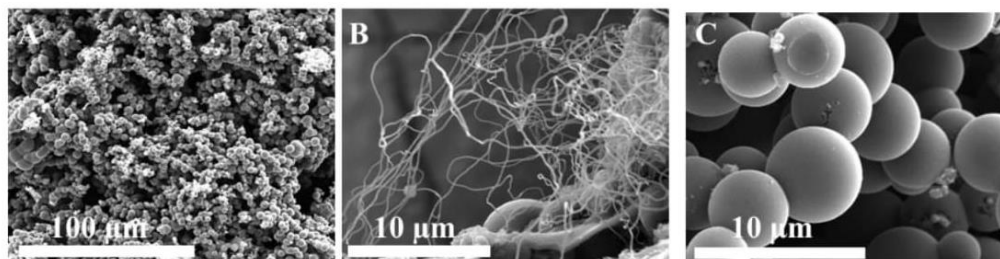


Figure S2. SEM images of (A) hydrothermally treated apricot sap resin and cobalt acetate (HT-APG-Co), (B) pyrolysed HT-APG-Co at 950°C with the presence of nitrogen precursor melamine (N-APG-Co), and (C) pyrolysed HT-APG-Co at 950°C without melamine (APG-Co)

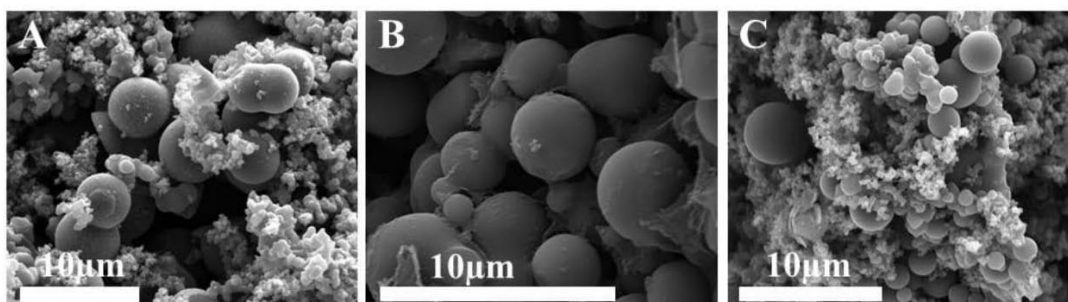


Figure S3. SEM images of (A) hydrothermally treated apricot sap resin (HT-APG), (B) pyrolysed HT-APG at 950°C with the presence of nitrogen precursor melamine (N-APG), and (C) pyrolysed HT-APG at 950°C without melamine (APG)

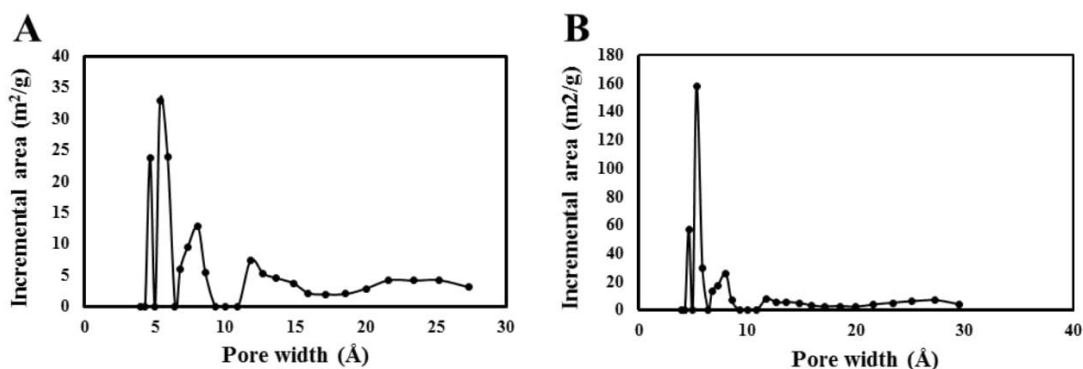


Figure S4. Pore size distribution of (A) APG-Fe and (B) APG-Co.

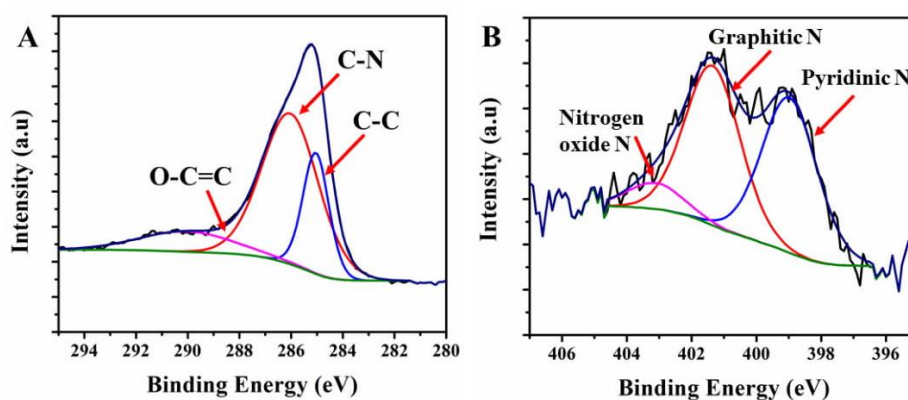


Figure S5. XPS core level spectra of N-APG-Fe for (A) C1s and (B) N1s.

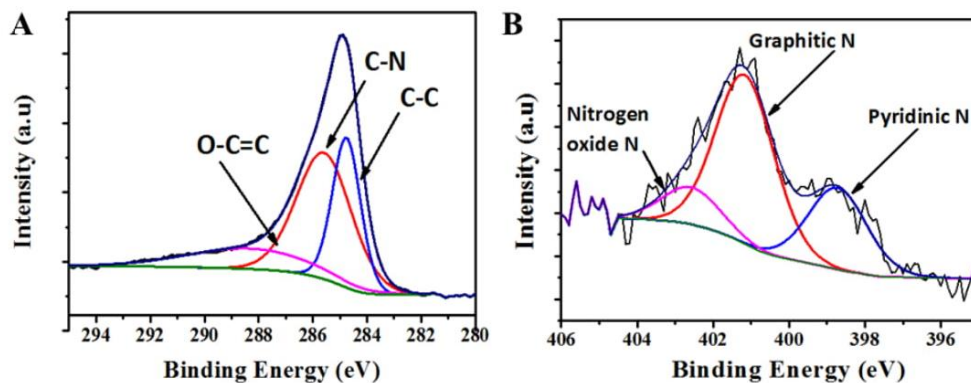


Figure S6. XPS core level spectra of N-APG-Co for (A) C1s and (B) N1s.

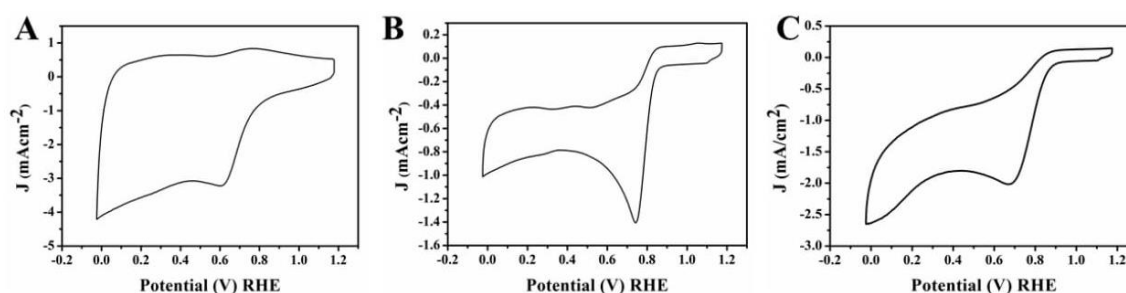


Figure S7. Cyclic Voltammetry of (A) N-APG, (B) N-APG-Fe and (C) N-APG-Co at a scan rate of 100 mV/s-1 in oxygen saturated 0.1M KOH solution.

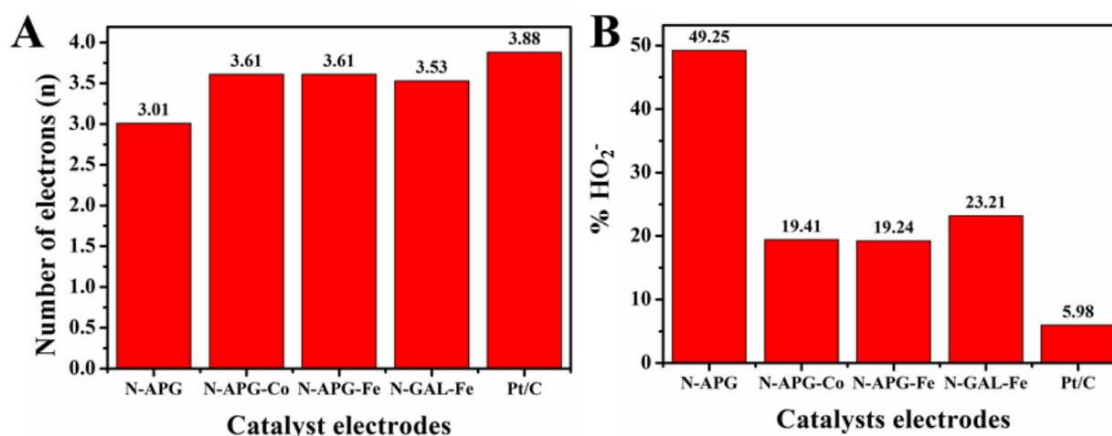


Figure S8. (A) Comparison of number of electrons and (B) % HO₂⁻ of N-APG, N-APG-Co, N-APG-Fe, N-GAL-Fe and Pt/C catalysts electrodes at 0.4V applied potential in oxygen saturated 0.10 M KOH electrolyte at 2000 rpm at a scan rate of 10 mV/s.

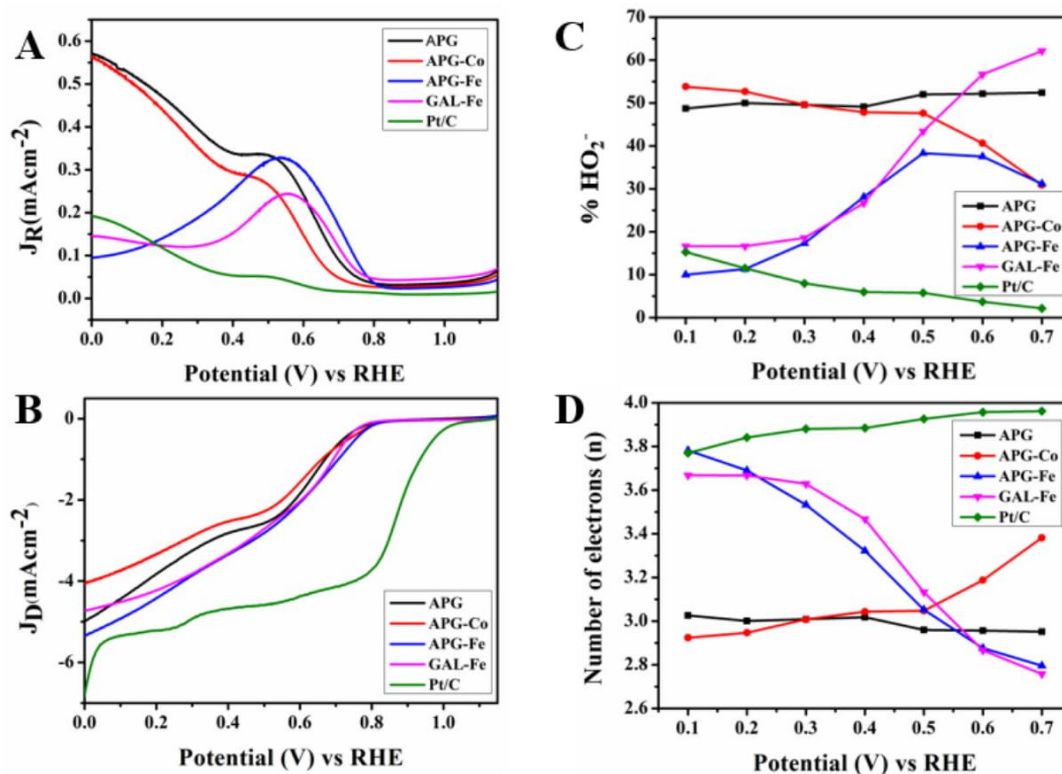


Figure S9. Rotating ring disc voltammograms of (A) ring current and (B) disc current of catalysts electrodes APG, APG-Co, APG-Fe, GAL-Fe and Pt/C, pyrolysed without the presence of melamine in oxygen saturated 0.1M KOH at 2000 rpm at a scan rate of 10mV/s. (C) Percentage peroxide, and (D) number of electrons of APG, APG-Fe, APG-Co and Pt/C electrodes at various potential calculated according to RRDE data.

Table S1. Electro chemical properties of non-doped apricot sap and galactose catalysts.

Product	Current density (mA/cm^2) at 0V	Onset potential (V) (RHE)	Number of electrons (n) (0.1-0.7 V)	$\% \text{HO}_2^-$ (0.1-0.7V)
APG	4.98	0.78	3.02-2.95	48.70-52.41
APG-Fe	5.33	0.80	3.78-2.79	10.90-60.21
APG-Co	4.05	0.80	2.92-3.38	53.81-30.91
GAL-Fe	4.72	0.82	3.66-2.75	16.60-62.10

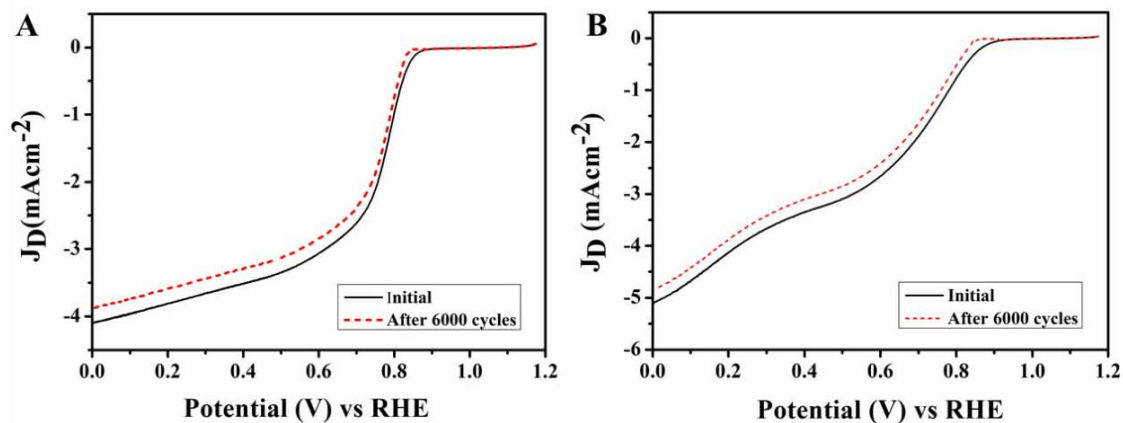


Figure S10. RDE polarisation curves of (A) N-APG-Co and (B) N-APG-Fe with a scan rate of 100 mV s^{-1} before and after 6000 potential cycles in an oxygen saturated KOH solution.

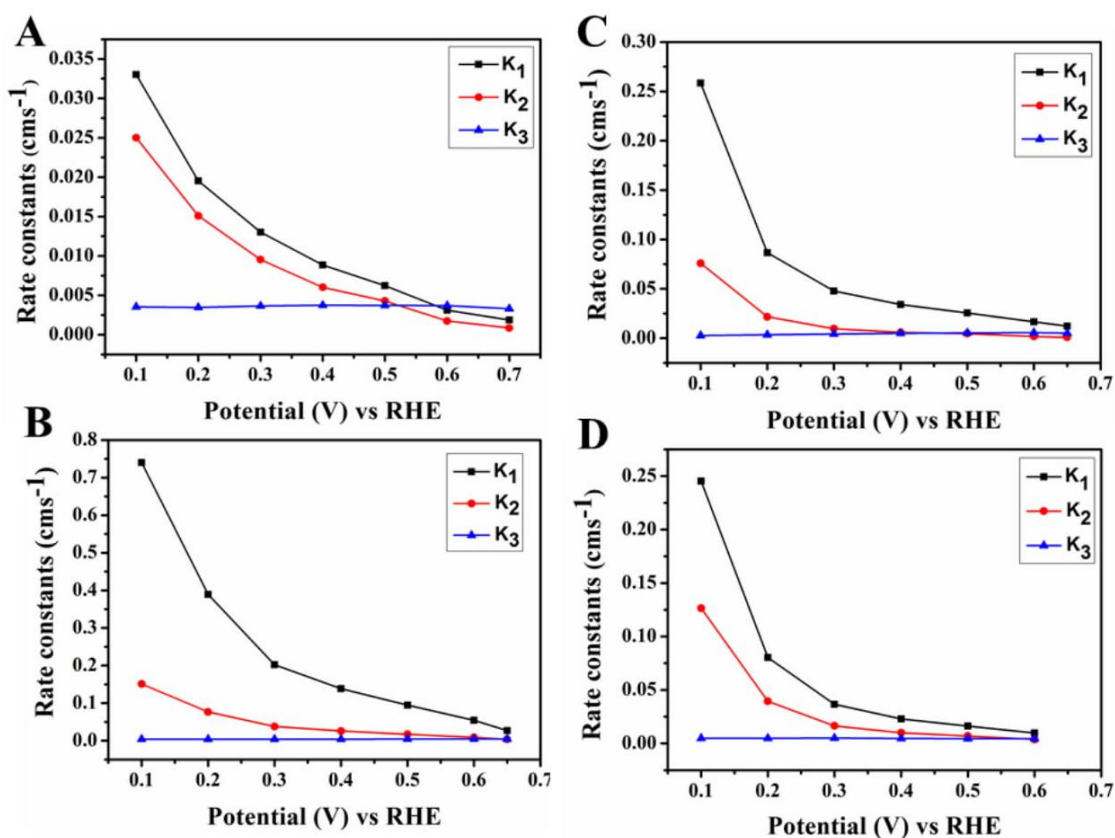


Figure S11. Rate constants of (A) N-APG, (B) N-APG-Co, (C) N-APG-Fe, and (D) N-GAL-Fe.

Table S2. comparison of k_1/k_2 of N-doped apricot and galactose catalysts

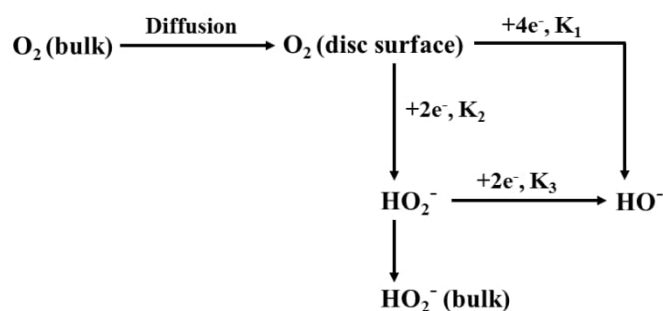
	k_1/k_2	
	Potential 0.1V (RHE)	Potential 0.65V (RHE)
N-APG	1.32	2.18
N-APG-Co	4.90	6.97
N-APG-Fe	3.40	14.14
N-GAL-Fe	4.30	6.40

Table S3. comparison of performance of N-APG-Fe, N-APG-Co and N-GAL-Fe with other similar carbon-based catalysts.

Material	Onset potential (V)	Number of electrons (n) / Potential (V) (RHE)	Reference
Soya -derived heteroatom doped carbon	0.96	3.70 / 0.625 V	[1]
N-doped mesoporous carbon spheres	0.86	3.40 / 0.575 V	[2]
N-doped hollow carbon spheres	0.80	3.82 / 0.575 V	[3]
Co-N-C hybrid using soya milk	0.80	3.70 / 0.675 V	[4]
3D-Integrated N-doped carbon sphere with N-CNT (N-GAL-Fe)	0.96	3.55 / 0.600 V	[8]
3D-Integrated N-doped carbon sphere with N-CF (N-APG-Co)	0.86	3.63 / 0.600 V	This study
3D-Integrated N-doped carbon sphere with N-CF (N-APG-Fe)	0.88	3.73 / 0.600 V	This study

Electron transfer kinetics

The electron transfer kinetic of the ORR was identified using RRDE voltametry (Scheme S1) [5, 6]. According to Damjanovic *et al.* [5] the electron transfer mechanism follows a direct four-electron pathway via k_1 kinetics (Scheme S1), in which oxygen is directly reduced to hydroxide anion (OH^-) or could be driven through a two-electron pathway via k_2 kinetics producing peroxide intermediates (HO_2^-), followed by reduction to hydroxide anion (OH^-) through another two electron pathway through k_3 kinetics.



Scheme S1. Proposed model for electrochemical reduction of oxygen proposed by Damjanovic *et al.* and Hsueh *et al.*

Hsueh *et al.*[6] suggested a series of equations (3, 4 and 5) to calculate the rate constants K_1 , K_2 and K_3 , where I_d , I_r , I_{dL} and ω are the disc current, ring current, limiting disc current and the rotation speed, respectively.

$$k_1 = S_1 Z_1 \frac{I_1^{N-1}}{I_1^{N+1}} \quad (3)$$

$$k_2 = \frac{2 S_2 Z_1}{I_1^{N+1}} \quad (4)$$

$$k_3 = \frac{N S_1 Z_2}{I_1^{N+1}} \quad (5)$$

Where S_1 and I_1 are the slope and intercept correspond to the I_d / I_r vs $\omega^{-1/2}$ plots and S_2 and is the slope of $I_{dL} / I_{dL} - I_d$ vs $\omega^{-1/2}$ plot. $Z_1 = 0.62 D_{\text{O}_2}^{2/3} V^{-1/6}$, $Z_2 = 0.62 D_{\text{H}_2\text{O}_2}^{2/3} V^{-1/6}$, $D_{\text{H}_2\text{O}_2}$ is $6.8 \times 10^{-6} \text{ cm}^2 \text{ s}^{-1}$ and N is the collection efficiency [7].

References

- [1] Rana, M.; Arora, G.; Gautam, U. K. N-and S-doped high surface area carbon derived from soya chunks as scalable and efficient electrocatalysts for oxygen reduction. *Sci. Technol. Adv. Mater.* **2015**, *16*, 014803.
- [2] Tang, J.; Liu, J.; Li, C.; Li, Y.; Tade, M. O.; Dai, S.; Yamauchi, Y. Synthesis of Nitrogen-Doped Mesoporous Carbon Spheres with Extra-Large Pores through Assembly of Diblock Copolymer Micelles. *Ang. Chem. Int. Ed.* **2015**, *54*, 588–593.
- [3] Li, Y.; Li, T.; Yao, M.; Liu, S. Metal-free nitrogen-doped hollow carbon spheres synthesized by thermal treatment of poly (o-phenylenediamine) for oxygen reduction reaction in direct methanol fuel cell applications. *J. Mater. Chem.* **2012**, *22*, 10911–10917.
- [4] Zhai, Y.; Zhu, C.; Wang, E.; Dong, S. Energetic carbon-based hybrids: green and facile synthesis from soy milk and extraordinary electrocatalytic activity towards ORR. *Nanoscale* **2014**, *6*, 2964–2970.
- [5] Damjanovic, A.; Genshaw, M. A.; Bockris, J. O. Distinction between intermediates produced in main and side electrodic reactions. *J. Chem. Phys.* **1966**, *45*, 4057–4059.
- [6] Hsueh, K.L.; Chin, D.L.; Srinivasan, S. Electrode kinetics of oxygen reduction: A theoretical and experimental analysis of the rotating ring-disc electrode method. *J. Electroanal. Chem. Interfacial Electrochem.* **1983**, *153*, 79–95.
- [7] Muthukrishnan, A.; Nabaie, Y.; Chang, C. W.; Okajima, T.; Ohsaka, T. A high-performance Fe and nitrogen doped catalyst derived from diazoniapentaphene salt and phenolic resin mixture for oxygen reduction reaction. *Catal. Sci. Technol.* **2015**, *5*, 1764–1774.

CHAPTER 4

The investigation of four different iron oxide nanoparticle phases dispersed in a 3-D graphene aerogel as ORR electrocatalysts.

Ramesh Karunakaran

School of Chemical Engineering, University of Adelaide, South Australia 5005, Australia

4.1 Chapter overview

Iron oxides are cheap materials compared to the relatively expensive Pt catalysts commonly used for ORR. Even though it is well known that iron oxide has low catalytic performance for ORR, their contributions as individual phases towards oxygen reduction have been not properly investigated. A synthesis procedure of four different phases of iron oxide nanoparticles (magnetite, maghemite, hematite and goethite) without using any nitrogen precursors is described in this chapter. The synthesised nanoparticles were dispersed on a 3-D graphene aerogel at low temperature (80 °C). This chapter investigates the influence of magnetite, maghemite, hematite and goethite iron oxide nanoparticles towards oxygen reduction. The exploration of this chapter has been discussed in a peer reviewed article (Chapter 4(a)), which is enclosed in the following pages with the supporting information.

All phases of synthesised iron oxide nanoparticles were confirmed based on the positions of the diffraction peaks determined by the XRD analysis. The different iron oxide nanoparticles synthesised were carefully embedded onto the 3-D graphene aerogel at low temperature (80°C) to avoid any possible phase changes due the thermal treatment. The investigation revealed that the iron oxide phases did not contribute effectively towards the reduction of oxygen. However, magnetite and maghemite with inverse spinal structures performed more efficiently than hematite and goethite with rhombohedral and orthorhombic crystal structures respectively. The influence of magnetism and electrical conductivity on ORR was also investigated and presented.

CHAPTER 4 (a)

Study of iron oxide nanoparticle phases in graphene aerogels for oxygen reduction reaction

Ramesh Karunagaran

School of Chemical Engineering, University of Adelaide, South Australia 5005, Australia

The chapter is based on the following peer-reviewed article:

R. Karunagaran, C. Coghlan, T. T. Tung, S.kabiri, D. Tran, C. Doonan, D. Losic “Study of iron oxide nanoparticle phases in graphene aerogels for oxygen reduction reaction” *New Journal of Chemistry*, 2017, **41**, 15180 - 15186. (Published)

Statement of Authorship

Title of Paper	Study of iron oxide nanoparticle phases in graphene aerogels for oxygen reduction reaction
Publication Status	<input checked="" type="checkbox"/> Published <input type="checkbox"/> Accepted for Publication <input type="checkbox"/> Submitted for Publication <input type="checkbox"/> Unpublished and Unsubmitted work written in manuscript style
Publication Details	<i>New Journal of Chemistry</i> , 2017, 41 , 15180-15186.

Principal Author

Name of Principal Author (Candidate)	Ramesh Karunakaran		
Contribution to the Paper	Under the supervision of D. Losic and Christian Doonan, I developed, designed and conducted the experiments, interpreted, processed the data and wrote the manuscript for submission.		
Overall percentage (%)	80%		
Certification:	This paper reports on the original research I conducted during the period of my Higher Degree by Research candidature and is not subjected to any obligations or contractual agreements with third party that would constrain its inclusion in this thesis. I am the primary author of this paper.		
Signature		Date	15 February 2018

Co-Author Contributions

By signing the Statement of Authorship, each author certifies that:

- i. the candidate's stated contribution to the publication is accurate (as detailed above);
- ii. permission is granted for the candidate to include the publication in the thesis; and
- iii. the sum of all co-author contributions is equal to 100% less the candidate's stated contribution.

Name of Co-Author	Tran Thanh Tung		
Contribution to the Paper	I helped Ramesh Karunakaran (candidate) with interpreting experimental results and improving the manuscript for submission. I give consent for Ramesh Karunakaran to present this paper for examination towards the Doctorate of Philosophy.		
Signature		Date	15 February 2018

Name of Co-Author	Diana Tran		
Contribution to the Paper	I helped Ramesh Karunakaran with designing experiments and improving the manuscript for submission. I give consent for Ramesh Karunakaran to present this paper for examination towards the Doctorate of Philosophy.		
Signature		Date	15 February 2018

Name of Co-Author	Shervin Kabiri		
Contribution to the Paper	I assisted Ramesh Karunakaran to prepare the graphene aerogels. I give consent for Ramesh Karunakaran to present this paper for examination towards the Doctorate of Philosophy.		
Signature		Date	15 February 2018

Name of Co-Author	Campbell Coghlan		
Contribution to the Paper	I acted as the secondary supervisor for Ramesh Karunakaran and helped him to design the experiments and improve the final draft of the manuscript for submission. I give consent for Ramesh Karunakaran to present this paper for examination towards the Doctorate of Philosophy.		
Signature		Date	15 February 2018

Name of Co-Author	Christian Doonan		
Contribution to the Paper	I acted as the secondary supervisor for Ramesh Karunakaran and aided in design and development of experiment and evaluation of manuscript for submission. I give consent for Ramesh Karunakaran to present this paper for examination towards the Doctorate of Philosophy.		
Signature		Date	15 February 2018

Name of Co-Author	Dusan Losic		
Contribution to the Paper	I acted as the Primary supervisor for Ramesh Karunakaran and aided in design and development of experiment and evaluation of manuscript for submission. I give consent for Ramesh Karunakaran to present this paper for examination towards the Doctorate of Philosophy.		
Signature		Date	15 February 2018



NJC

PAPER

View Article Online
View Journal | View Issue



Cite this: *New J. Chem.*, 2017, **41**, 15180

Received 11th August 2017,
Accepted 2nd November 2017

DOI: 10.1039/c7nj02979a

rsc.li/njc

Study of iron oxide nanoparticle phases in graphene aerogels for oxygen reduction reaction†

Ramesh Karunakaran,^a Campbell Coghlan,^b Tran Thanh Tung,^b Shervin Kabiri,^a Diana N. H. Tran,^b Christian J. Doonan,^b and Dusan Losic^b *^a

Iron oxide nanoparticles have been extensively used for energy production in fuel cells; however, the different phases of iron oxide have not been adequately investigated for their effect on the oxygen reduction reaction (ORR). The low temperature synthesis of four kinds of iron oxide nanoparticles with different phases was incorporated inside 3D reduced graphene oxide (rGO) aerogels and their electrochemical, catalytic and electron transfer properties were determined for ORR. The results showed that, at low potentials (0.20 V), rGO composites containing magnetite, maghemite and goethite catalyse ORR via four-electron transfer kinetics while hematite facilitated two-electron transfer kinetics. At higher potentials (0.70 V), all four catalysts proceeded via a two-electron pathway.

1. Introduction

Global energy demand is on the rise and these requirements are predominantly provided by non-renewable fossil fuels.¹ Energy production using fossil fuels is associated with a number of environmental concerns in addition to their finite nature.² These factors have forced a shift towards efficient and renewable energy sources to meet the current demand.^{1–3} These renewable sources include solar, wind, water and geothermal heat, which have all been used as alternative energy sources; however, these methods do not provide a consistent source of power.³ Fuel cells have emerged as a reliable and clean power generation source that can provide power more consistently than many other sources.⁴ Fuel cells electrochemically combine gaseous fuel (hydrogen) and an oxidant gas (typically oxygen from air) to produce electricity and heat through an oxygen reduction reaction (ORR).⁴ The efficiency of this process is controlled by the ORR catalyst and current generation catalysts have slow kinetics, are of high cost or are not environmentally friendly. These factors have combined to limit the development from the laboratory to industrial scale.⁵

While numerous catalysts have been developed, those containing platinum (Pt) have shown the best performance for ORR catalysis.^{6–8} However, these catalysts have drawbacks

including high cost, scarcity,⁹ crossover effects and carbon monoxide poisoning.¹⁰ Different chemical approaches have been implemented to develop low-cost catalysts without the use of precious metals (*i.e.* Pt). Among them, hetero atom (N, B, P and S) doped carbon materials,^{11–14} non-precious metal/hetero-atomic polymer composites,¹⁵ transition metal N_4 -macrocycles such as porphyrin¹⁶ and transition metal oxides¹⁷ have all shown to be effective catalysts for ORR. Transition iron oxides have been widely employed in ORR catalysis.^{18,19} The most common crystal phases of ferrous and ferric iron oxides are magnetite (Fe_3O_4), maghemite ($\gamma\text{-}Fe_2O_3$), hematite ($\alpha\text{-}Fe_2O_3$) and goethite ($\alpha\text{-}FeOOH$). Fe_3O_4 and $\gamma\text{-}Fe_2O_3$ both possess an inverse spinel structure and show ferrimagnetic properties at room temperature.^{20,21} In contrast, $\alpha\text{-}Fe_2O_3$ and $\alpha\text{-}FeOOH$ have rhombohedral²² and orthorhombic²³ crystal structures, respectively, and display anti-ferromagnetic properties.^{24,25} The existence of these iron oxides phases, which are unique in crystal structure and magnetic and electrical properties has allowed these materials to be tested for various applications such as magnetically guided drug delivery,²⁶ water remediation,^{27,28} cell separation,²⁹ magnetic resonance imaging,³⁰ dye removal,³¹ solar water splitting,³² cathodes in lithium batteries³³ and adsorbents for heavy metals.^{34,35}

Carbon supports such as carbon nanotubes and graphene are used to facilitate active site distribution, increase mass transportation and increase electrical conductivity.³⁶ Graphene oxide (GO), in contrast with graphene, is a hydrophilic material with poor electron conductivity. By reducing the functional groups (OH, COOH and epoxy) of GO to form rGO the electrical conductivity of the material is increased, which provides excellent support for the catalyst.³⁷ Liu *et al.*³⁸ recently compared the different phases of iron oxides/GO for their ORR activity by generating the iron oxides *in situ* by hydrothermal synthesis or

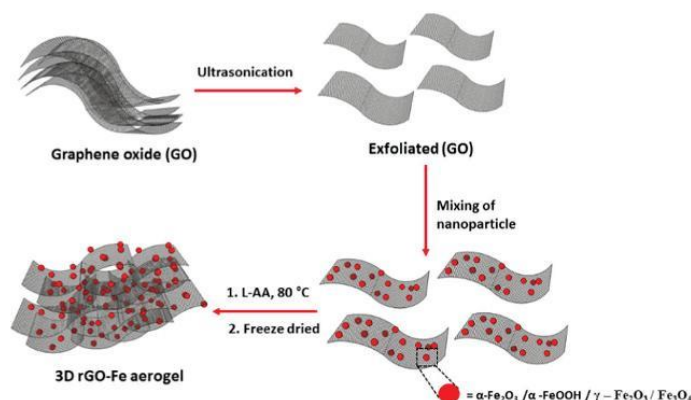
^a School of Chemical Engineering, University of Adelaide, SA, 5000, Australia.

E-mail: dusan.losic@adelaide.edu.au

^b Department of Chemistry, University of Adelaide, SA, 5000, Australia.

E-mail: Christian.doonan@adelaide.edu.au

† Electronic supplementary information (ESI) available: Images of rGO/iron oxide aerogels, Raman spectrums, cyclic voltammetry, conductivity measurements, RRDE measurements and rate constants of rGO/iron oxide aerogels. See DOI: 10.1039/c7nj02979a



Scheme 1 Schematic presentation of the formation of a rGO/iron oxide aerogel.

at a high annealing temperature (800 °C) doped with a nitrogen (N) precursor. The electron donor properties of N-doped adjacent carbon atoms trigger favourable diatomic O₂ adsorption by weakening the O₂ bond strength to facilitate ORR activity.^{39–42} However, the samples used two distinct methods—hydrothermal (no N-doping) and thermal annealing (resulting in N-doping)—which meant that the results do not reflect only the catalytic activity of the iron oxides. Therefore, to compare the contribution of different iron oxide nanoparticle phases towards ORR activity, these nanoparticles should be synthesised separately and attached to a graphene carbon support at low temperatures without using any nitrogen precursors.

In this study, four different phases of iron oxide were synthesised and incorporated into a 3D-rGO aerogel without the use of any nitrogen precursors (Scheme 1). The effect of different iron oxide phases as ORR catalysts for oxygen reduction was investigated. Currently, there is no comprehensive study evaluating the different phases of iron oxide nanoparticles in graphene aerogels as ORR catalysts. Knowledge of the chemical and structural composition of the prepared composites along with their electrochemical catalytic properties for ORR activity will aid in the design of new iron oxide catalysts.

2. Experimental

2.1 Materials and methods

Natural graphite rock (Uley, Eyre Peninsula, SA) was milled into a fine powder using a bench top ring mill (Rocklabs). Iron(II) sulphate heptahydrate (FeSO₄·7H₂O), polyethylene glycol (PEG), sodium hydroxide (NaOH), hydrogen peroxide (H₂O₂), iron(III) chloride hexahydrate (FeCl₃·6H₂O), iron(II) chloride tetra hydrate (FeCl₂·4H₂O), hydrochloric acid (HCl), potassium permanganate (KMnO₄), sulphuric acid (H₂SO₄), phosphoric acid (H₃PO₄), ethylene diamine, thiourea, sodium acetate, L-ascorbic acid and polyvinylpyrrolidone (PVP) were purchased from Sigma-Aldrich and Chem-Supply. A commercially available Pt/C (20% w/w) was used as the standard catalyst. The Nafion

dispersion (D1021-10% water base) was purchased from Fuel Cell Stores, USA.

2.2 Preparation of graphene oxide (GO)

Graphene oxide was synthesised using the improved Hummer's method.⁴³ A mixture of concentrated acids, H₂SO₄/H₃PO₄ (9 : 1), was added to a mixture of graphite flakes (3.0 g) and KMnO₄ (18.0 g). The reaction was then heated to 50 °C and stirred for 12 h. The solution was cooled and poured onto ice (400 mL) containing H₂O₂ (3 mL). The mixture was centrifuged (4000 rpm) for 2 h and the supernatant was removed. The precipitate was then washed in succession of water (2 × 200 mL), 30% HCl (2 × 200 mL) and ethanol (2 × 200 mL). The final product was collected and vacuum dried overnight at room temperature.

2.3 Synthesis of iron oxide nanoparticles

Fe₃O₄,⁴⁴ γ-Fe₂O₃,⁴⁵ α-Fe₂O₃⁴⁶ and α-FeOOH⁴⁷ nanoparticles were synthesised using previously established methods as outlined below.

2.3.1 Synthesis of Fe₃O₄ nanoparticles. Iron(II) sulphate heptahydrate (FeSO₄·7H₂O) (7.56 g) was dissolved in DI water (90 mL) at 30 °C. Polyethylene glycol (PEG-2000, 30 mL) was slowly added and stirred until it was dissolved. The pH was adjusted to 9.8 using 0.1 M NaOH solution. After adding 800 μL of H₂O₂ (30%) the solution was stirred for a further 20 min. Finally, the solution was transferred into an autoclave and heated for 5 h at 160 °C. The product was then washed 5 times with water and ethanol (5 × 40 mL) and dried at 70 °C.

2.3.2 Synthesis of γ-Fe₂O₃ nanoparticles. FeCl₂·4H₂O (39.76 g) and FeCl₃·6H₂O (16.29 g) were dissolved in 1 M HCl (100 mL). The pH of the solution was adjusted to 9.8 using 0.1 M NaOH solution and stirred for another 2 h. Finally, the product was centrifuged, washed 3 times with 40 mL DI water (3 × 40 mL) and once with ethanol, and dried for 6 h at 60–70 °C.

2.3.3 Synthesis of α-Fe₂O₃ nanoparticles. FeCl₃·6H₂O (4 mmol), sodium acetate (40 mmol) and PVP (1.0 g) were dissolved in DI water (30 mL) and stirred for 2 h at 40 °C. The solution was transferred into an autoclave and heated for 18 h

at 200 °C. Finally, the product was washed 3 times with 40 mL DI water and 3 times with 40 mL ethanol, respectively, and dried at 70 °C for 10 h.

2.3.4 Synthesis of α -FeOOH nanorods. Ethylene diamine (15 mmol), $\text{FeCl}_3 \cdot 6\text{H}_2\text{O}$ (11 mmol) and thiourea (13 mmol) were dissolved in DI water (40 mL) and the solution was stirred for 10 min. Then, the solution was transferred to an autoclave and heated for 5 h at 130 °C. The final product was obtained by centrifuging the product, washed with ethanol and water (1 : 1) (3×40 mL), and dried at 70 °C for 5 h.

2.4 Preparation of iron oxide nanoparticle/graphene aerogels

GO solution was prepared by ultrasonically dispersing 15 mg of GO in DI water (10 mL) for 2 h. The iron oxide suspension was prepared by dispersing the iron oxide nanoparticles (40 mg) with DI water (5 mL) and sonicated for 30 min. Then, both GO and iron oxide suspensions were transferred into glass test tubes (20×150 mm) and stirred using a magnetic stirrer for 10 min at room temperature. This was followed by the addition of L-ascorbic acid (0.15 g) to the suspension and further stirring for another 10 min. The pH of the suspension was adjusted accordingly to retain the relevant iron oxide phases in the anticipated rGO/iron oxide aerogels. For the preparation of the rGO/ Fe_3O_4 and rGO/ γ - Fe_2O_3 aerogels, the pH was adjusted to pH 10, while for the preparation of rGO/ α - Fe_2O_3 the suspension was neutralised to pH 7 using 0.1 M NaOH solution. No adjustment for pH was made for the preparation of rGO/ α -FeOOH, for which the as-prepared suspension showed a pH value of 3.2. After adjusting the pH, the as-prepared rGO/iron oxide suspensions were then heated for 5 h at 80 °C in an oil bath without stirring or any disturbances until black coloured hydrogels were formed. The obtained hydrogels were then cooled to room temperature and the liquid phase was carefully drained using a plastic pipette. The glass tubes containing the hydrogels were freeze dried for 24 h to obtain the rGO/iron oxide aerogel. These aerogels synthesised using Fe_3O_4 , γ - Fe_2O_3 , α - Fe_2O_3 and α -FeOOH are referred to as rGO/ Fe_3O_4 , rGO/ γ - Fe_2O_3 , rGO/ α - Fe_2O_3 and rGO/ α -FeOOH, respectively, in this study. The reduced GO aerogel was produced as the reference material without the addition of any iron oxide nanoparticles and is referred to as rGO.

2.5 Preparation of catalytic ink

Catalytic ink was prepared by ultrasonically dispersing each catalyst (1 mg) in a 1% Nafion suspension (1 mL). The prepared ink (10 μL) was carefully deposited on both a glassy carbon rotating disc electrode (3 mm) and a rotating ring disc electrode (4 mm). The sample was allowed to dry in air for 12 h. A commercially available Pt/C catalyst (20 wt%) was prepared in a similar way and used as the standard catalyst.

2.6 Characterisation

2.6.1 Structural and chemical composition. The synthesised rGO/iron oxide aerogels were characterised using several analytical techniques; namely, scanning electron microscopy (SEM, Quanta 450, FEI, USA), transition electron microscopy

(TEM, Technai G2 Spirit, FEI, USA), Raman spectroscopy (LabRAM Evolution, Horiba Jvonyon, Japan) and X-ray diffraction (XRD, Miniflex 600, Rigaku, Japan). TEM samples were ultrasonicated in ethanol for 10 min, then drop casted onto copper grids and measured at an accelerating voltage of 120 kV. XRD measurements were performed at 40 kV and 15 mA in the range $2\theta = 20$ – 75° at a scan speed of $10^\circ\text{C min}^{-1}$. Raman analysis was carried out using a 532 nm laser using an integration time of 10 s for 3 accumulations with a retention time of 1 s. The laser power was kept at 10% to prevent any preheating of the sample, and a confocal size of 300 μm was used.

2.6.2 Electrochemical. The ORR reactions were conducted utilising a Rotating Ring Disc Electrode (RRDE) apparatus connected to a bi-potentiostat (CH 1760 C, CH Instruments Inc., USA) in a standard three-electrode cell with oxygen saturated KOH (0.1 mol L^{-1}) solution. The glassy carbon electrode, platinum electrode and reversible hydrogen electrode (RHE) were used as the working, counter and reference electrodes, respectively. The scan rate of the reaction was 0.10 V s^{-1} in the range 0–1.1 V. The cycle was repeated until stable voltammograms were obtained before the RRDE readings were derived at different speeds from 400 to 2400 rpm.

The reaction kinetics of the aerogels was examined by employing RRDE to quantify the overall electron transfer number (n) and percentage of hydrogen peroxide ($\% \text{HO}_2^-$), at rotation speeds from 400 to 2400 rpm in an oxygen-saturated 0.1 M KOH solution. To elucidate the overall number of electrons (n) and $\% \text{HO}_2^-$ produced in the ring against the applied potential, eqn (1) and (2) were employed.^{48,49}

$$n = \frac{4I_D}{I_D + \frac{I_R}{N}} \quad (1)$$

$$\% \text{HO}_2^- = 100 \frac{2I_R}{I_D N + I_R} \quad (2)$$

where I_D and I_R are the disc and ring currents, respectively, and N is the collection efficiency.

3. Results and discussion

3.1 Characterisation of synthesised materials

The typical morphology of the synthesised nanoparticles (Fe_3O_4 , γ - Fe_2O_3 , α - Fe_2O_3 and α -FeOOH) is shown in Fig. 1. The TEM images show well-defined nanoparticles for Fe_3O_4 (30–60 nm), γ - Fe_2O_3 (20–30 nm) and α - Fe_2O_3 (40–60 nm), and nanorods for α -FeOOH (150–200 nm).

These nanoparticles (NPs) were used to prepare rGO/iron oxide aerogels. Iron oxide nanoparticles were electrostatically bound to GO sheets through the carboxylic acid groups on the surface.⁵⁰ The protonation of the reducing agent (L-AA) further reduced the hydrophilicity of the GO sheets⁵¹ resulting in the formation of the 3D rGO/iron oxide aerogels. The morphology of the rGO/iron oxide aerogels was determined by SEM and is presented in Fig. 2. The SEM images of the aerogels show that the rGO sheets and iron oxide NPs formed porous 3D networks.

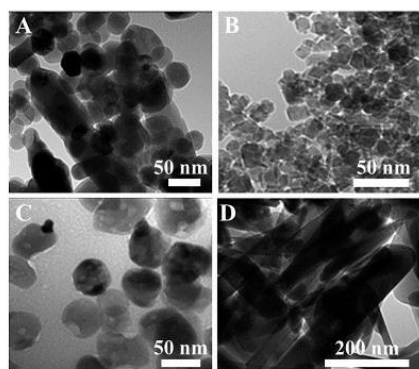


Fig. 1 TEM images of the (A) Fe_3O_4 , (B) $\gamma\text{-Fe}_2\text{O}_3$ and (C) $\alpha\text{-Fe}_2\text{O}_3$ nanoparticles and (D) $\alpha\text{-FeOOH}$ nanorods.

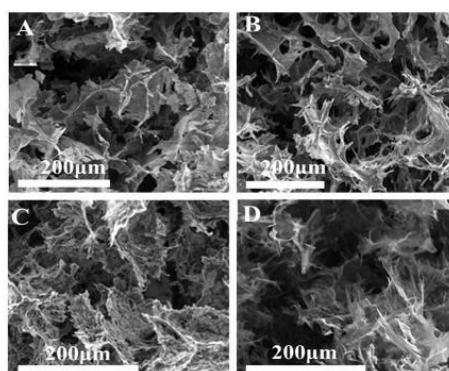


Fig. 2 SEM images of (A) $\text{rGO}/\text{Fe}_3\text{O}_4$, (B) $\text{rGO}/\gamma\text{-Fe}_2\text{O}_3$, (C) $\text{rGO}/\alpha\text{-Fe}_2\text{O}_3$ and (D) the $\text{rGO}/\alpha\text{-FeOOH}$ aerogel.

The TEM images of the iron oxide composites are also shown in Fig. S1 (ESI[†]).

The EDX analysis clearly shows the three major elements (C, O and Fe) in the composites (Fig. S2, ESI[†]). The loading capacity of iron nanoparticles in the different composites is detailed in Table S1 (ESI[†]).

The aerogels were exposed to an external magnet to examine their magnetic properties (Fig. S3, ESI[†]). The images show that $\text{rGO}/\text{Fe}_3\text{O}_4$ (Fig. S3A, ESI[†]) and $\text{rGO}/\gamma\text{-Fe}_2\text{O}_3$ (Fig. S3B, ESI[†]) containing ferromagnetic iron oxides displayed magnetic properties and were attracted to the external magnet. In contrast, $\text{rGO}/\alpha\text{-Fe}_2\text{O}_3$ (Fig. S3C, ESI[†]) and $\text{rGO}/\alpha\text{-FeOOH}$ (Fig. S3D, ESI[†]), which are anti ferromagnetic, did not show any attraction to the external magnet.

The XRD analysis presented in Fig. 3 confirmed the crystal phases of the magnetic and non-magnetic iron oxide NPs. Crystalline inverse spinel structures of Fe_3O_4 (JCPDS 65-3107)⁴⁴ and $\gamma\text{-Fe}_2\text{O}_3$ (JCPDS NO 39-1346)⁴⁵ were measured, whereas the rhombohedral phase of $\alpha\text{-Fe}_2\text{O}_3$ (JCPDS 84-0307)⁴⁶ and pure orthorhombic phase of $\alpha\text{-FeOOH}$ (JCPDC 29-0713) were detected.⁴⁷

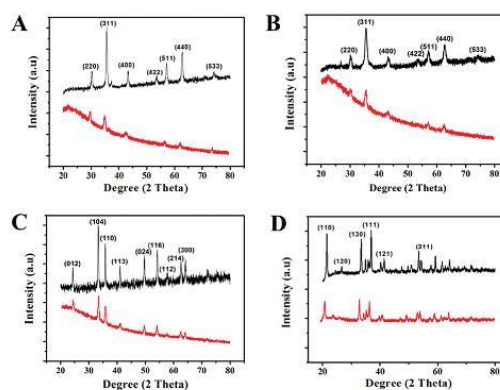


Fig. 3 XRD patterns of (A) Fe_3O_4 , (B) $\gamma\text{-Fe}_2\text{O}_3$, (C) $\alpha\text{-Fe}_2\text{O}_3$ and (D) $\alpha\text{-FeOOH}$ iron oxide nanoparticles (black) and the $\text{rGO}/\text{iron oxide}$ aerogel (red), respectively.

The XRD pattern of $\text{rGO}/\text{iron oxide}$ aerogels confirmed that the NPs were attached to the rGO sheets. The well-defined characteristic peaks of the iron nanoparticles in the composite materials confirm that there are no phase changes during the synthetic process, which is critical to individually analysing their electrocatalytic performances. The XRD image of GO is shown in the ESI[†] (Fig. S4). The disappearance of the peak at $2\theta = 10.3^\circ$, which corresponds to the (002) plane of GO in the $\text{rGO}/\text{iron oxide}$ aerogels, indicates the reduction of oxygenate groups.^{52,53} This diffraction peak, however, is not noticeable due to the low crystallinity of the structure compared with metal oxide materials.

Further changes in the structures were measured by Raman. For all aerogels, two characteristic peaks were present in the Raman spectra at 1350 and 1583 cm^{-1} , which were assigned to the D and G bands for the graphene structures, respectively.⁵⁴ The G band relates to the formation of sp^2 carbons (C-C) while the D band illustrates the structural defects induced in the graphitic structure (sp^2 bonded carbon), such as layer distortion, rotation and oxygen invasion.⁵⁵ The higher intensity ratio of I_D/I_G observed in the aerogels compared with GO was due to the presence of the iron oxide NPs within the rGO sheets causing an increase in the disorder of the D band (Fig. S5, ESI[†]).

3.2 Voltammetry characterisation using the rotating ring disc electrode technique

The catalytic ORR potential of the prepared FeNPs aerogels composites was confirmed by cyclic voltammetry (CV) (Fig. S6, ESI[†]). The voltammograms showed oxygen reduction cathodic peaks for $\text{rGO}/\text{Fe}_3\text{O}_4$ (0.57 V), $\text{rGO}/\gamma\text{-Fe}_2\text{O}_3$ (0.56 V), $\text{rGO}/\alpha\text{-Fe}_2\text{O}_3$ (0.55 V), $\text{rGO}/\alpha\text{-FeOOH}$ (0.57 V) and rGO (0.52 V). The cathodic peaks of all catalysts slightly shifted (positively) showing more ORR activity compared with rGO . The ORR electron transfer pathway was determined using the RRDE technique, which measures the electron transfer number and %hydroperoxyl anion ($\%\text{HO}_2^-$) evolved at the disc electrode. Comparative studies for

Table 1 Electrochemical properties of graphene/iron oxide aerogels

	Current density (mA cm ⁻²) at 0 V (RHE)	Onset potential (RHE) (V)	Number of electrons (<i>n</i>) 0.20–0.70 V (RHE)	% (HO ₂ ⁻) 0.20–0.70 V (RHE)
rGO/Fe ₃ O ₄	4.20	0.80	3.63–3.03	18.22–48.43
rGO/γ-Fe ₂ O ₃	4.22	0.81	3.74–3.09	12.62–45.04
rGO/α-Fe ₂ O ₃	3.58	0.78	3.10–2.41	44.58–79.26
rGO/α-FeOOH	3.96	0.79	3.60–2.68	19.73–65.61
rGO	2.69	0.78	3.22–2.30	38.60–81.73
Pt/C	5.62	0.98	3.76–3.95	11.52–2.15

the ring and disc currents (Fig. S7, ESI[†]) of the aerogels, rGO and Pt/C catalyst (141 μg cm⁻² catalysts) have shown the measured onset potential and current densities (Table 1). The comparison of the linear sweep voltammetry (LSV) of the bare glassy carbon electrode with rGO and rGO/Fe₃O₄, rGO/γ-Fe₂O₃, rGO/α-Fe₂O₃ and rGO/α-FeOOH (Fig. S8, ESI[†]) shows that the onset potential of the rGO/iron oxide catalysts and rGO has shifted more positively compared with the onset potential of the bare glassy carbon electrode (0.68 V) showing ORR activity.

The linear sweep voltammetry (LSV) (Fig. S8, ESI[†]) of the catalysts revealed that the ORR is carried out through mixed kinetic and diffusion controlled mechanisms releasing HO₂⁻. In contrast, the LSV of the standard Pt/C catalysts showed a mixed kinetic and diffusion region at a high over potential (0.94–0.82 V) that eventually approached the current limiting value below 0.82 V.⁵⁶ The negative onset potential of the aerogels when contrasted against the standard Pt/C (0.98 V) indicated that the oxygen coverage and diffusion on the surface of the aerogels were less efficient. However, rGO/γ-Fe₂O₃ showed the highest onset potential of 0.81 V. The standard rGO material had the lowest current density and onset potential, indicating that the presence of iron oxides on the aerogels initiated the catalytic activity for ORR.

The number of electrons transferred (Fig. 4) for the ORR reaction and the %HO₂⁻ generated at the ring electrode were determined using eqn (1) and (2) (detailed in the experimental section) and the data are shown in Table 1. The highest percentage of the unwanted intermediate material, HO₂⁻, was found in α-Fe₂O₃ and rGO. The three other aerogels had less than half the %HO₂⁻ of rGO, indicating that a significant increase in efficiency had been achieved. All of the aerogel electron transfer numbers descended, which is in contrast with the standard

Pt/C catalysts, which ascended when the potential was increased from 0.20 to 0.70 V (Fig. 4). Both ferromagnetic aerogels (rGO/Fe₃O₄ and rGO/γ-Fe₂O₃) contributed more effectively than the antiferromagnetic rGO/α-Fe₂O₃ and rGO/α-FeOOH for ORR, which confirms the findings of Zeng *et al.*⁵⁷ and Wang *et al.*⁵⁸ who reported that magnetic catalytic activity was enhanced for ORR by improving mass transport of oxygen at the electrode–electrolyte interface. The antiferromagnetic aerogels showed lower ORR catalytic activity; however, rGO/α-FeOOH showed greater activity than rGO/α-Fe₂O₃. Cheng *et al.*⁵⁹ investigated the influence of spinel structures on the reactivity of ORR using Density Functional Theory (DFT) to fit the experimental data. It was reported that the spinel structures are able to provide an increased number of active sites for M–O₂ adsorption and drive the ORR reaction towards a four-electron pathway. Wu *et al.*⁶⁰ reported that the inverse spinel structures could adsorb O₂ with an elongated O–O bond compared with the normal spinel structure, which facilitated O–O bond cleavage to increase ORR activity. In contrast, rhombohedral⁶¹ or orthorhombic⁶² phases that have been tested with different metals did not show high activities towards ORR. Higher activities were only present when these iron oxides were converted to cubic structures.^{61,62} Fe₃O₄ possesses an inverse spinel crystal structure with alternating octahedral and octahedral-tetrahedral layers with some Fe⁺³ cations that are occupied in tetrahedral positions, and the remaining Fe³⁺ and the Fe²⁺ are placed in the octahedral sites. γ-Fe₂O₃ also has an inverse spinel structure similar to Fe₃O₄ where the Fe³⁺ ions are placed in both the tetrahedral and octahedral sites with vacancies in the cation sublattice.^{63,64} The enhanced catalytic activity of Fe₃O₄ and γ-Fe₂O₃ can be attributed to the greater number of oxygen adsorption active sites

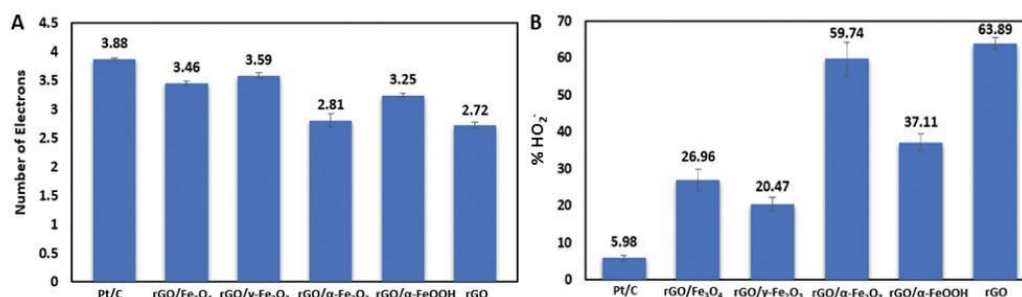


Fig. 4 Comparison of (A) the electron transfer number and (B) the %HO₂⁻ of rGO/Fe₃O₄, rGO/γ-Fe₂O₃, rGO/α-Fe₂O₃, rGO/α-FeOOH, rGO and the Pt/C electrodes at potential 0.40 V in oxygen-saturated 0.1 M KOH at 1600 rpm at a scan rate of 10 mV s⁻¹.

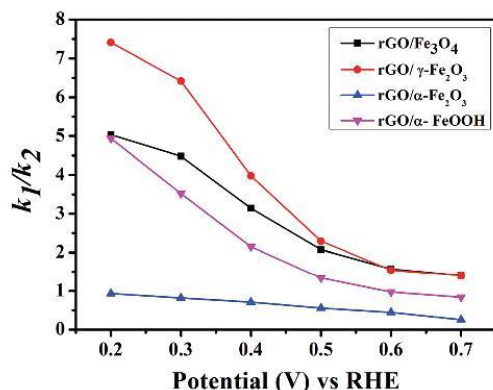


Fig. 5 The potential dependence of k_1/k_2 values of rGO/Fe₃O₄, rGO/γ-Fe₂O₃, rGO/α-Fe₂O₃ and rGO/α-FeOOH in the potential range of 0.20–0.70 V.

and easy O₂ cleavage provided by the inverse spinel structures of both Fe₃O₄ and γ-Fe₂O₃.

Electrical conductivity for ORR catalysts to transport electrons is also important for catalytic activity.⁶⁵ The conductivity of the aerogels was measured (ESI† Section 1, Table S2) and it was found to be consistent with the exception of rGO/α-Fe₂O₃, which had a conductivity that was an order of magnitude lower than that of the other aerogels. This is consistent with the lower catalytic activity of rGO/α-Fe₂O₃ due to the reduction in electron transport efficiency for ORR catalysis.

The electron transfer kinetics was determined using equations proposed by Hsueh *et al.*⁶⁶ based on the model by Damjanovic *et al.*⁶⁷ (ESI† Section 2). The ratios of k_1/k_2 were plotted for each aerogel from their individual kinetics (Fig. S9, ESI†) to analyse the dependence of k_1 and k_2 kinetics and are presented in (Fig. 5). At 0.20 V, the k_1/k_2 ratio for the materials is >5 with the exception of rGO/α-Fe₂O₃, which has a k_1/k_2 ratio of <1. This indicates that, with the exception of rGO/α-Fe₂O₃, the reaction proceeds *via* a four-electron transfer pathway at lower potentials, indicating that oxygen is being reduced to OH⁻ without the formation of the intermediate hydroperoxyl ion.

4. Conclusions

Four different iron oxide phases (Fe₃O₄, γ-Fe₂O₃, α-Fe₂O₃ and α-FeOOH) were successfully synthesised and bound to rGO sheets forming 3D-rGO/iron oxide aerogels at low temperatures. Their phase structures remained unchanged after binding, which is critical for analysing the individual properties of each material. An electrochemical study showed that the ferromagnetic aerogels (rGO/Fe₃O₄ and rGO/γ-Fe₂O₃) have the highest activity in terms of onset potential and electron transfer number due to their inverse spinel structure, magnetic properties and electrical conductivity. All of the aerogels, with the exception of α-Fe₂O₃, proceeded *via* a four-electron transfer pathway at lower potential regions. At a high potential (0.70 V), all of the aerogels were driven through the two-electron pathway producing HO₂⁻ as an

intermediate. The activity of the catalysts can be attributed to a combination of factors, such as crystal structure, oxidation state, carbon support, electrical conductivity and magnetism. This study reveals that the four different iron phases (Fe₃O₄, γ-Fe₂O₃, α-Fe₂O₃ and α-FeOOH) tested show different catalytic activity and, in particular, the different phases strongly adjust the level of HO₂⁻ generation in the process. However, further studies on the effect of particle size and shape, electron conductivity and magnetism on catalytic reactivity should also be performed to understand the influence of iron oxide in the graphene structure.

Conflicts of interest

There are no conflicts to declare.

Acknowledgements

The authors acknowledge the support of the Australian Research Council (IH 150100003), the Australian Research Council Research Hub for Graphene Enabled Industry Transformation, the Australian Solar Thermal Research Initiative (ASTRI), the School of Chemical Engineering of the University of Adelaide and the School of Chemistry of the University of Adelaide. The technical support provided by Adelaide Microscopy was also greatly appreciated.

References

- S. Shafiee and E. Topal, *Energy Policy*, 2009, **37**, 181–189.
- M. Kampa and E. Castanas, *Environ. Pollut.*, 2008, **151**, 362–367.
- V. Ediger and E. Kentel, *Energy Convers. Manage.*, 1999, **40**, 743–755.
- S. A. Boudghene and E. Traversa, *Renewable Sustainable Energy Rev.*, 2002, **6**, 295–304.
- Z. Yang, Z. Yao, G. Li, G. Fang, H. Nie, Z. Liu, X. Zhou, X. Chen and S. Huang, *ACS Nano*, 2012, **6**, 205–211.
- S. Zhang, X. Yuan, J. N. C. Hin, H. Wang, K. A. Friedrich and M. Schulze, *J. Power Sources*, 2009, **194**, 588–600.
- N. Markovic, T. Schmidt, V. Stamenkovic and P. Ross, *Fuel Cells*, 2001, **1**, 105–116.
- N. M. Markovic, H. A. Gasteiger and P. N. Ross, *J. Phys. Chem.*, 1995, **99**, 3411–3415.
- L. Qu, Y. Liu, J. Baek and L. Dai, *ACS Nano*, 2010, **4**, 1321–1326.
- V. Komanicky, A. Menzel and H. You, *J. Phys. Chem. B*, 2005, **109**, 23550–23557.
- C. Xiong, Z. Wei, B. Hu, S. Chen, L. Li, L. Guo, W. Ding, X. Liu, W. Ji and X. Wang, *J. Power Sources*, 2012, **215**, 216–220.
- L. Yang, S. Jiang, Y. Zhao, L. Zhu, S. Chen, X. Wang, Q. Wu, J. Ma, Y. Ma and Z. Hu, *Angew. Chem., Int. Ed.*, 2011, **123**, 7270–7273.
- J. Wu, Z. Yang, X. Li, Q. Sun, C. Jin, P. Strasser and R. Yang, *J. Mater. Chem. A*, 2013, **1**, 9889–9896.
- W. Li, D. Yang, H. Chen, Y. Gao and H. Li, *Electrochim. Acta*, 2015, **165**, 191–197.
- R. Bashyam and P. Zelenay, *Nature*, 2006, **443**, 63–66.

- 16 S. Yoshimoto, J. Inukai, A. Tada, T. Abe, T. Morimoto, A. Osuka, H. Furuta and K. Itaya, *J. Phys. Chem. B*, 2004, **108**, 1948–1954.
- 17 R. J. Toh, Z. Sofer and M. Pumera, *ChemPhysChem*, 2015, **16**, 3527–3531.
- 18 X. Zhang, X. Wang, L. Le, A. Ma and S. Lin, *J. Mater. Chem. A*, 2015, **3**, 19273–19276.
- 19 M. Sun, Y. Dong, G. Zhang, J. Qu and J. Li, *J. Mater. Chem. A*, 2014, **2**, 13635–13640.
- 20 C. Pecharrómán, T. Gonzalez-Carreno and J. E. Iglesias, *Phys. Chem. Miner.*, 1995, **22**, 21–29.
- 21 D. Thapa, V. R. Palkar, M. B. Kurup and S. K. Malik, *Mater. Lett.*, 2004, **58**, 2692–2694.
- 22 R. Voskanyan, R. Levitin and V. Shchurov, *J. Exp. Theor. Phys.*, 1968, **26**, 302–304.
- 23 J. Forsyth, I. Hedley and C. Johnson, *J. Phys. C: Solid State Phys.*, 1968, **1**, 179.
- 24 M. Chirita, I. Grozescu, L. Taubert, H. Radulescu, E. Princz, É. Stefanovits-Bányai, C. Caramalau, L. Bulgariu, M. Macoveanu and C. Muntean, *Chem. Bull.*, 2009, **54**, 1–8.
- 25 E. Zepeda-Alarcon, H. Nakotte, A. F. Gualtieri, G. King, K. Page, S. C. Vogel, H. W. Wang and H. R. Wenk, *J. Appl. Crystallogr.*, 2014, **47**, 1983–1991.
- 26 J. Roger, J. Pons, R. Massart, R. A. Halbreich and J. Bacri, *Eur. Phys. J.: Appl. Phys.*, 1999, **5**, 321–325.
- 27 C. T. Yavuz, J. Mayo, W. Y. William, A. Prakash, J. C. Falkner, S. Yean, L. Cong, H. J. Shipley, A. Kan and M. Tomson, *Science*, 2006, **314**, 964–967.
- 28 A. Etale, H. Tutu and D. C. Drake, *Appl. Water Sci.*, 2016, **6**, 187–197.
- 29 A. Ito, H. Jitsunobu, Y. Kawabe, H. Ijima and M. Kamihira, *Tissue Eng., Part C*, 2009, **15**, 413–423.
- 30 D. Fiorani, A. Testa, F. Lucari, F. D'orazio and H. Romero, *Physica B*, 2002, **320**, 122–126.
- 31 J. Wu, J. Wang, H. Li, Y. Du, K. Huang and B. Liu, *J. Mater. Chem. A*, 2013, **1**, 9837–9847.
- 32 Y. Lin, S. Zhou, S. W. Sheehan and D. Wang, *J. Am. Chem. Soc.*, 2011, **133**, 2398–2401.
- 33 D. Larcher, C. Masquelier, D. Bonnin, Y. Chabre, V. Masson, J. B. Leriche and J. M. Tarascon, *J. Electrochem. Soc.*, 2003, **150**, A133–A139.
- 34 I. Andjelkovic, D. H. H. Tran, S. Kabiri, S. Azari, M. Markovic and D. Losic, *ACS Appl. Mater. Interfaces*, 2015, **7**, 9758–9766.
- 35 A. Jaiswal, S. Banerjee, R. Mani and M. C. Chattopadhyaya, *J. Environ. Chem. Eng.*, 2013, **1**, 281–289.
- 36 S. Tang, H. Huangfu, Z. Dai, L. Sui and Z. Zhu, *Int. J. Electrochem. Sci.*, 2015, **10**, 7180–7191.
- 37 C. Xu, X. Shi, A. Ji, L. Shi, C. Zhou and Y. Cui, *PLoS One*, 2015, **10**, e0144842.
- 38 X. Liu and W. Hu, *RSC Adv.*, 2016, **6**, 29848–29854.
- 39 Y. Tang, B. L. Allen, D. R. Kauffman and A. Star, *J. Am. Chem. Soc.*, 2009, **131**, 13200–13201.
- 40 D. W. Wang and D. Su, *Energy Environ. Sci.*, 2014, **7**, 576–591.
- 41 Z. Yang, H. Nie, X. Chen, X. Chen and S. Huang, *J. Power Sources*, 2013, **236**, 238–249.
- 42 V. Nallathambi, J. W. Lee, S. P. Kumaraguru, G. Wu and B. N. Popov, *J. Power Sources*, 2008, **183**, 34–42.
- 43 D. C. Marcano, D. V. Kosynkin, J. M. Berlin, A. Sinitskii, Z. Sun, A. Slesarev, L. B. Alemany, W. Lu and J. M. Tour, *ACS Nano*, 2010, **4**, 4806–4814.
- 44 G. Li, Y. Jiang, K. Huang, P. Ding and J. Chen, *J. Alloys Compd.*, 2008, **466**, 451–456.
- 45 E. Darezereshki, *Mater. Lett.*, 2010, **64**, 1471–1472.
- 46 M. Zhu, Y. Wang, D. Meng, X. Qin and G. Diao, *J. Phys. Chem. C*, 2012, **116**, 16276–16285.
- 47 R. Zamiri, H. Ahangar, A. Zakaria, G. Zamiri, H. Bahari and G. C. Drummen, *J. Nanopart. Res.*, 2014, **16**, 1–10.
- 48 S. Dou, L. Tao, J. Huo, S. Wang and L. Dai, *Energy Environ. Sci.*, 2016, **9**, 1320–1326.
- 49 Y. Liang, Y. Li, H. Wang, J. Zhou, J. Wang, T. Regier and H. Dai, *Nat. Mater.*, 2011, **10**, 780–786.
- 50 O. C. Compton, Z. An, K. W. Putz, B. J. Hong, B. G. Hauser, L. C. Brinson and S. T. Nguyen, *Carbon*, 2012, **50**, 3399–3406.
- 51 J. Zhang, H. Yang, G. Shen, P. Cheng, J. Zhang and S. Guo, *Chem. Commun.*, 2010, **46**, 1112–1114.
- 52 T. T. Tung, R. Karunakaran, D. N. H. Tran, B. Gao, S. Chowdhury, I. Pillin, M. Castro, J. F. Feller and D. Losic, *J. Mater. Chem. C*, 2016, **4**, 3422–3430.
- 53 T. T. Tung, J. Yoo, F. K. Alotaibi, Md. J. Nine, R. Karunakaran, M. Krenzs, G. T. Nguyen, D. N. H. Tran, J. F. Feller and D. Losic, *ACS Appl. Mater. Interfaces*, 2016, **8**, 16521–16532.
- 54 T. T. Tung, R. Karunakaran, D. N. H. Tran, B. Gao, S. Chowdhury, I. Pillin, M. Castro, J. F. Feller and D. Losic, *J. Mater. Chem. C*, 2016, **4**, 3422–3430.
- 55 C. Y. Yang, C. L. Wu, Y. H. Lin, L. H. Tsai, Y. C. Chi, J. H. Chang, C. I. Wu, H. K. Tsai, D. P. Tsai and G. R. Lin, *Opt. Mater. Express*, 2013, **3**, 1893–1905.
- 56 B. Narayanamoorthy, K. K. R. Datta and S. Balaji, *J. Colloid Interface Sci.*, 2012, **387**, 213–220.
- 57 J. Zeng, S. Liao, J. Y. Lee and Z. Liang, *Int. J. Hydrogen Energy*, 2010, **35**, 942–948.
- 58 L. Wang, H. Yang, J. Yang, Y. Yang, R. Wang, S. Li, H. Wang and S. Ji, *Ionics*, 2016, **22**, 2195–2202.
- 59 F. Cheng, J. Shen, B. Peng, Y. Pan, Z. Tao and J. Chen, *Nat. Chem.*, 2011, **3**, 79–84.
- 60 G. Wu, J. Wang, W. Ding, Y. Nie, L. Li, X. Qi, S. Chen and Z. Wei, *Angew. Chem., Int. Ed.*, 2016, **55**, 1340–1344.
- 61 D. Zhang, Y. Song, Z. Du, L. Wang, Y. Li and J. B. Goodenough, *J. Mater. Chem. A*, 2015, **3**, 9421–9426.
- 62 Y. Feng, T. He and N. Alonso-Vante, *ECS Trans.*, 2009, **25**, 167–173.
- 63 A. Espinosa, A. Serrano, A. Liavona, J. J. de la Morena, M. Abuin, A. Figuerola, T. Pellegrino, J. Fernandez, M. Garcia-Hernandez and G. Castra, *Meas. Sci. Technol.*, 2011, **23**, 015602.
- 64 A. S. Teja and P. Y. Koh, *Prog. Cryst. Growth Charact. Mater.*, 2009, **55**, 22–45.
- 65 K. Venkidusamy, M. Megharaj, U. Schröder, F. Karouta, S. V. Mohan and R. Naidu, *RSC Adv.*, 2015, **5**, 100790–100798.
- 66 K. L. Hsueh, D. T. Chin and S. Srinivasan, *J. Electroanal. Chem. Interfacial Electrochem.*, 1983, **153**, 79–95.
- 67 A. Damjanovic, M. A. Genshaw and J. O. Bockris, *J. Chem. Phys.*, 1966, **45**, 4057–4059.

Electronic Supplementary Material (ESI) for New Journal of Chemistry.
This journal is © The Royal Society of Chemistry and the Centre National de la Recherche Scientifique 2017

Supporting information for

Study of iron oxide nanoparticle phases in graphene aerogels for oxygen reduction reaction

Ramesh Karunakaran¹, Campbell Coghlan², Tran T. Tung¹, Shervin Kabiri¹, Diana N. T. Tran¹,
Christian J. Doonan^{2*}, Dusan Losic^{1*}

¹School of Chemical Engineering, University of Adelaide, SA, Australia

²Department of Chemistry, University of Adelaide, SA, Australia

*Prof. Dusan Losic,
School of Chemical Engineering,
The University of Adelaide,
Adelaide, SA, 5005 Australia,
Phone: +61 8 8013 4648,
Email: Dusan.losic@adelaide.edu.au

*Dr. Christian Doonan,
Department of Chemistry,
The University of Adelaide,
Adelaide, SA, 5005 Australia,
Phone: +61 8 83135770,
Email: Christian.doonan@adelaide.edu.au

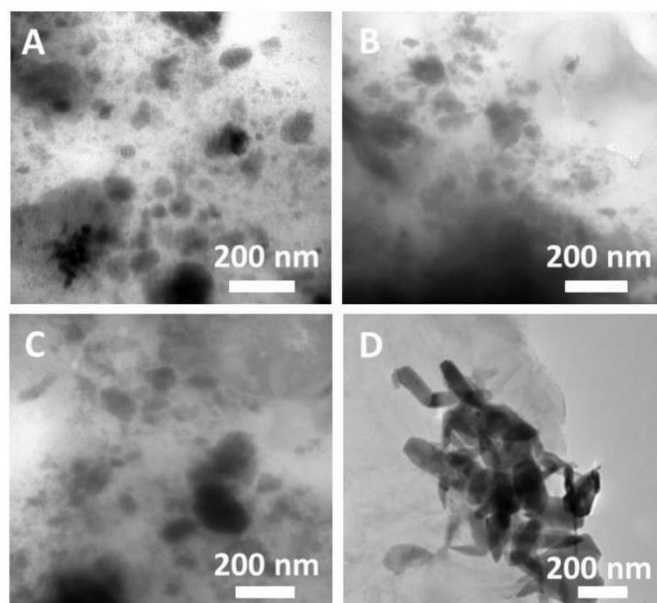


Fig. S1 TEM images of (A) rGO/Fe₃O₄, (B) rGO/γ-Fe₂O₃, (C) rGO/α-Fe₂O₃ and (D) rGO/α-FeOOH aerogel.

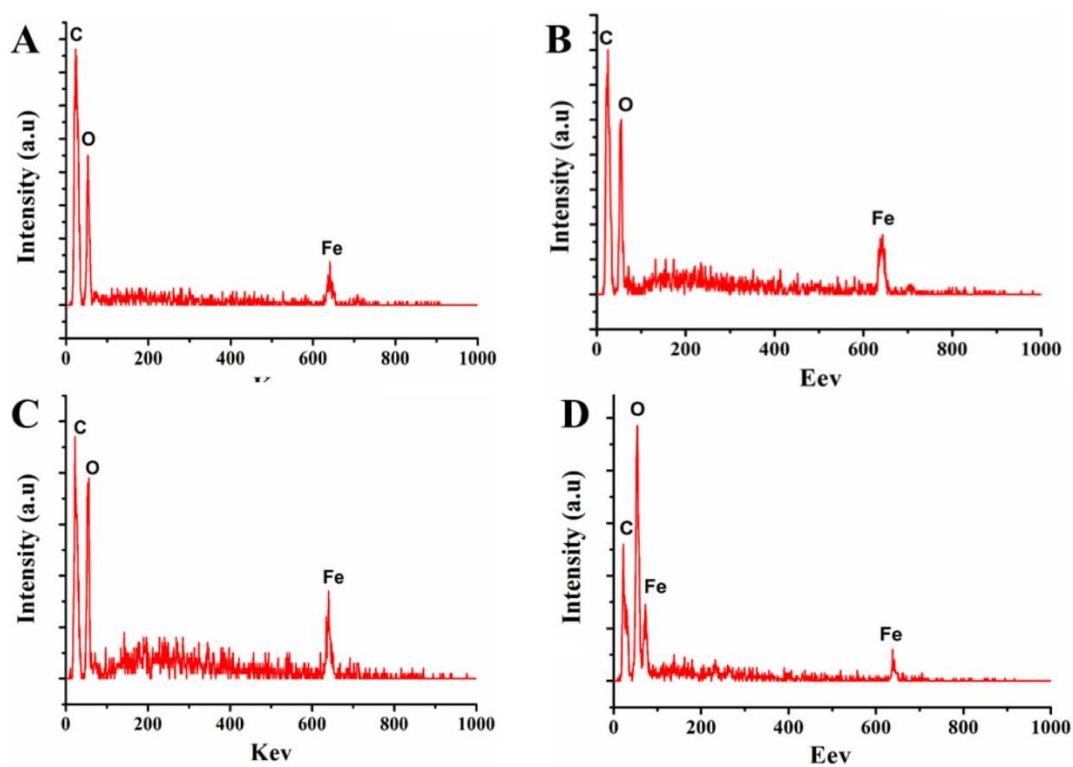


Fig. S2 EDX analysis of (A) rGO/Fe₃O₄, (B) rGO/γ-Fe₂O₃, (C) rGO/α-Fe₂O₃ and (D) rGO/α-FeOOH aerogel

Table S1 Atomic % of C, O and Fe present in (A) rGO/Fe₃O₄, (B) rGO/γ-Fe₂O₃, (C) rGO/α-Fe₂O₃ and (D) rGO/α-FeOOH aerogel determined by EDX analysis.

Catalyst	Atomic %		
	C	O	Fe
rGO/Fe ₃ O ₄	18.87	56.36	24.77
rGO/γ-Fe ₂ O ₃	17.60	52.96	29.44
rGO/α-Fe ₂ O ₃	42.60	33.18	24.22
rGO/α-FeOOH	26.73	46.89	26.36

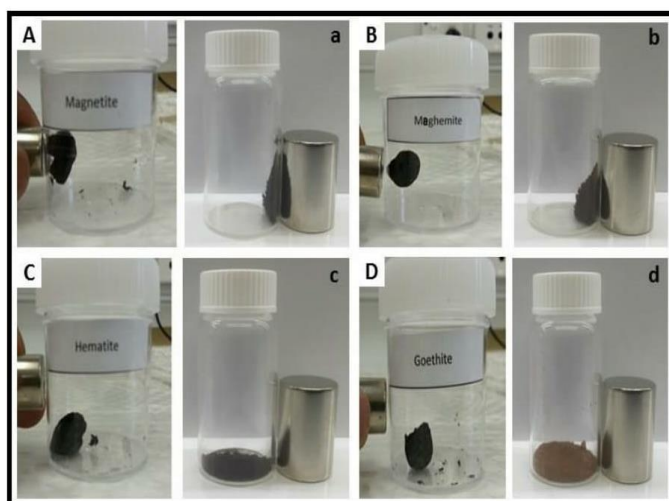


Fig. S3 Photographic image of (A) rGO/Fe₃O₄ and (a) Fe₃O₄ nanoparticle, (B) rGO/γ-Fe₂O₃ and (b) γ-Fe₂O₃ nanoparticle, (C) rGO/ α-Fe₂O₃ and (c) α-Fe₂O₃ nanoparticles and (D) rGO/ α-FeOOH and (d) α-FeOOH nanoparticle exposed to an external magnet.

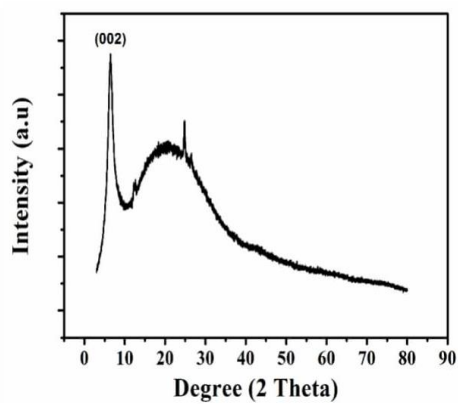


Fig. S4 XRD pattern of GO.

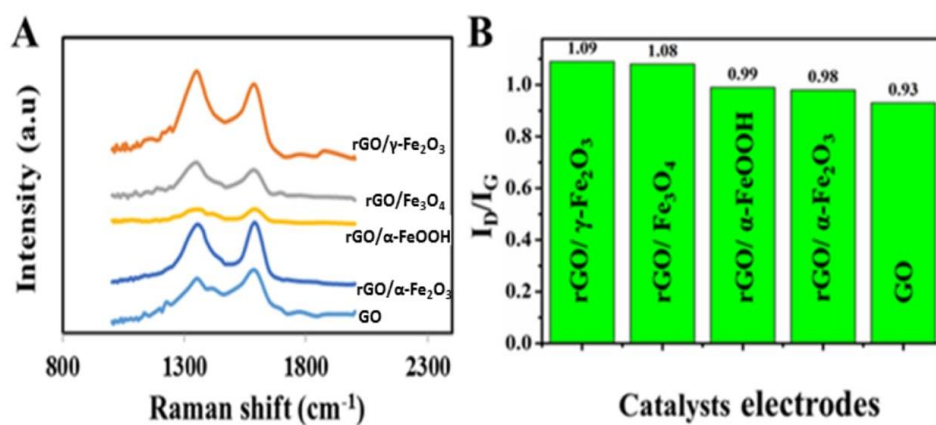


Fig. S5 (A) Raman spectrum and B) I_D/I_G ratio of all synthesized aerogels and GO

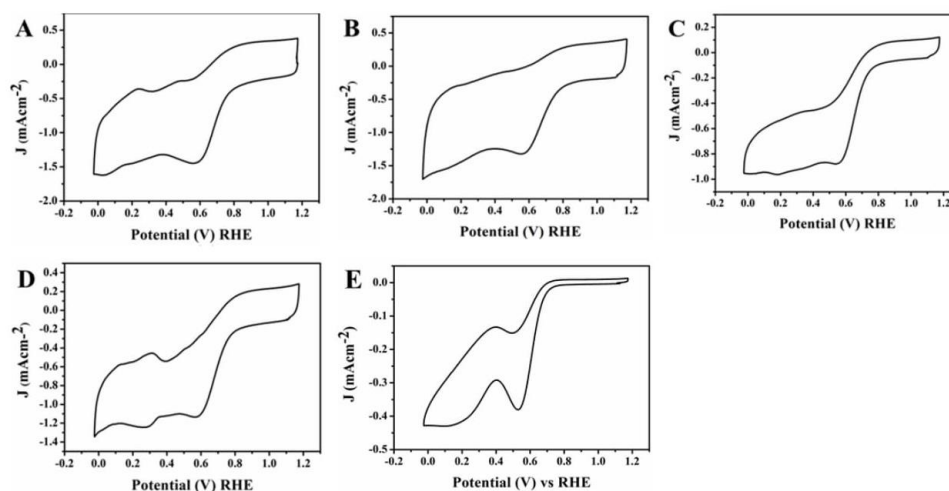


Fig. S6 CV curves of (A) rGO/Fe₃O₄ (B) rGO/γ-Fe₂O₃ (C) rGO/α-FeOOH, (D) rGO/α-FeOOH and (E) rGO at a scan rate of 100 mV s⁻¹ in oxygen saturated 0.1 M KOH solution.

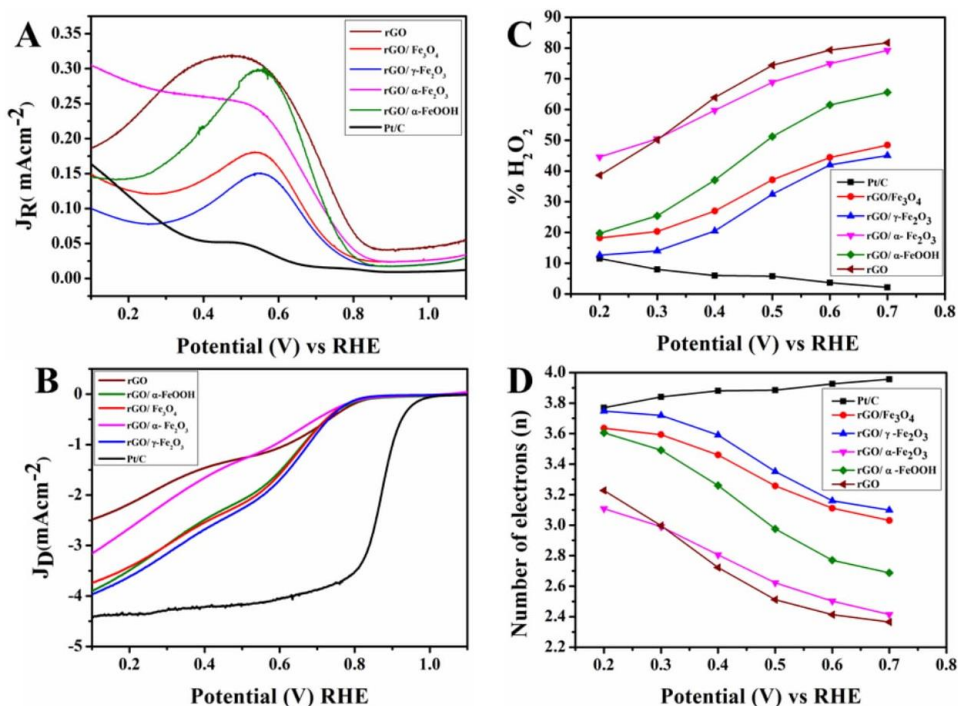


Fig. S7 RRDE voltammograms of (A) ring current, (B) disc current of rGO/Fe₃O₄, rGO/γ-Fe₂O₃, rGO/α-Fe₂O₃, rGO/α-FeOOH, rGO and Pt/C electrodes in oxygen saturated 0.1M KOH at 1600 rpm at a scan rate of 10 mV/s. (C) Percentage peroxide and (D) number of electrons of rGO/Fe₃O₄, rGO/γ-Fe₂O₃, rGO/α-Fe₂O₃, rGO/α-FeOOH, rGO and Pt/C electrodes at various potential calculated according to RRDE data.

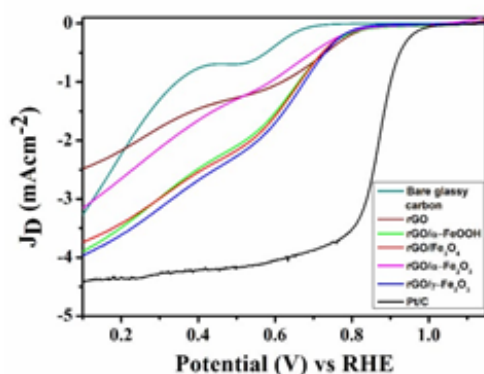


Fig. S8 Comparison of the LSV of the catalysts with the glassy carbon electrode in oxygen saturated 0.1M KOH at 1600 rpm at a scan rate of 10 mV/s.

S1 Conductivity measurements

The electrical conductivity of the rGo/iron oxide catalysts were conducted using the following equation S1[1].

$$\sigma = \frac{l}{RA} \quad (S1)$$

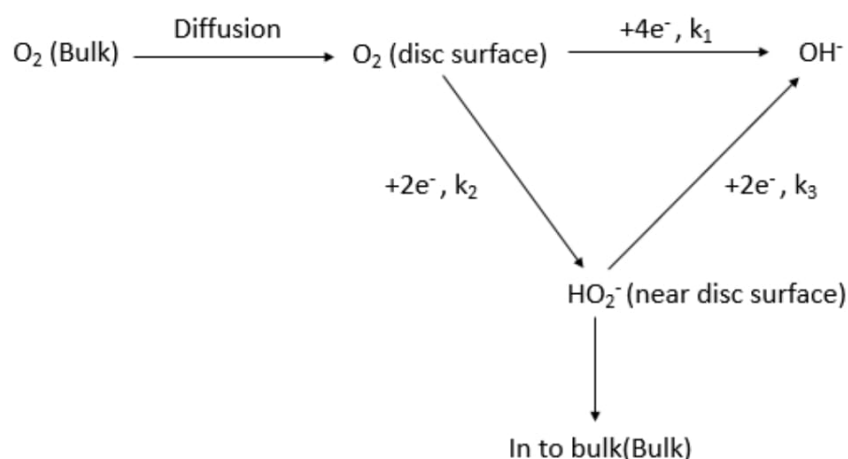
Where σ , l , R and A are the conductivity (S/m), length (m), electrical resistance (Ω) and cross sectional area (m^2) respectively. Samples for the measurement of conductivity was prepared by pressing (50 PSI) them in to a 10 mm diameter cylinder of 1mm thickness. To measure the conductivity, the as-prepared catalysts samples were placed in between two gold plated glass electrodes and connected to a two-probe digital multi meter (Fluke -87V) to measure the resistance. The conductivity was measured by using the resistance, length and area in to equation S1.

Table S2. Conductivity measurements of GN/Fe₃O₄, GN/γ-Fe₂O₃, GN/α-Fe₂O₃ and GN/α-FeOOH catalysts.

Graphene/iron oxide aerogel	Conductivity (S/m)
GN/ Fe ₃ O ₄	3.54 x 10 ⁻⁴
GN/ γ-Fe ₂ O ₃	2.75 x 10 ⁻⁴
GN/ α-Fe ₂ O ₃	2.58 x 10 ⁻⁵
GN/ α-FeOOH	2.97 x 10 ⁻⁴

S2 Electron transfer kinetics

The reaction pathway suggested by Damjanovic *et al* [2] for oxygen reduction is shown in Scheme S1.



Scheme S1. Schematic representation of electrochemical reduction of oxygen in basic medium [2, 3].

Here, K_1 represents the direct reduction of oxygen to OH⁻ ion without the formation of any intermediate, which is desorbed and detected by the ring of the rotating ring disc electrode and K_2 is the overall formation of the adsorbed peroxide and K_3 is the rate constant for the

reduction of peroxides. It can be assumed that the HO_2^- ion maintains an adsorption-desorption equilibrium depending on the applied potential [4].

Hsueh *et al.*[3] used a series of equations to calculate the rate constants K_1 , K_2 and K_3 using the values of the intercept and the slope of plots of I_d / I_r vs $\omega^{-1/2}$ and $I_{dL} / (I_{dL} - I_d)$ vs $\omega^{-1/2}$, where I_d , I_r , I_{dL} and ω are the disc current, ring current, limiting disc current and the rotation speed respectively. The limiting disc current for these calculated was derived as the current at 0.0 V potential at 2400 rpm. The following equations (S2, S3 and S4) were used to calculate the rate constants [3, 5].

$$K_1 = S_1 Z_1 \frac{I_1 N - 1}{I_1 N + 1} \quad (\text{S2})$$

$$K_2 = \frac{2 S_2 Z_1}{I_1 N + 1} \quad (\text{S3})$$

$$K_3 = \frac{N S_1 Z_2}{I_1 N + 1} \quad (\text{S4})$$

Where S_1 and I_1 are the slope and intercept correspond to the I_d / I_r vs $\omega^{-1/2}$ plots and S_2 is the slope of $I_{dL} / (I_{dL} - I_d)$ vs $\omega^{-1/2}$ plot. $Z_1 = 0.62 D_{\text{O}_2}^{2/3} V^{-1/6}$, $Z_2 = 0.62 D_{\text{H}_2\text{O}_2}^{2/3} V^{-1/6}$, $D_{\text{H}_2\text{O}_2}$ is $6.8 \times 10^{-6} \text{ cm}^2 \text{ s}^{-1}$ and N is the collection efficiency [5].

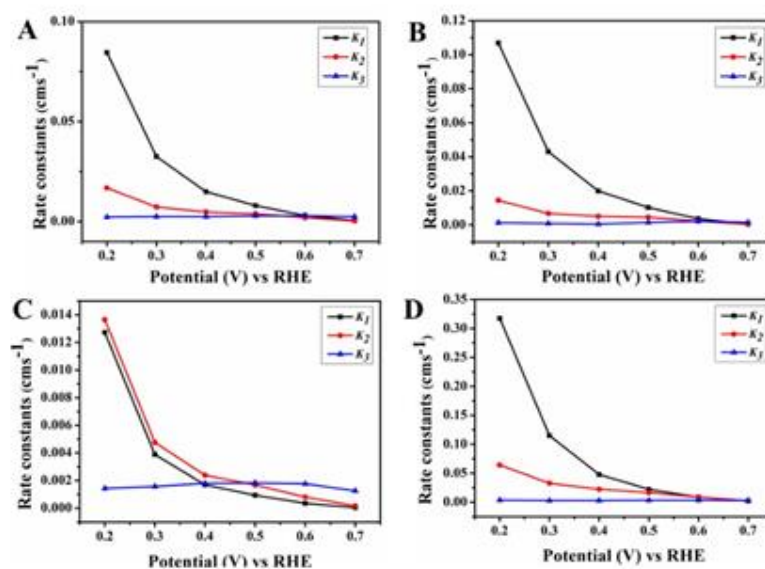


Fig. S9 Comparison of individual rate constants (K_1, K_2, K_3) of (A) rGO/ Fe_3O_4 (B) rGO/ $\gamma\text{-Fe}_2\text{O}_3$ (C) rGO/ $\alpha\text{-Fe}_2\text{O}_3$ and (D) rGO/ $\alpha\text{-FeOOH}$.

References

1. S. Ramesh, G. Upender, K. J. Raju, G. Padmaja, S. M. Reddy and C. Reddy, *J. Mod. Phys.*, 2013, **4**, 33461
2. A. Damjanovic, M. A. Genshaw and J. O. Bockris, *J. Chem. Phys.*, 1966, **45**, 4057
3. K. L. Hsueh, D. T. Chin and S. Srinivasan, *J. Electroanal. Chem. Interfacial Electrochem.*, 1983, **153**, 79
4. C. A. C. Sequeira, D. M. F. Santos and W. B. B. Batista, *J. Braz. Chem. Soc.*, 2006, **17**, 910
5. A. Muthukrishnan, Y. Nabaee, C. W. Chang, T. Okajima and T. Ohsaka, *Catal. Sci. Tech.*, 2015, **5**, 1764

CHAPTER 5

Investigation of a synthesise procedure of a unique 3-D macroporous ORR electrocatalyst using sulphonated aniline oligomers and its PF and rGO composites.

Ramesh Karunagaran

School of Chemical Engineering, University of Adelaide, South Australia 5005, Australia

5.1 Chapter overview

This chapter describes a detailed investigation on the synthesis of an SAO with defined microstructures and its conversion to a 3-D macroporous graphitic carbon structure utilising SO₂ gas formed as a decomposition product when heated above 266 °C. The composite materials synthesised individually using PF and rGO along with SAO also showed similar pattern. Macroporous graphitic carbon structures synthesised by pyrolysis of these composites using nitrogen precursors enhanced the ORR capability facilitating high mass transport of reactants and products and performed the ORR *via* a predominant four-electron pathway.

This chapter contains two papers with supplementary information:

The first paper (Chapter 5(a)) describes the investigation of SAO with defined micro structures using high aniline: oxidant mole ratio (10:1) and selected pH (above 4.6). The analysis of the morphology of these materials using TEM and SEM has revealed the presence of two different microstructures; micro flakes and micro rods. This chapter also identified the sulphonated aniline oligomers bound as phenazine structures initially formed micro sheets and stack together *via* π - π interaction or / and H-bonds reduce its surface energy to form micro flakes or rods. The stacking of multiple layers of micro sheets produced micro flakes and the stacking of few layers of micro sheets eventually were rolled to produce micro rods. FTIR and EDX analysis were conducted to determine and confirm the presence of sulphonic group.

The second paper (Chapter 5(b)) details the synthesis procedure of different composites materials of SAO using PF and rGO. A high temperature pulsed – gas sampling equipment coupled with a mass spectrometer used to analyse the decomposition gases of SAO at high temperature detected the release of SO₂ gas above 266 °C. Based on the hypothesis that the gas produced could be utilised to synthesise porous graphitic carbon materials, SAO and its composites (SAOPF and SAOrGO) were pyrolysed at high temperature (900 °C) in the

presence of nitrogen precursors. The N-SAOPF with higher concentration of pyridinic nitrogen species performed the ORR in an alkaline medium *via* a predominant four-electron transfer with an onset potential of 0.98 V (RHE) and N-SAO_rGO with higher concentration of graphitic nitrogen species showed higher current density (7.89 mAcm⁻²). The macrospores facilitated the mass transport of reactions and products to enhance the catalytic activity. The catalysts stability was also tested at 6000 repeated cycles at a scan rate of 100 mVs⁻¹. The results of the investigation have been presented and discussed in details as below.

CHAPTER 5(a)

A facile synthesis procedure for sulphonated aniline oligomers with distinct microstructures

Ramesh Karunakaran

School of Chemical Engineering, University of Adelaide, South Australia 5005, Australia

The chapter is based on the following peer-reviewed article:

R. Karunakaran, C. Coghlan, , D. Tran, T. T. Tung, Alexandre Burgen, C. Doonan, D. Losic “A facile synthesis procedure for sulphonated aniline oligomers with distinct microstructures, *Journal of Material Science*, 2018. (Submitted)

Statement of Authorship

Title of Paper	A facile synthesis procedure for sulphonated aniline oligomers with distinct microstructures.
Publication Status	<input type="checkbox"/> Published <input type="checkbox"/> Accepted for Publication <input checked="" type="checkbox"/> Submitted for Publication <input type="checkbox"/> Unpublished and Unsubmitted work written in manuscript style
Publication Details	<i>Journal of Material Science, 2018</i>

Principal Author

Name of Principal Author (Candidate)	Ramesh Karunakaran		
Contribution to the Paper	Under the supervision of D. Losic and Christian Doonan, I developed, designed and conducted the experiments, interpreted, processed the data and wrote the manuscript for submission.		
Overall percentage (%)	80%		
Certification:	This paper reports on the original research I conducted during the period of my Higher Degree by Research candidature and is not subjected to any obligations or contractual agreements with third party that would constrain its inclusion in this thesis. I am the primary author of this paper.		
Signature		Date	15 February 2018

Co-Author Contributions

By signing the Statement of Authorship, each author certifies that:

- the candidate's stated contribution to the publication is accurate (as detailed above);
- permission is granted for the candidate to include the publication in the thesis; and
- the sum of all co-author contributions is equal to 100% less the candidate's stated contribution.

Name of Co-Author	Tran Thanh Tung		
Contribution to the Paper	I helped Ramesh Karunakaran (candidate) with interpreting experimental results and improving the manuscript for submission. I give consent for Ramesh Karunakaran to present this paper for examination towards the Doctorate of Philosophy.		
Signature		Date	15 February 2018

Name of Co-Author	Alexandre Burgun		
Contribution to the Paper	I assisted Ramesh Karunakaran to conduct NMR analysis and interpreted the results for Ramesh Karunakaran. I give consent for Ramesh Karunakaran to present this paper for examination towards the Doctorate of Philosophy.		
Signature		Date	15 February 2018

Name of Co-Author	Diana Tran		
Contribution to the Paper	I helped Ramesh Karunakaran with designing experiments and improving the manuscript for submission. I give consent for Ramesh Karunakaran to present this paper for examination towards the Doctorate of Philosophy.		
Signature		Date	15 February 2018

Name of Co-Author	Campbell Coghlan		
Contribution to the Paper	I acted as the secondary supervisor for Ramesh Karunakaran and helped him to design the experiments and improve the final draft of the manuscript for submission. I give consent for Ramesh Karunakaran to present this paper for examination towards the Doctorate of Philosophy.		
Signature		Date	15 February 2018

Name of Co-Author	Christian Doonan		
Contribution to the Paper	I acted as the secondary supervisor for Ramesh Karunakaran and aided in design and development of experiment and evaluation of manuscript for submission. I give consent for Ramesh Karunakaran to present this paper for examination towards the Doctorate of Philosophy.		
Signature		Date	15 February 2018

CHAPTER 5(a): R. Karunakaran, C. Coghlan, D. Tran, T. T. Tung, Alexandre Burgen, C. Doonan, D. Losic "A facile synthesis procedure for sulphonated aniline oligomers with distinct microstructures, *Journal of Material Science*, 2018. **(Submitted)**

Name of Co-Author	Dusan Losic		
Contribution to the Paper	I acted as the Primary supervisor for Ramesh Karunakaran and aided in design and development of experiment and evaluation of manuscript for submission. I give consent for Ramesh Karunakaran to present this paper for examination towards the Doctorate of Philosophy.		
Signature		Date	15 February 2018

A facile synthesis procedure for sulphonated aniline oligomers with distinct microstructures

Ramesh Karunakaran,^[a] Campbell Coghlan,^[a] Diana Tran,^[a] Tran Thanh Tung,^[a] Alexandre Burgun,^[b] Christian Doonan,^{*,[b]} Dusan Losic,^{*,[a]}

^[a] R. Karunakaran, D. Tran, C. Coghlan, T. T. Tung and D. Losic, School of Chemical Engineering, Engineering North Building, University of Adelaide, SA, 5005, Australia.

^[b] Christian Doonan, A. Burgun, School of Physical Sciences, Physics Building, University of Adelaide, SA, 5005, Australia

^[*] Prof D. Losic, School of Chemical Engineering, Engineering North Building, University of Adelaide, SA, 5005, Australia. E-mail: D. Losic: dusan.losic@adelaide.edu.au

Prof Christian Doonan, School of Physical Sciences, Physics Building, University of Adelaide, SA, 5005, Australia. E-mail: Christian.doonan@adelaide.edu.au

Keywords: polyaniline • sulphonated polyaniline • micro structures • phenazine • pH

Abstract

Well-defined sulphonated aniline oligomer (SAO) microstructures with rods and flakes morphologies were successfully synthesized using an aniline and oxidant with mole ratio of 10:1 in ethanol and acidic conditions (pH 4.8). The synthesized oligomers showed excellent dispersibility and assembled as well-defined structures in contrast to the shapeless aggregated material produced in a water medium. The synergistic effects between the monomer concentration, oxidant concentration, pH and reaction medium are shown to be controlling parameters to generate SAO microstructures with distinct morphologies, either micro sheets or micro rods.

Introduction

Polyaniline (PANI) has emerged as the first conducting polymer whose electronic properties can be altered by protonation and charge-transfer doping [1-2]. Although PANI was initially synthesized in the 19th century, extensive research began after Epstein *et al.* [3] reported that the protonation of emeraldine form of PANI can be transferred into a synthetic metal. Since this discovery, PANI has been widely used for many applications including corrosion protection of metals [4], rechargeable battery [5], super capacitors [6], organic field transistors [7], polymer light diodes [8], solar cells [9] and energy storage and conversion [2].

PANI is synthesized by the chemical oxidation process of aniline using a strong oxidizing agent such as ammonium persulfate (APS) in an acidic aqueous medium (e.g. 1 M hydrochloric acid

(HCl)) [10]. The properties and the molecular structures of PANI can be controlled using different synthetic routes. These changes are associated with the monomer, oxidant and dopant concentrations, nature of the dopant, molar ratio of aniline to oxidant and dopant, reaction temperature and medium, or pH [11, 12]. In a typical PANI synthesis both oligomeric and polymeric structures are formed, each releasing protons when the aniline molecules bind to each other, and resulted in a decrease of the solution pH [13]. The micro structures of PANI form a variety of structures including sheets, flakes, tubes, rods, tower-like rods, spheres and granules [10-11]. Since aniline and its polymerisation products are organic bases, the pH of the medium alters the surface chemistry and the reaction kinetics to enable its polymerisation products to align as diverse structures [10].

Aniline is a weak base with a protonation constant (pK_a) of 4.5, it exists as neutral and protonated aniline depending on the acidity of the reaction medium. According to Stejskal *et al.* [14] both neutral aniline and anilinium cations coexist equally at pH 4.6. At higher pH values neutral aniline dominates in the reaction medium and under strong acidic conditions anilinium cations excessively prevail. These two species have different oxidation potentials and oxidize at different rates. For example, neutral aniline has a lower oxidation potential than the anilinium cation [14]. A typical PANI synthesis using aniline and APS proceeds via three oxidation phases in a mildly acidic media. Initially, the oxidation of the neutral aniline molecule occurs at $pH > 3.5$ with a fast and exothermic reaction to produce aniline oligomers. At pHs lower than 3.5 the material proceeds through an induction period of polymerisation of aniline. Finally, at $pH < 2.5$ fast exothermic polymerisation of anilinium cations occurs by releasing large number of protons to produce PANI. The highly conjugated conductive PANI synthesized at low pH has been widely used in optical [15], catalytic and electrical [16] applications. However, the multidimensional structures produced by PANI disperse poorly in water due to their large size and obtaining microstructures with good dispersibility and processability remains a challenge [17].

To overcome its poor dispersibility required for many of these applications Yue *et al.* [1] further modified the chemical structure of PANI by inserting a sulfonic group (SO_3H) into PANI and reported the first self-doped high molecular weight sulphonic acid ring substituted conductive polyaniline in 1990. The SO_3H groups in the PANI chain altered the properties of the parent material and provided unique properties such as self-doping, increase solubility in aqueous and organic solvents, environmental stability, thermal stability, easy processability, chemical,

electro chemical and optical properties different to those of the PANI [18-21]. However, the structural property of PANI or sulphonated PANI has not been fully investigated because the synthesized products consist of larger and less ordered domains, entanglement of chains, polydispersity and coils, and interacts with solvents in the reaction media. Therefore, defined molecular structures such as oligomers with flexible side groups could provide a model to understand molecular arrangements, provide attractive properties and be tuned for use in different applications.

The self-assembly of aniline oligomers and their structures have been investigated and reported in the past [22-25]. Several investigations have been carried out to identify the formation of aniline oligomers and the reported evidence suggests that they are formed at $\text{pH} > 3.5$ where reactive neutral aniline is freely present [10-14, 26-27] At this pH, neutral aniline is easily oxidised to form ortho or para coupled aniline molecules by the reduction of APS, yielding phenazine-like structures [11] Zujovic et al. [27] investigated the morphology of micro structures formed at higher pH and reported the formation of thin nanosheets formed by an inter chain ordering of oligomer products with lamellar structures via intermolecular hydrogen bonding and π - π stacking interaction. These hydrophobic nanosheets have high surface area and stack to form layered sheets with lamellar structures, or curl as nanotubes to reduce their surface energy [13]. However, synthesis of these nanostructures becomes unfeasible because the polymerisation reaction proceeds through a "falling pH" process to produce granular PANI structures at low pH values ($\text{pH} < 2$). As the reaction proceeds, the acidity of the media increases following the release of two hydrogen atoms when the aniline polymer chain is formed resulting in the formation of sulfuric acid [13]. Therefore, to obtain oligomeric nanostructures the reaction should be conducted in a slightly acidic media ($\text{pH} > 3.5$) without undergoing the "falling pH" effect. Huang et al. [12] synthesized well dispersed PANI nanotubes in methanol which suppressed the agglomeration of the nano structures produced. The methanol molecules also formed strong intermolecular H-bonding with PANI [28] and pushed the polymer chains apart by forming hydrogen bonds perpendicular to the PANI chains. [29] The ethanol molecules allowed the PANI particles to be well dispersed molecular structures with defined morphology [30]. Therefore, ethanol was used as the medium in the polymerisation process to synthesize well dispersed nano structures with a defined morphology.

In this paper, to address the limitation of previous procedures a facile approach to synthesize well-dispersed homogeneous sulphonated aniline oligomers with micro structures consisting of micro flakes and micro rods is developed. The optimal monomer to oxidant ratio to maintain the pH of the reaction media above $\text{pH} > 3.5$ was established using low concentrations of aniline (50 mM) and APS (5 mM), using ethanol as the solvent to reduce agglomeration. The synthesized microstructures of sulphonated aniline oligomers were characterised to determine their structure and properties. The mechanisms of the micro sheet formation and the pattern of assembly of the micro structures are also discussed. Furthermore, this research provides a greater understanding of the molecular arrangements of sulphonated aniline oligomers, which can be used for different applications.

Experimental Section

Materials

Aniline (Reagent Plus, 99%), ammonium persulphate ($(\text{NH}_4)_2\text{S}_2\text{O}_8$, APS), hydrochloric acid (HCl) and ethanol were purchased from Sigma-Aldrich and Chem Supply.

Methods

Preparation of sulfonated PANI oligomers

Aniline (5 mL, 5.19 g, 0.05 mol) was dissolved in 40 mL of ethanol and separately, APS (1.35g, 0.005 mol) was dissolved in 6 mL of 1 M HCL. The solutions were mixed at 5 °C for 30 min using a magnetic stirrer and then continued stirring at room temperature for 16 h. The precipitate was then collected, centrifuged at 4200 rpm, washed with ethanol for 2 hours in a Soxhlet extractor and vacuum dried overnight.

Characterization

The solid state cross-polarisation ^{13}C NMR spectrum obtained for sulphonated PANI was acquired on a Bruker 200 Avance spectrometer equipped with a 4.7 T wide-bore superconducting magnet operating at a resonance frequency of 50.33 MHz. The sample was packed into a 7 mm diameter zirconia rotor with Kel-F end caps and spun at 5 kHz. Chemical shift values were calibrated to the methyl resonance of hexamethylbenzene at 17.36 ppm and a 50 Hz Lorentzian line broadening was applied to the acquired spectrum. The cross-polarisation pulse sequence used a 3.2 μs , 195 w, 90° pulse, a contact time of 1 ms and a recycle

delay of 1s and 50,000 scans were collected. The absolute signal intensity obtained for the sample was corrected for that derived from an empty rotor. Scanning electron microscopy (SEM) images and energy-dispersive X-ray spectroscopy (EDX) were obtained using Quanta 450, FEI, USA at an accelerating voltage of 10 KeV. Samples for SEM was placed on a carbon tape attached to an aluminium stud and coated with platinum. For EDX, three reading were recorded and the average was recorded. X-ray diffraction (XRD) was performed at 40 kV and 15 mA in the range of $2\theta = 3 - 50^\circ$ at a speed of $10^\circ/\text{min}$ using Miniflex 600, Rigaku, Japan. Fourier transform infrared (FTIR) spectroscopy was conducted using a Spectrum 100, Perkin Elmer, USA. Samples were dissolved in ethanol and the spectra were recorded on a Shimadzu UV-1700 spectrometer (FTIR, Japan). pH measurements were conducted using a Mettler Toledo pH meter. The pH meter was calibrated using standard buffer solutions before readings were obtained. The electrical conductivity of the SAO was conducted using the following equation.

$$\sigma = \frac{l}{RA} \quad (S1)$$

Where σ , l , R and A are the conductivity (S/m), length (m), electrical resistance (Ω) and cross-sectional area (m^2) respectively. SAO for the measurement of conductivity was prepared by pressing (50 PSI) them in to a 10 mm diameter cylinder of 1mm thickness. Conductivity was measured by placing SAO in between two gold plated glass electrodes and connected to a two-probe digital multi meter (Fluke -87V) to measure the resistance. The conductivity was measure by using the resistance, length and area in equation S1.

Results and Discussion

To understand influence of temperature and pH conditions on synthetic process the pH and time dependence graph plotted against the temperature for the first 45 min is presented in Fig. 1. The figure shows a constant pH of 4.8 after 4 min of reaction time providing an ideal pH condition for oligomer formation. The pH of the aniline dispersed in ethanol immediately dropped from 8.4 to 4.8 after the addition of APS in 0.13 M HCl solution. The temperature of the reaction medium simultaneously increased from 18.6°C to 25.7°C showing exothermic reaction between neutral aniline molecules and APS has occurred to produce aniline oligomers [13]. The continuous drop in temperature after 10 min shows the reaction has taken place only for a short period of time. Since low concentration of APS was used, it was completely consumed by the excess neutral aniline present in the reaction media within a short period. The

pH of the reaction medium greater than 3.5 along with the evidence of the exothermic reaction showed that the reaction has proceeded via oligomer formation.

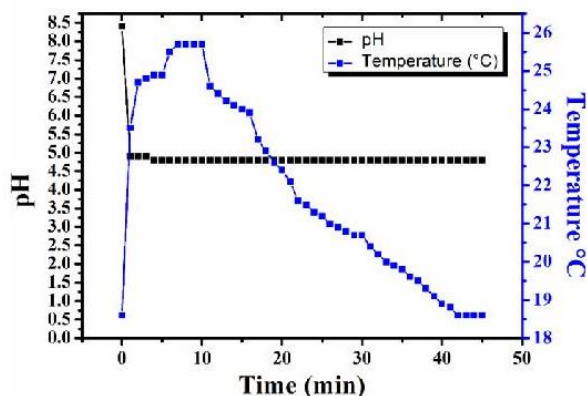


Figure 1. Change in temperature and pH against time in the course of the oxidation of aniline (50 mM) initiated by APS (5 mM) in 0.13 M HCl solution.

The SEM images of the aniline oligomeric structures in the presence of water (Fig.2A) and ethanol (Fig.2B) presented in Fig.2 showed shapeless agglomerates for polymerisation conducted in water and well dispersed micro structures, consisting of micro flakes and micro rods for reaction performed in ethanol. The TEM images (Fig.2C) show that the micro flakes are formed by the parallel alignment of several individual micro sheets. Fig.2D suggests that the micro sheets are rolled up to form the micro rods. The shapeless aggregates formed in water were similar to the aggregates previously reported by Konyushenko *et al.*, which were synthesized using 200 mM aniline and 25 mM APS in 0.40 M acetic acid medium [13]. However, the micro structures formed in ethanol showed significantly different morphology to the previously reported nanoflakes synthesized by Zujovic *et al.* [27] in the presence of 24 mM aniline and APS in 4mM HCl solution.

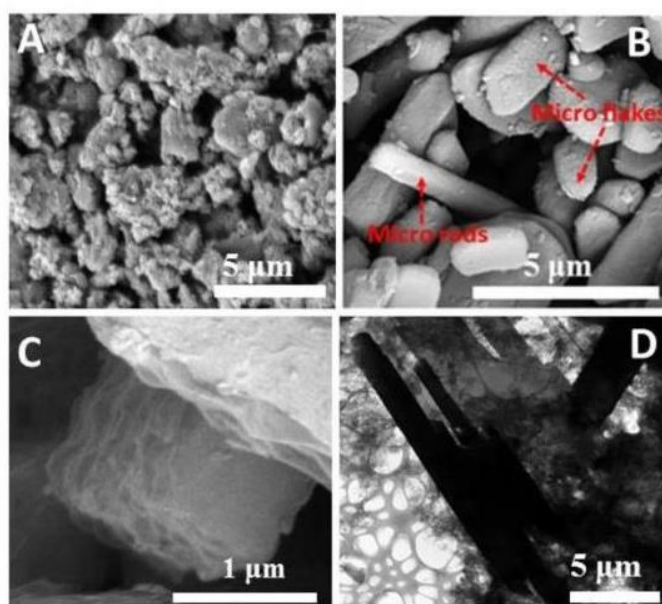


Figure 2. SEM image of the micro structures of the aniline oligomers formed in the presence of reaction medium (A) water and (B) ethanol. TEM images of (C) micro flakes and (D) micro rods formed in the presence of ethanol.

Previous studies suggest that methanol and ethanol can significantly interfere with aniline to stabilise the synthesized products and suppress agglomeration by forming H-bonds with PANI molecules or wrapping around PANI particles [12, 29-30]. A comparison of structures formed using different reaction conditions is shown in Table 1.

Table 1. Comparison of the micro structures formed using different reaction conditions.

Aniline concentration (mM)	APS concentration (mM)	Products formed	Medium	Structures formed			Reference
				Aggregates	Flakes (μm)	Rods (μm)	
200	25	AO	Water	Shapeless aggregates			[13]
24	24	AO	Water		L = 1.5 W = 1.0 T = 0.01	none	[27]
50	5	SAO	Water	Shapeless aggregates			This study
50	5	SAO	Ethanol		L = 3.0 W = 2.0 T = 0.4	L = 5.0	This study

L = Length, W= width, T=Thickness AO- aniline oligomers

To investigate and confirm the presence of sulphonate groups in the synthesized sulphonated aniline microstructures we conducted EDX elementary analysis (Fig.3A) of the microstructures which revealed the presence of 21.97, 18.51, 24.14 and 35.37 wt % of carbon, nitrogen, oxygen and sulphur, respectively. The high wt% of oxygen and sulphur present in the EDX analysis confirm that the aniline oligomers were sulfonated. To further analyse the presence of sulphonated groups in the aniline oligomers, we performed a FTIR analysis on our products. The FTIR spectra of aniline oligomers (Fig.3B) show intense peaks at 3025, 3195, 1414, 1046 and 609 cm^{-1} . The peaks at 3025 and 3195 cm^{-1} are ascribed to the C-H aromatic stretching vibration [31] and to hydrogen bonded N-H stretching of aniline oligomers, respectively [25]. The band at 1414 cm^{-1} is ascribed to the totally symmetrical stretching of phenazine heterocyclic rings [12, 32]. The band at 1046 cm^{-1} is the characteristic peak of S=O stretching vibration mode in sulphonic groups linked by covalent bonds to the benzene ring [25, 33-34]. The peak at 609 cm^{-1} corresponds to the vibration modes of C-S bond [33-35]. These intensified peaks observed at 1414, 1046 and 609 cm^{-1} confirmed that the microsheets consist of orderly arranged sulphonated phenazine ring.

Solid state ^{13}C NMR was conducted to verify the structure of sulphonated PANI (Fig.3C). The acquired spectrum shows peaks at 125.27, 134.42 and 146.00 ppm corresponding to sp^2 carbons from the aromatic ring [35-37]. The peaks at 224.18, 232.44, 34.53 and 25.29 ppm are spinning side bands derived from the large resonances found near 125.27 ppm. The shoulder found at 138.06 ppm can be attributed to the carbon bound to the phenyl $-\text{SO}_3\text{H}$ group and confirms the formation of the sulphonated poly-aniline [37-39]. The UV-Vis spectrum of SAO (Fig.3D) showed a single peak at 285 nm ascribed to the phenazine moieties formed [40, 41] via strong $\pi - \pi$ interaction [21, 42]. The absence of peaks below 285 nm shows that the oligomers are not conjugated [43]. The low conductivity ($2.04 \times 10^{-8} \text{ Scm}^{-1}$) measured on the SAO also confirmed that the oligomers are not conjugated.

The diffraction pattern of SAO was obtained using XRD analysis (Fig.4). The intense peak at $2\theta = 6.4^\circ$ with a spacing of 13.8 Å is a characteristic peak for periodically aligned polymer chains [26, 44-45]. This peak have been interpreted differently in several publications, and can arise from the formation of lamella between aniline chains [44], the increase of interlayer distance by the presence of a dopant [45], or formation of periodic lamella between PANI

chains and sulfate counterions [26]. Therefore, the peak at $2\theta = 6.4^\circ$ is assigned to the periodic lamella between sulphonated oligomeric aniline chains.

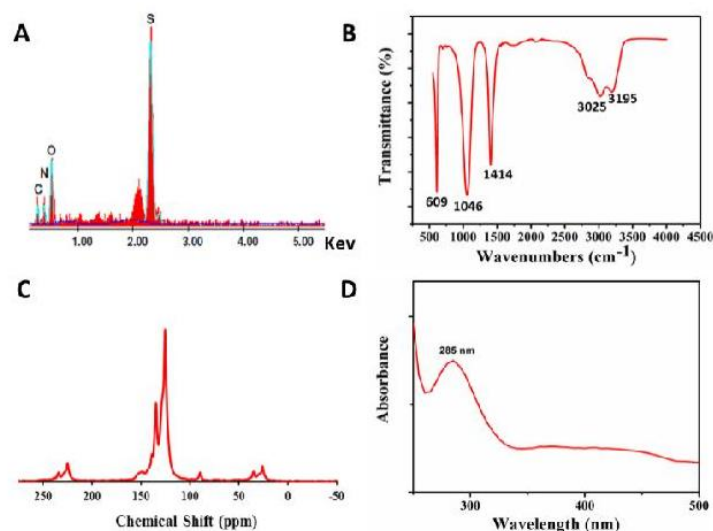


Figure 3. (A) EDX, (B) FTIR, (C) ¹³C solid state NMR and (D) UV-Visible spectrum of sulphonated PANI.

The peak at 16.9° (corresponding to a spacing of 5.2 \AA) is attributed to the parallel repeat unit of polymer chains [46]. The peaks at 18.4° [26, 47] and 20.4° [48] corresponding to a d-spacing of 4.7 and 4.3 \AA , respectively, is due to the parallel positioning of the polymer chain, whereas, the peaks at 25.5° (d-spacing = 3.4 \AA) [48] and 29.5° (d-spacing = 3.02 \AA) [49] are assigned to the perpendicular arrangement of the polymer chain. The peak at 23.1° can be assigned to the periodicity caused by π - π stacking of oligomers [26]. The XRD pattern confirmed sulphonated aniline molecules are orderly arranged in a lamella structure.

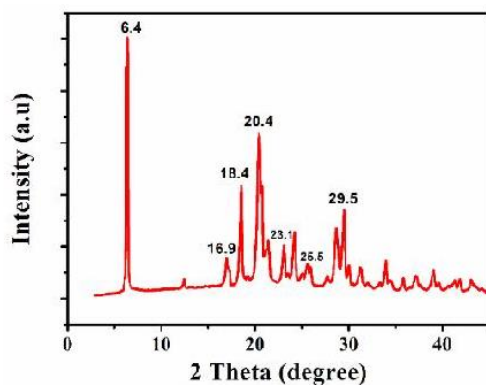
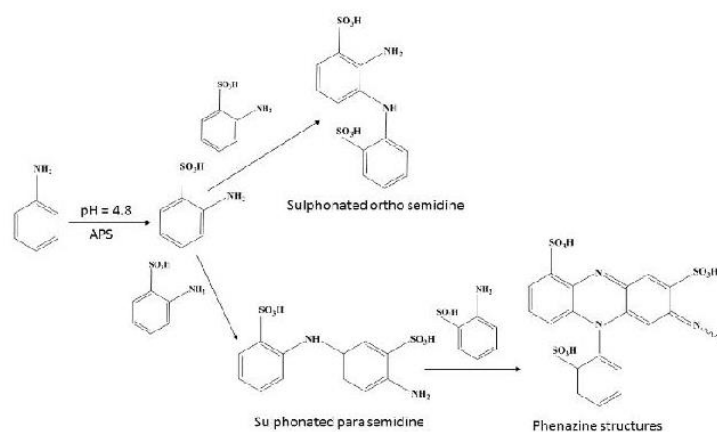


Figure 4. XRD image of sulphonated PANI oligomers

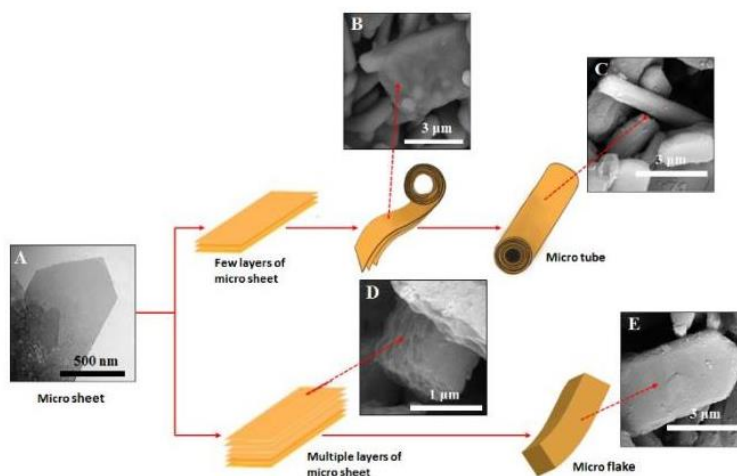
Mechanism of microstructures formation

Based on the mechanism suggested by Kriz *et al.* [50] and Stejskal *et al.* [14] for aniline oligomers, the mechanism for the formation of SAO with phenazine structures is presented in Scheme 1. Initially, both sulphonated ortho- semidine and sulphonated para-semidines are formed. The sulphonated para semidines then further react with sulphonated aniline molecules to produce planar sulphonated phenazine containing oligomeric structures.



Scheme 1. Reaction pathways for the sulphonated PANI oligomers.

Previous studies showed that when aniline is oxidised at $\text{pH} > 3.5$ in the presence of neutral aniline, oligomers containing ortho or para substituted monomer units along with phenazine rings can be formed [51]. The synthesized product which was characterised by EDX, FTIR, ^{13}C NMR, UV- Visible and XRD clearly indicated that the micro structures formed are sulphonated and orderly arranged in a phenazine structure.



Scheme 2. Schematic representation of the formation of microrods and microflakes.

Zujovic *et al.* [27] suggest that these cyclic structures can be interconnected with directed inter molecular hydrogen bonding and $\pi - \pi$ interaction to form nanosheets. These bonding interactions align towards an internal ordering and determine the size of the nanosheet. The microstructures formed suggest that the internal ordering of these interconnected cyclic structures via hydrogen bonding and $\pi - \pi$ interaction has been extended until they form micro sheets. The rapid drop in pH and the immediate increase of temperature in Fig. 1 show that rapid intensification of the oligomerisation process has taken place, because of the low amount of APS being fully consumed by the excess of aniline. Viva *et al.* [52] reported that at low concentrations of monomers, formation of head-to-head phenazine structures is favoured. As a result, more phenazine structures have been formed in the oligomer with higher degree of uniformity and aligned towards regular orientation [11]. In particular, aniline trimers containing phenazine moiety are hydrophobic and possess a flat molecular structure, which could stack one dimensionally via by $\pi - \pi$ or roll to reduce their exposed surface energy [14, 27]. The SEM conducted on the micro structures did not show any evidence of thin nanorods, but rather showed relatively thick nanorods (width - 0.3 μm). Therefore, we assumed that the few layers of micro sheets stacked together by $\pi - \pi$ interaction rolled (Scheme 2B) to reduce its surface energy to form micro rod (Scheme 2C). Conversely, the micro sheets aligned as few layers (Scheme 2D) to reduce the surface energy. The multiple stacking of these micro sheets ultimately lose energy to roll and form nanorods, which eventually settle as micro flakes (Scheme 2E). The synthetic procedure described in this study to obtained well defined SAO micro structures, open doors to the synthesis of less aggregated, well dispersed and well defined micro structures oligomers with functional groups.

Conclusions

This study demonstrates a synthetic procedure to synthesize sulphonated aniline oligomers with well-defined micro structures comprise of micro sheets and micro rods in the presence of ethanol. The comparison of the synthesis conducted in the presence of water showed formation of shapeless aggregates, confirming that ethanol significantly reduces the agglomeration of micro structures. The ideal pH conditions (pH 4.8) was confirmed under which neutral aniline can be present in the reaction medium to perform oligomer formation, was achieved by using a 10:1 aniline/APS mole ratio. The excess aniline present in the mixture rapidly consumed the APS and formed inter-connected phenazine structures via hydrogen bonding and $\pi - \pi$ interaction to form micro structures. The mechanism of the formation of the micro structures

is revealed that goes through several stages from 2D planar sheets and their transformation into tubular and layered flake structures. The process to synthesize these sulphonated aniline oligomeric microstructures with a phenazine structure is scalable and controllable toward different morphologies that could be used for a wide range of industrial and medical applications. The phenazine structures and its derivatives are widely explored as antitumor, antibacterial, anti-fungi and anti-leprosy agents and these products can be adapted for these applications.

Acknowledgements

The authors thank the support of Australian Research Council (IH 150100003), Australian Research Council Research Hub for Graphene Enabled Industry Transformation, The Australian Solar Thermal Research Initiative (ASTRI), The University of Adelaide, School of Chemical Engineering, The University of Adelaide, School of Chemistry. The technical support provided by Adelaide microscopy, micro analysis research facility at Flinders Microscopy (Flinders University) was great appreciated.

Conflict of Interest

There is no conflict of interest.

References

1. Yue J, Epstein AJ (1990) Synthesis of self-doped conducting polyaniline. *J Am Chem Soc* 112: 2800-2801.
2. Wang H, Lin J, Shen ZX (2016) Polyaaniline (PANi) based electrode materials for energy storage and conversion. *J Sci Adv Mater Dev* 1: 225-255.
3. Epstein AJ, Ginder JM, Zuo F, Woo HS, Tanner DB, Richter AF, Angelopoulos M, Huang WS, MacDiarmid AG (1987): Insulator-to-metal transition in polyaniline: Effect of protonation in emeraldine. *Synth Met* 21: 63-70.
4. Gvozdrenović M, Jugović B, Jambrec D, Stevanović J, Grgur B (2012) Application of polyaniline in corrosion protection of metals. *Zaš mater* 53: 353-360.
5. Ghanbari K, Mousavi M, Shamsipur M (2006) Preparation of polyaniline nanofibers and their use as a cathode of aqueous rechargeable batteries. *Electrochim Acta* 52:1514-1522.

6. Zhang K, Zhang LL, Zhao X, Wu J (2010) Graphene/polyaniline nanofiber composites as supercapacitor electrodes. *Chem Mater* 22:1392-1401.
7. Jussila S, Puustinen M, Hassinen T, Olkkonen J, Sandberg HG, Solehmainen K (2012) Self-aligned patterning method of poly (aniline) for organic field-effect transistor gate electrode. *Org Electron* 13:1308-1314.
8. Yang Y, Heeger A (1994) Polyaniline as a transparent electrode for polymer light-emitting diodes: Lower operating voltage and higher efficiency. *Appl Phys Lett* 64:1245-1247.
9. Lim KG, Ahn S, Kim H, Choi MR, Huh DH, Lee TW (2016) Self-Doped conducting polymer as a hole-extraction layer in organic-inorganic hybrid perovskite solar cells. *Adv Mater Interfaces* 3:1-7.
10. Zujovic Z, Webber AL, Travas-Sejdic J, Brown SP (2015) Self-assembled oligoanilinic nanosheets: Molecular structure revealed by solid-state NMR spectroscopy. *Macromolecules* 48: 8838-8843.
11. Sapurina IY, Stejskal J (2010) The effect of pH on the oxidative polymerization of aniline and the morphology and the properties of the products. *Russ Chem Rev* 79:1123-1143.
12. Huang YF, Lin CW (2009) Introduction of methanol in the formation of polyaniline nanotubes in an acid-free aqueous solution through a self-curling process. *Polymer* 50:775-782.
13. Konyushenko E, Trchová M, Stejskal J, Sapurina I (2010) The role of acidity profile in the nanotubular growth of polyaniline. *Chem Pap* 64: 56-64.
14. Stejskal J, Sapurina I, Trchová M (2010) Polyaniline nanostructures and the role of aniline oligomers in their formation. *Progress in Polymer Science* 35:1420-1481.
15. Bhadra S, Khastgir D, Singha NK, Lee JH (2009) Progress in the preparation, processing and application of polyaniline. *Prog Polym Sci* 34:783-810.
16. Colteville D, Le Méhauté A, Challioui C, Mirebeau P, Demay JN (1999) Industrial applications of polyaniline. *Synth Met* 101:703-704.
17. Ma Y, Zhang H, Hou C, Qiao M, Chen Y, Zhang H, Zhang Q (2017) Multidimensional polyaniline structures from micellar templates. *J Mater Sci* 52: 2995 - 3002.
18. Yue J, Wang ZH, Cromack KR, Epstein AJ, MacDiarmid AG (1991) Effect of the sulfonic acid group on polyaniline backbone. *J Am Chem. Soc* 113:2665-2671.

19. Yue J, Epstein A, Zhong Z, Gallagher P, MacDiarmid A (1991) Thermal stabilities of polyanilines. *Synth Met* 41:765-768.
20. Shimizu S, Saitoh T, Uzawa M, Yuasa M, Yano K, Maruyama T, Watanabe K (1997) Synthesis and applications of sulfonated polyaniline. *Synth Met* 85:1337-1338.
21. Liao Y, Strong V, Chian W, Wang X, Li XG, R. B. Kaner RB (2012) Sulfonated polyaniline nanostructures synthesized via rapid initiated copolymerization with controllable morphology, size, and electrical properties. *Macromolecules* 45:1570-1579.
22. Cao Y, Li S, Xue Z, Guo D (1986) Spectroscopic and electrical characterization of some aniline oligomers and polyaniline. *Synth Met* 16:305-315.
23. Zhang W, Feng J, MacDiarmid A, Epstein A (1997) Synthesis of oligomeric aniline. *Synth Met* 84:119-120.
24. Wienk M, Janssen R (1997) High-spin cation radicals of meta-para aniline oligomers. *J Am Chem Soc* 119:4492-4501.
25. Stejskal J, Trchová M (2012) Aniline oligomers versus polyaniline. *Polym Int* 61:240-251.
26. Zujovic ZD, Laslau C, Bowmaker GA, Kilmartin PA, Webber AL, Brown SP, Travas-Sejdic J (2009) Role of aniline oligomeric nanosheets in the formation of polyaniline nanotubes. *Macromolecules* 43:662-670.
27. Zujovic ZD, Laslau C, Travas-Sejdic J (2011) Lamella-structured nanoflakes comprised of stacked oligoaniline nanosheets. *Chem Asian J* 6:791-796.
28. Al-Ghamdi A, Al-Saigh ZY (2002) Surface and thermodynamic characterization of conducting polymers by inverse gas chromatography: I. Polyaniline. *J Chromatogr A*: 969:229-243.
29. Zhou S, Wu T, Kan J (2007) Effect of methanol on morphology of polyaniline. *Eur Polym J* 43:395-402.
30. Kan J, Lv R, Zhang S (2004) Effect of ethanol on properties of electrochemically synthesized polyaniline. *Synth Met* 145:37-42.
31. Hussain AA, Sharma S, Pal AR, Bailung H, Chutia J, Patil DS (2012) Role of plasma parameters on the conjugated structure retention in polyaniline thin film. *Plasma Chem Plasma Process* 32:817-832.

32. Viva F, Andrade E, Molina F, Florit M (1999) Electropolymerization of 2-methoxy aniline. Electrochemical and spectroscopical product characterization. *J Electroanal Chem* 471:180-189.
33. Trchová M, Šedenková I, Konyushenko EN, Stejskal J, Holler P, Ciric-Marjanovic G (2006) Evolution of polyaniline nanotubes: the oxidation of aniline in water. *J Phys Chem B* 110:9461-9468.
34. Perrin F, Phan T, Nguyen D (2015) Synthesis and characterization of polyaniline nanoparticles in phosphonic acid amphiphile aqueous micellar solutions for waterborne corrosion protection coating. *J Polym Sci Part A Polym Chem* 53:1606-1616.
35. Júnior A, Santos JH, Bertuol DA, Meneguzzi A, Ferreira CA, Amado FDR (2013) Cater oil and commercial thermoplastic polyurethane membranes modified with polyaniline: A comparative study. *Mater Res* 16:860-866.
36. Rao PS, Sathyanarayana DN, Palaniappan S (2002) Polymerization of aniline in an organic peroxide system by the inverted emulsion process. *Macromolecules* 35:4988-4996.
37. Si Y, Samulski ET (2008) Synthesis of water soluble graphene. *Nano Lett* 8:1679-1682.
38. Lee D (2013) Preparation of a sulfonated carbonaceous material from lignosulfonate and its usefulness as an esterification catalysts. *Molecules* 18:8168-8180.
39. Lam E, Chong JH, Majid E, Liu Y, Hrapovic S, Leung ACW, Luong JHT (2012) carbocatalytic dehydration of xylose to furfural in water. *Carbon* 50:1033-1043.
40. Díaz FR, del Valle MA, Borrego ED, Gacitúa MA, Camarada MB, Antilén MP, Del Río R., Arteaga GC (2009) Electro-synthesis and characterization of Oanisidine Oligomers. 10 ° Congresso Brasileiro de Polimeros.
41. Saluja P, Chaudhary A, Khurana JM (2014) Synthesis of novel fluorescent benzo [a] pyrano [2, 3-c] phenazine and benzo [a] chromeno [2, 3-c] phenazine derivatives via facile four-component domino protocol. *Tetrahedron Lett* 55:3431-3435.
42. Venancio EC, Wang PC, MacDiarmid A (2006) The azanes: A class of material incorporating nano/micro self-assembled hollow spheres obtained by aqueous oxidative polymerization of aniline. *Synth Met* 156:357-369.
43. Angélica del Valle M, Díaz FR, Bodini ME, Alfonso G, Soto GM, Borrego ED (2005) Electrosynthesis and characterization of o-phenylenediamine oligomers. *Polym Int* 54:526-532.

44. Jana T, Chatterjee J, Nandi AK (2002) Sulfonic acid doped thermoreversible polyaniline gels. 3. Structural investigation. *Langmuir* 18:5720-5727.
45. Zhang L, Long Y, Chen Z, Wan M (2004) The effect of hydrogen bonding on self-assembled polyaniline nanostructures. *Adv Funct Mater* 14:693-698.
46. Liu W, Yan X, Chen J, Feng Y, Xue Q (2013) Novel and high-performance asymmetric micro-supercapacitors based on graphene quantum dots and polyaniline nanofibers. *Nanoscale* 5:6053-6062.
47. Jin E, Liu N, Lu X, Zhang W (2007) Novel micro/nanostructures of polyaniline in the presence of different amino acids via a self-assembly process. *Chem Lett* 36:1288-1289.
48. Prathap MUA, Srivastava R (2011) Morphological controlled synthesis of macro-/nano-polyaniline. *J Polym Res* 18:2455-2467.
49. Belaabed B, Wojkiewicz JL, Lamouri, El Kamchi N, Redon N (2012) Thermomechanical behaviors and dielectric properties of polyaniline-doped paratoluene sulfonic acid/epoxy resin composites. *Polym Adv Technol* 23:1194-1201.
50. Křiž J, Starovoytova L, Trchová M, Konyushenko EN, Stejskal J (2009) NMR investigation of aniline oligomers produced in the early stages of oxidative polymerization of aniline. *J Phys Chem B* 113:6666-6673.
51. Zhang L, Zujovic ZD, Peng H, Bowmaker GA, Kilmartin PA, Trivas-Sejdic (2008) Structural characterization of polyaniline nanotubes synthesized from different buffer solutions. *J Macromolecules* 41:8877-8884.
52. Viva F, Andrade E, Florit M, Molina F (2002) Electropolymerization of 2-methoxyaniline. Polymerization kinetics and phenazineinsertion at low monomer concentration. *Phys Chem Chem Phys* 4:2293-2300.

CHAPTER 5(b)

A unique N-doped macro porous oxygen reduction electro catalyst synthesised using sulphonated aniline oligomers, phenol formaldehyde and reduced graphene oxide composites

Ramesh Karunakaran

School of Chemical Engineering, University of Adelaide, South Australia 5005, Australia


The chapter is based on the following peer-reviewed article:

R. Karunakaran, C. Coghlan, D. Tran, T. T. Tung, C. Shearer, Alexander Burgun, C. Doonan, D. Losic “A unique N-doped macro porous oxygen reduction electro catalyst synthesised using sulphonated aniline oligomers, phenol formaldehyde and reduced graphene oxide composites, 2018, *Materials*. (Final stage of submission)

Statement of Authorship

Title of Paper	A unique N-doped macro porous oxygen reduction electro catalyst synthesised using sulphonated aniline oligomers, phenol formaldehyde and reduced graphene oxide composites		
Publication Status	<input type="checkbox"/> Published	<input type="checkbox"/> Accepted for Publication	
	<input type="checkbox"/> Submitted for Publication	<input checked="" type="checkbox"/> Unpublished and Unsubmitted work written in manuscript style	
Publication Details	<i>Materials</i> , 2018		


Principal Author

Name of Principal Author (Candidate)	Ramesh Karunakaran		
Contribution to the Paper	Under the supervision of D. Losic and Christian Doonan, I developed, designed and conducted the experiments, interpreted, processed the data and wrote the manuscript for submission.		
Overall percentage (%)	80%		
Certification:	This paper reports on the original research I conducted during the period of my Higher Degree by Research candidature and is not subjected to any obligations or contractual agreements with third party that would constrain its inclusion in this thesis. I am the primary author of this paper.		
Signature		Date	15 February 2018

Co-Author Contributions

By signing the Statement of Authorship, each author certifies that:

- i. the candidate's stated contribution to the publication is accurate (as detailed above);
- ii. permission is granted for the candidate to include the publication in the thesis; and
- iii. the sum of all co-author contributions is equal to 100% less the candidate's stated contribution.

Name of Co-Author	Tran Thanh Tung		
Contribution to the Paper	I helped Ramesh Karunakaran (candidate) with interpreting experimental results and improving the manuscript for submission. I give consent for Ramesh Karunakaran to present this paper for examination towards the Doctorate of Philosophy.		
Signature		Date	15 February 2018

CHAPTER 5(b): R. Karunakaran, C. Coghlan, D. Tran, T. T. Tung, Alexander Burgun, C. Shearer, C. Doonan, D. Losic "A unique N-doped macroporous oxygen reduction electro catalyst synthesised using sulphonated aniline oligomers, phenol formaldehyde and reduced graphene oxide composites" *Materials*, 2018. **(Final stage of publication)**

Name of Co-Author	Cameron Sherear		
Contribution to the Paper	I conducted the XPS analysis and interpreted the results for Ramesh Karunakaran. I give consent for Ramesh Karunakaran to present this paper for examination towards the Doctorate of Philosophy.		
Signature		Date	15 February 2018

Name of Co-Author	Alexander Burgun		
Contribution to the Paper	I assisted Ramesh Karunakaran to conduct Thermometric - mass spectroscopy analysis and interpreted the results for Ramesh Karunakaran. I give consent for Ramesh Karunakaran to present this paper for examination towards the Doctorate of Philosophy.		
Signature		Date	15 February 2018

Name of Co-Author	Diana Tran		
Contribution to the Paper	I helped Ramesh Karunakaran with designing experiments and improving the manuscript for submission. I give consent for Ramesh Karunakaran to present this paper for examination towards the Doctorate of Philosophy.		
Signature		Date	15 February 2018

Name of Co-Author	Campbell Coghlan		
Contribution to the Paper	I acted as the secondary supervisor for Ramesh Karunakaran and helped him to design the experiments and improve the final draft of the manuscript for submission. I give consent for Ramesh Karunakaran to present this paper for examination towards the Doctorate of Philosophy.		
Signature		Date	15 February 2018

CHAPTER 5(b): R. Karunakaran, C. Coghlan, D. Tran, T. T. Tung, Alexander Burgun, C. Shearer, C. Doonan, D. Losic "A unique N-doped macroporous oxygen reduction electro catalyst synthesised using sulphonated aniline oligomers, phenol formaldehyde and reduced graphene oxide composites" *Materials*, 2018. **(Final stage of publication)**

Name of Co-Author	Christian Doonan		
Contribution to the Paper	I acted as the secondary supervisor for Ramesh Karunakaran and aided in design and development of experiment and evaluation of manuscript for submission. I give consent for Ramesh Karunakaran to present this paper for examination towards the Doctorate of Philosophy.		
Signature		Date	15 February 2018

Name of Co-Author	Dusan Losic		
Contribution to the Paper	I acted as the Primary supervisor for Ramesh Karunakaran and aided in design and development of experiment and evaluation of manuscript for submission. I give consent for Ramesh Karunakaran to present this paper for examination towards the Doctorate of Philosophy.		
Signature		Date	15 February 2018



1 Article

2 **A unique N-doped macro porous oxygen reduction**
3 **electro catalyst synthesised using sulphonated aniline**
4 **oligomers, phenol formaldehyde and reduced**
5 **graphene oxide composites.**

6 Ramesh Karunakaran¹, Campbell Coghlan², Diana Tran¹, Tran Thanh Tung^a, Alexander Burgun,
7 Cameron Shearer^c Christian Doonan^{2*}, Dusan Losic^{1*}

8

9 ¹ School of Chemical Engineering, University of Adelaide, SA 5005, Australia

10 ² School of Chemistry, University of Adelaide, SA 5005, Australia

11 ³ School of Chemical and Physical Sciences, Flinders University, SA 5042, Australia

12 * Correspondence: Dusan.losic@adelaide.edu.au; Tel.: +61-8-8013-4648

13 Academic Editor: Professor Thomas Nann

14 Received: date; Accepted: date; Published: date

15

16 **Abstract:** Macro porous carbon structures has been extensively used for the energy production in
17 fuel cells because of its capability to perform a smooth and rapid electrochemical oxygen reduction
18 reaction (ORR) by facilitating efficient mass transfer and diffusion of reactants and the by-products.
19 Herein, we have demonstrated synthesis procedure to synthesise a unique macro porous carbon
20 material composed of micro porous structure by the pyrolysis of sulphonated aniline oligomers
21 (SAO) in the presence of nitrogen compound of melamine achieved N-doped SAO (N-SAO).
22 Pyrolysis of composites of: (1) SAO and phenol formaldehyde resin (PF) and (2) SAO and reduced
23 graphene oxide (rGO) in the presence of nitrogen precursor (melamine) resulted in N-doped SAOPF
24 (N-SAOPF) and N-doped SAOrGO (N-SAOrGO), respectively. These showed similar macro porous
25 structures. Temperature dependant mass spectrum of SAO in the temperature range of 30 – 275 °C
26 showed the release of sulphur dioxide gas (SO₂) at 266 °C which is responsible for the formation of
27 macro porous structures. The N-SAO, N-SAOPF and N-SAOrGO were used as electro catalysts for
28 ORR in alkaline medium and investigated their performance. While the N-SAO/PF showed the
29 highest onset potential of 0.98 V (RHE), the N-SAOrGO showed the highest current density of 7.89
30 mA/cm² at 0.00 V (RHE). Interestingly, all catalysts showed a four – electron reaction pathway for
31 ORR.

32 **Keywords:** Oxygen reduction reaction (ORR); catalysis; carbon nanotubes; sulphonated aniline
33 oligomers; N-doped carbon

34

35 **1.0 Introduction**

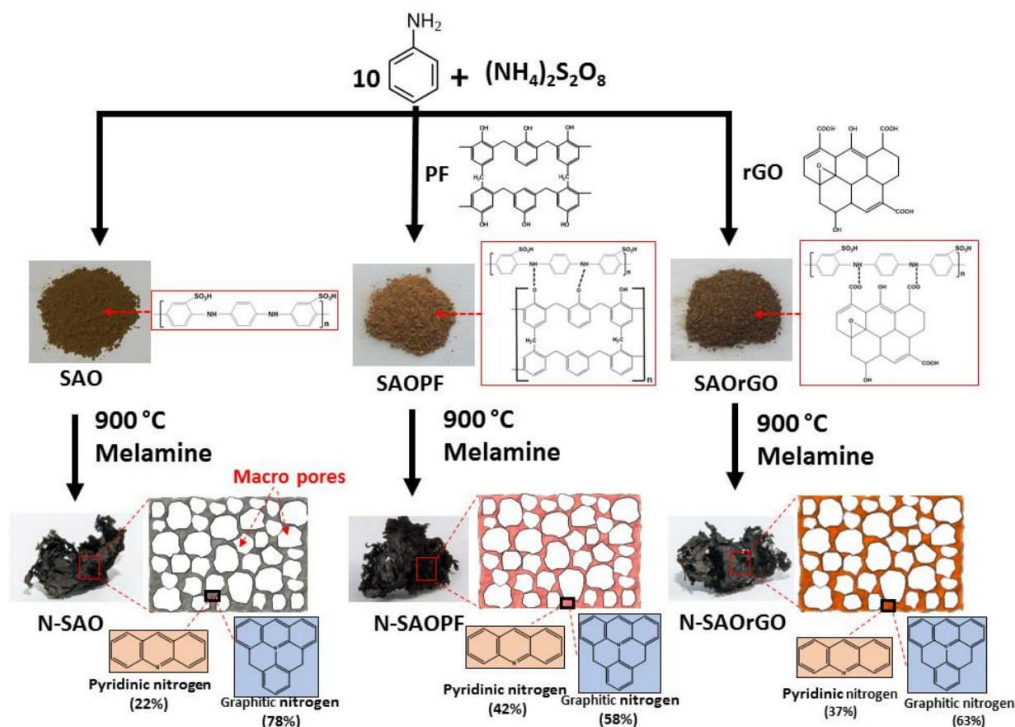
36 Fuel cells are considered as a promising sustainable and renewable energy devices, which could
37 supply the energy demand created by the depletion of fossil fuel [1]. These are devices are based on
38 electrochemically combine hydrogen (H₂) and oxygen (O₂) to produce electricity and heat via an
39 oxygen reduction reaction [2]. However, the practical use of fuel cell has been hindered due to the
40 slow kinetics of the ORR catalysts used in the fuel cell [3]. Platinum (Pt) catalysts have dominated as

41 the preferred ORR catalysts for its activity, stability and selectivity for many years. However, because
42 of the high cost, scarcity and its susceptibility to time dependent drift and CO deactivation of Pt
43 catalysts, a need to find alternative cost effective and freely available catalysts has become inevitable
44 [4].

45 Nitrogen doped carbon materials such as carbon black (N-doped CB) [5], mesoporous carbon
46 materials (N-doped MPC) [6], N-doped carbon nanotubes (N-CNTs) [7] and N-doped graphene [4]
47 has been used to synthesise N-doped carbon catalysts for ORR. Gong et al. [7] initially synthesised
48 vertically aligned N-doped CNT and disclosed that the electron accepting ability of the nitrogen
49 atom, could generate a net positive charge on the adjacent carbon atom to facilitate diatomic O₂
50 adsorption [8]. Carbon materials used for ORR catalysts should possess large surface area for
51 dispersing the catalytic nanoparticles, provide stability, high electrical conductivity and porosity to
52 perform efficient mass transfer and diffusion of reactants and the by-products [9]. Many researches
53 have been conducted in the past to determine the effect of the mesoporous carbon on ORR activity
54 [9, 10]. Mesoporous carbon (2 – 50 nm in diameter) has outperformed micro porous carbon materials
55 (< 2 nm in diameter) as preferred ORR catalyst due to high surface area and efficient mass transfer.
56 However, to perform a smooth and rapid electrochemical reaction such as ORR, fast mass exchange
57 of reactants and products are essential and mesoporous are incapable providing efficient
58 reactant/product transfer [11]. Liang et al. [12] synthesised different pore sizes of 3D ordered
59 microporous g-C₃N₄/C by tailoring the pore sizes using different sized silica spheres and
60 demonstrated that macropores (150 nm) facilitated efficient reactant/ product mass transfer and
61 showed outstanding ORR catalytic performance compared to mesopores (12 nm). However, since the
62 large pore sizes of macropores provide low active sites for ORR activity [11]. Therefore, materials
63 possess high surface area are commonly incorporated in to macro porous structures [11]. In this
64 context, to provide larger surface area and additional active sites, mesoporous materials with high
65 surface area are blended with carbon catalysts [13, 14]. Mesoporous phenol formaldehyde resin (PF)
66 synthesised by thermal cross linking of resol is one of commonly used as a material used to introduce
67 mesoporosity to carbon catalysts [11]. On the other hand, graphene with its outstanding properties
68 such as large specific theoretical surface area (2630 m²g⁻¹) [15], high young modulus (approx 1.0 TPa)
69 [16], high intrinsic mobility (200, 000 cm²v⁻¹s⁻¹) [17] and thermal conductivity (approx. 5000 Wm⁻¹K⁻¹)
70 [18] to provide mechanical stability and to increase charge transfer of electrons to assists catalytic
71 reactions [19, 20]. Carbon composite materials synthesised with PF and graphene has shown
72 outstanding catalytic activity for ORR [11, 21].

73 In this study, macro porous graphitic carbon composite materials were synthesised to enhance the
74 ORR activity by facilitating efficient reactant and product mass transfer using two-step process: (1)
75 preparation of composites of SAO with PF and rGO and (2) pyrolysis of these composites in the
76 presence of melamine. In order to generate additional active sites for ORR, PF was composite with
77 SAO. Thermoset PF resins under heat treatment forms mesoporous carbon materials and provide
78 additional active sites for ORR [22]. On the other hand, to increase the electro charge transfer of the
79 catalyst material, rGO was composite with SAO. During heat treatment, rGO can be reduced to more
80 graphene structures and increase the electro charge transfer of the catalyst material to facilitate ORR
81 [23]. The scheme of the synthesis procedure of N-doped catalysts is presented in Scheme1. The
82 performance of these N-doped materials (N-SAO, N-SAO PF and N-SAO rGO) were evaluated as
83 electro catalysts for ORR in alkaline medium.

84



85

86 Scheme 1: Schematic representation of synthesis procedures of composite materials of SAO and N-doped
87 catalysts.

88

89 2.0 Experimental

90 2.1 Materials

91 Natural graphitic rock (Uley, Eyre Peninsula, SA) was milled into a fine powder using a bench top
92 ring mill (Rocklabs). Aniline (Reagent Plus, 99%), ammonium persulphate ((NH₄)₂S₂O₈, APS),
93 hydrogen peroxide (H₂O₂), hydrochloric acid (HCl), potassium permanganate (KMnO₄), sulphuric
94 acid (H₂SO₄), phosphoric acid (H₃PO₄), ethanol, phenol, paraformaldehyde was purchased from
95 Sigma-Aldrich and Chem Supply.

96 2.2 Methods

97 2.2.1 Preparation of sulfonated polyaniline

98 Aniline (5 mL, 5.19 g, 0.05 mol) was dissolved in 40 mL of ethanol and separately, APS (1.35 g, 0.005
99 mol) was dissolved in 6 mL of 1M HCL. The solutions were mixed at 5 °C for 30 min using a magnetic
100 stirrer and then continued stirring at room temperature for 16 hours. The product was then collected
101 and centrifuged at 4200 rpm in a centrifuge. The precipitate was collected and continuously washed
102 with ethanol for several hours in a Soxhlet extractor and vacuum dried for overnight.

103 2.2.2 Preparation of SAO/ reduced graphene oxide (rGO) composite material (SAOrGO)

104 2.2.2.1 Preparation of graphene oxide (GO)

105 GO was synthesised using the improved Hummer's method [24]. A mixture of concentrated acids
106 H₂SO₄/ H₃PO₄ (9:1) was added to a mixture of graphite flakes (3.0 g) and KMnO₄ (18.0 g). The solution
107 was then heated to 50 °C and stirred for 12 h. The solution was cooled and poured onto ice (400 mL)

108 containing H₂O₂ (3 mL). The mixture was centrifuged (4000 rpm) for 4 h and the supernatant was
109 removed. The precipitate was then washed in succession of water (2 x 200 mL), 30% HCl (2 x 200 mL)
110 and ethanol (2 x 200 mL). The final product was collected, and vacuum dried overnight at room
111 temperature.

112 **2.2.2.2 Preparation of SAOrGO composite**

113 GO (30 mg) was sonicated with 15 mL of distilled water for 1 hour. The GO suspension was diluted
114 with 15 mL ethanol and transferred in to a Teflon autoclave and heated in an oven for 90 min at 150
115 °C. The auto clave was cooled and 5 mL of the hydrothermally reduced GO (rGO) was collected and
116 mixed with aniline (5 mL, 5.19 g, 0.055 mol) dissolved in 40 mL of ethanol for 10 min. Then APS
117 (1.35g, 0.005 mol) was dissolved in 6 mL of 1M HCL. The solutions were mixed at 5°C for 30 min
118 using a magnetic stirrer and then continued stirring at room temperature for 16 hours. The product
119 was then collected and centrifuged at 4200 rpm in a centrifuge. The precipitate was collected and
120 continuously washed with ethanol for several hours in a Soxhlet extractor and vacuum dried for
121 overnight.

122 **2.2.3 Preparation of SAO / phenol formaldehyde resin (PF) composite (SAOPF)**

123 **2.2.3.1 Preparation of PF**

124 PF was synthesised using a minor modification to the procedure suggested by Meng *et.al.*[25] Briefly,
125 phenol (0.22 mol) was melted for 10 min at 35 °C. Then NaOH (0.1 mol) was dissolved in 12 mL of
126 distilled water and mixed with the melted phenol and stirred in a magnetic stirrer for 5 min. Then
127 formaldehyde (para formaldehyde (10.40 g) in 28 mL distilled water) was added dropwise to the
128 phenol suspension and mixed for 25 min at 80 °C until a transparent orange colour was obtained.
129 Finally, the suspension was cooled, and the pH was adjusted to 3 by adding concentrated HCl
130 solution. The product was allowed it to settle overnight and the PF resin (10 mL) was collected and
131 diluted with 5 mL of ethanol to prepare the PF resin solution.

132 **2.2.3.2 Preparation of SAOPF composite.**

133 PF resin solution (7.5 mL) was mixed 12.5 mL of ethanol and 15 mL of distilled water and
134 hydrothermally heated for 90 min at 150 °C in a Teflon autoclave. The hydrothermally heated product
135 was cooled, and 5 mL of the hydrothermally treated resin solution was collected and mixed with
136 aniline (5 mL, 5.19 g, 0.055 mol) dissolved in 40 mL of ethanol for 10 min. Then similar procedure as
137 for PA was followed. Then APS (1.35g, 0.005 mol) was separately dissolved in 6 mL of 1M HCL.
138 The rest of the experimental procedure was conducted similar to that of synthesis of SAO.

139

140 **2.2.4.1 Preparation of rGOPF composites**

141 The rGOPF was prepared using hydro thermally synthesised rGO/ PF suspension. The suspension (5
142 mL) was mixed with the oxidising agent APS (1.35g, 0.005 mol) which was dissolved in 6 mL of 1M
143 HCL. The experimental procedure was carried out using similar procedure as per SAO without using
144 aniline the monomer aniline.

145 **2.2.5 Preparation of pyrolysed and N-doped catalysts**

146 **2.2.5.1 Preparation of pyrolysed catalysts (P-SAO, P-SAO_rGO, P-SAOPF, and P-rGOPF)**

147 SAO, SAO_rGO, SAOPF, and rGOPF (1.0 g) were placed on ceramic boats and separately pyrolysed
148 in a tubular furnace at 900 °C for 30 min under argon. The temperature was raised at the rate of 10
149 °C/ min. The annealed products were referred as P-SAO, P-SAO_rGO, P-SAOPF, and P-rGOPF,
150 respectively.

151 **2.2.5.2 Preparation of N-doped catalysts (N-SAO, N-SAO_rGO, N-SAOPF, and N-rGOPF).**

152 SAO, SAO_rGO, SAOPF, and rGOPF (1.0 g) were separately mixed with melamine (1:10 w/w) using a
153 mortar/ pestle and separately pyrolysed in a tubular furnace at 900 °C for 30 min under argon. The
154 temperature was raised at the rate of 10 °C/ min. The N-doped products were referred as N-SAO, N-
155 SAO_rGO, N-SAOPF, and N-rGOPF, respectively.

156

157 **2.3 Preparation of catalytic ink**

158 Catalytic ink was prepared by ultra-sonication of each catalyst (2 mg) and suspended in Nafion
159 suspension (1 mL of 1%). The prepared ink (10 µL) was carefully deposited on both a glassy carbon
160 rotating disc electrode (3 mm) and rotating ring disc electrode (4 mm). The sample was allowed to
161 dry in air for 12 hours.

162

163 **2.4 Characterisations**

164 **2.4.1 Structural and chemical composition characterizations**

165 Scanning electron microscopy (SEM) images and energy-dispersive X-ray spectroscopy (EDX) were
166 obtained using Quanta 450, FEI, USA at an accelerating voltage of 10 KeV. For EDX three reading
167 were recorded and the average was recorded. Transition electron microscopy (TEM) investigation
168 was carried out using Technai G2 Spirit, FEI, USA, operated at 120 keV. X-ray diffraction (XRD) XRD
169 was performed at 40 kV and 15 mA in the range of $2\theta = 3^\circ - 50^\circ$ at a speed of 10°/min using Miniflex
170 600, Rigaku, Japan, gas adsorption isotherms were conducted using a Micromeritics 3-Flex or
171 ASAP2020 analyser (Micro metrics Instruments Corporation, Norcross, GA, USA). Fourier transform
172 infrared (FTIR) spectroscopy was conducted using Spectrum 100, Perkin Elmer, USA. Raman analysis
173 was conducted using a LabRAM Evolution, Horiba Jvon, Japan using a 532 nm wavelength. XPS was
174 conducted on a custom-built SPECS instrument (Berlin, Germany). All XPS measurements were
175 performed on sample prepared by drop casting onto Si using a non-monochromatic Mg source
176 operating at 120 Kev and 200W. High resolution XPS spectra were collected using a pass energy of
177 10 eV with an energy step of 0.1e V.

178

179 **2.4.2 Electro chemical characterisation**

180 The ORR reactions were conducted utilising a Rotating Ring Disc Electrode (RRDE) apparatus
181 connected to a bi potentiostat (CH 1760 C, CH Instruments Inc., USA) in a standard three electrode
182 cell with oxygen saturated KOH (0.1 mol L⁻¹) solution. The glassy carbon electrode platinum and
183 reversible hydrogen electrode (RHE) were use as the working, counter and reference electrodes,
184 respectively. The scan rate of the reaction was 0.01 Vs⁻¹ in the range of 0 and 1.1 V. Cyclic voltammetry
185 plots were obtained at a scan rate of 100 mVs⁻¹ in oxygen saturated 0.1M KOH solution

186 The reaction kinetics of the catalysts was examined by employing RRDE to quantify the overall
187 electron transfer number (*n*) and percentage of hydrogen peroxide (% HO₂), at rotation speeds from

188 400 to 2400 rpm in an oxygen saturated 0.10 M KOH solution. To elucidate the overall number of
189 electrons (n) and percentage of HO_2^- (% HO_2^-) produced in the ring against the applied potential
190 equation 1 & 2 were employed [27, 28].

191
$$n = \frac{4I_D}{I_D + \frac{I_R}{N}} \quad (1)$$

192
$$\%HO_2^- = 100 \frac{2I_R}{I_D N + I_R} \quad (2)$$

193 Where I_D and I_R are the disc and ring currents, respectively and N is the collection efficiency.

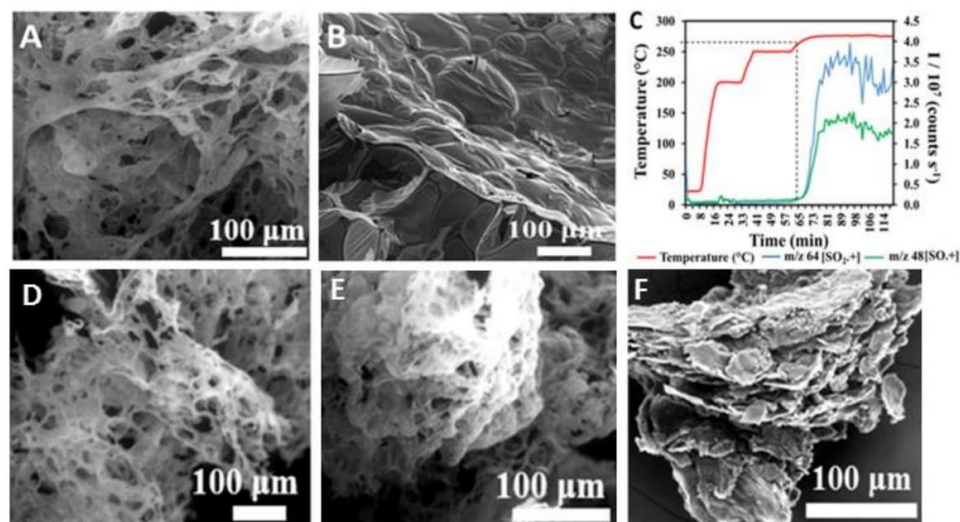
194 3. Results and Discussion

195 3.1. Structural characterisation

196 The SEM image of the pyrolysed SAO in the presence of melamine (N-SAO) and without melamine
197 (P-SAO) at 900 °C under Ar environment is presented in Fig.1A and B, respectively. Fig.1A shows the
198 presence of macropores (10 – 50 μm) for N-doped catalysts. Similar pores were observed for the N-
199 doped composites of SAO with rGO (N-SAO/rGO) (Fig. 1D) and PF (N-SAO/PF)(Fig.1E). For
200 comparison study, we synthesised a blend of rGO and PF (rGO/PF) without SAO. The blend of both
201 rGO and PF was used instead of rGO and PF because both rGO and PF under the similar synthesis
202 conditions did not provide enough yield. The EDX analysis conducted on the doped samples verified
203 the presence of N. The EDX analysis showed 8.96, 4.50, 2.84 and 3.44 wt% of N for N-SAO, N-
204 SAO/rGO, N-SAO/PF and N-rGO/PF, respectively.

205 Interestingly, all catalysts (N-SAO, N-SAO/rGO and N-SAO/PF) with SAO showed the formation of
206 micro pores. However, such pores were not observed for rGO/PF (Fig.1F). We hypothesised the
207 porous structure was formed as a result of a gas formed during the pyrolysis process of SAO. To
208 examine this hypothesis, we conducted a thermogravimetric analysis on SAO without the N-precursor
209 melamine using a custom-build high temperature pulsed-gas sampling equipment coupled with a
210 mass spectrometer for real-time analysis of the gaseous fragments. The detailed experimental
211 procedure is presented in the experimental section. The analysis revealed that the mass spectrometer
212 detected the fragments of m/z 64 [SO_2^+] and m/z 48 [SO^+] at 266 °C confirming release of SO_2 (Fig.
213 1C). We deduced the SO_2 gas was formed by the decomposition of sulphonate groups attached to
214 SAO. To obtain an overview of the morphology of SAO without the presence of N-precursors during
215 the pyrolysis process and to determine the influence of released SO_2 gas, we pyrolysed SAO at 900 °C
216 using similar conditions to that of synthesis of N-doped catalysts. The SEM image of the pyrolysed
217 P-SAO showed inter-connected bubble like structures with macro pores in the range of 50 – 100 μm
218 (Fig. 1B) confirming the influence of SO_2 gas to form porous structures.

219
220



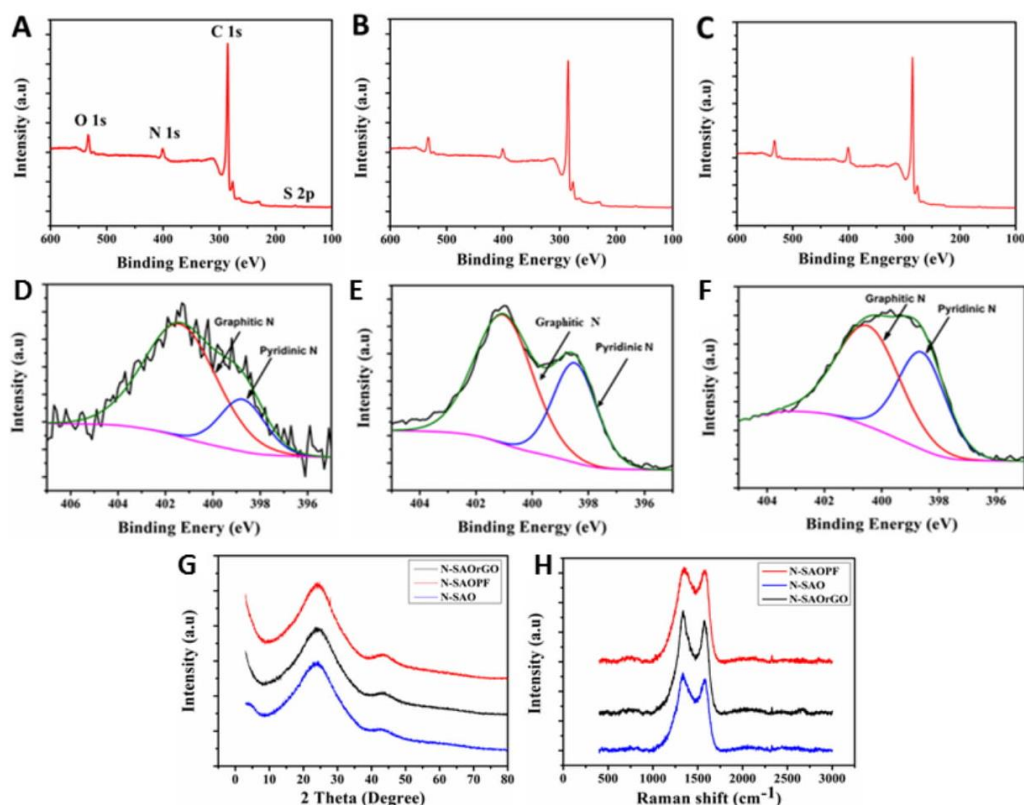
221
222 **Figure 1.** SEM images of (A) N-SAO, (B) P-SAO, (D) N-SAO_rGO, (E) N-SAOPF and (F) N-rGOPF. (C) The
223 temperature dependant mass spectrum of SAO in the temperature range of 30 – 275 °C.
224

225 To investigate the presence of different chemical species present in N-SAO, N-SAO_rGO, N-SAOPF
226 and N-rGOPF, we conducted a XPS survey spectrum on these samples. The survey spectrum of N-
227 SAO (Fig.2A) shows predominant C 1s peak at *ca.* 285.1 eV along with N 1s at *ca.* 400.6 eV, O 1s
228 peak at *ca.* 532.1 eV and a very low intenced S 2p peak at *ca.* 163.1 eV [29-31]. The presence of N1s
229 peak reveals that the N-doping of the graphitic carbon structure has been established. The low
230 intenced S 2p peak showed the existance of small amounts of residual sulphur in the materials due
231 to decomposition of sulphates. However, the atomic concentration of this peak is less than 0.80 %.
232 The survey peaks conducted for the N-doped SAO composite materials N-SAO_rGO (Fig.2B) and N-
233 SAOPF (Fig.2C) also showed similar patterns. The details of the survey spectrum is presented in
234 Table S1.

235 To probe the different nitrogen species present in the graphitic frame work, we carried out high
236 resolution N 1s measurements on N-SAO, N-SAO_rGO and N-SAOPF and presented in Fig 2D-F. The
237 high resolution XPS N 1s spectrum on these catalyts revealed the presence of two characteristic
238 peaks of pyridinic (~398.4 eV) and graphitic (~401.3 eV) nitrogen atoms with in the graphitic
239 carbon structure. For ORR reactions, both pyridinic and graphitic nitrogen contribute differently
240 towards ORR catalytic activity [32]. Although it is still controversial the role of each of these active
241 sites, it is widely believed that pyridinic nitrogen improves the onset potential while the graphitic
242 nitrogen determines the limiting current density [32]. Pyridinic nitrogen alters the band structure of
243 carbon by providing one *p* electrons to the aromatic π system and raise the density of π state near the
244 Fermi level to enhance the electro-donating capability of the ORR eletro-catalyst [32]. The pyridinic
245 nitrogen induce high positive charge density on adjacent carbon atoms and increase the electron
246 donor properties of these carbon atoms to adsorb O₂. This diatomic oxygen adsorption on the carbon
247 atom adjacent to pyridinic nitrogen weakens the O-O bond and facilitate ORR reaction [32].

248 The comparison of the % atomic concentrations of these peaks (Table 1) reveal that the pyridinic
249 nitrogen concentration of SAO composites (N-SAO_rGO and N-SAOPF) is higher than that of N-SAO.
250 This shows that the the pyridinic nitrogen substitution has effectively occurs via PF and rGO

251 compared to SAO. N-SAOPF showed the highest % atomic concentration of pyridinic nitrogen
 252 (42.4%) while N-SAOGO showed 36.69%. The analysis shows SAO facilitates more graphitic N
 253 substitution and less pyridinic N substitution.
 254



255
 256 **Figure 2.** Survey spectrum of (A) N-SAO, (B) N-SAOGO and (C) N-SAOPF and high resolution N1s XPS
 257 spectrum of (D) N-SAO, (E) N-SAOGO, and (F) N-SAOPF. (G) XRD pattern and (H) Raman peaks of N-
 258 SAO, N-SAOGO and N-SAOPF.

259 **Table 1.** Percentage atomic concentration of nitrogen species present in N-SAO, N-SAOGO and N-
 260 SAOPF.

Nitrogen species	% Atomic concentration		
	N-SAO	N-SAOGO	N-SAOPF
Pyridinic nitrogen	22.24	36.69	42.40
Graphitic nitrogen	77.76	63.31	57.60

261
 262 XRD and Raman analysis was conducted to analysed the presence of graphitic carbon materials in
 263 the product. The XRD patterns (Fig. 2G) and Raman analysis (Fig.2H) conducted on N-doped
 264 materials shows the materials are composed of graphitic carbon materials. The two distinctive XRD
 265 peaks at 24.0 and 43.5 °C are attributed to the (002) reflection in turbostratic graphitic carbons and
 266 (101) Bragg reflexion in graphitic carbon [33]. Raman analysis on the composite materials exhibits
 267 two peaks around 1340 and 1575 cm⁻¹ corresponding to D band and G band of graphitic carbon. The
 268 graphitic peaks D and G arises due to the E_{2g} vibrational mode of the C-C bond stretching and the

269 disorder peak due the A1g vibrational mode [34]. The intensity ratio of the D and G band (I_D/I_G)
270 determine the diffects associated with the pyrolysed and N-doped samples, where a higher intesity
271 (I_D/I_G) ratio show more defects [34]. The calculated intensity ratios (I_D/I_G) showed 1.07, 1.08 and 1.02
272 for N-SAO, N-SAO_rGO and N-SAOPF, respectively. The higher intensity ratio shows reasonable
273 distortion to the graphitic framework has taken place due to N-doping.

274

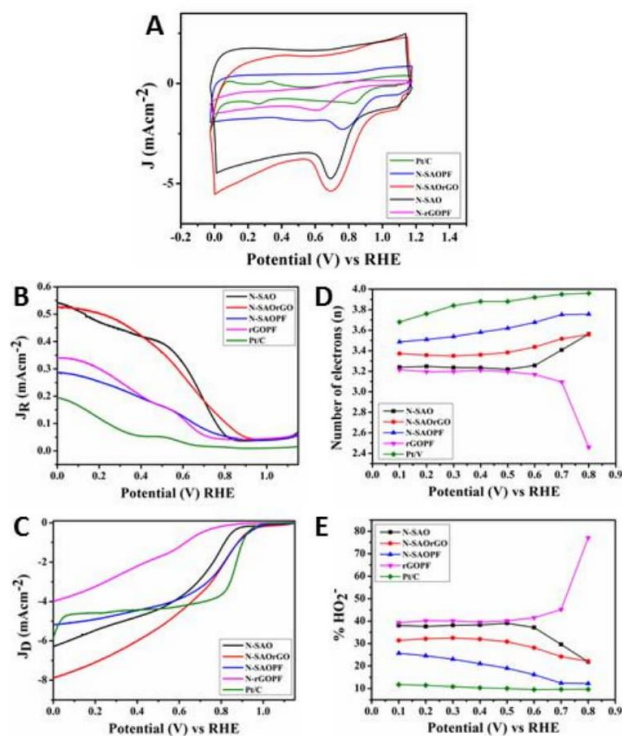
275 **3.2 Electrochemical characterisation of catalytic performances for ORR.**

276 The electrochemical catalytic activity for ORR of N-doped (N-SAO, N-SAO_rGO, N-SAOPF and N-
277 rGOPF) catalysts were examined by cyclic voltammetry (CV) and presented in Fig. 3A in an O₂
278 saturated 0.10 M KOH solution in the potential range of 0.00 to 1.20 V. The voltammograms show for
279 all catalysts the CV curves displayed a well defined oxygen reduction cathodic peaks centered at 0.67,
280 0.68, 0.76 and 0.59 V, for N-SAO, N-SAO_rGO, N-SAOPF and N-rGOPF, respectively, demonstrating
281 catalytic activity for ORR. The ORR cathodic peak positively shifted in the order of N-SAOPF > N-
282 SAO_rGO > N-SAO > N-rGOPF. This reveals the N-doped composite materials of SAO (N-SAO_rGO
283 and N-SAOPF) has enhance the catalytic activity of ORR than that of N-SAO. It is interesting to note
284 that the cathodic peaks have shifted positively according to the increasing percentage of pyridinic
285 nitrogen seen in Table 1.

286 To quantify the ORR electron transfer pathway, we employed RRDE technique to accurately measure
287 the ring and disc currents, electron transfer number and percentage of hydrogen peroxide (% HO₂)
288 generated at the disc electrode using N-doped electro catalysys in 0.10 M KOH on oxygen saturated
289 solution [35] (Fig.3) . The ring (Fig. 3B) and disc (Fig. 3C) currents of N-SAO, N-SAO_rGO, N-SAOPF,
290 and N-rGOPF electro-catalysts was analysed at 2000 rpm at a scan rate of 10 mV/s. The ORR onset
291 potential measured for these catalysts is displayed in Table 2 and Fig. 4A. The results showed the
292 onset potential increased in the order of N-SAOPF (0.98) > N-SAO_rGO (0.93 V) > N-SAO (0.87 V) >
293 N-rGOPF (0.78V). The results showed the catalysts possess macropores demonstrated higher ORR
294 activity compared to N-rGOPF. The ORR onset potential of N-SAOPF showed similar or almost
295 similar values as the standard Pt/C catalysts (0.98 V). Conversely, the current density of the catalysts
296 increased in the order of N-SAO_rGO (7.89 mAcm⁻²) > N-SAO (6.29 mAcm⁻²) > N-SAOPF (5.18 mAcm⁻²)
297 > N- rGOPF (3.99 mAcm⁻²) at 0.00 V (RHE) (Fig.4B and Table 2). Lai et al.[36] investigated the
298 active site of the N-doped non-metallic catalysts and reported pyridinic nitrogen species improves
299 the onset potentials while the graphitic nitrogen determine the limiting current density. Our results
300 were consistent with the finding of Lai et al. [36]. The N-SAOPF with the higher % atomic
301 concentration of pyridinic nitrogen showed the highest positive onset potential compared to other
302 N-doped catalysts. However, it showed low limiting current density due to the lower graphitic N
303 content and non-conductive nature of PF polymer. Conversely, N-SAOGO showed the highest
304 limiting current density due to the presence of more conductive graphene formed within the
305 composite material as a result of thermal reduction of rGO which facilitate electron charge transfer
306 [19]. Moreover, the presence of higher graphitic N species further increased the current density [36].
307 The synergetic effect of both conductivity of graphene along with graphitic N species showed higher
308 limiting current density for SAO_rGO nearly 65% more than that of standard Pt/C catalyst at 0.00 V
309 (RHE).

310 The number of electron transferred and % HO₂ generated in the potential region 0.00 - 1.15 V are
311 presented in Fig.3D and E, respectively. The comparison of number of electron transferred (Fig.4C

312 and Table 2) and % HO₂⁻ yield (Fig.4D and Table 2) at 0.5V revealed N-SAOPF showed the highest
313 electron transfer number (3.62) with the lowest % HO₂⁻ yield (19.02%). According to Liu *et al.* [32],
314 pyridinic nitrogen can weaken the diatomic O-O bond of O₂ attached to the carbon atom adjacent
315 to the pyridinic nitrogen. Pyridinic nitrogen provides one *p* electron to the aromatic π system of the
316 carbon matrix to increase the electron donating capability of carbons adjacent to nitrogen to weaken
317 the O-O bond strength and facilitate ORR reaction [32]. The highest ORR catalytic activity displayed
318 by N-SAOPF can be attributed to the presence of % atomic percentage of pyridinic nitrogen.
319 Furthermore, the mesoporous nature of the PF also could have contributed to the mass transfer of
320 reactants and products. However, TEM images conducted on these samples could not detect these
321 pores. Conversely, N-SAOGO with graphitic nitrogen showed lower catalytic activity for ORR than
322 N-SAOPF. The ORR was performed via 3.38 electrons with the yield of 30.84% HO₂⁻. The half-wave
323 potential ($E_{1/2}$) of the catalysts positively increased according to N-SAOPF (0.79 V) > N-SAO_rGO (0.66
324 V) > N-SAO (0.65 V) > N-rGOPF (0.44 V) showing the ORR performed through both mixed diffusion
325 and kinetic regions where current is controlled by both mass transport and kinetics of electron
326 transfer [37]. The $E_{1/2}$ of the catalysts shifted more negatively compared to the $E_{1/2}$ of the standard
327 Pt/C catalyst (0.88 V). However, among all catalysts $E_{1/2}$ of N-SAOPF shifted more positively and
328 attained limiting current with a low range of over potentials in the mixed kinetics and diffusion range
329 revealing the coverage of high oxygen adsorption. Liu *et al.* [38] reported that the catalysts with N-C
330 active sites more likely to shift the $E_{1/2}$ negatively. Therefore, the negative shift of the $E_{1/2}$ of the
331 catalysts can be attributed to their N-C active sites. However, according to the authors $E_{1/2}$ can be
332 shifted positively by the by the addition of Fe-N-C or Co-N-C active sites [38].
333 The RRDE voltammogram conducted on non - doped catalysts are were also evaluated and shown
334 in Fig S1 and Table S2. The comparison of the onset potential, current density, number of electron
335 transferred and % HO₂⁻ generated of doped and non – doped catalysts are shown in Fig.4. The
336 comparison shows onset potential, current density, number of electron transferred and % HO₂⁻ has
337 significantly increased due to N-doping.

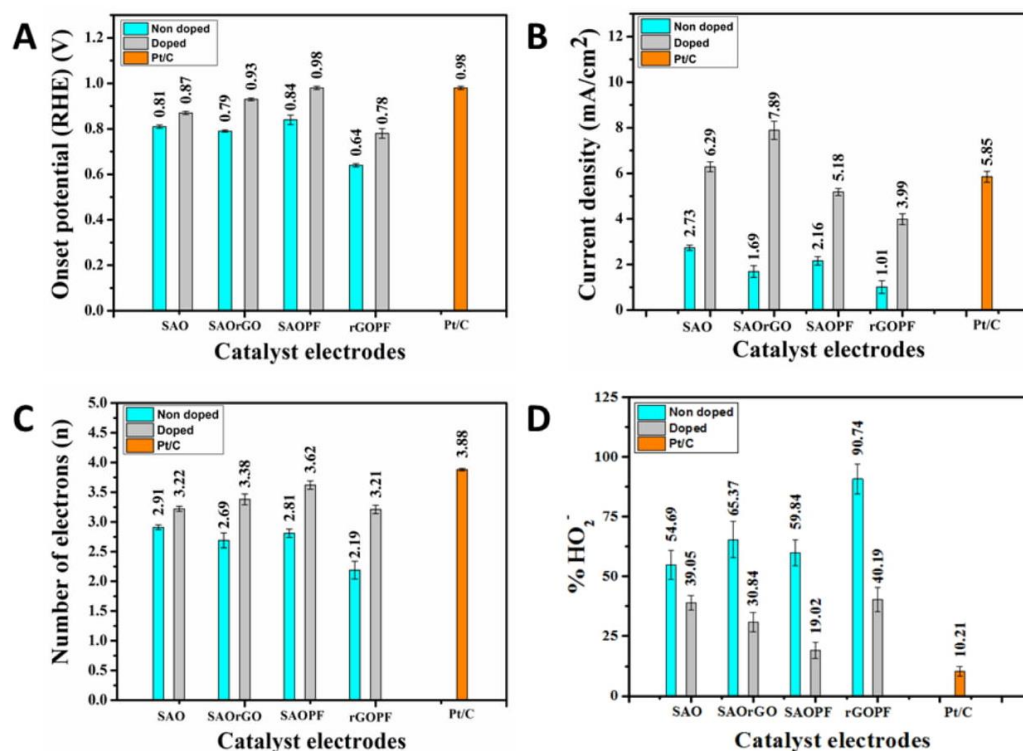


338
 339 **Figure 3.** (A) Comparison of cyclic voltammograms of N-SAO, N-SAO/GO, N-SAO/PF, N-SAO/GO/PF and Pt/C
 340 catalysts at a scan rate of 10 mV s⁻¹ in oxygen saturated 0.10 M KOH solution. Rotating ring disc voltammograms
 341 of (B) ring current, (C) disc current of N-SAO, N-SAO/GO, N-SAO/PF, N-SAO/GO/PF and Pt/C electrodes in
 342 oxygen saturated 0.1M KOH at 2000 rpm at a scan rate of 10 mV/s. (D) number of electrons and (E) percentage
 343 peroxide of N-SAO, N-SAO/GO, N-SAO/PF, N-SAO/GO/PF and Pt/C electrodes at various potentials calculated
 344 according to RRDE data.

345 **Table 2.** Electrochemical properties of the N-doped aniline oligomers and composite of aniline
 346 oligomers catalysts.

Catalysts	Current density (mA/cm ²) at 0.00 V (RHE)	Onset potential (RHE) (V)	Half-wave potential (RHE) (V)	Number of electrons (n) (0.10 - 0.80 V) (RHE)	% H ₂ O ₂ (0.10 - 0.80V) (RHE)
N-SAO	6.29	0.87	0.65	3.23 - 3.56	38.82 - 21.86
N-SAO/GO	7.89	0.93	0.66	3.37 - 3.55	31.88 - 22.13
N-SAO/PF	5.18	0.98	0.79	3.48 - 3.75	25.67 - 12.12
N-SAO/GO/PF	3.99	0.78	0.44	3.21 - 2.45	39.28 - 77.07
Pt/C	5.85	0.98	0.88	3.68 - 3.98	11.73 - 9.65

347



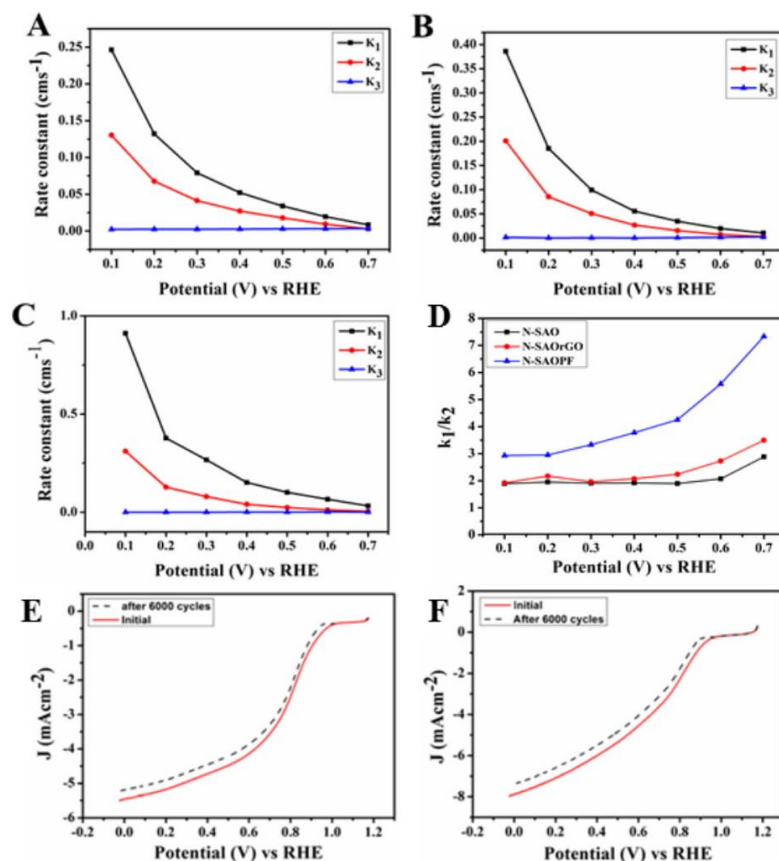
348

349 **Figure 4.** (A) onset potential, (B) current density at 0.00V (RHE), (C) comparison of number of electrons (at 0.50
 350 V) and (D) % HO₂⁻ (at 0.50 V) of non-doped (light blue) and doped (grey) SAO, SAOrGO, SAOPF, rGOPF and
 351 Pt/C catalysts in oxygen saturated 0.10 M KOH electrolyte at 2000 rpm at a scan rate of 10 mV/s.

352

353 To further investigate the electron transfer kinetics of the N-doped catalysts, the scheme suggested
 354 by Damjanovic *et.al* [39] detailed in SI was used. The rate constants of N-SAO, N-SAO_rGO and N-
 355 SAOPF and N-SAO_rGOPF calculated based on these equations in the potential region 0.10 - 0.70 V
 356 (Fig.5A-C) shows that the ORR was predominantly driven by a four - electron pathways. The
 357 calculated value of the ratio of k_1/k_2 presented in Fig.5D showed $k_1/k_2 > 1$ for all catalysts. Among N-
 358 SAO, N-SAO_rGO and N-SAOPF catalysts the highest k_1/k_2 ratio was seen for N-SAOPF while N-SAO
 359 showed the lowest k_1/k_2 values. This furthermore reveal that the N-SAOPF with high percentage of
 360 atomic concentration of pyridinic nitrogen has dominated the ORR catalytic performance. The
 361 stability of N-SAO_rGO and N-SAOPF was evaluated by cycling the catalysts between 0.0 V and 1.15
 362 V at 100 mV S⁻¹ in an O₂ saturated 0.10 M KOH solution. Fig.5E and F shows after 6,000 cycles the
 363 onset potential of N-SAO_rGO and N-SAOPF has shifted 40 and 30 mV negatively showing only a
 364 slight deterioration of the catalysts.

365



366

367 **Figure 5.** Rate constants of (A) N-SAO, (B) N-SAO/GO and (C) N-SAO/PF, (D) The ratio of rate constant K_1/K_2
 368 for N-SAO, N-SAO/GO, N-SAO/PF and N-SAO/GO/PF in the potential range of 0.1 – 0.7 V. RDE polarisation
 369 curves of (E) N-SAO/PF and (F) N-SAO/GO with a scan rate of 10 mV s^{-1} before and after 6000 potential cycles in
 370 0.10 M Oxygen saturated KOH.

371 4. Conclusions

372 This study demonstrated a unique synthesis method to synthesise N-doped macro porous carbon
 373 catalysts using SAO and its composites with PF and rGO. Thermal treatment on SAO decomposed
 374 the sulphonated groups attached to aniline oligomers and released SO_2 gas to form macro porous
 375 catalysts. The macro porous structures of synthesised N-doped N-SAO, N-SAO/GO and N-SAO/PF
 376 facilitated mass transport of reactants and products to provided ORR catalytic activity. N-doped
 377 composites of SAO, N-SAO/GO and N-SAO/PF showed diverse electro catalytic properties for ORR
 378 compared to N-SAO. Incorporation of PF and rGO to SAO facilitated formation of more pyridinic
 379 nitrogen species. N-SAO/PF with highest % atomic concentration of pyridinic nitrogen showed highest
 380 onset potential, highest electro transfer number and lowest % HO_2^- yield. Conversely, SAO/GO
 381 produced more graphene nitrogen species to increased the limiting current density.

382 The excellent ORR properties the catalysts showed for these materials will open doors for the
 383 generation of a new state of art macro porous N-doped carbon catalyst for ORR. Different materials

384 which have demonstrated high catalytic potential for ORR such as CNT and single or few layer
385 graphene can be blended with SAO to synthesise new catalysts. Furthermore, transition metals such
386 as Fe and Co can be used to synthesise composite material of SAO to generate more Fe-N-C or Co-
387 N-C active sites to enhance ORR reaction.

388 **Supplementary Materials:** SEM images of N-SAO_rGO, N-SAOPF and N-rGOPF, Survey spectrum of N-SAO,
389 Table S1. Atomic concentrations of N-doped catalysts, XRD pattern and Raman peaks of N-SAO, N-SAO_rGO
390 and N-SAOPF, Cyclic voltammetry plots of N-SAO, N-SAO_rGO, N-SAOPF, and N-rGOPF, Rotating ring disc
391 voltammograms of P-SAO, P-SAO_rGO, P-SAOPF, P-rGOPF and Pt/C electrodes, Rate constants of N-SAO, N-
392 SAO_rGO and N-SAOPF, Stability test of N-SAO_rGO and N-SAO

393 **Acknowledgments:**

394 The authors thank the support of Australian Research Council (IH 150100003), Australian Research Council
395 Research Hub for Graphene Enabled Industry Transformation, The Australian Solar Thermal Research Initiative
396 (ASTRI), The University of Adelaide, School of Chemical Engineering, The University of Adelaide, School of
397 Chemistry. The technical support provided by Adelaide microscopy, micro analysis research facility at Flinders
398 Microscopy (Flinders University) was great appreciated.

399

400 **Author Contributions:** R.K. performed the experiments and analyzed the data, C.S. conducted the XPS analysis,
401 C.C. and D.L. conceived and designed the experiments, and all other authors assisted in writing the manuscript.

402 **Conflicts of Interest:** The authors declare no conflict of interest.

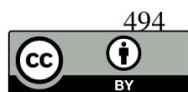
403

404 **9. References**

- 405 1. Stambouli, A.B.; Traversa, E. Solid oxide fuel cells (SOFCs): a review of an environmentally clean and
406 efficient source of energy. *Renewable and Sustainable Energy Rev.* **2002**, *6*, 433-455.
- 407 2. Larminie, J.; Dicks A.; McDonald M.S. Fuel cell systems explained. *J. Wiley Chichester* UK2003.
- 408 3. Sheng, W.; Gasteiger H.A.; Shao-Horn Y. Hydrogen oxidation and evolution reaction kinetics on
409 platinum: acid vs alkaline electrolytes. *J. Electrochem. Soc.* **2010**, *157*, B1529-B1536.
- 410 4. Qu L.; Liu Y.; Baek J. B.; Dai L. Nitrogen-doped graphene as efficient metal-free electrocatalyst for oxygen
411 reduction in fuel cells. *ACS Nano* **2010**, *4*, 1321-1326.
- 412 5. N.P. Subramanian N.P.; Li X.; Nallathambi V.; Kumaraguru S.P.; Colon-Mercado H.; Wu G.; Lee J.W.;
413 B.N. Popov B.N. Nitrogen-modified carbon-based catalysts for oxygen reduction reaction in polymer
414 electrolyte membrane fuel cells. *J. Power Sources* **2009**, *188*, 38-44.
- 415 6. Niu W.; Li L.; Liu X.; Wang N.; Liu J.; Zhou W.; Tang Z.; Chen S. Mesoporous N-doped carbons prepared
416 with thermally removable nanoparticle templates: an efficient electrocatalyst for oxygen reduction
417 reaction. *J. Am. Chem.Soc.* **2015**, *137*, 5555-5562.
- 418 7. Gong K.; Du F.; Xia Z.; Durstock M.; Dai L.; Nitrogen-Doped Carbon Nanotube Arrays with High
419 Electrocatalytic Activity for Oxygen Reduction. *Science*, **2009**, *323*, 760-764.
- 420 8. Tang, Y.; Allen B.L.; Kauffman D.R; Star A. Electrocatalytic Activity of Nitrogen-Doped Carbon Nanotube
421 Cups. *J. Am. Chem. Soc.* **2009**, *131*, 13200-13201.
- 422 9. Xu J.; Zhao T. Mesoporous carbon with uniquely combined electrochemical and mass transport
423 characteristics for polymer electrolyte membrane fuel cells. *RSC Advances* **2013**, *3*, 16-24.
- 424 10. Liu R.; Wu D.; Feng X.; Müllen K. Nitrogen-Doped Ordered Mesoporous Graphitic Arrays with High
425 Electrocatalytic Activity for Oxygen Reduction. *Angew. Chem.* **2010**, *122*, 2619-2623.

- 426 11. Liang J.; Du X.; Gibson C.; Du X.W.; Qiao S.Z. N-Doped Graphene Natively Grown on Hierarchical
427 Ordered Porous Carbon for Enhanced Oxygen Reduction. *Advanced Materials* 2013, 25, 6226-6231.
- 428 12. Liang J.; Zheng Y.; Chen J.; Liu J.; Hulicova-Jurcakova D.; Jaroniec M.; Qiao S.Z. Facile Oxygen Reduction
429 on a Three-Dimensionally Ordered Macroporous Graphitic C₃N₄/Carbon Composite Electrocatalyst.
430 *Angew. Chem.* 2012, 124, 3958-3962.
- 431 13. Xiao M.; Zhu J.; Feng L.; Liu C.; Xing W. Meso/Macroporous Nitrogen-Doped Carbon Architectures with
432 Iron Carbide Encapsulated in Graphitic Layers as an Efficient and Robust Catalyst for the Oxygen
433 Reduction Reaction in Both Acidic and Alkaline Solutions. *Advanced materials*, 2015, 27, 2521-2527.
- 434 14. Chai G.S.; Shin I.; Yu J.S. Synthesis of ordered, uniform, macroporous carbons with mesoporous walls
435 templated by aggregates of polystyrene spheres and silica particles for use as catalyst supports in direct
436 methanol fuel cells. *Advanced Materials*, 2004, 16, 2057-2061.
- 437 15. Geim A.K.; Novoselov K.S. The rise of graphene. *Nature Materials*, 2007, 6, 183-191.
- 438 16. Lee C.; Wei X.; Kysar J.W.; Hone J.; Measurement of the elastic properties and intrinsic strength of
439 monolayer graphene. *Science*, 2008, 321, 385-388.
- 440 17. Bolotin K.I.; Sikes K.; Jiang Z.; Klima M.; Fudenberg G.; Hone J.; Kim P.; Stormer H. Ultrahigh electron
441 mobility in suspended graphene. *Solid State Commun.* 2008, 146, 351-355.
- 442 18. Balandin A.A.; Ghosh S.; Bao W.; Calizo I.; Teweldebrhan D.; Miao F.; Lau C.N. Superior thermal
443 conductivity of single-layer graphene. *Nano letters*, 2008, 8, 902-907.
- 444 19. Li H.; Yu K.; Li C.; Tang Z.; Guo B.; Lei X.; Fu H.; Zhu Z. Charge-transfer induced high efficient hydrogen
445 evolution of MoS₂/graphene cocatalyst. *Scientific reports*, 2015, 5, 18730.
- 446 20. Stergiou A.; Pagona G.; Tagmatarchis N. Donor-acceptor graphene-based hybrid materials facilitating
447 photo-induced electron-transfer reactions. *Beilstein J. Nanotechnol.* 2014, 5, 1580.
- 448 21. Wu Z.-S.; Sun Y.; Tan Y.Z.; Yang S.; Feng X.; Müllen K. Three-dimensional graphene-based macro-and
449 mesoporous frameworks for high-performance electrochemical capacitive energy storage. *J. Am. Chem. Soc.*
450 2012, 134, 19532-19535.
- 451 22. Sattler K.D. Carbon Nanomaterials Sourcebook. *CRC Press*, 2016.
- 452 23. Goumri M.; Lucas B.; Ratier B.; Baitoul M. Electrical and optical properties of reduced graphene oxide and
453 multi-walled carbon nanotubes based nanocomposites: A comparative study. *Opt. Mater.* 2016, 60, 105-113.
- 454 24. Marcano D.C.; Kosynkin D.V.; Berlin J.M.; Sinitskii A.; Sun Z.; Slesarev A.; Alemany L.B.; Lu W.; Tour J.M.
455 Improved synthesis of graphene oxide. *ACS Nano*, 2010, 4, 4806-4814.
- 456 25. Meng Y.; Gu D.; F. Zhang, Shi Y.; Yang H.; Li Z.; Yu C.; Tu B.; Zhao D. Ordered mesoporous polymers and
457 homologous carbon frameworks: amphiphilic surfactant templating and direct transformation. *Angew.*
458 *Chem.* 2005, 117, 7215-7221.
- 459 26. Burgun A.; Coghlan C.J.; Huang D.M.; Chen W.; Horike S.; Kitagawa S.; Alvino J.F.; Metha G.F.; Sumbly
460 C.J.; Doonan C.J. Mapping-Out Catalytic Processes in a Metal–Organic Framework with Single-Crystal X-
461 ray Crystallography. *Angew. Chem.Int. Ed.* 2017, 56, 8412 - 8416.
- 462 27. Wang S.; Dou S.; Tao L.; Huo J.; Dai L. Etched and Doped Co₉S₈/Graphene Hybrid for Oxygen
463 Electrocatalysis. *Energy Environ. Sci.* 2016, 9, 1320 - 1326.
- 464 28. Liang Y.; Li Y.; Wang H.; Zhou J.; Wang J.; Regier T.; Dai H. Co₃O₄ nanocrystals on graphene as a
465 synergistic catalyst for oxygen reduction reaction. *Nat Mater*, 2011, 10, 780-786.
- 466 29. Ahmed M.H.; Byrne J.A.; McLaughlin J.; Ahmed W. Study of human serum albumin adsorption and
467 conformational change on DLC and silicon doped DLC using XPS and FTIR spectroscopy.
468 *J. Biomater. nanobiotechnol.* 2013, 4, 194.

- 469 30. Nath M.; Satishkumar B.; Govindaraj A.; Vinod C.; Rao C.N.R. Production of bundles of aligned carbon
470 and carbon–nitrogen nanotubes by the pyrolysis of precursors on silica-supported iron and cobalt
471 catalysts. *Chem. Phys. Lett.* **2000**, 322, 333-340.
- 472 31. Smart R.S.C.; Skinner W.M.; Gerson A.R. XPS of sulphide mineral surfaces: metal-deficient, polysulphides,
473 defects and elemental sulphur. *Surf. interface anal.* **1999**, 28, 101-105.
- 474 32. Liu X.; Dai L. Carbon-based metal-free catalysts. *Nature Reviews Materials*, 1 (2016) 16064.
- 475 33. Liao Y.; Li X.-G.; Kaner R.B. Facile synthesis of water-dispersible conducting polymer nanospheres. *ACS*
476 *Nano*, **2010**, 4 5193-5202.
- 477 34. Palaniselvam T.; Aiyappa H.B.; Kurungot S. An efficient oxygen reduction electrocatalyst from graphene
478 by simultaneously generating pores and nitrogen doped active sites. *J. Mater.Chem.* **2012**, 22, 23799-23805.
- 479 35. Wu Z.-S.; Yang S.; Sun Y.; Parvez K.; Feng X.; Mullen K. 3D nitrogen-doped graphene aerogel-supported
480 Fe₃O₄ nanoparticles as efficient electrocatalysts for the oxygen reduction reaction. *J. Am. Chem. Soc.* **2012**,
481 134, 9082-9085.
- 482 36. Lai L.; Potts J.R.; Zhan D.; Wang L.; Poh C.K.; Tang C.; Gong H.; Shen Z.; Lin J.; Ruoff R.S. Exploration of
483 the active center structure of nitrogen-doped graphene-based catalysts for oxygen reduction reaction.
484 *Energy Environ. Sci.* **2012**, 5, 7936-7942.
- 485 37. Narayanamoorthy B.; Datta K.; Balaji S. Kinetics and mechanism of electrochemical oxygen reduction
486 using Platinum/clay/Nafion catalyst layer for polymer electrolyte membrane fuel cells. *J. Colloid Interface*
487 *Sci.* **2012**, 387, 213-220.
- 488 38. Liu Y. L.; Xu X. Y.; Shi C. X.; Ye X.-W.; Sun P.-C.; Chen T.-H. Iron–nitrogen co-doped hierarchically
489 mesoporous carbon spheres as highly efficient electrocatalysts for the oxygen reduction reaction. *RSC*
490 *Advances* **2017**, 7, 8879-8885.
- 491 39. Damjanovic A.; Genshaw M.A.; Bockris J.O. Distinction between Intermediates Produced in Main and
492 Side Electrode Reactions. *J. Chem. Phys.* **1966**, 45, 4057-4059.
- 493



© 2017 by the authors. Submitted for possible open access publication under the terms and conditions of the Creative Commons Attribution (CC BY) license (<http://creativecommons.org/licenses/by/4.0/>).

Supporting information for

A unique N-doped macro porous oxygen reduction electro catalyst synthesised using sulphonated aniline oligomers, phenol formaldehyde and reduced graphene oxide composites

Ramesh Karunakaran¹, Campbell Coghlan², Diana Tran¹, Tran Thanh Tung³, Alexander Burgun, Cameron Shearer^c, Christian Doonan^{2*}, Dusan Losic^{1*}

¹School of Chemical Engineering, University of Adelaide, SA, Australia

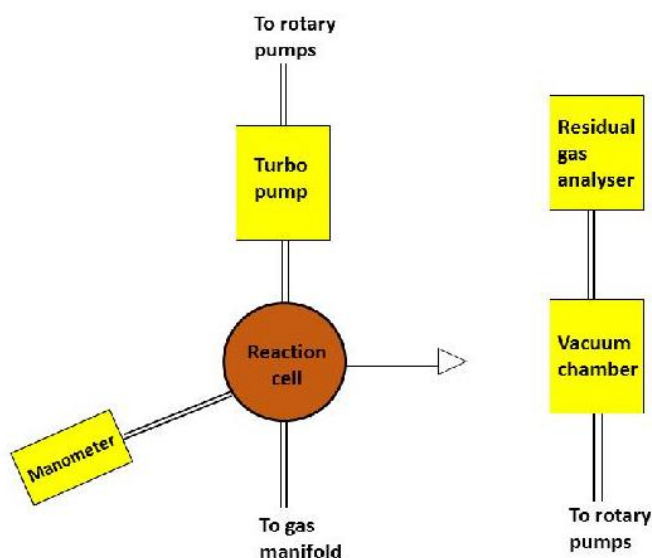
²School of Chemistry, University of Adelaide, SA, Australia

³School of Chemical and Physical Sciences, Flinders University, SA, Australia

*Corresponding author: Prof. Dusan Losic, Email: Dusan.losic@adelaide.edu.au, Phone: +61 8 8013 4648 or Christian.doonan@adelaide.edu.au; Tel.: +61 8 83135770

Thermometric-Mass spectrometer analysis

The thermometric-MS experiment was carried out using a custom-build high temperature pulsed-gas sampling equipment coupled with a mass spectrometer for real-time analysis of the gaseous mixture [1]. A schematic overview of the system is displayed in Scheme 2. The reaction cell is in direct contact with a copper block containing a 100 W heater cartridge controlled by a proportional-integral-derivative (PID) temperature controller (CAL Controls, Cal 3300) and K-type thermocouple attached to the side of the cell. The pressure in the reaction cell is monitored by a piezo-resistive manometer (Keller, Leo Record series, 30 bar range). The cell is connected to a pulsed nozzle (Parker, Series 9 Pulse Valve) which is used to pulse controlled amounts of gas from the reaction cell via a 1/16" stainless steel tube into the vacuum system, comprised of a residual gas analyser (RGA) for sampling of the gas mixture (*vide infra*). For our analysis, we loaded 10 mg of samples into the reaction cell and ramped for different temperatures including 30 °C to 200 °C and 200 °C -250 °C and 250 °C – 275 °C and paused the temperatures at 200 °C, 250 °C and 275 °C to determine any evolved gases.



Scheme S1. Schematic representation of custom-build high temperature pulsed-gas sampling equipment

Table S1. Atomic concentrations of N-doped catalysts

	N-SAO (% At)	N-SAO _r GO (%At)	N-SAO _r PF (%At)
C1s	87.01	90.53	85.45
N1s	8.78	4.86	8.89
O1s	3.96	4.04	4.89
S 2sp	0.25	0.57	0.77

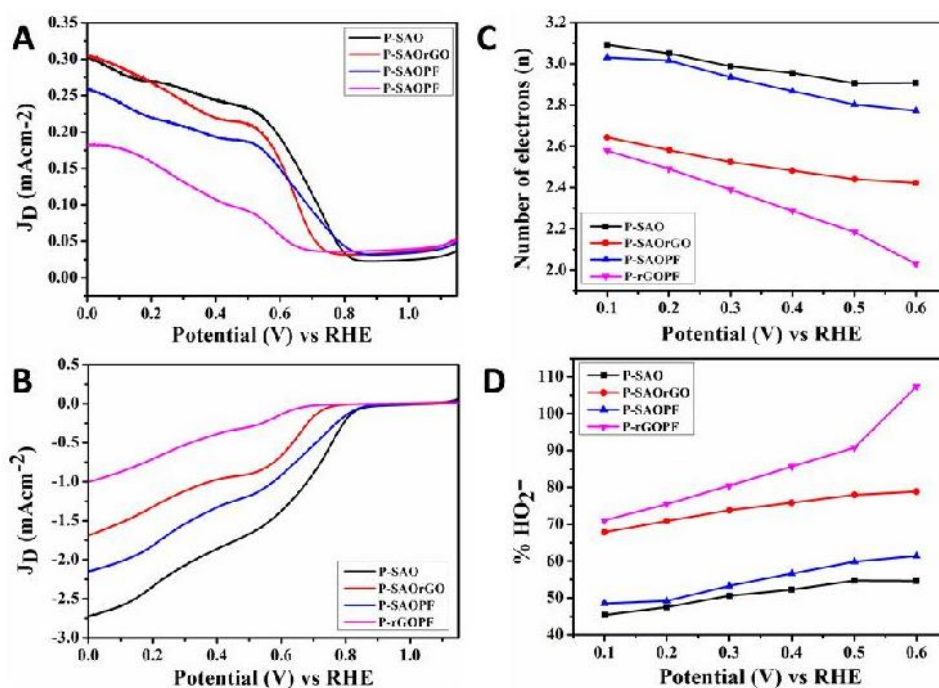


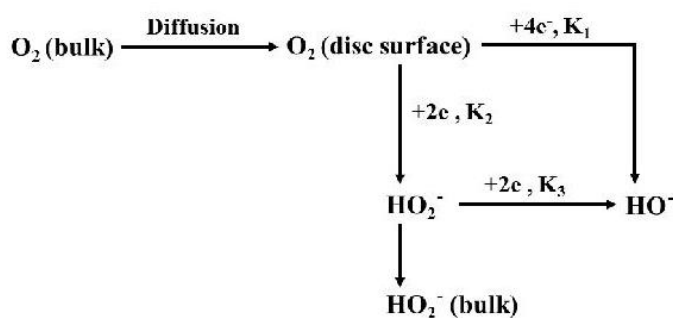
Figure S1. Rotating ring disc voltammograms of (A) ring current, (B) disc current of P-SAO, P-SAO_rGO, P-SAO_rPF and Pt/C electrodes in oxygen saturated 0.1M KOH at 2000 rpm at a scan rate of 10 mV/s. (C) number of electrons and (D) percentage peroxide of P-SAO, P-SAO_rGO, P-SAO_rPF and Pt/C electrodes at various potential calculated according to RRDE data.

Table S2. Electro chemical properties of the pyrolysed aniline oligomers and composite of aniline oligomers catalysts.

Catalysts	Current density (mA/cm ²) at 0.00 V (RHE)	Onset potential (RHE) (V)	Number of electrons (n) (0.10 - 0.80 V) (RHE)	% HO ₂ ⁻ (0.10 - 0.80V) (RHE)
P-SAO	2.73	0.81	3.09 - 2.90	45.45 - 54.60
P-SAO _r GO	1.69	0.74	2.64 - 2.42	67.84 - 78.68
P-SAOPF	2.16	0.84	3.03 - 2.77	48.50 - 61.35
P-rGOPF	1.01	0.64	2.57 - 2.03	71.06 - 107.40

Electron transfer kinetics

The electron transfer kinetic of the ORR was identified using RRDE voltametry (Scheme S1) [2, 3]. According to Damjanovic [2] *et al.* [2] the electron transfer mechanism follows a direct four-electron pathway via K₁ kinetics (Scheme S1), in which oxygen is directly reduced to hydroxide anion (OH⁻) or could be driven through a two-electron pathway via K₂ kinetics producing peroxide intermediates (HO₂⁻), followed by reduction to hydroxide anion (OH⁻) through another two electron pathway through K₃ kinetics.



Scheme S2: Proposed model for electrochemical reduction of oxygen proposed by Damjanovic *et al.* and Hsueh *et al.*

Hsueh *et al.* [3] suggested a series of equations (3, 4 and 5) to calculate the rate constants K_1 , K_2 and K_3 , where I_d , I_r , I_{dL} and ω are the disc current, ring current, limiting disc current and the rotation speed, respectively.

$$k_1 = S_1 Z_1 \frac{I_1^{N-1}}{I_1^{N+1}} \quad (3)$$

$$k_2 = \frac{2 S_2 Z_1}{I_1^{N+1}} \quad (4)$$

$$k_3 = \frac{N S_1 Z_2}{I_1^{N+1}} \quad (5)$$

Where S_1 and I_1 are the slope and intercept correspond to the I_d / I_r vs $\omega^{-1/2}$ plots and S_2 and is the slope of $I_{dL} / I_{dL} - I_d$ vs $\omega^{-1/2}$ plot. $Z_1 = 0.62 D_{O_2}^{2/3} V^{-1/6}$, $Z_2 = 0.62 D_{H_2O_2}^{2/3} V^{-1/6}$, $D_{H_2O_2}$ is $6.8 \times 10^{-6} \text{ cm}^2 \text{ s}^{-1}$ and N is the collection efficiency [4].

References

- [1] Burgun A.; Coghlan C.J.; Huang D.M.; Chen W.; Horike S.; Kitagawa S.; Alvino J.F.; Metha G.F.; Sumbly C.J.; Doonan C.J. Mapping-Out Catalytic Processes in a Metal–Organic Framework with Single-Crystal X-ray Crystallography. *Angew. Chem. Int. Ed.* **2017**, 56, 8412 - 8416.
- [2] Damjanovic A.; Genshaw M.A.; Bockris J.O. Distinction between Intermediates Produced in Main and Side Electrode Reactions, *J. Chem. Phys.* **1966**, 45, 4057-4059.
- [3] Hsueh K.L.; Chin D.T.; Srinivasan S. Electrode kinetics of oxygen reduction: A theoretical and experimental analysis of the rotating ring-disc electrode method. *J. Electroanal. Chem. Interfacial Electrochem.* **1983**, 153, 79-95.
- [4] Muthukrishnan A.; Nabae Y.; Chang C.W.; Okajima T.; Ohsaka T. A high-performance Fe and nitrogen doped catalyst derived from diazoniapentaphene salt and phenolic resin mixture for oxygen reduction reaction. *Catal. Sci. Technol.* **2015**, 5, 1764-1774.

CHAPTER 6

Investigation of the effect of different functional groups of organic materials on the long-term air stability of ZVI and the effect of air stabilised and less agglomerated ZVI nanoparticles on As adsorption.

Ramesh Karunagaran

School of Chemical Engineering, University of Adelaide, South Australia 5005, Australia

6.1 Chapter overview

This chapter deals with two major issues that hinders the potential of ZVI performing as outstanding adsorbents: air stability and agglomeration. To provide long-term air stability, organic materials with different functional groups such as hydroxyl, thiol, carboxyl and amine groups were investigated and the functional groups responsible for long-term air stability was identified. To reduce agglomeration, the air stable ZVI was dispersed in rGO and finally, these nanoparticles were explored for As removal. The investigation of this chapter has been discussed a peer reviewed article (Chapter 6a).

Chapter 6a contains one paper with supplementary information. The air stability of the ZVI coated with different functional groups was observed by exposing the ZVI nanoparticles to the atmosphere. ZVI nanoparticles coated with carboxyl groups using glycine or 3-mercaptopropionic acid provided long-term air stability and remained stable for more than 12 months. All other samples were instantly reacted with air or oxidised within three days. The presence of zero valent state of the iron was analysed by XRD analysis. The comparison of the XRD diffraction peaks of glycine coated ZVI (Gly-ZVI) before and after 12 months showed similar diffraction peaks confirming that the ZVI particles were not oxidised. To reduce the agglomeration of the ZVI particles due to magnetism, these particles were dispersed in rGO. The GlyZVI-rGO composites investigated for As adsorption showed outstanding adsorption efficiency for As (III) (400 mg/g) and As (V) (132 mg/g).

CHAPTER 6(a)

An atmospherically stable and agglomeration-free zero-valent iron reduced graphene oxide (ZVI-rGO) composite for high performing environmental remediation

Ramesh Karunagaran

School of Chemical Engineering, University of Adelaide, South Australia 5005, Australia

The chapter is based on the following peer-reviewed article:

R. Karunagaran, S. Kabiri, I. Andelkovic, C. Coghlan, D. Tran, C. Doonan, D. Losic “An atmospherically stable and agglomeration-free zero-valent iron reduced graphene oxide (ZVI-rGO) composite for high performing environmental remediation” *Journal of Chemical Engineering*. 2017. **(Submitted)**.

Statement of Authorship

Title of Paper	An atmospherically stable and agglomeration-free zero-valent iron reduced graphene oxide (ZVI-rGO) composite for high performing environmental remediation.		
Publication Status	<input type="checkbox"/> Published	<input type="checkbox"/> Accepted for Publication	<input checked="" type="checkbox"/> Submitted for Publication
		<input type="checkbox"/> Unpublished and Unsubmitted work written in manuscript style	
Publication Details	<i>Journal of Chemical Engineering</i> , 2017.		

Principal Author

Name of Principal Author (Candidate)	Ramesh Karunagaran		
Contribution to the Paper	Under the supervision of D. Losic and Christian Doonan, I developed, designed and conducted the experiments, interpreted, processed the data and wrote the manuscript for submission.		
Overall percentage (%)	80%		
Certification:	This paper reports on the original research I conducted during the period of my Higher Degree by Research candidature and is not subjected to any obligations or contractual agreements with third party that would constrain its inclusion in this thesis. I am the primary author of this paper.		
Signature		Date	15 February 2018

Co-Author Contributions

By signing the Statement of Authorship, each author certifies that:

- the candidate's stated contribution to the publication is accurate (as detailed above);
- permission is granted for the candidate to include the publication in the thesis; and
- the sum of all co-author contributions is equal to 100% less the candidate's stated contribution.

Name of Co-Author	Ivan Andelkovic		
Contribution to the Paper	I helped Ramesh Karunagaran (candidate) with manuscript preparation and interpretation of experimental results. I give consent for Ramesh Karunagaran to present this paper for examination towards the Doctorate of Philosophy.		
Signature		Date	15 February 2018

CHAPTER 6(a): R. Karunagaran, S. Kabiri, I. Andelkovic, C. Coghlan, D. Tran, C. Doonan, D. Losic “An atmospherically stable and agglomeration-free zero-valent iron reduced graphene oxide (ZVI-rGO) composite for high performing environmental remediation” *Journal of Chemical Engineering*, 2017. **(Submitted)**

Name of Co-Author	Shervin Kabiri		
Contribution to the Paper	I assisted Ramesh Karunagaran to conduct ICPMS analysis. I give consent for Ramesh Karunagaran to present this paper for examination towards the Doctorate of Philosophy.		
Signature		Date	15 February 2018

Name of Co-Author	Diana Tran		
Contribution to the Paper	I helped Ramesh Karunagaran with designing experiments and improving the manuscript for submission. I give consent for Ramesh Karunagaran to present this paper for examination towards the Doctorate of Philosophy.		
Signature		Date	15 February 2018

Name of Co-Author	Campbell Coghlan		
Contribution to the Paper	I acted as the secondary supervisor for Ramesh Karunagaran and helped him to design the experiments and improve the final draft of the manuscript for submission. I give consent for Ramesh Karunagaran to present this paper for examination towards the Doctorate of Philosophy.		
Signature		Date	15 February 2018

Name of Co-Author	Christian Doonan		
Contribution to the Paper	I acted as the secondary supervisor for Ramesh Karunagaran and aided in design and development of experiment and evaluation of manuscript for submission. I give consent for Ramesh Karunagaran to present this paper for examination towards the Doctorate of Philosophy.		
Signature		Date	15 February 2018

CHAPTER 6(a): R. Karunakaran, S. Kabiri, I. Andelkovic, C. Coghlan, D. Tran, C. Doonan, D. Losic “An atmospherically stable and agglomeration-free zero-valent iron reduced graphene oxide (ZVI-rGO) composite for high performing environmental remediation” *Journal of Chemical Engineering*, 2017. **(Submitted)**

Name of Co-Author	Dusan Losic		
Contribution to the Paper	I acted as the Primary supervisor for Ramesh Karunakaran and aided in design and development of experiment and evaluation of manuscript for submission. I give consent for Ramesh Karunakaran to present this paper for examination towards the Doctorate of Philosophy.		
Signature		Date	15 February 2018

***Manuscript**

[Click here to view linked References](#)

1
2
3
4
5
6
7
8
9
10
11
12
13
14
15
16
17
18
19
20
21
22
23
24
25
26
27
28
29
30
31
32
33
34
35
36
37
38
39
40
41
42
43
44
45
46
47
48
49
50
51
52
53
54
55
56
57
58
59
60

**An atmospherically stable and agglomeration free zero-valent iron reduced
graphene oxide (ZVI-rGO) composite for high performing environmental
remediation**

Ramesh Karunakaran,^{a,b} Shervin Kabiri,^{a,b} Ivan Andelkovic,^a Campbell Coghlan,^{a,b} Diana Tran,^{a,b}
Christian Doonan^{c*} and Dusan Losic^{a,b*}

^a School of Chemical Engineering, University of Adelaide, SA, Australia

^b ARC Research Hub for Graphene Enabled Industry Transformation, The University of Adelaide, Adelaide, SA
5005, Australia

^c School of Chemistry, University of Adelaide, Adelaide, SA 5005, Australia

*Corresponding author: Prof. Dusan Losic, Email: dusan.losic@adelaide.edu.au, Phone: +61 8 8013
4648 or christian.doonan@adelaide.edu.au; Phone: +61 8 83135770

Abstract

Zero-valent iron nanoparticles (ZVI-NPs) have been extensively investigated for water and soil remediation. However, the practical applications has been hindered due to their low air stability and tendency to agglomerate. To provide required stability in atmospheric environment, different coating approaches of ZVI have been explored, but with limited success and lack of knowledge which functional groups are responsible for the prolonged stability. To address this problem, we have explored role of different functional groups (amine, thiol, hydroxyl and carboxyl) assembled as monolayers on ZVI nanoparticles. Our results demonstrate that the ZVI coated with organic molecules contain carboxyl

1 groups such as glycine has unprecedent stability and shelf life (> 12 months) under atmospheric
2 conditions. To solve agglomeration problem these glycine protected ZVI-NPs were dispersed in reduced
3 graphene oxide (rGO) solution to make an atmospherically stable and aggregation-free ZVI-rGO
4 composites. Synthetised materials were characterised and environmental remedation performance was
5
6 evaluated using arsenic as a model pollutant. Outstanding adsorption efficiency for As(III) (400 mg/g)
7 and As(V) (132 mg/g) was obtained over a range of pHs. Experimental results confirmed that two major
8
9 constraints for the implementation of ZVI materials for environmental remediation, air stability and
10
11 agglomeration, are substantially improved. These results confirmed that he two major issues for the
12
13 implementation of ZVI materials for environmental remediation (air stability and agglomeration) are
14
15 successfully solved making ZVI-rGO composites an ideal sorbent for the removal of arsenic in broad
16
17 remediation applications.
18
19
20
21
22
23
24

25
26
27
28
29
30 **Keywords:** Zero valent iron, reduced graphene oxide, environmental remedation, air stability, adsorption,
31
32 arsenic
33
34
35
36
37

38 **1. Introduction**

39
40
41 Zero - valent iron (ZVI) consists of an elemental metallic iron core and iron oxide shell.[1] The metallic
42
43 iron possesses an overall zero charge and shows reactive electron - donating properties, while the iron
44
45 oxide shell offers active sites for adsorption of charged ions via coordinative and electro - static attraction
46
47 and/or surface complexations.[2,3] Over the past two decades, ZVI-NPs have been extensively explored
48
49 for environmental remediation of toxic contaminants in soil and water because of their high efficiency,
50
51 low cost and environmental friendly properties.[1,4] Moreover, they are recognized as excellent material
52
53 for ground water remediation because of their high reactivity, large surface area, fast reaction kinetics and
54
55
56
57
58 magnetic properties which facilitate their easy removal and recovery after the remediation process.[5]
59
60

1
2
3
4
5
6
7
8
9
10
11
12
13
14
15
16
17
18
19
20
21
22
23
24
25
26
27
28
29
30
31
32
33
34
35
36
37
38
39
40
41
42
43
44
45
46
47
48
49
50
51
52
53
54
55
56
57
58
59
60

Several synthesis methods have been used to synthesise ZVIs including liquid phase reduction, borohydride reduction,[6] gas phase reduction,[7] thermal decomposition,[8] ultrasound assisted method,[9] precision milling,[10] electro chemical,[11] and green synthesis.[12] The borohydride reduction method is the most commonly used because of its simplicity, reactivity and homogenous structure of the produced ZVI. ZVI particles are widely employed in remediation of chlorinated organic contaminants,[13,14] dyes,[15,16] phenols,[17,18] nitrobenzene,[19] herbicides,[20] radionuclides,[21] nitrates,[22] and heavy metals removal.[23–25]

17
18
19
20
21
22
23
24
25
26
27
28
29
30
31
32
33
34
35
36
37
38
39
40
41
42
43
44
45
46
47
48
49
50
51
52
53
54
55
56
57
58
59
60

Although the use of ZVIs for the removal of contaminants provides numerous advantages, there are still challenges for the large scale implementation of this technology. These challenges include instability and oxidation during storage under aerobic conditions for a prolonged periods and the rapid aggregation of particles. In order to solve these issues electro - static repulsion forces and steric stabilization of the ZVI surfaces were explored by altering the surface chemistry with a goal of providing chemical stability and oxidation resistance.[26,27] The organic molecules used to coat the ZVIs should not only provide protection against oxidation, but also act against aggregation through long range repulsive forces.[26,28] Steric stabilization was performed by coating the NPs with long chain organic molecules or hydrophilic polymers, which interact to prevent agglomeration.[28] For example, Phenrat et al.[29] used poly(styrene sulfonate), a strong anionic polyelectrolyte, and polyaspartate, a weak anionic polypeptide, to synthesise a ZVI material that was stable for several months. Feng and Zhao[30] applied a simple and green approach using starch to form a cluster structure with mono and bimetallic ZVI NPs under inert atmosphere for the degradation of organics. Wijesekara et al.[31] compared the stability of nano-ZVIs that had been exposed to starch and different mercapto acids. ZVIs coated with starch combusted after 3 days, whereas those coated with mercaptoacetic acid (MA), mercaptopropionic acid (MPA) and mercaptosuccinic (MS) acid were stable for 3 weeks. Other organic compounds, such as carboxymethyl cellulose,[32] polyacrylic acid,[33] and cellulose acetate[34] have also been used to coat ZVI particles but with limited success. Recent work by Soukupova et al.[35] using a non-ionic surfactant

1 prolonged the stability of ZVIs in air (two months) and reduced aggregation which could be effectively
2 used to remove contaminants such as tetrachloroethane. All these studies showed limited results to
3
4 provide required long term stability of ZVIs required for real environmental applications with lack of
5
6 fundamental knowledge about optimal chemistry of protective layer to provide binding, barrier and
7
8 repulsion properties.
9

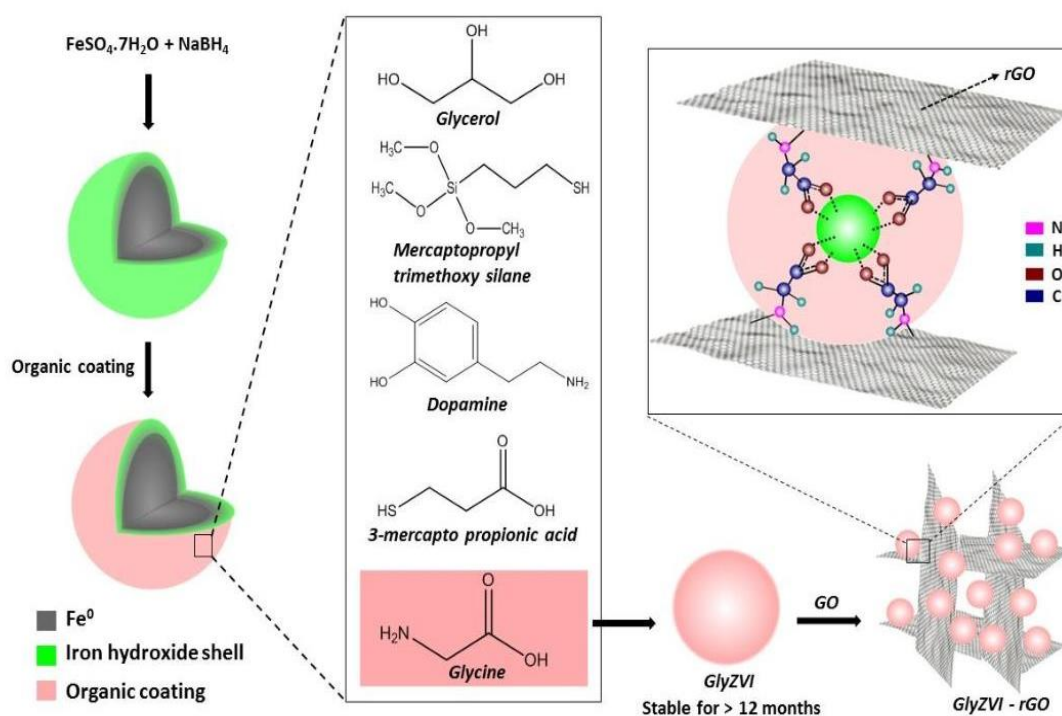
10
11 In order to prevent ZVIs aggregation, inert materials has been used as carriers such as
12
13 bentonite,[36] zeolite[37] and natural clays.[38] Bio char materials derived from rice hull[39] and
14
15 pine[40] have also been used as supporting materials. Recently graphene due to its large specific surface
16
17 area (2600 m²/g), good mechanical stability, tuneable surface chemistry and large scale production, has
18
19 emerged as a new and promising material for nanoparticle immobilization such as ZVIs.[41] ZVI-
20
21 graphene composites have already been synthesised and tested for the removal of uranium,[42]
22
23 arsenic[43] and lead.[44] While progress has been made either in stability under aerobic conditions or
24
25 reducing agglomeration, no efficient solution has been found for prevention of both, oxidation and
26
27 agglomeration of ZVI NPs. Nevertheless, ZVIs have been recognized as one of the most promising
28
29 materials for environmental remediation and overcoming these challenges is of critical importance that
30
31 can result in significant advances in this field and solve concerning environmental problems.
32
33
34
35
36
37

38
39 In this study, to address these two problems such as oxidation and agglomeration of ZVI NPs we
40
41 come with idea to engineer composites which are an atmospherically stable and agglomeration-free. In
42
43 the first optimization stage to select the organic layer with the best oxidation protective properties that
44
45 provide a long term stability of ZVI a series of organic molecules with different functional groups were
46
47 explored. Five coating small organic molecules with four different functional groups including -NH₂, -
48
49 OH, -COOH and -SH were initially tested as shown in Scheme 1. Based on stability performance ZVIs
50
51 coated with glycine that showed excellent atmospheric stability was further used in order to solve
52
53 aggregation problem in combination with reduced graphene oxide (rGO). The graphene/ZVI composite
54
55
56
57
58
59
60

was created with unique 3-d structures that showed reduced agglomeration of glycine modified ZVI-NPs.

The performance of the prepared glycine coated ZVI-rGO composites was finally tested for removal of arsenic ions (As(III) and As(V)) from water as a case study to demonstrate their environmental remediation performances .

1
2
3
4
5
6
7
8
9
10
11
12
13
14
15
16
17
18
19
20
21
22
23
24
25
26
27
28
29
30
31
32
33
34
35
36
37
38
39
40
41
42
43
44
45
46
47
48
49
50
51
52
53
54
55
56
57
58
59
60
..



Scheme 1. Schematic representation of different organic coating materials and synthesis of GlyZVI-rGO composite.

2. Materials and methods

Natural graphite flakes supplied from local company (Uley, Eyre Peninsula, South Australia) was milled into a fine powder using a bench top ring mill (Rocklabs). Iron sulphate heptahydrate ($\text{FeSO}_4 \cdot 7\text{H}_2\text{O}$), potassium permanganate (KMnO_4), sodium hydroxide (NaOH), 3-mercapto propionic acid (MPA), sodium borohydride (NaBH_4), glycine (Gly), glycerol, mercapto propyl tri methoxy silane (MPTMS) and

1 dopamine hydrochloride were purchased from Sigma Aldrich, and sulphuric acid (H_2SO_4), phosphoric
2 acid (H_3PO_4), 30% hydrogen peroxide (H_2O_2), 35% hydrochloric acid (HCl) and ethanol were purchased
3
4 from Chem Supply. All chemicals were used without further purification. Stock solutions (1000 ppm) of
5
6 arsenite (Na_2AsO_3) and arsenate ($Na_2HAsO_4 \cdot 7H_2O$) were purchased from Sigma Aldrich and prepared in
7
8 Milli-Q water (18.2 M Ω .cm at 25 °C, pH 5.6). Milli-Q water was used throughout the experiments unless
9
10 otherwise stated.

11 12 13 14 **2.1. Preparation of graphene oxide (GO)**

15
16
17 GO was synthesized from graphite flakes using the improved Hummer's method.[45] A mixture of
18
19 concentrated acids H_2SO_4/H_3PO_4 (9:1) was added to a mixture of graphite flakes (3.0 g) and $KMnO_4$ (18.0
20
21 g). The solution was then heated to 50 °C and stirred for 12 h. The solution was cooled and poured onto
22
23 ice (400 mL) containing H_2O_2 (3 mL). The mixture was centrifuged (4000 rpm) for 4 h and the
24
25 supernatant was removed. The precipitate was then washed in succession with water (2 x 200 mL), 30 %
26
27 HCl (2 x 200 mL) and ethanol (2 x 200 mL). The final product was collected and vacuum dried overnight
28
29
30
31
32 at room temperature.

33 34 35 **2.2. Preparation of zero valent irons (ZVI) nanoparticles**

36
37
38 Water (200 mL) was degassed with argon (Ar) in a 500 mL three necked flask for 15 min. 50 mL of the
39
40 degassed water containing $NaBH_4$ (0.05 mole) was transferred to a dropping funnel also under Ar. Iron
41
42 sulphate heptahydrate (14 mmol) was dissolved with the remaining 150 mL of degassed water and the
43
44 dissolved $NaBH_4$ solution was added drop wise to the iron solution over a period of 2 h where the pH of
45
46
47 the suspension was maintained at 8.

48 49 50 51 **2.3. Coating of ZVI nanoparticles with organic molecules**

52
53 To prevent the ZVI (Fe^0) surface from oxidising in the presence of air, five different coating molecules
54
55 including Gly, MPA, dopamine (Dop), glycerol and MPTMS were separately added to the reaction
56
57
58 mixture to yield a surface coated ZVI with organic compounds is shown in Scheme 1.
59
60

1 In separate experiments glycine (6.66 mmol in 3 mL of water), dopamine hydrochloride (6.66 mmol in 3
2 mL water), MPA (550 μ L), glycerol (600 μ L) or MPTMS (600 μ L) were separately added to the ZVI iron
3
4 solution. The solution was further mixed for 15 min then centrifuged at 4200 rpm for 5 min. Iron
5
6 solutions mixed with glycine, dopamine and glycerol were washed with DI water (3x), whereas the
7
8 solution mixed with MPA and MPTMS were washed with ethanol (3x). Finally, the precipitates were
9
10 freeze dried for 24 h and stored in a container for use. The different coated ZVI were denoted as GlyZVI,
11
12 DopZVI, MPAZVI, GlycerolZVI, and MPTMS/ZVI, for glycine, dopamine, MPA, glycerol, and
13
14 MPTMS, respectively.
15
16
17
18

19 **2.4. Preparation of ZVI and reduced GO (rGO) composite**

20 ZVI-rGO composites were synthesized using a similar preparation method to the ZVI coated materials.
21
22 The materials were subjected to an additional step after the addition of the coating agents. GO solution
23
24 (10 mL, 1.5 mg/mL) was degassed with Ar, then added to the iron solution (containing NaBH_4) in the
25
26 three-necked flask with the coating agent and mixed for an additional 15 min. The presence of NaBH_4 in
27
28 the iron solution also acts as a reducing agent to convert GO to reduced GO (rGO). The mixture was then
29
30 washed (DI water or ethanol), freeze dried and stored as previously stated above. The final products were
31
32 referred to as GlyZVI-rGO, DopZVI-rGO, MPAZVI-rGO, GlycerolZVI-rGO, and MPTMS/ZVI-rGO for
33
34 the glycine, dopamine, MPA, glycerol, and MPTMS composites, respectively.
35
36
37
38
39
40
41

42 **2.5. Characterizations**

43 Scanning electron microscopy (SEM, Quanta 450, FEI, USA), Transition electron microscopy (TEM,
44
45 Tecnai G2 Spirit, FEI, USA), Raman spectroscopy (LabRAM Evolution, Horiba Jvon Yvon, Japan) and
46
47 X-ray diffraction (XRD, Miniflex 600, Rigaku, Japan) were used to characterise the synthesised
48
49 materials. TEM samples were prepared by ultrasonating the materials in ethanol for 10 min, drop casted
50
51 onto copper grids and measured at an accelerating voltage of 120 kV. XRD measurements were
52
53 performed at 40 kV and 15 mA in the range between $2\theta = 20-80^\circ$ at a scan speed of $10^\circ/\text{min}$. Raman
54
55
56
57
58
59
60

1 analysis was carried out using a 532 nm laser. The laser power was kept at 10 % to prevent any
2 preheating of the sample and a confocal size of 300 μm was used. The sample was tested without any pre-
3 treatment in the range of 1100-1800 cm^{-1} using an integration time of 10 sec for 3 accumulations and the
4 retention time was set to 1 sec. A short scan range was selected as the materials were susceptible to
5 burning at prolong times from laser exposure. X-ray photoelectron spectroscopy (XPS) characterisation
6 was performed on an AXIS Ultra-DLD instrument (Kratos, UK) where sample was prepared by drop
7 casting onto a clean Si wafer using non-monochromatic Mg source operating at 120kV and 200W. High
8 resolution spectra was collected with a 0.1 eV step size. Casa XPSTM software was used for processing
9 and curve fitting of XPS data.
10
11
12
13
14
15
16
17
18
19

20 21 22 **2.6. Adsorption experiments**

23
24
25 Batch adsorption tests were carried out, individually for As(III) and As(V), to examine the effect of
26 contact time, pH and to determine the adsorption capacity of the adsorbent. Experiments were performed
27 in 200 mL plastic tubes with 5 mg of adsorbent and 100 mL of arsenic solution in DI water at room
28 temperature ($22\text{ }^{\circ}\text{C} \pm 1$) at 600 rpm on a magnetic stirrer.
29
30
31
32

33
34
35 For kinetic experiments, 5 mg/L arsenic solutions at pH 7 were mixed for 5, 10, 15, 20, 30, 45, 60, 120
36 and 180 min. After the specified contact times the suspensions were immediately filtered through a 0.22
37 μm Teflon filter and the arsenic concentrations were measured with Inductively Coupled Plasma-Mass
38 spectroscopy (ICP-MS 7500cs Agilent Technologies, USA).
39
40
41
42
43
44

45 The effect of pH on arsenic adsorption was examined between pH 3 and 10. Initial pH of 5 mg/L arsenic
46 solution was adjusted using diluted HCl or NaOH solution. After the addition of sorbent, the solutions
47 were mixed for 120 min then immediately filtered through a 0.22 μm Teflon filter and analysed. Isotherm
48 studies were carried out at pH 8 for As(V) and As(III). Experiments were performed by mixing
49 concentrations of As(V) or As(III) solutions with a constant dose of adsorbent (0.05 g/L) for 120 min.
50
51
52
53
54
55
56
57
58 The concentrations of arsenic were in the range of 3 to 150 mg/L.
59
60

3. Results and Discussion

3.1. Air stability of ZVI nanoparticles coated with different organic molecules

To prevent the ZVI surface from oxidising in the presence of air, five different organic molecules (glycine, MPA, dopamine, glycerol and MPTMS) different functional groups including, -NH₂, -OH, -COOH and -SH (Table S1) were explored. The air stability of the materials was tested by exposure to air (Scheme S1). ZVI composite materials coated with glycerol (GlyZVI) and MPTMS (MPTMSZVI) were found to be highly unstable and ignited instantly when exposed to air (Movie S1 available). Immediate oxidation and burning are indicating that the glycerol, containing -OH groups, and MPTMS, containing SH groups, did not form a stable protective coating around ZVI. In contrast, the ZVI coated with dopamine (DopZVI), containing both -NH₂ and -OH groups, did not aggressively react in air showing better protection capability. However, over the course of three days the particles changed colour from black to brown indicating that the protection is not stable. As the GlyZVI containing -OH groups did not contribute to the stable coating of the ZVI, it was hypothesised that the -NH₂ groups in dopamine interacts very weakly with the ZVI. In contrast, the highest stability obtained was for ZVI samples protected with MPA and Gly molecules. Both produced ZVI -NPs were stable in air for more than 12 months showing the best stability compared to other ZVI organic coatings reported in literature (Table S2). Our results indicate that -COOH group is responsible for coating and high protection of ZVI against oxidation. This is in agreement with the study of Kataby et al.[46] who proposed stronger chemical bonding between carboxylic acids and iron NPs than the bond formed between the iron and the thiol or the alcohol moiety. Simillar, Tao have found self-assembling of monolayers of alkanolic acids on the surface of other metals, like Ag, Cu and Al, creating highly dense film around metal particles.[47] Interpretation of our results in light of a previous studies suggests creation of protective coating by the chemical bonding of carboxylic group to the ZVI surface which results in an excellent stability in atmospheric environment. Although both GlyZVI and MPAZVI showed excellent stability under atmospheric conditions, GlyZVI was chosen

as a best candidate for immobilization on GO to prevent aggregation due to its lower toxicity and costs compared to MPA.

3.2. Structural and chemical characterization of GlyZVI and GlyZVI-rGO composites

The morphology of the synthesised GlyZVI-NPs and GlyZVI-rGO composites was examined by SEM and TEM as shown in Fig. 1. The particle size of GlyZVI was determined to be 100-200 nm in diameter which form an interconnected 2D chain of several microns (Fig.1A). The formation of this 2D nanoparticle chain is consequence of magnetic properties and surface charge of ZVI.[48] High magnification TEM of a single spherical GlyZVI nanoparticle (Fig. 1B) shows that the ZVI core is surrounded by an iron hydroxide shell approximately 4.2 nm thick. The GlyZVI-rGO composite prepared by dispersing GlyZVI onto rGO displayed reduced aggregation of the 2D chains in comparison to the original GlyZVI-NPs (Fig. 1C and D) confirming their successful immobilisation, reduced attraction and aggregation.

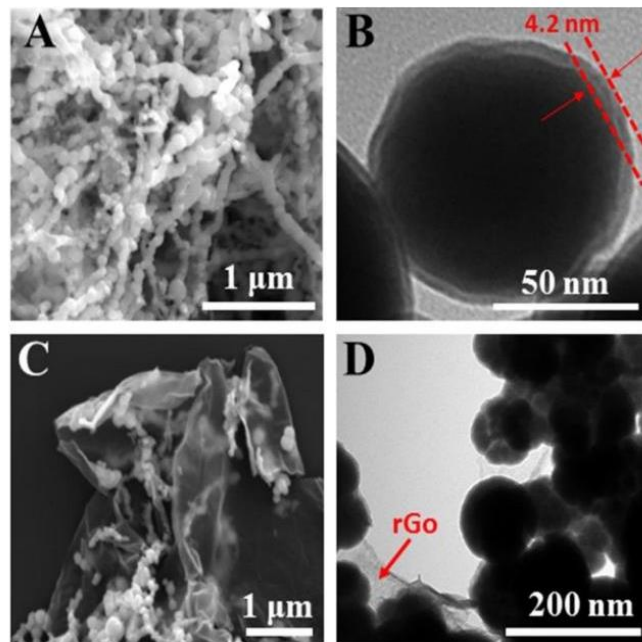


Figure 1. SEM image of A) GlyZVI nanoparticles B) TEM image of a single GlyZVI nanoparticle with iron hydroxide shell. C) SEM and D) TEM images of GlyZVI-rGO composite.

XRD analysis was conducted to verify that the zero oxidation state of iron was retained after the coating process. The XRD of GlyZVI (Fig. 2A) showed two dominant diffraction peaks at $2\theta = 44.8^\circ$ and 65.3° which are characteristic for the metallic iron.[49] No additional peaks in the XRD spectra for GlyZVI exposed to air at room temperature (22°C) for 12 months compared to the freshly prepared nanoparticles confirms the absence of newly formed crystal structures and the stability of the coated ZVI material.

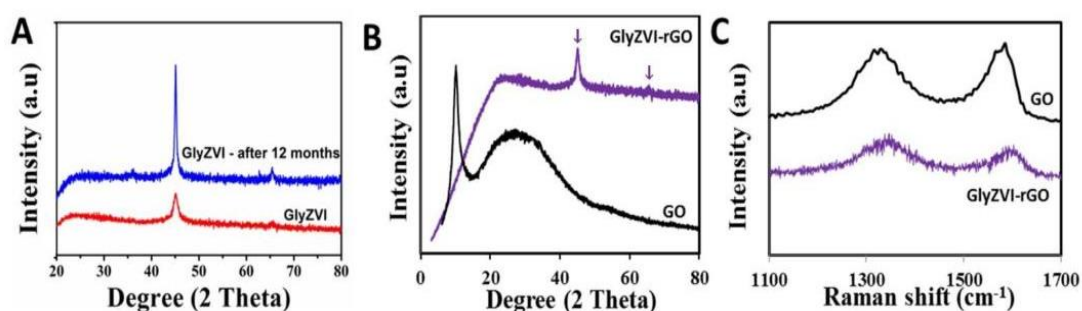


Figure 2. XRD patterns of A) GlyZVI nanoparticles freshly prepared and exposed to air for 12 months, B) GO and GlyZVI-rGO and C) Raman spectra of GO and GlyZVI-rGO composite.

The XRD patterns of GO and GlyZVI-rGO are shown in Fig. 2B. GO has a peak at $2\theta = 10.3^\circ$ corresponding to the (001) plane.[50] In contrast, the XRD pattern of GlyZVI-rGO shows two characteristic peaks at $2\theta = 44.9^\circ$ and 65.3° corresponding to (110) and (200) planes of metallic iron. The absence of the typical rGO peak around $2\theta = 25.0^\circ$ in the XRD pattern of GlyZVI-rGO suggests that the GlyZVI-NPs are preventing the rGO sheets from restacking.[51]

Raman spectra of GO and GlyZVI-rGO (Fig. 2C) showed typical D and G bands at 1346 cm^{-1} and 1594 cm^{-1} , respectively. The D band arises from the defect induced breathing mode of the C-C bond stretching in the sp^2 ring, while the G band is associated with the first order scattering of E_{2g} photons of

sp² carbon atoms.[52,53] The intensity ratio of the D and G band (I_D/I_G) of GlyZVI-rGO (1.10) is slightly higher than GO (0.98) indicating the decrease in the average size of sp² domains upon reduction of GO by ZVI to form rGO and the generation of new graphitic domains in the GlyZVI-rGO composite.[54]

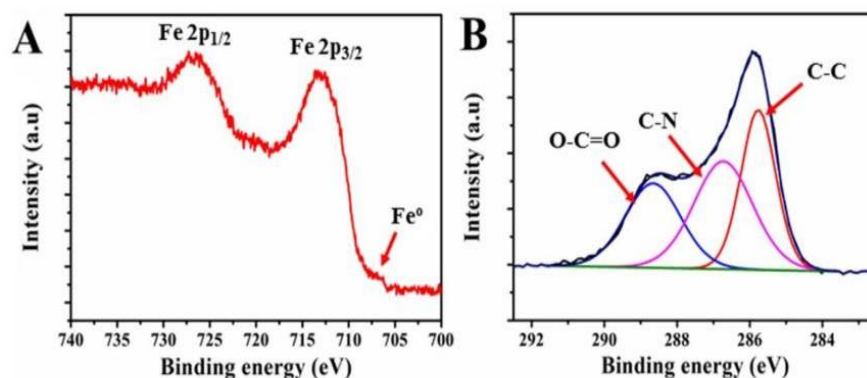


Figure 3. High resolution XPS spectra of A) Fe2p and B) C1s of GlyZVI

The glycine coating on the ZVI-NPs was characterized by probing the GlyZVI surface with XPS to obtain the deconvoluted XPS Fe2p and C1s spectrum as shown in Fig. 3. The high-resolution Fe 2p_{1/2} and Fe2p_{3/2} located at 726.67 and 712.96 eV (Fig. 3A), respectively corresponds to the Fe³⁺ oxidation state of iron hydroxides in the shell.[55] Small shoulder at around 706.0 – 707.0 eV can be seen, corresponding to the Fe⁰ peak of iron.[56] The high resolution C1s peak (Fig. 3B) showed three characteristic peaks corresponding to glycine, C-C (285.7 eV), C-N (286.7 eV) and O-C=O (288.6 eV).[57] XPS results further support TEM and XRD conclusions, confirming the chemistry of GlyZVI and successful coating of ZVI with glycine.

3.3. Adsorption kinetics

Both the prepared GlyZVI-rGO and GlyZVI materials were tested for arsenic (As(III) and As(V)) adsorption capacity over time (Fig. 4). Initially, the adsorption of both As(III) and As(V) species increased sharply (first 40 min) then gradually approached equilibrium (approx. 120 min). The results indicate that using rGO as a carrier of GlyZVI-NPs resulted in a significantly higher adsorption of both

As(III) and As(V). This enhancement attributed to the reduction in agglomeration of the nanoparticles and increased access of the binding sites of separated ZVI dispersed in graphene matrix.

Two kinetic models, the pseudo-first order (equation 1, ESI) and pseudo-second order (equation 2, ESI) were used to describe the kinetics of As(III) and As(V) adsorption. The plots obtained for As(III) and As(V) using GlyZVI and GlyZVI-rGO composites are shown in Fig. S1 and S2. The pseudo-second order kinetic model was found to be the most accurate representation of the data as shown by the R^2 in Table S3. As additional test of validation of the proposed kinetic models, comparison of the amount of arsenic sorbed derived from kinetic models with experimentally obtained values can be used.[58] Comparing the calculated values from the pseudo-first and pseudo-second order with the experimental values (Table S3) we can see further confirmation of the pseudo-second order model as the most suitable for describing the kinetics of As(III) and As(V) adsorption onto GlyZVI-rGO.

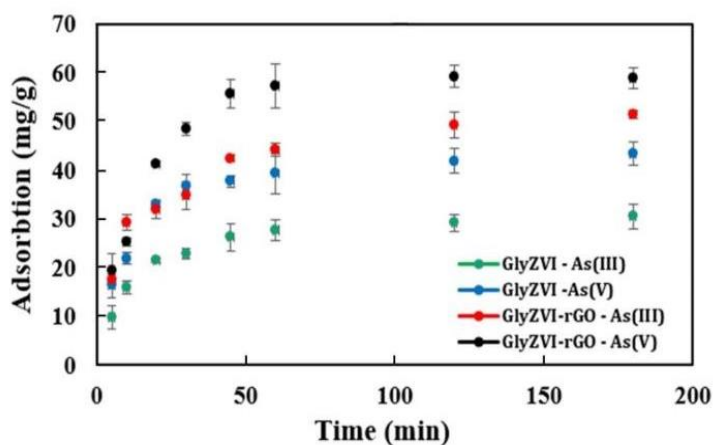


Figure 4. Adsorption kinetics of As(V) and As(III) at GlyZVI and GlyZVI-rGO composites. Conditions: pH = 7; As(III) and As(V) concentration = 5 mg/L; adsorbent dose = 0.05 g/L.

3.4. Effect of pH

The effect of pH on the adsorption of As(III) and As(V) on GlyZVI-rGO and GlyZVI was analysed in the pH range 3 - 10 (Fig. 5A and B). Although there is a difference in the ionisation state of As(III) (present as neutral H_3AsO_3 species at $pH < 9$) and As(V) (present as negatively charged $H_2AsO_4^-/HAsO_4^{2-}$ oxyanions) within the tested pH range, similar trends in the adsorption were observed. The fact that increase of pH from 4 to 9 did not significantly change the adsorption capacity of both arsenic species indicates that surface complexation governs the adsorption process rather than electrostatic interactions.[59] Further increase of pH to 10 resulted in a dramatic drop in Q_e value. Measurement of electrophoretic mobility at different pH values (Fig. S3) showed us that surface of Gly-ZVI and GlyZVI-rGO have net negative charge at pH higher than 7.9 ± 0.1 and 6.6 ± 0.1 , respectively. Dramatic drop in Q_e values at $pH > 9$ can be explained with increased electrostatic repulsion between negatively charged $HAsO_4^{2-}$ or $H_2AsO_3^-$ species and the negatively charged surface of adsorbent that has become the dominant force influencing the adsorption.⁶⁶ These results suggest efficient adsorption of both arsenic species in wide pH range, allowing broad environmental application of our composite.

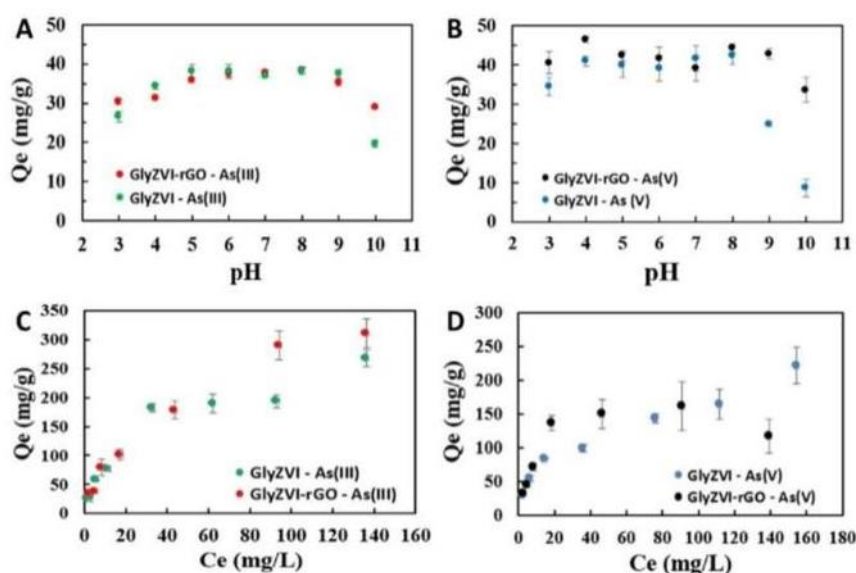


Figure 5. Adsorption capacity of GlyZVI-rGO and GlyZVI for A) As(III) and B) As(V) in the pH range of 3-10. Conditions: As(III) and As(V) concentration = 5 mg/L adsorption; adsorption time = 120 min;

1 adsorbent dose = 0.05 g/L. Adsorption capacity of GlyZVI-rGO and GlyZVI for C) As(III) and D) As(V)
2 as a function of As concentration. Conditions: pH = 8; adsorption time = 120 min; adsorbent dose = 0.05
3 g/L.
4

5 **3.5.Adsorption isotherm**

6
7
8 The adsorption capacity of As(III) and As(V) of both GlyZVI and GlyZVI-rGO composites with relation
9 to the equilibrium arsenic concentration is presented in Fig. 5C and D. The Freundlich and Langmuir
10 models (ESI) were used to analyse the adsorption against the initial concentration of arsenic at constant
11 temperature.[60,61] Freundlich model is an empirical model which assumes multilayer adsorption on a
12 heterogeneous surface while the Langmuir model is based on the assumption that adsorption is monolayer
13 on a homogenous surface with finite number of identical sites. The As(III) adsorption results were found
14 to fit well with both tested isotherm models (Fig. S4 and S5) with slightly better coefficient of correlation
15 (R^2) for the Freundlich model, while for As(V) the Langmuir model better described the adsorption for
16 GlyZVI-rGO (Table S4). The calculated adsorption capacities derived from the Langmuir model for
17 GlyZVI-rGO gave values of 400 mg/g and 132 mg/g for As(III) and As(V), respectively.
18
19
20
21
22
23
24
25
26
27
28
29
30
31
32

33 A comparison graph showing the effectiveness of the GlyZVI-rGO composite against other ZVI
34 composites reported in literatures is presented in Fig. 6.[62–65] The results show that the synthesized
35 GlyZVI-rGO composite has the highest As(III) adsorption (400 mg/g) compared with these materials.
36
37
38
39
40
41
42
43
44
45
46
47
48
49
50
51
52
53
54
55
56
57
58
59
60
61

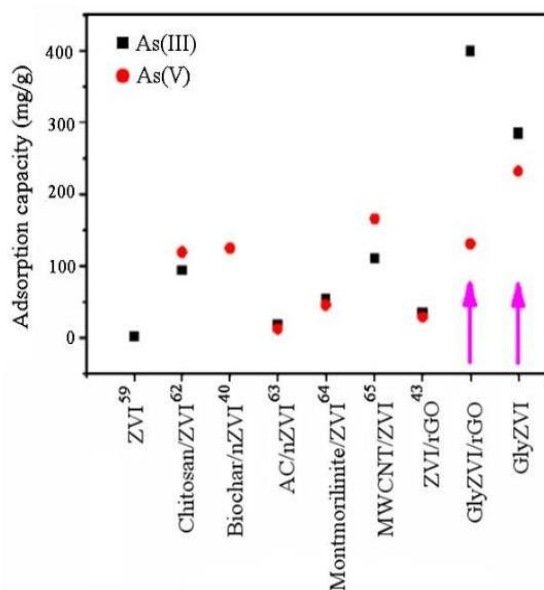


Figure 6. Comparison of the effectiveness of adsorbents for arsenic adsorption reported in literature, and GlyZVI and GlyZVI-rGO

4. Conclusions

In this work, five organic molecules with four different functional groups were explored as a protective coating for ZVI-NPs and their impact on oxidation stability was examined. Results showed excellent air stability (> 12 months) for ZVIs coated with Gly or MPA which indicates that the presence of -COOH groups is critical for efficient protection of ZVIs from atmospheric oxidation. The GlyZVI was chosen as a best candidate for further combination with rGO and create GlyZVi-rGO composite that is shown significantly reduced agglomeration of GlyZVI-NPs and solving another key challenge associated with using ZVIs in environmental remediation. The performance of prepared GlyZVI-rGO composites was evaluated for adsorption of arsenic as a case study of water remediation. Both the GlyZVI and GlyZVI-rGO showed excellent arsenic uptake across a range of pHs values. GlyZVI-rGO composite showed an outstanding capacity for As(III) (400 mg/g) and As(V) (132 mg/g) with >50 % of arsenic adsorbed within 30 min. Results presented in this study demonstrate excellent performances of GlyZVI-rGO composite

1 including long-term stability, reduced aggregation and ultra-high adsorption capacity for As adsorption
2 that outperform all previous reports on ZVI materials. Considering scalable and environmentally friendly
3
4 preparation of GlyZVI-rGO composite make these materials very attractive material for broad practical
5
6 applications for removal of toxic contaminates in water and soil.
7
8
9

10 11 **Conflicts of interest**

12
13
14 There are no conflicts to declare.
15
16
17
18
19

20 **Acknowledgments**

21
22
23 The authors thank the support of Australian Research Council (IH 150100003), Australian Research
24
25 Council Research Hub for Graphene Enabled Industry Transformation, The Australian Solar Thermal
26
27 Research Initiative (ASTRI), and The University of Adelaide, School of Chemical Engineering, and
28
29 School of Chemistry. The technical support provided by Adelaide Microscopy and the Micro Analysis
30
31 Research Facility at Flinders Microscopy (Flinders University) was greatly appreciated.
32
33
34
35
36
37

38 **Associated content**

39
40
41 Table of coating agents used, graphs for pseudo first and second order kinetics of GlyZVI-rGO for As(III)
42
43 and As(V), graphs of zeta potential of GlyZVI and GlyZVI-rGO, graphs of Langmuir and Freundlich
44
45 models of GlyZVI-rGO for As(III) and As(V).
46
47
48
49
50
51

52 **5. References**

53
54
55 [1] Y. Mu, F. Jia, Z. Ai, L. Zhang, Iron oxide shell mediated environmental remediation properties of
56
57 nano zero-valent iron, *Environ. Sci. Nano.* 4 (2017) 27–45. doi:10.1039/C6EN00398B.
58
59
60

- 1
2
3
4
5
6
7
8
9
10
11
12
13
14
15
16
17
18
19
20
21
22
23
24
25
26
27
28
29
30
31
32
33
34
35
36
37
38
39
40
41
42
43
44
45
46
47
48
49
50
51
52
53
54
55
56
57
58
59
60
- [2] X. Li, W. Zhang, Sequestration of Metal Cations with Zerovalent Iron Nanoparticles A Study with High Resolution X-ray Photoelectron Spectroscopy (HR-XPS), *J. Phys. Chem. C*. 111 (2007) 6939–6946. doi:10.1021/jp0702189.
- [3] W. Yan, A.A. Herzing, C.J. Kiely, W. Zhang, Nanoscale zero-valent iron (nZVI): Aspects of the core-shell structure and reactions with inorganic species in water, *J. Contam. Hydrol.* 118 (2010) 96–104. doi:https://doi.org/10.1016/j.jconhyd.2010.09.003.
- [4] X. Guan, Y. Sun, H. Qin, J. Li, I.M.C. Lo, D. He, H. Dong, The limitations of applying zero-valent iron technology in contaminants sequestration and the corresponding countermeasures: The development in zero-valent iron technology in the last two decades (1994–2014), *Water Res.* 75 (2015) 224–248. doi:https://doi.org/10.1016/j.watres.2015.02.034.
- [5] J. Liu, A. Liu, W-X. Zhang, The influence of polyelectrolyte modification on nanoscale zero-valent iron (nZVI): Aggregation, sedimentation, and reactivity with Ni(II) in water, *Che. Eng J.* 2016 303 (2016) 268-274
- [6] Y. Xi, M. Mallavarapu, R. Naidu, Reduction and adsorption of Pb²⁺ in aqueous solution by nano-zero-valent iron—A SEM, TEM and XPS study, *Mater. Res. Bull.* 45 (2010) 1361–1367. doi:https://doi.org/10.1016/j.materresbull.2010.06.046.
- [7] L.B. Hoch, E.J. Mack, B.W. Hydutsky, J.M. Hershman, J.M. Skluzacek, T.E. Mallouk, Carbothermal Synthesis of Carbon-supported Nanoscale Zero-valent Iron Particles for the Remediation of Hexavalent Chromium, *Environ. Sci. Technol.* 42 (2008) 2600–2605. doi:10.1021/es702589u.
- [8] S. Laurent, D. Forge, M. Port, A. Roch, C. Robic, L. Vander Elst, R.N. Muller, Magnetic Iron Oxide Nanoparticles: Synthesis, Stabilization, Vectorization, Physicochemical Characterizations, and Biological Applications, *Chem. Rev.* 108 (2008) 2064–2110. doi:10.1021/cr068445e.

- 1 [9] M.R. Jamei, M.R. Khosravi, B. Anvaripour, A novel ultrasound assisted method in synthesis of
2 NZVI particles, *Ultrason. Sonochem.* 21 (2014) 226–233.
3 doi:<https://doi.org/10.1016/j.ultsonch.2013.04.015>.
4
5
6
7 [10] S. Li, W. Yan, W. Zhang, Solvent-free production of nanoscale zero-valent iron (nZVI) with
8 precision milling, *Green Chem.* 11 (2009) 1618–1626. doi:10.1039/B913056J.
9
10
11 [11] S.-S. Chen, H.-D. Hsu, C.-W. Li, A new method to produce nanoscale iron for nitrate removal, *J.*
12 *Nanoparticle Res.* 6 (2004) 639–647. doi:10.1007/s11051-004-6672-2.
13
14
15 [12] G.E. Hoag, J.B. Collins, J.L. Holcomb, J.R. Hoag, M.N. Nadagouda, R.S. Varma, Degradation of
16 bromothymol blue by “greener” nano-scale zero-valent iron synthesized using tea polyphenols, *J. Mater.*
17 *Chem.* 19 (2009) 8671–8677. doi:10.1039/B909148C.
18
19
20 [13] H. Kim, H.-J. Hong, J. Jung, S.-H. Kim, J.-W. Yang, Degradation of trichloroethylene (TCE) by
21 nanoscale zero-valent iron (nZVI) immobilized in alginate bead, *J. Hazard. Mater.* 176 (2010) 1038–
22 1043. doi:<https://doi.org/10.1016/j.jhazmat.2009.11.145>.
23
24
25 [14] J.-W. Moon, H.-S. Moon, H. Kim, Y. Roh, Remediation of TCE-contaminated groundwater using
26 zero valent iron and direct current: experimental results and electron competition model, *Environ. Geol.*
27 48 (2005) 805–817. doi:10.1007/s00254-005-0023-1.
28
29
30 [15] Y.-T. Lin, C.-H. Weng, F.-Y. Chen, Effective removal of AB24 dye by nano/micro-size zero-
31 valent iron, *Sep. Purif. Technol.* 64 (2008) 26–30. doi:<https://doi.org/10.1016/j.seppur.2008.08.012>.
32
33
34 [16] H.-Y. Shu, M.-C. Chang, C.-C. Chen, P.-E. Chen, Using resin supported nano zero-valent iron
35 particles for decoloration of Acid Blue 113 azo dye solution, *J. Hazard. Mater.* 184 (2010) 499–505.
36
37
38 doi:<https://doi.org/10.1016/j.jhazmat.2010.08.064>.
39
40
41 [17] A. Shimizu, M. Tokumura, K. Nakajima, Y. Kawase, Phenol removal using zero-valent iron
42 powder in the presence of dissolved oxygen: Roles of decomposition by the Fenton reaction and
43
44
45
46
47
48
49
50
51
52
53
54
55
56
57
58
59
60

adsorption/precipitation, J. Hazard. Mater. 201–202 (2012) 60–67.

1
2 doi:<https://doi.org/10.1016/j.jhazmat.2011.11.009>.

3
4 [18] R. Chand, N.H. Ince, P.R. Gogate, D.H. Bremner, Phenol degradation using 20, 300 and 520kHz
5 ultrasonic reactors with hydrogen peroxide, ozone and zero valent metals, Sep. Purif. Technol. 67 (2009)
6 103–109. doi:<https://doi.org/10.1016/j.seppur.2009.03.035>.

7
8 [19] W. Yin, J. Wu, P. Li, X. Wang, N. Zhu, P. Wu, B. Yang, Experimental study of zero-valent iron
9 induced nitrobenzene reduction in groundwater: The effects of pH, iron dosage, oxygen and common
10 dissolved anions, Chem. Eng. J. 184 (2012) 198–204. doi:<https://doi.org/10.1016/j.cej.2012.01.030>.

11
12 [20] S.H. Joo, A.J. Feitz, T.D. Waite, Oxidative Degradation of the Carbothioate Herbicide, Molinate,
13 Using Nanoscale Zero-Valent Iron, Environ. Sci. Technol. 38 (2004) 2242–2247. doi:10.1021/es035157g.

14
15 [21] J.N. Fiedor, W.D. Bostick, R.J. Jarabek, J. Farrell, Understanding the Mechanism of Uranium
16 Removal from Groundwater by Zero-Valent Iron Using X-ray Photoelectron Spectroscopy, Environ. Sci.
17 Technol. 32 (1998) 1466–1473. doi:10.1021/es970385u.

18
19 [22] J.-Y. Jeong, H.-K. Kim, J.-H. Kim, J.-Y. Park, Electrochemical removal of nitrate using ZVI
20 packed bed bipolar electrolytic cell, Chemosphere. 89 (2012) 172–178.
21 doi:<https://doi.org/10.1016/j.chemosphere.2012.05.104>.

22
23 [23] S.R. Kanel, B. Manning, L. Charlet, H. Choi, Removal of Arsenic(III) from Groundwater by
24 Nanoscale Zero-Valent Iron, Environ. Sci. Technol. 39 (2005) 1291–1298. doi:10.1021/es048991u.

25
26 [24] X. Li, J. Cao, W. Zhang, Stoichiometry of Cr(VI) Immobilization Using Nanoscale Zerovalent
27 Iron (nZVI): A Study with High-Resolution X-Ray Photoelectron Spectroscopy (HR-XPS), Ind. Eng.
28 Chem. Res. 47 (2008) 2131–2139. doi:10.1021/ie061655x.

29
30 [25] A.W. Lothongkum, S. Suren, S. Chaturabul, N. Thamphiphit, U. Pancharoen, Simultaneous
31 removal of arsenic and mercury from natural-gas-co-produced water from the Gulf of Thailand using
32

synergistic extractant via HFSLM, *J. Memb. Sci.* 369 (2011) 350–358.

1
2 doi:<https://doi.org/10.1016/j.memsci.2010.12.013>.

3
4
5 [26] J. Adusei-Gyamfi, V. Acha, Carriers for nano zerovalent iron (nZVI): synthesis, application and
6 efficiency, *RSC Adv.* 6 (2016) 91025–91044. doi:10.1039/C6RA16657A.

7
8
9
10 [27] Y.-P. Sun, X.-Q. Li, W.-X. Zhang, H.P. Wang, A method for the preparation of stable dispersion
11 of zero-valent iron nanoparticles, *Colloids Surfaces A Physicochem. Eng. Asp.* 308 (2007) 60–66.
12
13 doi:<https://doi.org/10.1016/j.colsurfa.2007.05.029>.

14
15
16
17
18 [28] A. Tiraferri, K.L. Chen, R. Sethi, M. Elimelech, Reduced aggregation and sedimentation of zero-
19 valent iron nanoparticles in the presence of guar gum, *J. Colloid Interface Sci.* 324 (2008) 71–79.
20
21 doi:<https://doi.org/10.1016/j.jcis.2008.04.064>.

22
23
24
25
26 [29] T. Phenrat, N. Saleh, K. Sirk, H.-J. Kim, R.D. Tilton, G. V Lowry, Stabilization of aqueous
27 nanoscale zerovalent iron dispersions by anionic polyelectrolytes: adsorbed anionic polyelectrolyte layer
28 properties and their effect on aggregation and sedimentation, *J. Nanoparticle Res.* 10 (2008) 795–814.
29
30
31
32
33 doi:10.1007/s11051-007-9315-6.

34
35
36 [30] F. He, D. Zhao, Manipulating the Size and Dispersibility of Zerovalent Iron Nanoparticles by Use
37 of Carboxymethyl Cellulose Stabilizers, *Environ. Sci. Technol.* 41 (2007) 6216–6221.
38
39
40
41
42
43
44
45
46
47
48
49
50
51
52
53
54
55
56
57
58
59
60
doi:10.1021/es0705543.

[31] S.S.R.M.D.H.R. Wijesekara, B.F.A. Basnayake, M. Vithanage, Organic-coated nanoparticulate
zero valent iron for remediation of chemical oxygen demand (COD) and dissolved metals from tropical
landfill leachate, *Environ. Sci. Pollut. Res.* 21 (2014) 7075–7087. doi:10.1007/s11356-014-2625-1.

[32] F. He, D. Zhao, J. Liu, C.B. Roberts, Stabilization of Fe–Pd Nanoparticles with Sodium
Carboxymethyl Cellulose for Enhanced Transport and Dechlorination of Trichloroethylene in Soil and
Groundwater, *Ind. Eng. Chem. Res.* 46 (2007) 29–34. doi:10.1021/ie0610896.

1 [33] B. Schrick, B.W. Hydutsky, J.L. Blough, T.E. Mallouk, Delivery Vehicles for Zerovalent Metal
2 Nanoparticles in Soil and Groundwater, *Chem. Mater.* 16 (2004) 2187–2193. doi:10.1021/cm0218108.

3
4 [34] L. Wu, M. Shamsuzzoha, S.M.C. Ritchie, Preparation of Cellulose Acetate Supported Zero-Valent
5 Iron Nanoparticles for the Dechlorination of Trichloroethylene in Water, *J. Nanoparticle Res.* 7 (2005)
6 469–476. doi:10.1007/s11051-005-4271-5.
7
8

9
10 [35] J. Soukupova, R. Zboril, I. Medrik, J. Filip, K. Safarova, R. Ledl, M. Mashlan, J. Nosek, M.
11 Cernik, Highly concentrated, reactive and stable dispersion of zero-valent iron nanoparticles: Direct
12 surface modification and site application, *Chem. Eng. J.* 262 (2015) 813–822.
13 doi:https://doi.org/10.1016/j.cej.2014.10.024.
14
15

16 [36] G. Sheng, X. Shao, Y. Li, J. Li, H. Dong, W. Cheng, X. Gao, Y. Huang, Enhanced Removal of
17 Uranium(VI) by Nanoscale Zerovalent Iron Supported on Na–Bentonite and an Investigation of
18 Mechanism, *J. Phys. Chem. A.* 118 (2014) 2952–2958. doi:10.1021/jp412404w.
19
20

21 [37] S.A. Kim, S. Kamala-Kannan, K.-J. Lee, Y.-J. Park, P.J. Shea, W.-H. Lee, H.-M. Kim, B.-T. Oh,
22 Removal of Pb(II) from aqueous solution by a zeolite–nanoscale zero-valent iron composite, *Chem. Eng.*
23 *J.* 217 (2013) 54–60. doi:https://doi.org/10.1016/j.cej.2012.11.097.
24
25

26 [38] X. Li, Y. Zhao, B. Xi, X. Mao, B. Gong, R. Li, X. Peng, H. Liu, Removal of nitrobenzene by
27 immobilized nanoscale zero-valent iron: Effect of clay support and efficiency optimization, *Appl. Surf.*
28 *Sci.* 370 (2016) 260–269. doi:https://doi.org/10.1016/j.apsusc.2016.01.141.
29
30

31 [39] J. Yan, L. Han, W. Gao, S. Xue, M. Chen, Biochar supported nanoscale zerovalent iron composite
32 used as persulfate activator for removing trichloroethylene, *Bioresour. Technol.* 175 (2015) 269–274.
33 doi:https://doi.org/10.1016/j.biortech.2014.10.103.
34
35
36
37
38
39
40
41
42
43
44
45
46
47
48
49
50
51
52
53
54
55
56
57
58
59
60

1
2 [40] S. Wang, B. Gao, Y. Li, A.E. Creamer, F. He, Adsorptive removal of arsenate from aqueous
3 solutions by biochar supported zero-valent iron nanocomposite: Batch and continuous flow tests, *J.*
4 *Hazard. Mater.* 322 (2017) 172–181. doi:<https://doi.org/10.1016/j.jhazmat.2016.01.052>.

5
6
7 [41] M.J. Allen, V.C. Tung, R.B. Kaner, Honeycomb Carbon: A Review of Graphene, *Chem. Rev.* 110
8 (2010) 132–145. doi:10.1021/cr900070d.

9
10 [42] Z.-J. Li, L. Wang, L.-Y. Yuan, C.-L. Xiao, L. Mei, L.-R. Zheng, J. Zhang, J.-H. Yang, Y.-L. Zhao,
11 Z.-T. Zhu, Z.-F. Chai, W.-Q. Shi, Efficient removal of uranium from aqueous solution by zero-valent iron
12 nanoparticle and its graphene composite, *J. Hazard. Mater.* 290 (2015) 26–33.
13 doi:<https://doi.org/10.1016/j.jhazmat.2015.02.028>.

14
15 [43] C. Wang, H. Luo, Z. Zhang, Y. Wu, J. Zhang, S. Chen, Removal of As(III) and As(V) from
16 aqueous solutions using nanoscale zero valent iron-reduced graphite oxide modified composites, *J.*
17 *Hazard. Mater.* 268 (2014) 124–131. doi:<https://doi.org/10.1016/j.jhazmat.2014.01.009>.

18
19 [44] H. Jabeen, K.C. Kemp, V. Chandra, Synthesis of nano zerovalent iron nanoparticles – Graphene
20 composite for the treatment of lead contaminated water, *J. Environ. Manage.* 130 (2013) 429–435.
21 doi:<https://doi.org/10.1016/j.jenvman.2013.08.022>.

22
23 [45] D.C. Marcano, D. V Kosynkin, J.M. Berlin, A. Sinitskii, Z. Sun, A. Slesarev, L.B. Alemany, W.
24 Lu, J.M. Tour, Improved Synthesis of Graphene Oxide, *ACS Nano.* 4 (2010) 4806–4814.
25 doi:10.1021/nn1006368.

26
27 [46] G. Kataby, M. Cojocar, R. Prozorov, A. Gedanken, Coating Carboxylic Acids on Amorphous
28 Iron Nanoparticles, *Langmuir.* 15 (1999) 1703–1708. doi:10.1021/la981001w.

29
30 [47] Y.T. Tao, Structural comparison of self-assembled monolayers of n-alkanoic acids on the surfaces
31 of silver, copper, and aluminum, *J. Am. Chem. Soc.* 115 (1993) 4350–4358. doi:10.1021/ja00063a062.

- 1
2 [48] K. Siskova, J. Tucek, L. Machala, E. Otyepkova, J. Filip, K. Safarova, J. Pechousek, R. Zboril,
3
4 Air-stable nZVI formation mediated by glutamic acid: solid-state storable material exhibiting 2D chain
5 morphology and high reactivity in aqueous environment, *J. Nanoparticle Res.* 14 (2012) 805.
6
7 doi:10.1007/s11051-012-0805-9.
8
9
10 [49] L. Chekli, B. Bayatsarmadi, R. Sekine, B. Sarkar, A.M. Shen, K.G. Scheckel, W. Skinner, R.
11
12 Naidu, H.K. Shon, E. Lombi, E. Donner, Analytical characterisation of nanoscale zero-valent iron: A
13
14 methodological review, *Anal. Chim. Acta.* 903 (2016) 13–35.
15
16 doi:https://doi.org/10.1016/j.aca.2015.10.040.
17
18
19 [50] S. Ameer, I.H. Gul, N. Mahmood, M. Mujahid, Semiconductor-to-metallic flipping in a
20
21 ZnFe₂O₄–graphene based smart nano-system: Temperature/microwave magneto-dielectric spectroscopy,
22
23 *Mater. Charact.* 99 (2015) 254–265. doi:https://doi.org/10.1016/j.matchar.2014.11.018.
24
25
26 [51] S. Abdolhosseinzadeh, H. Asgharzadeh, H. Seop Kim, Fast and fully-scalable synthesis of
27
28 reduced graphene oxide, *Sci. Rep.* 5 (2015) 10160. http://dx.doi.org/10.1038/srep10160.
29
30
31 [52] G. Sobon, J. Sotor, J. Jagiello, R. Kozinski, M. Zdrojek, M. Holdynski, P. Paletko, J.
32
33 Boguslawski, L. Lipinska, K.M. Abramski, Graphene Oxide vs. Reduced Graphene Oxide as saturable
34
35 absorbers for Er-doped passively mode-locked fiber laser, *Opt. Express.* 20 (2012) 19463–19473.
36
37
38 doi:10.1364/OE.20.019463.
39
40
41 [53] A.C. Ferrari, J. Robertson, Interpretation of Raman spectra of disordered and amorphous carbon,
42
43
44 *Phys. Rev. B.* 61 (2000) 14095–14107. https://link.aps.org/doi/10.1103/PhysRevB.61.14095.
45
46
47 [54] S.-M. Bak, K.-W. Nam, C.-W. Lee, K.-H. Kim, H.-C. Jung, X.-Q. Yang, K.-B. Kim, Spinel
48
49 LiMn₂O₄/reduced graphene oxide hybrid for high rate lithium ion batteries, *J. Mater. Chem.* 21 (2011)
50
51 17309–17315. doi:10.1039/C1JM13741G.
52
53
54
55
56
57
58
59
60

1 [55] A. Sarkar, G.G. Khan, A. Chaudhuri, A. Das, K. Mandal, Multifunctional BiFeO₃/TiO₂ nano-
2 heterostructure: Photo-ferroelectricity, rectifying transport, and nonvolatile resistive switching property,
3
4 *Appl. Phys. Lett.* 108 (2016) 33112. doi:10.1063/1.4940118.
5

6
7 [56] Y.-P. Sun, X. Li, J. Cao, W. Zhang, H.P. Wang, Characterization of zero-valent iron
8
9 nanoparticles, *Adv. Colloid Interface Sci.* 120 (2006) 47–56.
10
11 doi:https://doi.org/10.1016/j.cis.2006.03.001.
12

13
14 [57] F.A. Permatasari, A.H. Aimon, F. Iskandar, T. Ogi, K. Okuyama, Role of C–N Configurations in
15
16 the Photoluminescence of Graphene Quantum Dots Synthesized by a Hydrothermal Route, *Sci. Rep.* 6
17
18 (2016) 21042. <http://dx.doi.org/10.1038/srep21042>.
19
20

21
22 [58] S. Sen Gupta, K.G. Bhattacharyya, Kinetics of adsorption of metal ions on inorganic materials: A
23
24 review, *Adv. Colloid Interface Sci.* 162 (2011) 39–58. doi:<http://dx.doi.org/10.1016/j.cis.2010.12.004>.
25
26

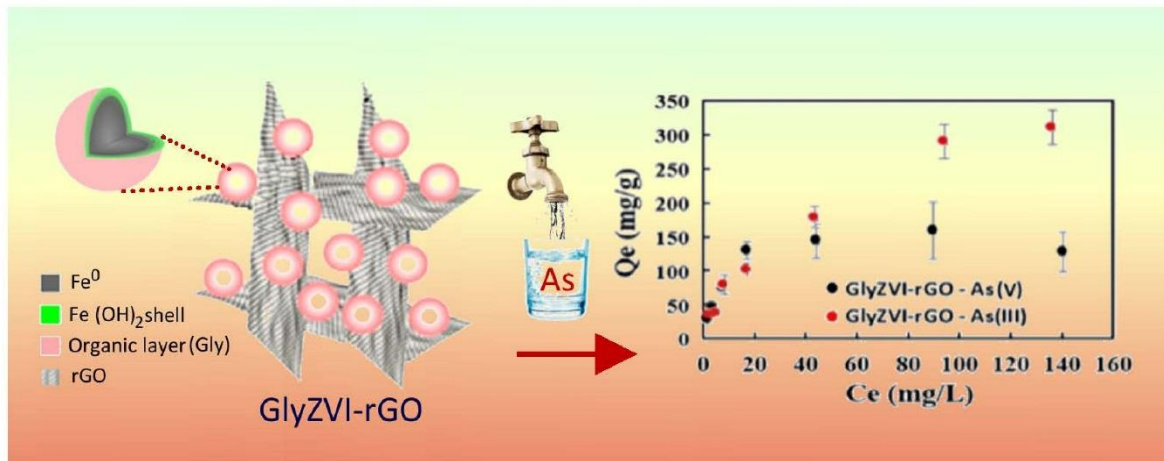
27
28 [59] V. Chandra, J. Park, Y. Chun, J.W. Lee, I.-C. Hwang, K.S. Kim, Water-Dispersible Magnetite-
29
30 Reduced Graphene Oxide Composites for Arsenic Removal, *ACS Nano.* 4 (2010) 3979–3986.
31
32 doi:10.1021/nn1008897.
33

34
35 [60] H. Freundlich, Über die absorption in lösungen, Über Die Adsorpt. Lösungen. (1906) 385–470.
36
37

38
39 [61] I. Langmuir, THE ADSORPTION OF GASES ON PLANE SURFACES OF GLASS, MICA
40
41 AND PLATINUM., *J. Am. Chem. Soc.* 40 (1918) 1361–1403. doi:10.1021/ja02242a004.
42
43

44
45 [62] A. Gupta, M. Yunus, N. Sankararamakrishnan, Zerovalent iron encapsulated chitosan nanospheres
46
47 – A novel adsorbent for the removal of total inorganic Arsenic from aqueous systems, *Chemosphere.* 86
48
49 (2012) 150–155. doi:https://doi.org/10.1016/j.chemosphere.2011.10.003.
50

51
52 [63] H. Zhu, Y. Jia, X. Wu, H. Wang, Removal of arsenic from water by supported nano zero-valent
53
54 iron on activated carbon, *J. Hazard. Mater.* 172 (2009) 1591–1596.
55
56 doi:https://doi.org/10.1016/j.jhazmat.2009.08.031.
57
58
59
60



Supporting information

An atmospherically stable and agglomeration-free zero-valent iron reduced graphene oxide (ZVI-rGO) composite for high performing environmental remediation

Ramesh Karunakaran,^{a,b} Shervin Kabiri,^{a,b} Ivan Andelkovic,^a Campbell Coghlan,^{a,b} Diana Tran,^{a,b} Christian Doonan^{c*} and Dusan Losic^{a,b*}

^a School of Chemical Engineering, University of Adelaide, SA, Australia

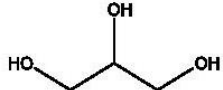
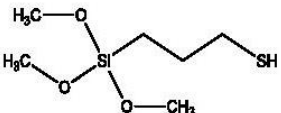
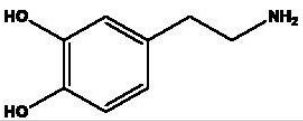
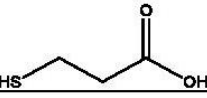
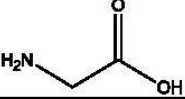
^b ARC Research Hub for Graphene Enabled Industry Transformation, The University of Adelaide, Adelaide, SA 5005, Australia

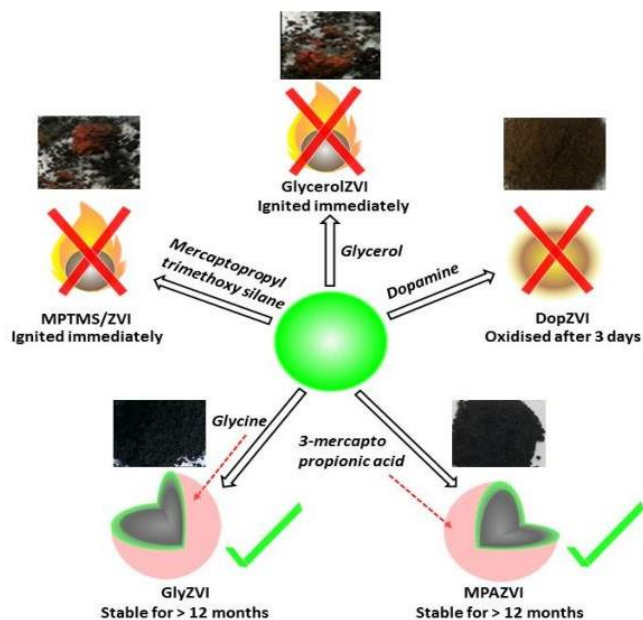
^c School of Chemistry, University of Adelaide, SA, Australia

*Corresponding author: Prof. Dusan Losic, Email: Dusan.losic@adelaide.edu.au, Phone: +61

8 8013 4648 or Christian.doonan@adelaide.edu.au; Phone: +61 8 83135770

Table S1. List chemicals used as coating material and the observation of air stability.

Chemical name	Structure	Functional groups
Glycerol		Hydroxyl
Mercaptopropyl trimethoxy silane		Thiol
Dopamine		Hydroxyl and amine
3-mercapto propionic acid		Thiol and carboxyl
Glycine		Amine and carboxyl



Scheme S1. Schematic presentation of the synthesised materials exposed to air.

Table S2. List of chemicals used as coating material and the observation of air stability.

Adsorbent	Coating agent	Support	Agglomeration	Stability (months)	pH	Concentration Range (mg/L)	Adsorbent dosage (g/L)	Adsorption capacity (mg/g)		Reference
								As (III)	As (V)	
ZVI	-	-	Yes	-	7	1	0.1	2	-	[1]
Chitosan stabilised ZVI	chitosan	-	Yes	-	7	1-20	5.0	94	119	[2]
Biochar-nZVI	-	Biochar	No	-	4.1	0-400	2.0	-	125	[3]
nZVI /AC	-	Activated carbon	No	-	6.5	2	1.0	18	12	[4]
nZVI/ Montmorillonite	-	Montmorillonite	No	-	7	5	1.0	55	46	[5]
MWCNT -ZVI	EDTA	MWCNT	No	-	7	0.1-1200	2.5	111	166	[6]
ZVI - rGO	-	rGO	No	-	7	1-10	0.4	35	29	[7]
GlyZVI-rGO	glycine	rGO	No	>12	8	0-150	0.05	400	131	This study
GlyZVI	glycine	-	Yes	>12	8	0-150	0.05	285	232	This study

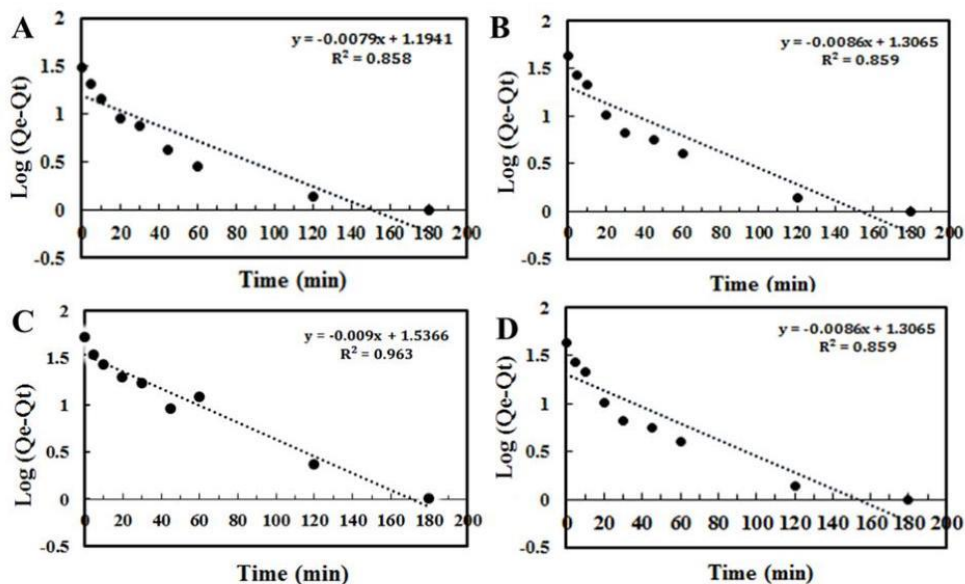


Figure S1. Pseudo-first-order kinetic plots for adsorption of A) As(III) and B) As(V) onto GlyZVI; C) As(III) and D) As(V) onto GlyZVI-rGO.

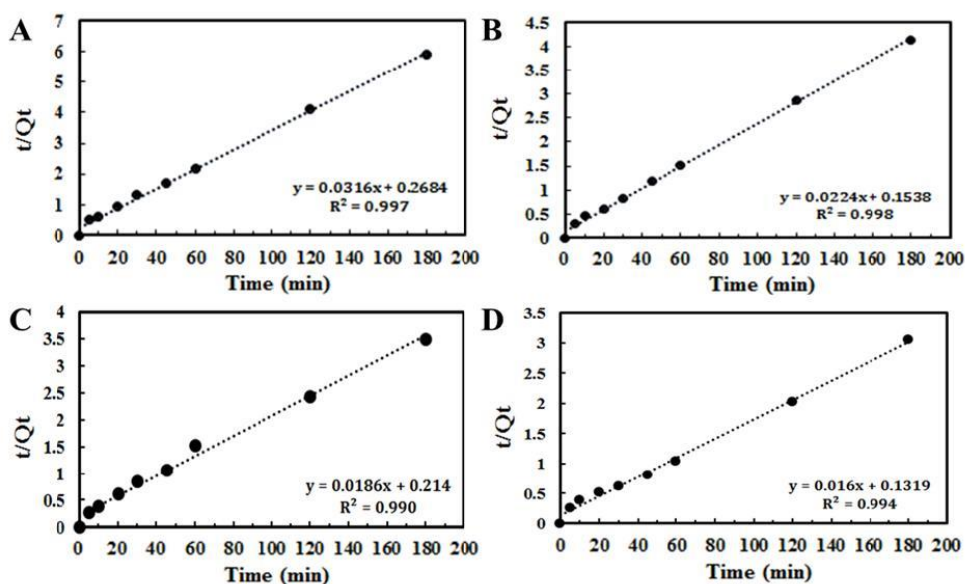


Figure S2. Pseudo-second-order kinetic plots for adsorption of A) As(III) and B) As(V) onto GlyZVI; C) As(III) and D) As(V) onto GlyZVI-rGO.

Pseudo-first order (1) and pseudo-second order (2) models[8]:

$$\log(Q_e - Q_t) = \log Q_e - K_1 t \quad (1)$$

$$\frac{t}{Q_t} = \frac{1}{Q_e^2 K_2} + \frac{t}{Q_e} \quad (2)$$

Where Q_e and Q_t are the amount (mg/g) of arsenic adsorbed at equilibrium and at time t (min) respectively, K_1 is the rate constant for the pseudo-first order adsorption (min^{-1}) and K_2 is the rate constant for the pseudo-second order adsorption ($\text{g mg}^{-1} \text{min}^{-1}$).

Table S3. Kinetic parameters for adsorption of As(III) and As(V) onto GlyZVI and GlyZVI-rGO composites

		Pseudo-first-order			Pseudo-second-order			Experimentally obtained Q_e (mg/g)
		K_1 (min^{-1})	Q_e (mg/g)	R^2	K_2 (g/mg min)	Q_e (mg/g)	R^2	
GlyZVI-rGO	As (III)	0.0207	34.4	0.963	0.0016	53.8	0.990	51.5
	As (V)	0.0285	31.1	0.889	0.0002	62.5	0.994	59.3
GlyZVI	As (III)	0.0182	15.6	0.858	0.0037	31.6	0.997	29.1
	AS (V)	0.0198	20.2	0.859	0.0033	44.6	0.998	43.4

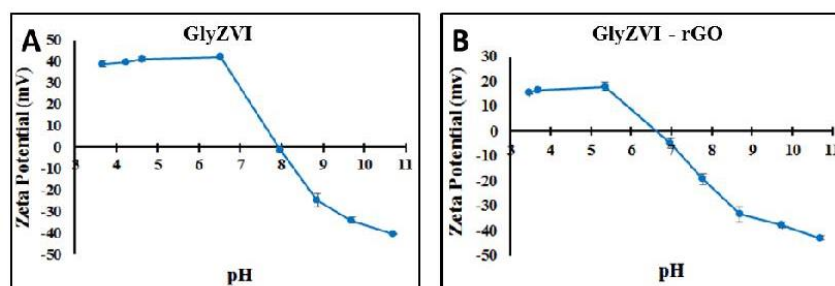


Figure S3. Zeta potential measurements for A) GlyZVI and B) GlyZVI-rGO.

The Freundlich and Langmuir models are described by equation 3 and 4, respectively[9,10]:

$$\log q_e = \log K_f + \frac{1}{n} \log C_e \quad (3)$$

$$\frac{C_e}{q_e} = \frac{1}{bQ_{max}} + \frac{C_e}{Q_{max}} \quad (4)$$

Where q_e (mg/g) is the amount of arsenic adsorbed per unit of adsorbent at equilibrium, K_f is the constant which can be used to relate the adsorption capacity, C_e (mg/L) is the equilibrium arsenic concentration, and n is the dimensionless Freundlich constant that is related to the intensity of the adsorption. In the Langmuir equation, b (L/mg) is the Langmuir constant related to the adsorption energy and Q_{max} (mg/g) is the amount adsorbed per unit weight of adsorbent required for monolayer capacity.

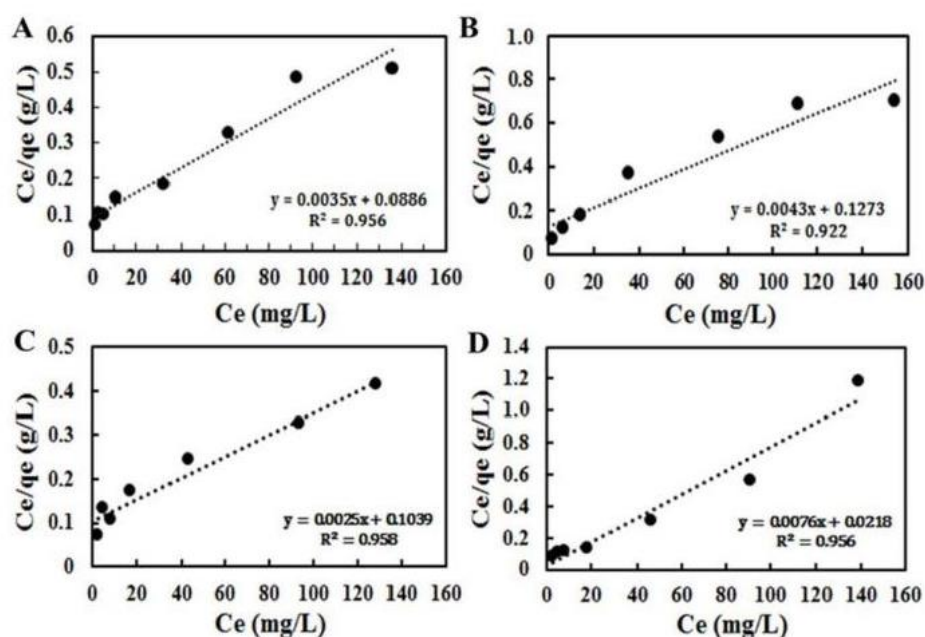


Figure S4. Langmuir plots for the for A) As(III) and B) As(V) adsorption onto GlyZVI; C) As(III) and D) As(V) adsorption onto GlyZVI-rGO.

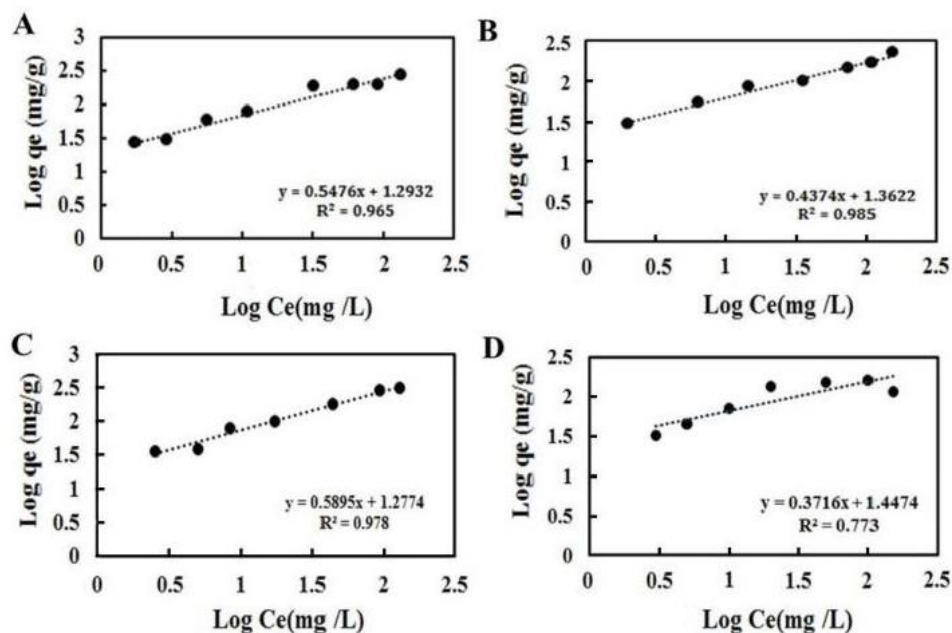


Figure S5. Freundlich plots for the for A) As(III) and B) As(V) adsorption onto GlyZVI; C) As(III) and D) As(V) adsorption onto GlyZVI-rGO.

Table S4. Langmuir and Freundlich parameters for the adsorption of As(III) and As(V) onto GlyZVI-rGO composite

		Freundlich model			Langmuir model		
		n	K _f	R ²	b (L/mg)	Q _{max} (mg/g)	R ²
GlyZVI-rGO	As (III)	1.69	16.79	0.977	0.021	400	0.958
	As (V)	2.65	28.01	0.773	0.349	132	0.956
GlyZVI	As (III)	1.82	19.64	0.965	0.039	286	0.956
	As (V)	2.28	23.02	0.985	0.033	233	0.922

References:

- [1] S.R. Kanel, B. Manning, L. Charlet, H. Choi, Removal of Arsenic(III) from Groundwater by Nanoscale Zero-Valent Iron, *Environ. Sci. Technol.* 39 (2005) 1291–1298. doi:10.1021/es048991u.
- [2] A. Gupta, M. Yunus, N. Sankararamkrishnan, Zerovalent iron encapsulated chitosan nanospheres – A novel adsorbent for the removal of total inorganic Arsenic from aqueous systems, *Chemosphere*. 86 (2012) 150–155. doi:https://doi.org/10.1016/j.chemosphere.2011.10.003.
- [3] S. Wang, B. Gao, Y. Li, A.E. Creamer, F. He, Adsorptive removal of arsenate from aqueous solutions by biochar supported zero-valent iron nanocomposite: Batch and continuous flow tests, *J. Hazard. Mater.* 322 (2017) 172–181. doi:https://doi.org/10.1016/j.jhazmat.2016.01.052.
- [4] H. Zhu, Y. Jia, X. Wu, H. Wang, Removal of arsenic from water by supported nano zero-valent iron on activated carbon, *J. Hazard. Mater.* 172 (2009) 1591–1596. doi:https://doi.org/10.1016/j.jhazmat.2009.08.031.
- [5] S. Bhowmick, S. Chakraborty, P. Mondal, W. Van Renterghem, S. Van den Berghe, G. Roman-Ross, D. Chatterjee, M. Iglesias, Montmorillonite-supported nanoscale zero-valent iron for removal of arsenic from aqueous solution: Kinetics and mechanism, *Chem. Eng. J.* 243 (2014) 14–23. doi:https://doi.org/10.1016/j.cej.2013.12.049.
- [6] N. Sankararamkrishnan, A. Gupta, S.R. Vidyarthi, Enhanced arsenic removal at neutral pH using functionalized multiwalled carbon nanotubes, *J. Environ. Chem. Eng.* 2 (2014) 802–810. doi:https://doi.org/10.1016/j.jece.2014.02.010.
- [7] C. Wang, H. Luo, Z. Zhang, Y. Wu, J. Zhang, S. Chen, Removal of As(III) and As(V)

from aqueous solutions using nanoscale zero valent iron-reduced graphite oxide

modified composites, *J. Hazard. Mater.* 268 (2014) 124–131.

doi:<https://doi.org/10.1016/j.jhazmat.2014.01.009>.

- [8] Y.S. Ho, G. McKay, Pseudo-second order model for sorption processes, *Process Biochem.* 34 (1999) 451–465. doi:[https://doi.org/10.1016/S0032-9592\(98\)00112-5](https://doi.org/10.1016/S0032-9592(98)00112-5).
- [9] H. Freundlich, Über die absorption in lösungen, Über Die Adsorpt. Lösungen. (1906) 385–470.
- [10] I. Langmuir, THE ADSORPTION OF GASES ON PLANE SURFACES OF GLASS, MICA AND PLATINUM., *J. Am. Chem. Soc.* 40 (1918) 1361–1403.
doi:[10.1021/ja02242a004](https://doi.org/10.1021/ja02242a004).

CHAPTER 7

CONCLUSIONS AND RECOMMENDATIONS FOR FUTURE WORKS

Ramesh Karunagaran

School of Chemical Engineering, University of Adelaide, South Australia 5005, Australia

7.1 CONCLUSION

The chapter overviews the contribution of whole thesis to improve carbon composite technology towards achieving solutions to constantly rising world's energy and environmental concerns. Initially, the in-depth knowledge of fabricating unique carbon composite materials and, the need to encounter world's critical energy and environmental issues such as seeking alternatives for fossil fuels to cater the rising energy demand, increasing CO₂ pollutions and arsenic contaminated drinking water, permitted design of unique carbon composites to drive set closer to find permeant solutions to these issues. The synthesise of hybrid structures comprises both N-doped CNTs and N-CMSs and composites of N-doped SAO with PF and rGO provided details understanding that additional active sites can be generated by hybrid or composite materials to drive ORR reactions more effectively. Furthermore, investigations on different composites of different irons oxide phases in graphene aerogels as catalysts for oxygen reduction revealed that low cost and abundantly available iron oxides have low reduction capacities to reduce oxygen irrespective of their phases. However, it provided vital information that their crystal structures, magnetic properties and electrical conductivity can influence the oxygen reduction capacities which opens opportunities to explore different elements with similar crystal structures for oxygen reduction purposes. Moreover, the investigation of the dependence of air stability of ZVI on different functional groups revealed vital information regarding air stability is greatly dependant on functional groups used to coat them. This investigation provided in depth understanding of the reasons for short term air stability reported in previous studies conducted on ZVI. This study identified the main drawbacks of ZVI air stability and particle agglomeration which have hindered the demonstration of the true potential of the ZVI over the years and provided effective solutions. This led to the synthesis of ZVI/rGO and ZVFe and ZVCo/rGO composites, which displayed

its true potentials and performed outstandingly as arsenic adsorbent. These easy, low cost and tailorable technologies can integrate into energy conversion and environmental remediation technologies to address the world energy and environmental crisis and create a safe and comfortable world to live. The following summarises the specific conclusions from the major investigations carried out as a part of this thesis.

7.1.1 A unique 3D nitrogen - doped carbon composite as high performance oxygen reduction catalysts

Bio source (galactose), maghemite nanoparticles and nitrogen precursor (melamine) was used to synthesise low cost and environmentally friendly carbon composite materials using two-step hydrothermal treatment and pyrolysis processes to explore the oxygen reduction capabilities in alkaline medium. The following points summarises the conclusions drawn from this study:

1. 3D N- doped carbon composite hybrid materials with integrated CNT and CMS morphologies can be synthesised using galactose, maghemite nanoparticles and melamine *via* two-step hydrothermal and pyrolysis process.
2. At elevated pyrolysis temperature (950 °C) the decomposed carbon and nitrogen products of melamine formed N-doped CNTs through the FeMNPC releases from the disruption of the carbon spheres.
3. Integrated structures of N-CNTs and N-CMS was observed only for GAL-Fe-N and similar structures were not detected for GAL-Fe-A or GAL-N. Therefore, it can be confirmed both Fe nanoparticles and N precursor is essential for formation of these hybrid structures.
4. The significant increase in the electron transfer number for GAL-Fe-N compared to GAL-N has demonstrated hybrid structures have contributed additional active sites for ORR.

5. The enhanced activity of GAL-Fe-N was attributed to the N-C active sites formed by pyridinic nitrogen structures with their strong Lewis basicity and electronic affinity in the N-CNT and N-carbon microspheres, which induced a high positive charge density on the adjacent carbon atoms. As a result, the electron donor properties of nitrogen-doped (N-doped) GAL-Fe-N triggered a favourable diatomic O-O adsorption weakening the O-O bond strength to facilitate ORR activity and drive the reaction *via* predominantly four - electron pathway.

7.1.2 Green Synthesis of three-dimensional hybrid N-doped ORR electro catalysts composed of nitrogen doped micro-spherical and nanotubular structures using Apricot Sap

Naturally occurring apricot sap, maghemite nanoparticles and nitrogen precursor (melamine) was used to synthesise low cost and environmentally friendly carbon composite materials using three-step apricot resin preparation, hydrothermal treatment and pyrolysis processes to explore the oxygen reduction capabilities in alkaline medium. The following points summarises the conclusions drawn from this study:

1. Hydrothermal reduction of apricot resin suspension in the presence of Fe and Co nanoparticles produced Fe and Co nanoparticle embedded carbon spheres formed as a consequence of dehydration and polymerisation of galactose present in apricot resin.
2. 3D N- doped carbon hybrid materials composed of micro-spherical and nanotubular structures can be synthesised using apricot sap, maghemite nanoparticles, cobalt precursors and melamine *via* three-step apricot resin preparation, hydrothermal treatment and pyrolysis process.

3. The MNPs initially embedded within the CMS diffused out of the CMS to catalyse formation of corrugated hollow N-CNT due to the surface destruction caused by the decomposition of melamine during pyrolysis.
4. Both N-APG-Fe and N-APG-Co with integrated N-doped micro-spherical and N-doped nanotubular structures catalyzed ORR by driving the ORR predominantly by four – electron transfer path way with low yeild of HO_2^- . The ORR activity of N-APG with solely micro-spherical structure was significantly lower than both N-APG-Fe and N-APG-Co which demonstrated hybrid structures has provided additional active site for ORR.
5. The enhanced activity of N-APG-Fe and N-APG-Co was attributed to the N-C active sites formed by electro negative pyridinic nitrogen species in the N-CNT and N-CMSs, which induced a high positive charge density on the adjacent carbon atoms to facilitate a favourable diatomic O-O adsorption to the adjacent carbon atom to the N species. This weakened the O-O bond strength to facilitate ORR activity and drive the reaction *via* predominantly four - electron pathway.

7.1.3 Study of iron oxide nanoparticle phases in graphene aerogels for oxygen reduction reaction

Four different iron oxide phases Fe_3O_4 , $\alpha\text{-Fe}_2\text{O}_3$, $\gamma\text{-Fe}_2\text{O}_3$ and $\alpha\text{-FeOOH}$ were investigated for their individual activity to reduce oxygen in alkaline medium. These different iron oxide phases were individually dispersed in 3D graphene aerogels at low temperature (80 °C) and their individual phases were retained in graphene aerogels. These iron oxide/rGO composites was investigated as ORR catalyst in alkaline medium. The following points summarises the conclusions drawn from this study:

1. All iron oxide phases showed low activity towards oxygen reduction compared to the standard Pt/C catalyst. However, the investigation revealed different phases of iron oxide alters the levels of electron transfer number and HO_2^- produced.
2. Ferromagnetic rGO/ Fe_3O_4 and rGO/ $\gamma\text{-Fe}_2\text{O}_3$ showed higher catalytic activity towards oxygen reduction compared to rGO/ $\alpha\text{-Fe}_2\text{O}_3$ and rGO/ $\alpha\text{-FeOOH}$. The higher ORR activity was attributed to their inverse spinel structures, magnetic and electrical conductivity of Fe_3O_4 and $\gamma\text{-Fe}_2\text{O}_3$. rGO/ $\alpha\text{-Fe}_2\text{O}_3$ showed the lowest ORR activity with low conductivity.
3. All catalysts, apart from $\alpha\text{-Fe}_2\text{O}_3$ proceeded *via* a four-electron transfer pathway at lower potential regions. At a high potential (0.70 V) all catalysts were driven through the two-electron pathway producing HO_2^- as an intermediate.

7.1.4 A facile synthesis procedure for sulphonated aniline oligomers with distinct microstructures

SAO with well defined micro structures was synthesised using excess aniline and low oxidant in ethanol at pH 4.8. The following points summarises the conclusions drawn from this study:

1. Synthesized SAO was comprised of well-defined micro structures with both micro sheets and micro rods in the presence of ethanol. The comparison of the synthesis conducted in the presence of water showed formation of shapeless aggregates, confirming that ethanol significantly reduced the agglomeration of micro structures by forming H-bonds with SAO molecules.
2. The presence of sulphonate groups was established by conducting EDX, FTIR and ^{13}C NMR techniques.

3. The mechanism of the formation of microstructures has revealed that it goes through several stages from 2D planar sheets and their transformation into tubular and layered flake structures *via* π - π interaction between 2D planer sheets.
4. Tubular structures were formed when the stacked 2D planar sheets tends to reduce their surface energy.

7.1.5 A unique N-doped macro porous oxygen reduction electro catalysts synthesised with sulphonated aniline oligomers and its phenol formaldehyde and reduced graphene oxide composites.

SAO and its composites made with phenol formaldehyde and reduced graphene oxide was pyrolysed in the presence of nitrogen precursor (melamine) and investigated for ORR catalytic activity in alkaline medium. The following points summarises the conclusions drawn from this study:

1. Pyrolysis of SAO, SAOrGO and SAOPF materials expanded and formed macro porous carbon structures.
2. The thermometric – mass spectrometer analysis conducted on pyrolysed SAO revealed the sulphonated groups attached to the SAO decomposes at 266 °C and release SO₂ gas which facilitated the expansion of SAO and its composite materials (SAOPF and SAOrGO) to form macro porous carbon structures.
3. The composite materials of SAO (N-SAOrGO and N-SAOPF) showed higher oxygen reduction capabilities compared to N-SAO with higher electron transfer numbers and lower HO₂⁻ yield.

4. N-SAOPF showed highest onset potential (0.98 V), highest eletro transfer number (3.62 at 0.50 V) and lowest % HO_2^- yield (19.02 % at 0.50 V). The enhanced activity was
5. attributed to the higher % atomic concentration of pyridinic nitrogen present in N-SAOPF.
6. N-SAOrgO displayed the highest limiting current density at 0 V (RHE) (7.89 mA/cm^2) which is nearly 65% higher than the standard Pt/C catalysts at similar potential. The increase in the limited current density is ascribed to the higher % atomic concentration of graphitic nitrogen present in N-SAOrgO.

7.1.6 An atmospherically stable and agglomeration-free zero-valent iron reduced graphene oxide (ZVI-rGO) composite for high performing environmental remediation

To establish the contribution of different organic functional groups towards providing long – term air stability for ZVI, the activity of organic materials with four different functional groups towards proving long – term air stability was investigated. The ZVI provided long – term air stability was dispersed in rGO to reduce particle agglomeration and tested for arsenic species adsorption in water. The following points summarises the conclusions drawn from this study:

1. Out of the five organic materials with different functional groups including thiol, hydroxyl, carboxylic and amine tested, carboxylic functional groups provided long-term air stability and remained stable for more than 12 months.
2. Organic materials with amine groups provided short term air stability up-to three days and eventually oxidised and changed colour. Organic materials containing hydroxyl and thiol groups could not provide air stability towards ZVI and reacted immediately when exposed to air.

3. Investigation on arsenic adsorption carried out using both glycine coated GlyZVI and GlyZVI-rGO revealed both materials showed outstanding arsenic adsorption capacities. However, the As (III) adsorption capacity on less aggregated GlyZVI-rGO (400 mg/g) was higher than aggregated GlyZVI (285.7 mg/g) and adsorbed >50 % of arsenic adsorbed within 30 min.

7.2 Recommendations for future work

1. Although numerous claims have been made regarding the ability of hybrid carbon materials to enhance ORR activity, only a handful of unique combinations have reached the ORR activity similar to that of the standard Pt/C catalysts. Notwithstanding the great process these hybrid carbon catalysts have achieved the past, there still remains a gap in identifying the ideal combination of hybrid material which provide greater active site for oxygen reduction. Therefore, carbon structures which have specific features to their structures such as graphene quantum dots, CNTs, graphene, carbon spheres and carbon nitrides should be strategically coupled in to composite arrangements to obtain ORR catalysts with high concentration of active species. The integrated combinations of these structure and the study of their catalytic performances are worthy of investigation as they have the potential to provide low cost, stable, easily scalable catalysts with increase catalysts activity.
2. The effect of particle size on ORR activity should be investigated for magnetite and maghemite with inverse spinel structures. Pt/C catalysts investigated for particle size dependence on ORR activity has demonstrated differences in surface activity at lower particle size range (2-10 nm). The investigation on particle size effect on magnetite and maghemite catalysts could provide a wide range of understanding of these catalysts.
3. Arsenic adsorption on zero valent cobalt has not been widely reported in the literature. Air stable, magnetic and less aggregated cobalt catalysts can be investigated and

reported for heavy metal remediation from drinking water. It is proposed, further optimization of this adsorbent toward and development of commercial adsorbent for two applications: removal As from drinking waters and for soil remediation.

APPENDIX

Copyrights obtained for the use of figures and tables in this thesis.

Ramesh Karunakaran

School of Chemical Engineering, University of Adelaide, South Australia 5005, Australia

APPENDIX: Copyrights obtained for the figures and tables used in this thesis.

1. Figure 1: Copyright 2016, Taylor & Francis. Reproduced with permission.

Citation:

S. K. Tiwari, V. Kumar, A. Huczko, R. Oraon, A. D. Adhikari and G. Nayak, *Critical Reviews in Solid State and Materials Sciences*, 2016, **41**, 257-317.

2. Figure 2. Copyright 2015, Elsevier Ltd. Reproduced with permission.

Citation:

K. N. Aboua, Y. A. Yobout, K. B. Yao, D. L. Gone and A. Trokourey, *Journal of Environmental Management*, 2015, **156**, 10-14.

3. Figure 3. Copyright 2011, Royal Society of Chemistry. Reproduced with permission.

Citation:

R. Chakrabarti, J. Delannoy, M. Couty and K. S. Schweizer, *Soft Matter*, 2011, **7**, 5397-5407.

4. Figure 4: Copyright 2007, Elsevier B. V. Reproduced with permission.

Citation:

L. Kao and T. Hsu, *Materials Letters*, 2008, **62**, 695-698.

5. Figure 5: Copyright 2014, Elsevier B. V. Reproduced with permission.

Citation:

N. Yang, Y. Chen, T. Ren, P. Zhang and D. Yang, *Sensors and Actuators: B Chemical*, 2015, **207**, 690-715.

6. Figure 6: Copyright 2012, Royal Society of Chemistry. Reproduced with permission.

Citation:

H. Huang, Y. Xia, X. Tao, J. Du, J. Fang, Y. Gan and W. Zhang, *Journal of Materials Chemistry*, 2012, **22**, 10452-10456.

7. Figure 7: This work is licenced under a Creative Commons Attribution-Non Commercial-No Derivatives 4.0 International Licence which allows to copy and share materials in any format or medium.

Citation:

O. T. Holton and J. W. Stevenson, *Platinum Metals Review*, 2013, **57**, 259-271.

8. Figure 8: Copyright 2014, Royal Society of Chemistry. Reproduced with permission.

Citation:

C. P. Ewels, D. Erbahar, P. Wagner, X. Rocquefelte, R. Arenal and P. Pochel, *Paraday Discussions*, 2014, **173**, 215-232.

9. Figure 9: US Energy Information Administration (EIA) allowed free access to the images with proper recognition of authors , year and the source.

Citation:

J. Conti, P. Holtberg, J. Diefenderfer, A. LaRose, J. Turnure and L. Westfall, *US Energy Information Administration (EIA)*, 2014, doi: DOE/EIA-0484.

10. Figure 10: Copyright 2012, Elsevier Ltd. Reproduced with permission.

Citation:

M. Höök and X. Tang, *Energy Policy*, 2013, **52**, 797-809.

11. Table 1: Copyright 2015, American Chemical Society. Reproduced with permission.

Citation:

X. Ge, A. Sumboja, D. Wu, T. An, B. Li, F. T. Goh, T. A. Hor, Y. Zong and Z. Liu, *ACS Catalysis*, 2015, **5**, 4643-4667.

12. Scheme 1: Copyright 2007, Elsevier B. V. Reproduced with permission.

Citation:

G. P. Rao, C. Lu and F. Su, *Separation and Purification Technology*, 2007, **58**, 224-231.

13. All schemes, figures and tables in Chapter 3(a): This is an open access article distributed under the Creative Commons Attribution Licence, which permits unrestricted use, distribution, and reproduction in any medium, provided the original work is properly cited (CC BY 4.0).
14. All schemes, figures and tables in Chapter 3(b): This is an open access article distributed under the Creative Commons Attribution Licence, which permits unrestricted use, distribution, and reproduction in any medium, provided the original work is properly cited (CC BY 4.0).
15. All schemes, figures and tables in Chapter 4(a): Copyright 2017, Royal Society of Chemistry. Reproduced with permission.

 **Copyright Clearance Center** RightsLink[®] [Home](#) [Account Info](#) [Help](#)

 **Taylor & Francis**
Taylor & Francis Group

Solid State and Materials Sciences

Title: Magical Allotropes of Carbon: Prospects and Applications
Author: Santosh K. Tiwari, Vijay Kumar, Andrzej Huczko, et al
Publication: Critical Reviews in Solid State and Materials Sciences
Publisher: Taylor & Francis
Date: Jul 3, 2016
Rights managed by Taylor & Francis

Logged in as:
Ramesh Karunagaran
[LOGOUT](#)

Thesis/Dissertation Reuse Request

Taylor & Francis is pleased to offer reuses of its content for a thesis or dissertation free of charge on resubmission of permission request if work is published.

[BACK](#)

[CLOSE WINDOW](#)

Copyright © 2018 Copyright Clearance Center, Inc. All Rights Reserved. [Privacy statement](#). [Terms and Conditions](#).
Comments? We would like to hear from you. E-mail us at customercare@copyright.com



Home

Account Info

Help



Title: Investigation of dye adsorption onto activated carbon from the shells of Macoré fruit
Author: Kouassi Narcisse Aboua, Yao Augustin Yobouet, Kouassi Benjamin Yao, Droh Lanciné Goné, Albert Trokourey
Publication: Journal of Environmental Management
Publisher: Elsevier
Date: 1 June 2015

Copyright © 2015 Elsevier Ltd. All rights reserved.

Logged in as:

Ramesh Karunakaran

Account # :
3001272744

LOGOUT

Order Completed

Thank you for your order.

This Agreement between Ramesh Karunakaran ("You") and Elsevier ("Elsevier") consists of your license details and the terms and conditions provided by Elsevier and Copyright Clearance Center.

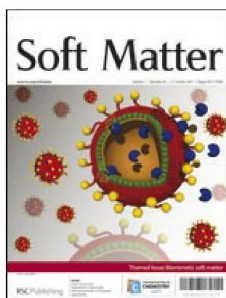
Your confirmation email will contain your order number for future reference.

[printable details](#)

License Number	4332550159659
License date	Apr 19, 2018
Licensed Content Publisher	Elsevier
Licensed Content Publication	Journal of Environmental Management
Licensed Content Title	Investigation of dye adsorption onto activated carbon from the shells of Macoré fruit
Licensed Content Author	Kouassi Narcisse Aboua, Yao Augustin Yobouet, Kouassi Benjamin Yao, Droh Lanciné Goné, Albert Trokourey
Licensed Content Date	Jun 1, 2015
Licensed Content Volume	156
Licensed Content Issue	n/a
Licensed Content Pages	5
Type of Use	reuse in a thesis/dissertation
Portion	figures/tables/illustrations
Number of figures/tables/illustrations	1
Format	electronic
Are you the author of this Elsevier article?	No
Will you be translating?	No
Order reference number	3001272744
Original figure numbers	Fig.1
Title of your thesis/dissertation	Graphitic carbon materials for energy and environment
Expected completion date	May 2018
Estimated size (number of pages)	275
Attachment	
Requestor Location	Ramesh Karunakaran Adelaide Univ Adelaide, 5005



[Home](#)
[Account Info](#)
[Help](#)

Title: Packing correlations, collective scattering and compressibility of fractal-like aggregates in polymer nanocomposites and suspensions
Author: Rajarshi Chakrabarti, Jean-Yves Delannoy, Marc Couty, Kenneth S. Schweizer
Publication: Soft Matter
Publisher: Royal Society of Chemistry
Date: May 5, 2011
 Copyright © 2011, Royal Society of Chemistry

Logged in as:
 Ramesh Karunakaran
 Account #:
 3001272744
[LOGOUT](#)

Order Completed

Thank you for your order.

This Agreement between Ramesh Karunakaran ("You") and Royal Society of Chemistry ("Royal Society of Chemistry") consists of your license details and the terms and conditions provided by Royal Society of Chemistry and Copyright Clearance Center.

Your confirmation email will contain your order number for future reference.

[printable details](#)

License Number	4332550466121
License date	Apr 19, 2018
Licensed Content Publisher	Royal Society of Chemistry
Licensed Content Publication	Soft Matter
Licensed Content Title	Packing correlations, collective scattering and compressibility of fractal-like aggregates in polymer nanocomposites and suspensions
Licensed Content Author	Rajarshi Chakrabarti, Jean-Yves Delannoy, Marc Couty, Kenneth S. Schweizer
Licensed Content Date	May 5, 2011
Licensed Content Volume	7
Licensed Content Issue	11
Type of Use	Thesis/Dissertation
Requestor type	academic/educational
Portion	figures/tables/images
Number of figures/tables/images	1
Distribution quantity	100
Format	electronic
Will you be translating?	no
Order reference number	3001272744
Title of the thesis/dissertation	Graphitic carbon materials for energy and environment
Expected completion date	May 2018
Estimated size	275
Attachment	
Requestor Location	Ramesh Karunakaran Adelaide Univ



- [Home](#)
- [Account Info](#)
- [Help](#)
-



Title: Silica template synthesis of ordered mesoporous carbon thick films with 35-nm pore size from mesophase pitch solution

Author: Li-Heng Kao, Tzu-Chien Hsu

Publication: Materials Letters

Publisher: Elsevier

Date: 29 February 2008

Copyright © 2007 Elsevier B.V. All rights reserved.

Logged in as:
Ramesh Karunakaran

Account #:
3001272744

[LOGOUT](#)

Order Completed

Thank you for your order.

This Agreement between Ramesh Karunakaran ("You") and Elsevier ("Elsevier") consists of your license details and the terms and conditions provided by Elsevier and Copyright Clearance Center.

Your confirmation email will contain your order number for future reference.

[printable details](#)

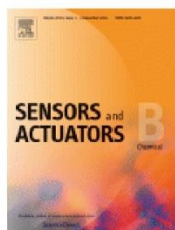
License Number	4332550780195
License date	Apr 19, 2018
Licensed Content Publisher	Elsevier
Licensed Content Publication	Materials Letters
Licensed Content Title	Silica template synthesis of ordered mesoporous carbon thick films with 35-nm pore size from mesophase pitch solution
Licensed Content Author	Li-Heng Kao, Tzu-Chien Hsu
Licensed Content Date	Feb 29, 2008
Licensed Content Volume	62
Licensed Content Issue	4-5
Licensed Content Pages	4
Type of Use	reuse in a thesis/dissertation
Portion	figures/tables/illustrations
Number of figures/tables/illustrations	1
Format	electronic
Are you the author of this Elsevier article?	No
Will you be translating?	No
Order reference number	3001272744
Original figure numbers	Fig.3
Title of your thesis/dissertation	Graphitic carbon materials for energy and environment
Expected completion date	May 2018
Estimated size (number of pages)	275
Attachment	
Requestor Location	Ramesh Karunakaran Adelaide Univ Adelaide, 5005 Australia Attn: Ramesh Karunakaran



Home

Account Info

Help



Title: Carbon nanotube based biosensors
Author: Ning Yang, Xianping Chen, Tianling Ren, Ping Zhang, Daoguo Yang
Publication: Sensors and Actuators B: Chemical
Publisher: Elsevier
Date: February 2015

Logged in as:
 Ramesh Karunakaran
 Account #: 3001272744

LOGOUT

Copyright © 2014 Elsevier B.V. All rights reserved.

Order Completed

Thank you for your order.

This Agreement between Ramesh Karunakaran ("You") and Elsevier ("Elsevier") consists of your license details and the terms and conditions provided by Elsevier and Copyright Clearance Center.

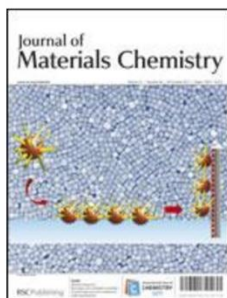
Your confirmation email will contain your order number for future reference.

[printable details](#)

License Number	4333420591535
License date	Apr 20, 2018
Licensed Content Publisher	Elsevier
Licensed Content Publication	Sensors and Actuators B: Chemical
Licensed Content Title	Carbon nanotube based biosensors
Licensed Content Author	Ning Yang, Xianping Chen, Tianling Ren, Ping Zhang, Daoguo Yang
Licensed Content Date	Feb 1, 2015
Licensed Content Volume	207
Licensed Content Issue	n/a
Licensed Content Pages	26
Type of Use	reuse in a thesis/dissertation
Portion	figures/tables/illustrations
Number of figures/tables/illustrations	1
Format	electronic
Are you the author of this Elsevier article?	No
Will you be translating?	No
Order reference number	3001272744
Original figure numbers	Fig.2
Title of your thesis/dissertation	Graphitic carbon materials for energy and environment
Expected completion date	May 2018
Estimated size (number of pages)	275
Attachment	
Requestor Location	Ramesh Karunakaran Adelaide Univ Adelaide, 5005 Australia Attn: Ramesh Karunakaran
Publisher Tax ID	GB 494 6272 12
Total	0.00 USD



RightsLink®



Title: Highly efficient electrolytic exfoliation of graphite into graphene sheets based on Li ions intercalation–expansion–microexplosion mechanism

Author: Hui Huang, Yang Xia, Xinyong Tao, Jun Du, Junwu Fang, Yongping Gan, Wenkui Zhang

Publication: Journal of Materials Chemistry

Publisher: Royal Society of Chemistry

Date: Apr 25, 2012

Copyright © 2012, Royal Society of Chemistry

Logged in as:
Ramesh Karunagaran
Account #:
3001272744

[LOGOUT](#)

Order Completed

Thank you for your order.

This Agreement between Ramesh Karunagaran ("You") and Royal Society of Chemistry ("Royal Society of Chemistry") consists of your license details and the terms and conditions provided by Royal Society of Chemistry and Copyright Clearance Center.

Your confirmation email will contain your order number for future reference.

[printable details](#)

License Number	4332541244261
License date	Apr 19, 2018
Licensed Content Publisher	Royal Society of Chemistry
Licensed Content Publication	Journal of Materials Chemistry
Licensed Content Title	Highly efficient electrolytic exfoliation of graphite into graphene sheets based on Li ions intercalation–expansion–microexplosion mechanism
Licensed Content Author	Hui Huang, Yang Xia, Xinyong Tao, Jun Du, Junwu Fang, Yongping Gan, Wenkui Zhang
Licensed Content Date	Apr 25, 2012
Licensed Content Volume	22
Licensed Content Issue	21
Type of Use	Thesis/Dissertation
Requestor type	academic/educational
Portion	figures/tables/images
Number of figures/tables/images	1
Distribution quantity	100
Format	electronic
Will you be translating?	no
Order reference number	3001272744
Title of the thesis/dissertation	Graphitic carbon materials for energy and environment
Expected completion date	May 2018
Estimated size	275
Attachment	

The Role of Platinum in Proton Exchange Membrane Fuel Cells



Authors: Holton, Oliver T.; Stevenson, Joseph W.




Source: Platinum Metals Review, Volume 57, Number 4, October 2013, pp. 259-271(13)

Publisher: Johnson Matthey

DOI: <https://doi.org/10.1595/147106713X671222>

This work is licensed under a Creative Commons Attribution-NonCommercial-NoDerivatives 4.0 International License.

[< previous article](#) | [view table of contents](#) | [next article >](#) [ADD TO FAVOURITES](#)

...						
Abstract	References	Citations	Supplementary Data	Article Media	Metrics	Suggestions

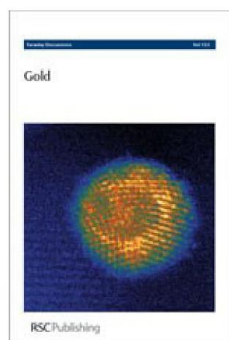
Proton exchange membrane fuel cells (PEMFCs) dominate the transportation fuel cell market and platinum



Home

Account Info

Help



Title: Nitrogen segregation in nanocarbons
Author: C. P. Ewels, D. Erbahar, Ph. Wagner, X. Rocquefelte, R. Arenal, P. Pochet, M. Rayson, M. Scardamaglia, C. Bittencourt, P. Briddon
Publication: Faraday Discussions
Publisher: Royal Society of Chemistry
Date: Jun 13, 2014
 Copyright © 2014, Royal Society of Chemistry

Logged in as:

Ramesh Karunakaran

Account #: 3001272744

LOGOUT

Order Completed

Thank you for your order.

This Agreement between Ramesh Karunakaran ("You") and Royal Society of Chemistry ("Royal Society of Chemistry") consists of your license details and the terms and conditions provided by Royal Society of Chemistry and Copyright Clearance Center.

Your confirmation email will contain your order number for future reference.

[printable details](#)

License Number	4332551433990
License date	Apr 19, 2018
Licensed Content Publisher	Royal Society of Chemistry
Licensed Content Publication	Faraday Discussions
Licensed Content Title	Nitrogen segregation in nanocarbons
Licensed Content Author	C. P. Ewels, D. Erbahar, Ph. Wagner, X. Rocquefelte, R. Arenal, P. Pochet, M. Rayson, M. Scardamaglia, C. Bittencourt, P. Briddon
Licensed Content Date	Jun 13, 2014
Licensed Content Volume	173
Licensed Content Issue	0
Type of Use	Thesis/Dissertation
Requestor type	academic/educational
Portion	figures/tables/images
Number of figures/tables/images	1
Distribution quantity	100
Format	electronic
Will you be translating?	no
Order reference number	3001272744
Title of the thesis/dissertation	Graphitic carbon materials for energy and environment
Expected completion date	May 2018
Estimated size	275
Attachment	
Requestor Location	Ramesh Karunakaran



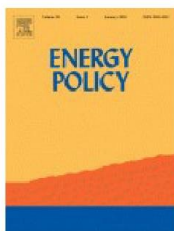
The screenshot shows the EIA website's 'Copyrights and Reuse' page. At the top, there is a dark blue navigation bar with the EIA logo on the left and links for 'Sources & Uses', 'Topics', and 'Geography' in the center. A search bar on the right contains the text 'Search eia.gov'. Below the navigation bar is a left-hand sidebar titled 'About EIA' with a list of menu items: 'Our Work', 'EIA News and Events', 'Our Organization', 'Budget, Plans & Performance', 'Our History', 'EIA Conference', and 'Policies & Procedures'. The 'Policies & Procedures' section is expanded, showing sub-links for 'Information Quality Guidelines', 'EIA Standards Manual', and 'Statement of Commitment to...'. The main content area is titled 'Copyrights and Reuse' and contains three sections: 'Public domain and use of EIA content', 'Quoting EIA content and translations', and 'Protected materials'. The 'Protected materials' section includes a small image of a padlock.

Public domain and use of EIA content
U.S. government publications are in the public domain and are not subject to copyright protection. You may use and/or distribute any of our data, files, databases, reports, graphs, charts, and other information products that are on our website or that you receive through our email distribution service. However, if you use or reproduce any of our information products, you should use an acknowledgment, which includes the publication date, such as: "Source: U.S. Energy Information Administration (Oct 2008)."

Quoting EIA content and translations
When quoting EIA text, the acknowledgment should clearly indicate which text is EIA content and which is not. When translating EIA content into another language, please indicate the organization responsible for the translation and provide a link back to the original EIA web page in the acknowledgment.

Protected materials
You may see on our website documents, illustrations, photographs, or other information resources contributed or licensed by private individuals, companies, or organizations that may be protected by U.S. and foreign copyright laws. Transmission or reproduction of protected items beyond that allowed by [fair use](#) as defined in the copyright laws requires the written permission of the copyright owners.





Title: Depletion of fossil fuels and anthropogenic climate change—A review
Author: Mikael Höök, Xu Tang
Publication: Energy Policy
Publisher: Elsevier
Date: January 2013
 Copyright © 2012 Elsevier Ltd. All rights reserved.

Logged in as:
 Ramesh Karunakaran
 Account #:
 3001272744
[LOGOUT](#)

Order Completed

Thank you for your order.

This Agreement between Ramesh Karunakaran ("You") and Elsevier ("Elsevier") consists of your license details and the terms and conditions provided by Elsevier and Copyright Clearance Center.

Your confirmation email will contain your order number for future reference.

[printable details](#)

License Number	4332780483896
License date	Apr 19, 2018
Licensed Content Publisher	Elsevier
Licensed Content Publication	Energy Policy
Licensed Content Title	Depletion of fossil fuels and anthropogenic climate change—A review
Licensed Content Author	Mikael Höök, Xu Tang
Licensed Content Date	Jan 1, 2013
Licensed Content Volume	52
Licensed Content Issue	n/a
Licensed Content Pages	13
Type of Use	reuse in a thesis/dissertation
Portion	figures/tables/illustrations
Number of figures/tables/illustrations	1
Format	electronic
Are you the author of this Elsevier article?	No
Will you be translating?	No
Order reference number	3001272744
Original figure numbers	Fig.3
Title of your thesis/dissertation	Graphitic carbon material for enegy and environment
Expected completion date	May 2018
Estimated size (number of pages)	275
Attachment	
Requestor Location	Ramesh Karunakaran Adelaide Univ Adelaide, 5005 Australia Attn: Ramesh Karunakaran
Publisher Tax ID	GB 494 6272 12
Total	0.00 USD



RightsLink®

Home

Account Info

Help



Title: Oxygen Reduction in Alkaline Media: From Mechanisms to Recent Advances of Catalysts
Author: Xiaoming Ge, Afriyanti Sumboja, Delvin Wu, et al
Publication: ACS Catalysis
Publisher: American Chemical Society
Date: Aug 1, 2015
Copyright © 2015, American Chemical Society

Logged in as:

Ramesh Karunakaran

Account #:
3001272744

LOGOUT

PERMISSION/LICENSE IS GRANTED FOR YOUR ORDER AT NO CHARGE

This type of permission/license, instead of the standard Terms & Conditions, is sent to you because no fee is being charged for your order. Please note the following:

- Permission is granted for your request in both print and electronic formats, and translations.
- If figures and/or tables were requested, they may be adapted or used in part.
- Please print this page for your records and send a copy of it to your publisher/graduate school.
- Appropriate credit for the requested material should be given as follows: "Reprinted (adapted) with permission from (COMPLETE REFERENCE CITATION). Copyright (YEAR) American Chemical Society." Insert appropriate information in place of the capitalized words.
- One-time permission is granted only for the use specified in your request. No additional uses are granted (such as derivative works or other editions). For any other uses, please submit a new request.

If credit is given to another source for the material you requested, permission must be obtained from that source.

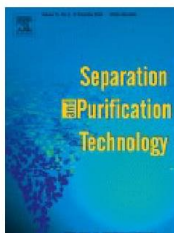
BACK

CLOSE WINDOW

Copyright © 2018 Copyright Clearance Center, Inc. All Rights Reserved. [Privacy statement](#). [Terms and Conditions](#). Comments? We would like to hear from you. E-mail us at customercare@copyright.com



[Home](#)
[Account Info](#)
[Help](#)

Title: Sorption of divalent metal ions from aqueous solution by carbon nanotubes: A review
Author: Gadupudi Purnachadra Rao, Chungsyng Lu, Fengsheng Su
Publication: Separation and Purification Technology
Publisher: Elsevier
Date: 1 December 2007
 Copyright © 2007 Published by Elsevier B.V.

Logged in as:
 Ramesh Karunakaran
 Account #: 3001272744
[LOGOUT](#)

Order Completed

Thank you for your order.

This Agreement between Ramesh Karunakaran ("You") and Elsevier ("Elsevier") consists of your license details and the terms and conditions provided by Elsevier and Copyright Clearance Center.

Your confirmation email will contain your order number for future reference.

[printable details](#)

License Number	4332560452561
License date	Apr 19, 2018
Licensed Content Publisher	Elsevier
Licensed Content Publication	Separation and Purification Technology
Licensed Content Title	Sorption of divalent metal ions from aqueous solution by carbon nanotubes: A review
Licensed Content Author	Gadupudi Purnachadra Rao, Chungsyng Lu, Fengsheng Su
Licensed Content Date	Dec 1, 2007
Licensed Content Volume	58
Licensed Content Issue	1
Licensed Content Pages	8
Type of Use	reuse in a thesis/dissertation
Portion	figures/tables/illustrations
Number of figures/tables/illustrations	1
Format	electronic
Are you the author of this Elsevier article?	No
Will you be translating?	No
Order reference number	3001272744
Original figure numbers	Fig.1
Title of your thesis/dissertation	Graphitic carbon material for energy and environment
Expected completion date	May 2018
Estimated size (number of pages)	275
Attachment	
Requestor Location	Ramesh Karunakaran Adelaide Univ Adelaide, 5005 Australia Attn: Ramesh Karunakaran
Publisher Tax ID	GB 494 6272 12



Title: Study of iron oxide nanoparticle phases in graphene aerogels for oxygen reduction reaction

Author: Ramesh Karunakaran, Campbell Coghlan, Tran Thanh Tung, Shervin Kabiri, Diana N. H. Tran, Christian J. Doonan, Dusan Losic

Publication: New Journal of Chemistry

Publisher: Royal Society of Chemistry

Date: Nov 3, 2017

Copyright © 2017, Royal Society of Chemistry

Logged in as:
Ramesh Karunakaran
Account #:
3001272744

[LOGOUT](#)

Order Completed

Thank you for your order.

This Agreement between Ramesh Karunakaran ("You") and Royal Society of Chemistry ("Royal Society of Chemistry") consists of your license details and the terms and conditions provided by Royal Society of Chemistry and Copyright Clearance Center.

Your confirmation email will contain your order number for future reference.

[printable details](#)

License Number	4345970421097
License date	May 11, 2018
Licensed Content Publisher	Royal Society of Chemistry
Licensed Content Publication	New Journal of Chemistry
Licensed Content Title	Study of iron oxide nanoparticle phases in graphene aerogels for oxygen reduction reaction
Licensed Content Author	Ramesh Karunakaran, Campbell Coghlan, Tran Thanh Tung, Shervin Kabiri, Diana N. H. Tran, Christian J. Doonan, Dusan Losic
Licensed Content Date	Nov 3, 2017
Licensed Content Volume	41
Licensed Content Issue	24
Type of Use	Thesis/Dissertation
Requestor type	non-commercial (non-profit)
Portion	figures/tables/images
Number of figures/tables/images	15
Distribution quantity	100
Format	electronic
Will you be translating?	no
Order reference number	3001272744
Title of the thesis/dissertation	Graphitic carbon material for energy and environment
Expected completion date	May 2018
Estimated size	275
Attachment	
Requestor Location	Ramesh Karunakaran Adelaide Univ